

Spatial Temporal Distribution of Helical Gyrotactic Swimmers

Thesis submitted in accordance
with the requirements of the
University of Liverpool
for the degree of
Doctor in Philosophy
by
Mari Alqarni
May 2018

Abstract

We consider a spherical swimmer that undergoes helical motion due to the existence of a propulsive torque which is not parallel to a propulsive force that pulls the cell through the fluid. In addition, the cell is bottom-heavy; the centre of gravity is offset from the centre of buoyancy which generates a gravitational torque. In the presence of shear, fluid viscosity generates a further torque. Because cells swim at low Reynolds number, these torques are balanced.

This thesis extends the model developed in Bearon (2013) in two distinct directions. Firstly, we consider an extension to the case of a flow where the shear varies with position. We consider a downward flow in a vertical channel. We observe that depending on the parameters, cells may exhibit the classical accumulation towards the centre of the channel or display a new focussing away from the centre.

Secondly, we develop the model to describe randomness associated with changes in cell orientation. This is done by developing a Fokker-Planck equation for helical swimmers in terms of Euler angles. The classical Fokker-Planck equation obtained by Pedley and Kessler (1992) is a special case of the equation derived in this thesis. To implement this model numerically as an individual based model, we derive the corresponding stochastic differential equations.

The Fokker-Planck equation and stochastic differential equation are extended to examine the spatial-temporal distribution of helical swimmers. We explore in detail how the horizontal distribution of cells in channel flow evolves to an equilibrium state, and how the evolution depends on the model parameters.

For non-helical swimmers, we compare the result of the model to the recent experiments of Croze et. al (2017).

Acknowledgements

I would like to thank my supervisor Rachel Bearon for her support, patience and guidance towards the PhD degree. I have learnt a lot with you and my words can not express my heartfelt gratitude and appreciation for all the support and time you had provided during my study. I would like also to thank all members of Mathematical Biology group who gave valuable comments on my presentations. Thank you goes also to my annual panel members Bakhti Vasiev and Ozgur Selsil for their valuable discussion and comments on every annual report.

I would like to thank my parents, my wife, my children, my brothers and sisters for their unconditional love and support. I dedicate this thesis to them.

I would like to acknowledge the Government of Saudi Arabia for financially sponsoring my postgraduate studies.



Contents

Abstract	ii
Acknowledgements	iii
Symbols	x
1 Introduction	1
1.1 Introduction	1
1.2 Gyrotactic swimming trajectories	5
1.3 Fokker–Planck equation	9
1.4 Mechanistic model for helical gyrotaxis	17
1.5 Thesis Outline	22
2 Deterministic model for helical gyrotactic swimmers focussing in channels	24
2.1 Introduction	24
2.2 Non-dimensional orientation model	25
2.3 Cell trajectories in channel flow	29
2.4 Cell orientation in terms of Euler angles	36
2.5 Conclusion	43
3 Orientation distribution of gyrotactic helical swimmers	45
3.1 Introduction	45
3.2 Random walk on a unit sphere	46
3.3 Orientation distribution of non-helical swimmers	51
3.3.1 Gravitactic cells in still fluid	54
3.3.2 Uniform shear flow	58

CONTENTS

3.4	Fokker–Planck Equation for helical swimmers	60
3.4.1	Infinitesimal rotation	64
3.4.2	Infinitesimal rotation generators	65
3.4.3	Fokker–Planck equation	66
3.4.4	Derivation of stochastic differential equation for gyrotactic helical swimmers	68
3.5	Numerical simulation of stochastic differential equation for gyrotactic helical swimmers	71
3.5.1	Gyrotactic bias of helical swimmers in still fluid	75
3.5.2	Uniform flow	79
3.6	Conclusion	95
4	Spatial distribution of stochastic gyrotactic helical swimmers	97
4.1	Introduction	97
4.2	Unbiased diffusion motion in still fluid	100
4.2.1	Stochastic differential equation	102
4.2.2	Linear relationship	103
4.3	Uniform shear flow	111
4.3.1	Spatial-orientation model for non-helical gravitactic swimmers	112
4.3.2	Spatio-orientation model for helical gravitactic swimmers .	113
4.4	Non-uniform shear flow	126
4.4.1	Spatio-orientation model for non-helical gyrotactic swimmers	126
4.4.2	Spatio-orientation model for helical gyrotactic swimmers .	132
4.4.3	Testing stochastic differential equation for non-helical swimmers	147
4.5	Conclusion	152
5	Conclusions	154
5.1	Summary of thesis	154
5.2	Discussion	158
5.3	Potential future work	161
A	Stochastic differential equations	166

CONTENTS

A.1	Connection between Fokker-Planck equation and stochastic differential equation	167
A.2	Euler–Maruyama method	169
A.3	Expectation of non-linear stochastic differential equation	171
B	Derivation of stochastic differential equation 4.27	172
C	Additional figures to Chapter 3	175
D	Additional figures to Chapter 4	178
D.1	Non-helical swimmers	178
D.2	Helical swimmers	180
E	Matlab codes	186
E.1	Matlab codes for Chapter 2	186
E.2	Matlab codes for Chapter 3	201
E.3	Matlab Codes for Chapter 4	224
	Bibliography	255

Symbols

Chapter 1

ν	Swimming speed of the cell.
L	Length scale of cell body.
ρ	Density of the fluid.
μ	Viscosity of the fluid.
p	Pressure.
\mathbf{u}	Fluid flow.
R_e	Reynolds number.
CG	Centre of gravity.
CB	Centre of buoyancy.
h	The distance between CG and CB .
\mathbf{p}	Unit vector in the direction of swimming.
\mathbf{k}	Unit vector in the vertical direction.
\mathbf{L}_g	Gravitational torque acting on a cell.
\mathbf{L}_ν	Viscous torque acting on a cell.
$\boldsymbol{\omega}$	Vorticity of fluid.
\mathbf{V}	Velocity of fluid.
$\boldsymbol{\Omega}$	Angular velocity of the cell.
α_0	Dimensionless measure of the cell eccentricity.
a	Major axis of the cell.
b	Minor axis of the cell.
\mathbf{E}	Rate of strain tensor.
α_{\parallel}	Dimensionless resistance coefficient for rotation about an axis parallel to \mathbf{p} .
α_{\perp}	Dimensionless resistance coefficient for rotation about an axis perpendicular to \mathbf{p} .

CONTENTS

B	Gyrotactic reorientation time scale.
d_t	Brownian translational diffusion coefficient.
d_r	Brownian rotational diffusion coefficient.
κ	Boltzmann's constant.
\mathbf{V}_r	Velocity of the cell relative to its mean.
V_s	Mean cell swimming speed.
\mathbf{q}	Mean swimming direction of the cell.
\mathbf{D}	Diffusion tensor of the cell.
\mathbf{G}	Velocity gradient of fluid.
\mathbf{n}	Unit vector in the direction of the propulsive torque.
R	Reorientation time scale associated with the propulsive torque.
Chapter 2	
\mathbf{x}	Cell position.
\mathbf{V}	Fluid velocity.
$\nu\mathbf{p}$	Swimming velocity of the cell.
Ω	Angular velocity of the cell.
Θ	Non-dimensional propulsive torque strength relative to gravitational torque.
Ψ	Non-dimensional viscous torque strength relative to gravitational torque.
ν	Non-dimensional swimming speed of the cell.
U	Flow speed at the centre of the channel.
L	The distance from the centre of the channel to a wall.
Ψ_{max}	Shear strength.
γ	The angle between the propulsive force and torque.
XYZ	Space fixed frame.
xyz	Body fixed frame.
$\mathbf{i}, \mathbf{j}, \mathbf{k}$	Orthonormal basis vectors for the space axes XYZ .
$\mathbf{e}_1, \mathbf{e}_2, \mathbf{e}_3$	Orthonormal basis vectors for the body axes xyz .
Chapters 3 and 4	
d_r	Dimensional rotational diffusion.
Ω	Angular velocity of the cell.
\mathbf{p}	Unit vector in the direction of cell swimming.
Ψ	Non-dimensional viscous torque strength.

CONTENTS

D_r	Non-dimensional rotational diffusion coefficient.
$\langle . \rangle$	Ensemble average.
Θ	Non-dimensional propulsive torque strength.
γ	The angle between the propulsive force and torque.
\mathbf{q}	Mean swimming direction of the cell.
\mathbf{D}	Non-dimensional diffusion tensor of the cell.
n	Cell concentration.
D_t	Non-dimensional translational diffusion coefficient.
ν	Swimming speed.

Chapter 1

Introduction

1.1 Introduction

Microorganisms are among the most essential creatures on the Earth in view of their decent variety and biomass as well as their significant importance to ecosystems and industrial applications. Microorganisms have been used widely in the industry. Bacteria are used to manufacture antibiotics [108]. In 1929, Alexander Fleming discovered penicillin where he used bacterium *Staphylococcus aureus* [102]. Furthermore, microorganisms can be used in fermentation processes, where cells are used for instance to produce amino acids [111]. In the last decade, microorganisms have been used to develop potential energy resources. Microalgae can accumulate extensive amount of lipids such as triglycerides which can be turned into biofuel [25, 26]. Microalgae appear to displace fossil diesel [25].

Marine phytoplankton are important for the ecosystem and biogeochemical cycles such as carbon, nitrogen, phosphorus, iron and silicon cycles [19]. They consume carbon dioxide and release oxygen. Some of this carbon can be carried into the deep oceans and as a consequence oceans contain about 50 times more soluble inorganic carbon than the atmosphere [89]. Phytoplankton undergo photosynthesis due to chlorophyll presence in the cells so that they can turn

the light into energy. Some phytoplankton can also obtain additional energy through the consumption of other organisms. Phytoplankton are too small to be seen by a naked eye. Their size range from $1\mu\text{m}$ to a few millimeters [50]. They accumulate in large enough numbers to discolour water either green, red, or brown. They are also the primary player in the foundation of the marine food web [73]. Under favourable circumstances, phytoplankton can undergo rapid growth and can easily be seen as blooms [91]. They are important in different natural phenomena. For example, they provide food for other organisms, from microscopic zooplankton to large animals like whales [89]. Some phytoplankton species can produce red tides such as *dinoflagellates* and *diatoms* [98]. However, about 90% of these *diatoms* species can produce harmful blooms (HABs) [96] which may kill marine life [53,96].

The distribution of phytoplankton is very heterogeneous. Vertical movements enable cells to relocate to the depth of ocean which permits them access to abundant nutrients and decreases the predation risks [18]. Furthermore, the cells stay within the well-lit area during the day [94] which allows the photosynthesis process. Thin layers have thickness which varies from less than a meter to a few meters in depth and can extend to few kilometres in the horizontal direction [33]. It comprises different species of microorganism. Durham and Stocker [37] discuss some characteristics of the thin layers such as the criteria of identifying a thin layer and the frequency and persistence of thin layers. They state that a thin layer may last from a few hours to weeks. Many thin layers contain motile cells [16,69,100]. However, non-motile cells such as diatoms do commonly exist [3,99]. Despite this, more investigation about the importance of motility within thin layers is required [37].

Some of motile phytoplankton are eukaryotic, which means cells have a nucleus and other organelles enclosed within a membrane, and are able to swim through fluid by propagating bending waves along their supple flagella [50]. Some green algae beat with two flagella in a breaststroke movement, or they may swim in run and tumble mode in response to chemical gradient as found in the alga *Chlamydomonas reinhardtii* [87]. However, many dinoflagellates swim using

different flagella for propulsion and steering mechanisms [42].

At the small spatial scale of microorganisms, the environment is dominated by the viscous forces. Microorganisms swim by waving and rotating their appendages, which are called flagella or cilia, at low Reynolds number $Re \ll 1$. This number is a dimensionless quantity which measures the ratio of the inertial forces relative to viscous forces and is defined as $Re = \frac{\nu L \rho}{\mu}$ where ν is the swimming speed, L is the length scale of the cell body, and ρ and μ are the density and viscosity of the fluid. As an example of Reynolds number, for a typical bacterium such as *E. coli* with $\nu \approx 10 \mu\text{m s}^{-1}$ and $L \approx 1 - 10 \mu\text{m}$, $Re \approx 10^{-5} - 10^{-4}$.

At zero Reynolds number, the Navier-Stokes equation takes the dimensionless form

$$-\nabla \mathbf{p} + \nabla^2 \mathbf{u} = 0, \tag{1.1}$$

$$\nabla \cdot \mathbf{u} = 0, \tag{1.2}$$

where p is the pressure and \mathbf{u} is the fluid flow. This equation is linear and independent of time. The no-slip boundary conditions is considered at a rigid boundary. This means that at the the rigid boundary we have $\mathbf{u} = \mathbf{0}$. Later, we shall require an expression for the viscous torque exerted on a sphere. In order to obtain this, it is necessary to solve the Stokes equations subject to the no-slip boundary conditions. A consequence of time independence and linearity in Equation (1.1) is Scallop theorem [88] which states that a swimmer must have a swimming stroke that is not time reversible if it is to move [110].

Collisions between a cell and fluid molecules leads to a random displacement of its centre of mass over time. This process is known as Brownian motion [109]. Furthermore, the cells are advected by the flow. These motions are passive motion. However, the cells also transform energy into work in order to move to a desirable environment, an active motion. For the cell to move, it has to generate a force which is called a thrust [109]. For the thrust to be generated, the appendages deform in time-periodic way [70]. The cell moves its flagella or cilia forwards and backwards which creates a bending and twisting wave. For

example, *Chlamydomonas* and *Dunaliella* swim by moving two flagella at ≈ 50 Hz [50].

Microorganisms display different swimming trajectories. For instance, on the surface of *Escherichia coli* there are flagella which bundle behind the cell in a way that it push the cell through fluid in a motion known as a run. The viscous stress lead to a flagellum rotates in the other direction and consequently the cell show tumbling and changing in swimming direction [11]. Some microorganisms undergo taxis, a term that means a response in the swimming direction to the direction of the stimulus source [24]. A response of the cell to the stimulus would require either a large cell size to differentiate organelles' ability to sense a gradient or a memory of progressive levels while in movement [24]. Examples of some taxes are discussed below.

Most microorganisms respond to different chemical substances found in their environment by migrating towards favourable chemicals such as nutrients or away from unfavourable chemicals [106]. Such a response to stimulus is called chemotaxis [15]. Chemotaxis has been observed in many bacteria such as *E. coli*, and green algae such as *Chlamydomonas reinhardtii* exhibit a response to chemical stimuli [48].

Microorganisms also response to light stimuli in which they swim towards the light which is needed for photosynthesis to produce energy. For instance, *Chlamydomonas* algae, which have been used in many flagellar dynamics model system [109], have two flagella each about $12\mu m$ in length which extend from one end of the cell [47]. These two flagella are labeled as cis and trans because of their position with respect to the eye spot which is a a light-detecting organelle. The eye spot is used during phototaxis which means the cells swim towards the light source when it is beneficial for the cell or away from it when it is harmful.

Many motile phytoplankton swim vertically parallel to gravity. Such swimming bias is called gravitaxis or geotaxis [64]. Different hypotheses were proposed to explain this mechanism. Lebert and Hader [71] states that the density difference between the cell and the medium deforms different parts of the cell

membrane which cause the gravitactic orientation bias. Kessler [64, 65] states that the mass distribution of the cell is anisotropic which causes the cells to swim upwards against the gravity. This hypothesis is termed as bottom-heavy and is considered the most acceptable orientation mechanism in flagellated cells such as *Chlamydomonas* [13, 56, 82, 83]. When the cells swim in a fluid flow, the viscosity generates another torque, viscous torque, acting on the cell. The combination of the gravitational and viscous torques affect the swimming behaviour of the cell and such mechanism is termed gyrotaxis [64]. This mechanism will be discussed in the following section and will be considered in this thesis. Another mechanism that describes the cell orientation in a preferred direction aligned with the flow streamlines is called rheotaxis which depends on the shape of the cell [83]. Kaya and Koser [63] discussed rheotaxis trajectories in *E. coli* experimentally. They found that at the channel surface, the cell orientation altered from facing upstream (positive rheotaxis) to facing across the flow as the shear strength is increased. Kantsler et al. [62] discussed rheotaxis in mammalian spermatozoa where the shear rate, wall steric interactions and the cell chirality were shown to guide the steady spiralling trajectories.

1.2 Gyrotactic swimming trajectories

We consider a bottom-heavy cell of density ρ . The centre of gravity \mathbf{CG} is displaced backward relative to the centre of buoyancy \mathbf{CB} . The gravitational torque tends to maintain the centre of the gravity below the centre of buoyancy and the distance between the two centres is denoted by h , (Figure 1.1). Kessler [64] estimates that the magnitude of h varies from 1 – 5% of the mean cell radius for the case of *Dunaliella tertiolecta*. The gravitational force is assumed to act on the cell vertically downward and the buoyant force, because of the pressure gradient in the fluid, acts upward. We denote the swimming direction by a unit vector \mathbf{p} , and \mathbf{k} is a unit vector in the vertical direction. If \mathbf{p} and \mathbf{k} are not parallel, the cell experiences an external torque that acts in such a way as to maintain the centre of gravity below the centre of buoyancy [64] and reduce the

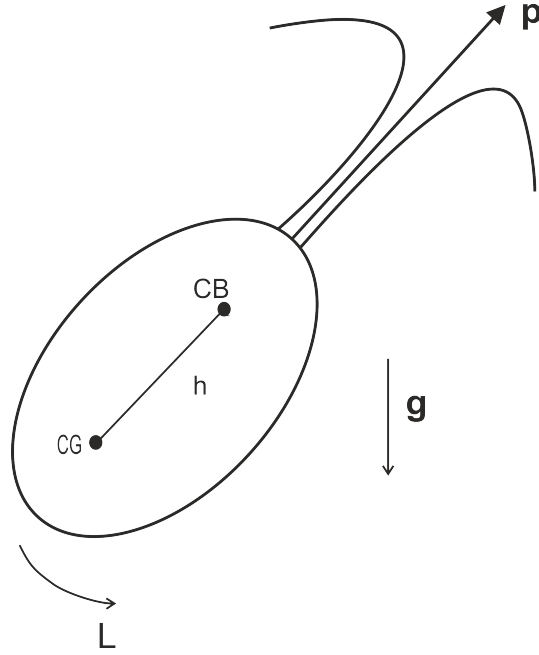


Figure 1.1: **Orientation of cells.** Gravitational force \mathbf{g} is exerted on the cell at point CG in the downwards direction and buoyancy force exerts an upward force through the centre of buoyancy CB . The distance between the two centres is denoted by h . The cell is reoriented by the gravitational torque of magnitude L . Adapted from [65].

angle between \mathbf{p} and \mathbf{k} [83]. This torque is the gravitational torque which is given by [83]

$$\mathbf{L}_g = L\mathbf{p} \wedge \mathbf{k}, \quad (1.3)$$

where $L = hmg$ m is the mass of the cell and g is the gravitational constant. The cell swimming velocity is $\nu\mathbf{p}$.

The viscous torque acting on the cell is given by [83]

$$\mathbf{L}_v = \mathbf{Y} \cdot \left[\frac{1}{2}\boldsymbol{\omega} - \boldsymbol{\Omega} + \alpha_0\mathbf{p} \wedge (\mathbf{E} \cdot \mathbf{p}) \right], \quad (1.4)$$

where

$$\mathbf{Y} = \mu\nu_0 [\alpha_{\parallel}\mathbf{p}\mathbf{p} + \alpha_{\perp}(\mathbf{I} - \mathbf{p}\mathbf{p})], \quad (1.5)$$

where $\boldsymbol{\omega} = \nabla \wedge \mathbf{V}$ is the vorticity of fluid that has velocity \mathbf{V} , $\boldsymbol{\Omega}$ is the angular velocity of the cell, $\alpha_0 = \frac{a^2 - b^2}{a^2 + b^2}$ is a dimensionless measure of the cell eccentricity

where a and b are the major and minor axes of the cell, and $\mathbf{E} = \frac{1}{2}(\nabla\mathbf{V} + (\nabla\mathbf{V})^T)$ is the rate of strain tensor of fluid. The cell volume and the fluid viscosity are ν_0 and μ respectively. The dimensionless α_{\parallel} and α_{\perp} are the resistance coefficients for rotation about axes parallel and perpendicular to \mathbf{p} respectively. Pedley and Kessler [83] defined the angular velocity of the cell as

$$\boldsymbol{\Omega} = \Omega_{\parallel}\mathbf{p} + \mathbf{p} \wedge \dot{\mathbf{p}}, \quad (1.6)$$

where $\Omega_{\parallel} = \boldsymbol{\Omega} \cdot \mathbf{p}$.

Since the microorganisms swim at small Reynolds number, all torques should be balanced, i.e $\mathbf{L}_g + \mathbf{L}_v = \mathbf{0}$. Taking the cross product of $\mathbf{L}_g + \mathbf{L}_v$ with \mathbf{p} , we obtain

$$\frac{d\mathbf{p}}{dt} = \frac{1}{2B}[\mathbf{k} - (\mathbf{k} \cdot \mathbf{p})\mathbf{p}] + \frac{1}{2}\boldsymbol{\omega} \wedge \mathbf{p} + \alpha_0\mathbf{p} \cdot \mathbf{E} \cdot (\mathbf{I} - \mathbf{p}\mathbf{p}), \quad (1.7)$$

where $B = \frac{\mu\alpha_{\perp}}{2g\rho h}$ is the gyrotactic reorientation time scale. The first term on the right describes the cell's bias to remain along the vertical direction due to being bottom-heavy, the second term describes the vorticity that tends to turn the cell due to the viscosity torque acting on the cell, and the third term gives the rate of strain of fluid that exerts a torque on the cell.

The swimming direction is defined in spherical coordinates as

$$\mathbf{p} = (\sin\theta \cos\phi, \sin\theta \sin\phi, \cos\theta), \quad (1.8)$$

where θ is the angle between \mathbf{p} and the vertical direction and ϕ is the angle between the projection of \mathbf{p} onto the horizontal plane measured relative to the x -axis.

Equation (1.7) is used deterministically (i.e in the absence of randomness) to determine the swimming direction of a cell \mathbf{p} as a function of time regardless of any initial condition. The solution tends to a stable equilibrium \mathbf{p}^e in time of order B [83]. If the flow is homogeneous or the time scale of variation of $\boldsymbol{\omega}$ is large compared with B , then the cell trajectory can be calculated by setting $\mathbf{p} = \mathbf{p}^e$ for

all time; however, this is true whenever a stable equilibrium, \mathbf{p}^e , exists [83, 104]. Otherwise, \mathbf{p} will follow an orbit in the unit sphere \mathbf{p} -space [83].

Equation (1.7) also predicts that the equilibrium orientation is stable below a critical value of shear strength $S = |\boldsymbol{\omega}|$ where S has a dimensional unit s^{-1} . For instance, for spherical cells in a simple shear where the velocity gradient is parallel to gravity, $\sin \theta = BS$ for $S < 1$ in the equilibrium scheme whereas for $S > 1$ the cell tumbles [50].

The cell position can be obtained by integrating the velocity resulting from the flow velocity \mathbf{V} and the swimming velocity $\nu\mathbf{p}$ [36]

$$\frac{d\mathbf{x}}{dt} = \mathbf{V} + \nu\mathbf{p}. \quad (1.9)$$

Microorganisms swim in random trajectories. The motion of gyrotactic cells in still fluid can be described as a biased random walk [57].

Thermal Brownian motion can be used to obtain an estimate for translational diffusion d_t and rotational diffusion d_r coefficients. These coefficients are calculated using the thermal energy. As explained by Berg [14], the Brownian translational and rotational diffusion coefficients are

$$d_t = \frac{\kappa T}{f}, \quad d_r = \frac{\kappa T}{f_r}, \quad (1.10)$$

where f is the frictional drag coefficient, f_r is the rotational frictional drag coefficient, Boltzmann's constant $\kappa = 1.38 \times 10^{-16} \text{ cm}^2 \text{ g s}^{-2} \text{ K}^{-1}$ [67] and T is the absolute temperature given in Kelvin. The dimensional units for d_t and d_r are $\text{cm}^2 \text{ s}^{-2}$ and s^{-2} , respectively.

For spherical cells, the total translational force acting on a cell of radius r through an incompressible viscous fluid is $f = 6\pi\mu r$ as Stokes' law states [2], and the rotational force is $f_r = 8\pi\mu r^3$, where μ is the fluid viscosity constant. Substituting these forces into Equation (1.10), we conclude that the translational diffusion for

spherical cells is [14]

$$d_t = \frac{\kappa T}{6\pi\mu r}, \quad (1.11)$$

and rotational diffusion is

$$d_r = \frac{\kappa T}{8\pi\mu r^3}, \quad (1.12)$$

where dynamic viscosity of fluid $\mu = 9 \times 10^{-3} \text{ g cm}^{-1}\text{s}^{-1}$ [85].

The randomness may be a result of biological behaviour of the cell. For *Chlamydomonas nivalis* which has diameter $10\mu\text{m}$ and swimming speed $\nu = 50\mu\text{m s}^{-1}$ [83], effective rotational diffusion which captures intrinsic randomness in swimming behaviour is $d_r = 0.067\text{s}^{-1}$ whilst the Brownian rotational diffusion is $d_r = 1.3 \times 10^{-3}\text{s}^{-1}$.

To describe the motion of individual gyrotactic microorganisms, Pedley and Kessler [82] derived a Fokker–Planck equation which express the motion as a probability function in terms of the position and orientation at time t . This equation is discussed below.

1.3 Fokker–Planck equation

Microorganisms swim in random directions. In the absence of any taxis, the swimming direction \mathbf{p} is therefore a random variable with isotropic probability function $f(\mathbf{p}) = \frac{1}{4\pi}$. Pedley and Kessler [82] proposed a Fokker–Planck equation that describes the orientation of the gyrotactic cells in shear flow. The equation is given by

$$\frac{\partial f}{\partial t} + \nabla_{\mathbf{p}} \cdot (\dot{\mathbf{p}}f) = d_r \nabla_{\mathbf{p}}^2 f, \quad (1.13)$$

where $f = f(\mathbf{p}, t)$ is the probability function of finding a cell with orientation \mathbf{p} at time t , $\dot{\mathbf{p}}$ is the rate of change in the cell orientation given by Equation (1.7),

and d_r is the rotational diffusion that has dimensional unit s^{-1} . Assuming the magnitude of d_r^{-1} is much smaller than the time scale for fluid flow variation, f is a stationary function; the first term was neglected in Equation (1.13). Using Equation (1.7) one can obtain a solution $f(\mathbf{p})$; however, it maybe be difficult to obtain a closed form solution in the general case. Pedley and Kessler [83] use the Fokker–Planck equation to give an estimate for the mean swimming direction and diffusivity tensor for the cell which are given respectively by

$$\mathbf{q} = \int_S \mathbf{p} f(\mathbf{p}) dS, \quad (1.14)$$

$$\mathbf{D}(t) = \int_0^\infty \langle \mathbf{V}_r(t) \mathbf{V}_r(t-t') \rangle dt', \quad (1.15)$$

where S is the surface of the unit sphere, and \mathbf{V}_r is the cell velocity relative to its mean velocity $\mathbf{V}_c = V_s \mathbf{q}$ where V_s is the mean cell swimming speed. Note that computing the diffusivity tensor requires prior knowledge of the cell velocities. If V_s is constant the cell takes τ time to settle to a favoured direction [13] then

$$\mathbf{D} = \int_0^\infty \langle (\mathbf{V}_c - \langle \mathbf{V}_c \rangle) (\mathbf{V}_c - \langle \mathbf{V}_c \rangle) \rangle dt' \quad (1.16)$$

and consequently

$$\mathbf{D} = V_s^2 \tau \langle (\mathbf{p} - \mathbf{q})(\mathbf{p} - \mathbf{q}) \rangle. \quad (1.17)$$

In case of no shear flow, Equation (1.13) in steady form becomes

$$\frac{1}{\sin \theta} \left(\frac{\partial}{\partial \theta} \sin \theta \frac{\partial f}{\partial \theta} \right) + \frac{1}{\sin^2 \theta} \frac{\partial^2 f}{\partial \phi^2} = -\lambda \left(\sin \theta \frac{\partial f}{\partial \theta} + 2 \cos \theta f \right), \quad (1.18)$$

where $\lambda = (2Bd_r)^{-1}$. Note this expression for λ is corrected in Pedley and Kessler [83] by factor of 2. This equation is solved subject to f being positive and finite and satisfying the normalization condition

$$\int_{\phi=0}^{2\pi} \int_{\theta=0}^{\pi} f(\theta, \phi) \sin \theta d\theta d\phi = 1. \quad (1.19)$$

The solution, obtained by Brenner and Weissmann [21] and reported in Pedley and Kessler [82], is given by the Fisher distribution

$$f = \frac{\lambda}{4\pi \sinh \lambda} \exp(\lambda \cos \theta). \quad (1.20)$$

When λ is small this means the randomness in the cell orientation dominates the gravity torque and vice versa when λ is large [83]. The mean swimming direction is

$$\mathbf{q} = (0, 0, \coth \lambda - 1/\lambda), \quad (1.21)$$

and the diagonal entries of \mathbf{D} are

$$D_{11} = D_{22} = V_s^2 \tau K_1 / \lambda, \quad D_{33} = V_s^2 \tau K_2 \quad (1.22)$$

where $K_1 = \coth \lambda - 1/\lambda$ and $K_2 = 1 - \coth^2 \lambda + 1/\lambda^2$.

In case of shear flow, Bees et al [13] obtained an analytical approximation to the solution of the steady Fokker–Planck equation using a spherical harmonic expansion. For a two dimensional flow, the cell orientation probability density function is symmetric about the plane and only even spherical harmonics in ϕ are needed [13]. They expanded f in terms of spherical harmonics

$$f = \sum_{n=0}^{\infty} \sum_{m=0}^n A_n^m \cos m\phi P_n^m(\cos \theta), \quad (1.23)$$

where P_n^m are Legendre polynomials [5]. They used properties of Legendre polynomials to obtain a system of equations which was truncated and then solved using computer algebra to obtain expressions for A_n^m .

Frankel and Brenner [43, 44] developed Taylor dispersion theory for dilute suspensions. The probability density function, $P(\mathbf{x}, \mathbf{p}, t)$, of finding a cell at position \mathbf{x} with orientation \mathbf{p} at time t satisfies

$$\frac{\partial P}{\partial t} + \nabla_{\mathbf{x}} \cdot \mathbf{J} + \nabla_{\mathbf{p}} \cdot \mathbf{j} = 0, \quad (1.24)$$

where the probability current densities are given by

$$\mathbf{j} = \dot{\mathbf{p}}P - d_r \nabla_{\mathbf{p}} P \quad \text{orientation space flux density} \quad (1.25)$$

$$\mathbf{J} = \dot{\mathbf{x}}P - d_t \nabla_{\mathbf{x}} P \quad \text{physical space flux density.} \quad (1.26)$$

This equation will be described in more detail in Chapter 4.

The probability density function, $P(\mathbf{p}, \mathbf{x}, t)$ is also assumed to satisfy

$$\int_{x_\infty} \int_{S_2} P d\mathbf{p} d^3\mathbf{x} = 1 \quad \text{for all } t > 0, \quad (1.27)$$

where x_∞ is the whole Euclidean space and S_2 is the unit sphere. The initial condition is taken to be

$$P(\mathbf{p}, \mathbf{x}, 0) = \delta(\mathbf{x} - \mathbf{x}')\delta(\mathbf{p} - \mathbf{p}'), \quad (1.28)$$

where $\delta(\cdot)$ is the delta function. To ensure that P decays exponentially at infinity, the boundary condition are imposed

$$|\mathbf{x} - \mathbf{x}'|^m (P, \mathbf{J}, \mathbf{j}) = (0, \mathbf{0}, \mathbf{0}) \quad \text{as } |\mathbf{x} - \mathbf{x}'| \rightarrow \infty \quad (1.29)$$

for $m = 0, 1, \dots$.

Ezhilan and Saintillan [40] analysed the transport properties of a dilute suspension of self propelled particles in channel flow. In their model, they considered a Fokker–Planck equation (1.24) with Robin boundary condition at walls

$$D_t \frac{\partial P}{\partial t} = \nu \cos \theta P \quad (1.30)$$

In their model the parameter $A = \frac{D_t D_r}{\nu}$ which its inverse measures the propulsion strength. In the case of zero shear flow, accumulation close to the wall was observed and the thickness of the accumulation layer scaled as $\frac{D_t}{\nu}$ when $A \ll 1$ and with $\sqrt{\frac{D_t}{D_r}}$ when $A \gg 1$. In the case of weak shear strength, they showed that shear rotation of the cells within the accumulation layer cause upwards swimming near the walls. For strong shear, they identify three regions within

the channel: near the walls where the accumulation layer thickness is $\delta \approx A\text{Pe}_s$ where Pe_s is the swimming Péclet number; near the centre of the channel where the thickness of depletion is $\delta \approx \sqrt{\frac{\text{Pe}_s}{\text{Pe}}}$; and a shear trapping away from these two regions where the accumulation can be approximated by a uniform distribution.

A key difference between the Fokker–Planck equation proposed by Pedley and Kessler [82] and that developed by Frankel and Brenner [43, 44] is that the latter defined the probability density function P in terms of the cell position \mathbf{x} and orientation \mathbf{p} at time t rather than only in terms of the orientation \mathbf{p} .

Instead of seeking a solution in high dimension, for a choice of the initial orientation, the averaged orientation probability density function for the asymptotic long time description is

$$\bar{P}(\mathbf{x}, t | \mathbf{x}', \mathbf{p}') = \int_{S_2} P(\mathbf{x}, \mathbf{p}, t | \mathbf{x}', \mathbf{p}') d\mathbf{p}. \quad (1.31)$$

By examining the long time behaviour, \bar{P} was shown to satisfy the following Fokker–Planck equation

$$\frac{\partial \bar{P}}{\partial t} + \nabla_{\mathbf{x}} \cdot \bar{\mathbf{J}} = 0, \quad (1.32)$$

where

$$\bar{\mathbf{J}} = [\mathbf{V}(\mathbf{x}') + (\mathbf{x} - \mathbf{x}') \cdot \mathbf{G} + \mathbf{U}] \bar{P} - \mathbf{D} \cdot \nabla_{\mathbf{x}} \bar{P}, \quad (1.33)$$

where $\mathbf{G} = (\nabla \mathbf{V})^T$ is the velocity gradient, and \mathbf{U} and \mathbf{D} are the drift velocity and effective diffusion respectively [56]. This equation can alternatively be understood as the cells concentration, $n(\mathbf{x}, t)$.

Hill and Bees [56] used the results of [44] to obtain expressions for the drift

velocity and effective diffusion

$$\mathbf{U} = \int_S P_0^\infty(\mathbf{p}) V_s \mathbf{p} dS \quad (1.34)$$

$$\mathbf{D} = V_s \int_S P_0^\infty(\mathbf{p}) [\mathbf{B}\mathbf{p}]^{sym} dS, \quad (1.35)$$

where $P_0^\infty = \lim_{t \rightarrow \infty} \int_{\mathbf{x}^\infty} P(\mathbf{x}, \mathbf{p}, t | \mathbf{x}', \mathbf{p}') d^3\mathbf{x}$ satisfies the steady Fokker–Planck equation in orientation space, i.e. it is same as the f we introduced in Equation (1.13), and $[\cdot]^{sym}$ denotes the symmetric part of the tensor. The vector field \mathbf{B} is interpreted as the long time limit of the difference between the average position of the particle given its orientation is \mathbf{p} and its average position averaged over all orientation [56] and satisfies

$$\nabla_{\mathbf{p}} \cdot [\dot{\mathbf{p}} P_o^\infty \mathbf{B} - d_r \nabla_{\mathbf{p}} (P_o^\infty \mathbf{B})] - P_o^\infty \mathbf{B} \cdot \mathbf{G} = P_o^\infty (V_s \mathbf{p} - \mathbf{U}), \quad (1.36)$$

subject to

$$\int_S P_o^\infty \mathbf{B} dS = 0. \quad (1.37)$$

Defining Péclet number $Pe = \frac{G}{d_r}$, Equation (1.36) becomes [56]

$$\nabla_{\mathbf{p}} \cdot [Pe \hat{\mathbf{p}} \mathbf{b} - \nabla_{\mathbf{p}} \mathbf{b}] - Pe \mathbf{b} \cdot \hat{\mathbf{G}} = P_o^\infty (\mathbf{p} - \mathbf{q}), \quad (1.38)$$

where $\mathbf{b} = \frac{d_r}{V_s} P_o^\infty \mathbf{B}$, $\hat{\mathbf{G}} = \frac{\mathbf{G}}{G}$, and $\hat{\mathbf{p}} = \frac{1}{G} \dot{\mathbf{p}}$ where $G = \|\mathbf{G}\|$. Constraint (1.37) thus becomes

$$\int_S \mathbf{b} dS = 0. \quad (1.39)$$

The drift velocity and the effective diffusion are thus computed using [56]

$$\mathbf{U} = \int_S f V_s \mathbf{p} dS = V_s \mathbf{q}, \quad (1.40)$$

$$\mathbf{D} = \frac{V_s^2}{d_r} \int_S [\mathbf{b}\mathbf{p}]^{sym} dS. \quad (1.41)$$

These two quantities are important in modelling a suspension of microorganisms. The concentration of the cells, n , satisfies the advection–diffusion equation

$$\frac{\partial n}{\partial t} = -\nabla_{\mathbf{x}} \cdot \left[\left(\mathbf{V} + V_s \mathbf{q} \right) n - \frac{\nu^2}{d_r} \mathbf{D} \cdot \nabla_{\mathbf{x}} n \right]. \quad (1.42)$$

The first two terms on the right hand side represent the advection of the cells by the fluid velocity and the cell motion due to the swimming, and the last term represents the diffusivity of the cells. They can be evaluated either using Fokker–Planck equation theory or Taylor dispersion theory.

In two dimensional vertical Poiseuille flow, Bearon et al. [10] discussed the motion of the cells across the streamlines of the flow. For small constant shear, the horizontal components of velocity drift and effective diffusion are [10]

$$q_x = \frac{Pr}{2\kappa} \left(\frac{1}{I_0(\kappa)^2} - 1 + \alpha_0 \frac{I_2(\kappa)}{I_0(\kappa)} \right) \quad (1.43)$$

$$D_{xx} = \frac{1}{\kappa^2} \left(1 - \frac{1}{I_0(\kappa)^2} \right), \quad (1.44)$$

where $Pr = \frac{G}{d_r}$ is the non-dimensional shear strength, $\kappa = \frac{1}{2Bd_r}$ is the non-dimensional gravitational time scale, I_0 is the modified Bessel function of the first kind and zero order. For large shear value

$$q_x = -\frac{\kappa}{Pr(1 + \alpha_0)}, \quad (1.45)$$

$$D_{xx} = \frac{2 - \alpha_0}{Pr^2(1 - \alpha_0)(1 + \alpha_0)^2}. \quad (1.46)$$

To derive Equations (1.43-1.46), we consider a two–dimensional flow and a perturbation expansion for f and \mathbf{b} . Detailed derivation is given in [10].

For Poiseuille flow, locally the shear was assumed constant such that Equations (1.45-1.46) were valid. We will re-visit Equation (1.42) in Chapter 4 when studying the accumulation of non-helical swimmers in a vertical channel.

In a shallow suspension of cells, where the cells swim upwards against the gravity, the up-swimming cells form a layer of cells. Cells are slightly denser than the fluid

they swim in [65]. The top layer therefore becomes denser than the lower which results in gravitactic instability. Such pattern is called bioconvection [83]. The name was introduced in 1961 [86]. It is analogous to Rayleigh–Benard convection [58]. Hill and Pedley [58] considered equation (1.42) coupled with Navier–Stokes equations to predict the pattern formation in bioconvection. They considered uniform and shallow suspension of *Chlamydomonas nivalis*. They found that the unstable horizontal length scale is about 9 mm. Recently, Hwang and Pedley [59] studied the source of instability in a shallow suspension. They analysed the impact of the flow on stabilizing or destabilizing the suspension. They found that in weak flow the gyrotactic instability and diffusion-oriented mechanisms rule the behaviour of high wave number stabilization while gravitational overturning rules the low wave number destabilization as a consequence of the thickness of unstable layer near the surface due to the shear. Also, they found that above a critical shear rate, all wave numbers are stabilized and hence the bioconvection is suppressed.

Many phytoplankton do not swim in a straight line, instead they swim in helical paths [17, 29, 51]. Jennings [60] proposed that helical trajectories enable microorganism to move along the direction of the stimulus. Microorganisms can adjust their helical movement in response to two stimuli phototaxis and chemotaxis. Such a biased motion is called helical klinotaxis [29]. This orientation was developed theoretically and observed experimentally during chemotaxis in *Paramecium*, and in the bacterium *Thiovulum* [48]. Pak and Lauga [81] proposed a mechanistic model using a squirmer model which undergoes helical trajectories if the net forces and net torques are not parallel. In the following section, we give a brief review of the mechanistic model proposed by [6] to understand helical trajectories in uniform shear flow.

1.4 Mechanistic model for helical gyrotaxis

A mechanistic model that describes the helical motion of gyrotactic cells was developed by Bearon [6] using *Heterosigma akashiwo* algae. In this section we give an overview of the model and the main results that are relevant to developing the model in the subsequent chapters of the thesis.

Heterosigma is a fast swimmer with vertical biased swimming speed $\nu = 85 \mu\text{m s}^{-1}$ [8]. It can swim in helical trajectories represented as the instantaneous axis of the helix [30], straight paths, or even display transition between the two modes [8].

Heterosigma akashiwo is asymmetrical cell of dimension $12 - 23 \mu\text{m}$ in length and $8 - 12 \mu\text{m}$ in width [105] (Figure 1.2). The cell does not have a rigid cell wall which allows the cell to change its shape [90]. It has two flagella that arise from separate pits in the flagellar groove [105] which are equal in length and both have the same length as the cell [103]. The anterior-facing flagellum provides a propulsive force which generates a swimming velocity $\nu\mathbf{p}$ where \mathbf{p} is a unit vector embedded in the cell. This force pulls the cell through the fluid [90]. The second flagellum, which has unclear purpose [54], is proposed to generate a propulsive torque in the direction of the unit vector \mathbf{n} . Thus, the cell undergoes helical motions [51]. This organism is bottom-heavy which generates gravity torque in the direction $-\mathbf{p} \wedge \mathbf{k}$.

To compute Reynolds number for *Heterosigma akashiwo*, we note that the fluid density and viscosity are $\rho = 10^3 \text{ kg m}^{-3}$ and $\mu = 10^{-3} \text{ Pa s}$ respectively [70]. Therefore $\text{Re} = 0.001 - 0.002$.

In Figure 1.3, we depict the cell and the torques acting on it. The cell swims according to the following ordinary differential equations

$$\frac{d\mathbf{x}}{dt} = \mathbf{V} + \nu\mathbf{p}, \quad (1.47)$$

$$\frac{d\mathbf{p}}{dt} = \boldsymbol{\Omega} \wedge \mathbf{p}, \quad (1.48)$$

$$\frac{d\mathbf{n}}{dt} = \boldsymbol{\Omega} \wedge \mathbf{n}, \quad (1.49)$$

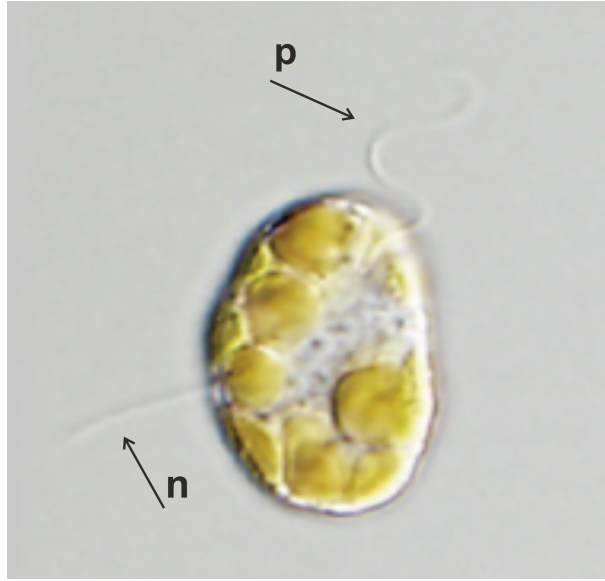


Figure 1.2: *Heterosigma akashiwo*. The cell has two flagella, one the pulls the cell through the fluid (denoted by \mathbf{p}) and another flagellum has unclear purpose (denoted by \mathbf{n}). Reprinted from [39] with permission of Phycologia .

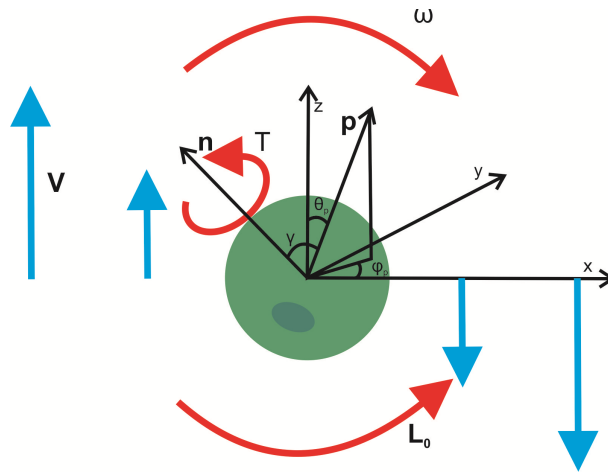


Figure 1.3: **Diagram of a model organism and its coordinate system.** The cell orientation is described by two unit vectors, \mathbf{p} and \mathbf{n} . The vector \mathbf{p} is represented in spherical polar coordinates by the angles (θ_p, ϕ_p) . The angle γ is the (constant) angle between the vectors \mathbf{p} and \mathbf{n} . The cell swims in the direction \mathbf{p} and is situated in vertical shear flow with velocity \mathbf{V} represented by the vertical arrows. The cell is reoriented by the three torques indicated by the curved arrows: gravity, of magnitude L_0 , due to being bottom heavy as indicated by the shaded ellipse; viscosity, in that it is rotated due to the vorticity of the flow $\boldsymbol{\omega}$ and an intrinsic torque of magnitude T in the direction of \mathbf{n} . Taken from [4].

where \mathbf{x} is the cell position, \mathbf{V} is the local fluid velocity, $\nu\mathbf{p}$ is the cell swimming velocity, and the angular velocity $\boldsymbol{\Omega}$ is defined as

$$\boldsymbol{\Omega} = \frac{1}{2B}\mathbf{p} \wedge \mathbf{k} + R\mathbf{n} + \frac{1}{2}\boldsymbol{\omega}, \quad (1.50)$$

where $\frac{1}{2B}$ (denoted by G in [6]) and R are reorientation time scales associated with the gravitational and propulsive torques, respectively, \mathbf{k} is a unit vector in the direction of z -axis, and $\boldsymbol{\omega} = \nabla \wedge \mathbf{V}$ is the vorticity of the fluid. Throughout the thesis we consider $\boldsymbol{\omega} = \omega\mathbf{j}$ because we consider a flow in xz -plane. The quantities $\frac{1}{2B}$ and R in (1.50) are given as $\frac{1}{2B} = \frac{L_o}{8\pi\mu a^3}$, $R = \frac{T}{8\pi\mu a^3}$ where μ is the fluid viscosity, a is the radius of the cell, and L_o and T are the magnitude of gravity and propulsive torques respectively. The angular velocity equation is obtained by setting the total torque on the cell to be zero. To explain this more, the torque on the cell from intrinsic motion and gravity is given by

$$\mathbf{L} = L_o\mathbf{p} \wedge \mathbf{k} + T\mathbf{n}. \quad (1.51)$$

We add here the propulsive torque to the gravitational torque given by Equation (1.3).

From Equation (1.4) if we restrict attention to spherical cells, $\alpha_0 = 0$, then $\mathbf{Y} = \mu\nu\alpha_\perp\mathbf{I}$, where $\alpha_\perp = 6$ [59] and $\nu = \frac{4}{3}\pi a^3$. Therefore, the viscous torque on the sphere rotating with angular velocity $\boldsymbol{\Omega}$ in the presence of the vorticity $\boldsymbol{\omega}$ is given by [66]

$$\mathbf{L}_v = 8\pi\mu a^3\left(\frac{1}{2}\boldsymbol{\omega} - \boldsymbol{\Omega}\right). \quad (1.52)$$

Since microorganisms swim at low Reynolds number and the torques are balanced, then setting $\mathbf{L} + \mathbf{L}_v = \mathbf{0}$ we obtain Equation (1.50).

Using spherical coordinates, we write the unit vector \mathbf{p} as

$$\mathbf{p} = (\sin\theta_p \cos\phi_p, \sin\theta_p \sin\phi_p, \cos\theta_p),$$

where θ_p is the angle that the vector \mathbf{p} makes with vertical and ϕ_p is the angle that the projection of \mathbf{p} makes with x -axis. In the same way we can define the angles θ_n and ϕ_n to describe the vector \mathbf{n} .

To convert vector Equations (1.48-1.49) into scalar ordinary differential equations for the variables $\sin \theta_p, \cos \phi_p, \sin \theta_n$ and $\cos \phi_n$, we consider a general unit vector \mathbf{u} with angular velocity $\boldsymbol{\Omega}$, then

$$\begin{aligned} \frac{d\mathbf{u}}{dt} &= \boldsymbol{\Omega} \wedge \mathbf{u} \\ &= \frac{1}{2B} [(\mathbf{u} \cdot \mathbf{p})\mathbf{k} - (\mathbf{u} \cdot \mathbf{k})\mathbf{p}] + R\mathbf{n} \wedge \mathbf{u} + \frac{1}{2}\boldsymbol{\omega} \wedge \mathbf{u}. \end{aligned} \quad (1.53)$$

Define the orthonormal spherical polar coordinate system

$$\mathbf{u} = (\sin \theta_u \cos \phi_u, \sin \theta_u \sin \phi_u, \cos \theta_u), \quad (1.54)$$

$$\mathbf{e}_{\theta_u} = (\cos \theta_u \cos \phi_u, \cos \theta_u \sin \phi_u, -\sin \theta_u), \quad (1.55)$$

$$\mathbf{e}_{\phi_u} = (-\sin \phi_u, \cos \phi_u, 0). \quad (1.56)$$

Since $\mathbf{u} = \mathbf{u}(\theta, \phi)$, by chain rule we write

$$\frac{d\mathbf{u}}{dt} = \mathbf{e}_{\theta_u} \frac{d\theta}{dt} + \sin \theta_u \mathbf{e}_{\phi_u} \frac{d\phi}{dt} \quad (1.57)$$

To get expressions for $\frac{d\theta}{dt}$ and $\frac{d\phi}{dt}$ we take the dot product of Equation (1.53) with \mathbf{e}_{θ_u} and then with \mathbf{e}_{ϕ_u} to get expression for $\frac{d\theta_u}{dt}$ and then $\frac{d\phi_u}{dt}$ respectively. We finally replace u by p and n to obtain the following set of ordinary differential equations that describes the orientation of the cell

$$\frac{d\theta_p}{dt} = -\frac{1}{2B} \sin \theta_p + R \sin \theta_n \sin(\phi_n - \phi_p) + \frac{1}{2}\omega \cos \phi_p, \quad (1.58)$$

$$\sin \theta_p \frac{d\phi_p}{dt} = -R [\sin \theta_n \cos \theta_p \cos(\phi_n - \phi_p) - \cos \theta_n \sin \theta_p] - \frac{1}{2}\omega \cos \theta_p \sin \phi_p, \quad (1.59)$$

$$\frac{d\theta_n}{dt} = -\frac{1}{2B} \sin \theta_p \cos(\phi_p - \phi_n) + \frac{1}{2}\omega \cos \phi_n, \quad (1.60)$$

$$\sin \theta_p \frac{d\phi_n}{dt} = \cos \theta_n \left[\frac{1}{2B} \sin \theta_p \sin(\phi_n - \phi_p) - \frac{1}{2}\omega \sin \phi_n \right]. \quad (1.61)$$

We define the angle γ between \mathbf{p} and \mathbf{n} by

$$\mathbf{p} \cdot \mathbf{n} = \sin \theta_p \sin \theta_n \cos(\phi_p - \phi_n) + \cos \theta_p \cos \theta_n = \cos \gamma. \quad (1.62)$$

This angle is constant because \mathbf{p} and \mathbf{n} are assumed to be embedded in the cell and the cell is rotating with angular velocity of the cell. If $\gamma = 0$, then \mathbf{p} and \mathbf{n} are identical; hence the swimming trajectories can be determined using Equations(1.58-1.59). This means that the model recovers the case for non-helical swimmers.

In case of uniform vertical shear flow $\mathbf{V} = -\omega x \mathbf{k}$. The equilibrium orientation is given by

$$\mathbf{p}^e = (p_x^e, p_y^e, p_z^e) \quad (1.63)$$

where

$$p_x^e = B\omega - 2BR\sqrt{1 - \frac{1}{B^2\omega^2} \cos^2 \gamma}, \quad (1.64)$$

$$p_y^e = -\frac{2R}{\omega} \cos \gamma, \quad (1.65)$$

$$p_z^e = \sqrt{1 - (p_x^e)^2 - (p_y^e)^2}. \quad (1.66)$$

This equilibrium is feasible when $\frac{1}{B\omega} \cos \gamma \leq 1$ so that p_x^e is real. Note that this constraint is not sufficient for \mathbf{p} to be a real value. We will impose another constraint on p_z^e in the next chapter.

In case of zero shear flow, cells swim upwards in helical trajectories (Figure 4.17a). In case of vertical downwards uniform flow $\mathbf{V} = -\omega x \mathbf{k}$; when the shear flow is weak, the cells swim downwards in the positive x direction and the helical motions are suppressed. Increasing the shear further results in cells swimming in the positive x direction towards downwards flow.

The propulsive torque strength effect the swimming trajectories. For strong shear the helical motion may be suppressed and cells can swim upwards as shown in Figure 4.22c.

1.5 Thesis Outline

In Chapter 1 we have presented an overview and background for microorganism swimming trajectories.

Chapter 2 is an extension of the model presented in [6] to the case of non-uniform shear flow where the cell orientation is a function of variable vorticity. This work has been published in Physics of Fluids journal [4]. For non-helical swimmers the classical accumulation in the center of downward Poiseuille flow in a vertical channel is observed. For helical swimmers, depending on the propulsive torque strength, cells may exhibit the classical focussing in the centre of the channel or accumulate away from the centre. We conclude this chapter by converting the orientation equations of helical cells $\theta_p, \phi_p, \theta_n, \phi_n$ to Euler angles θ, ϕ, ψ . This conversion enables us to derive Fokker–Planck equation for helical swimmers because it reduces the number of degrees of freedom from four to three.

We start Chapter 3 by reviewing the random walk on a unit sphere. The probability distribution function of this Brownian motion is the solution of the diffusion equation in spherical coordinates (θ, ϕ) . Using Gardiner [45], we write the stochastic differential equation (SDE) that describes the randomness generated by Brownian motion. This SDE has a drift term which is called spurious drift. In a similar way, we derive the stochastic differential equation (SDE) for non-helical gyrotactic swimmers. Such swimmers are biased by gravitational and vorticity torques which form the drift term in the SDE in addition to the spurious drift. We also use the numerical simulations of SDEs to compare the orientation distribution with FPE solution in still fluid. We then derive the Fokker–Planck equation (FPE) for the helical swimmers by first expressing FPE in terms of the generators of infinitesimal rotation about the body fixed axes and then using the relationship between these generators and Euler angles. We lastly derive the SDE that describes the orientation of the helical swimmers.

In Chapter 4 we consider the spatial distribution of cells. We first consider the case of no bias swimmer in still fluid. Then we consider the non-helical swimmers

and helical swimmers in uniform flow. We will examine the effect of randomness and bias coefficients on swimming behaviour. Lastly, we consider the case where the shear is a function of the cells' position and discuss the impact of randomness and bias coefficients on accumulation in the channel. We also compare results from our stochastic differential equations simulations with recent experiments of the non-helical swimmer alga *Dunaliella salina*.

In Chapter 5 we provide a summary of thesis and some potential future researches which are extension of the model discussed in thesis.

Chapter 2

Deterministic model for helical gyrotactic swimmers focussing in channels

2.1 Introduction

In this chapter, we extend the model developed by Bearon [6] to the case of non-uniform flow. We consider downward Poiseuille flow in a vertical channel between two parallel walls where the vorticity is no longer constant but will vary across the channel. We analyse the orientation of the cells as a function of vorticity. We investigate how the model parameters alter the focussing behaviour and in particular show that accumulation away from the centre of the channel can occur depending on the parameters values. This work has been published in *Physics of Fluids* [4].

The cell's orientation is described by four angles, but rotation of a cell in space with respect to a system of reference fixed in space requires three degrees of freedom [76]. To write the orientation of the cell with three degrees of freedom, we use Euler angles (θ, ϕ, ψ) in Section 2.4 where θ and ϕ have the same definitions as θ_p and ϕ_p given in [6] respectively, and ψ is the angle that describes the rotation

of the propulsive torque with respect to the swimming direction. Euler angles will then be used to develop a Fokker–Planck equation for helical gyrotactic swimmers in the next chapter.

2.2 Non-dimensional orientation model

We consider a self-propelled cell which generates a propulsive force in the direction of the unit vector \mathbf{p} and a propulsive torque in the direction of the unit vector \mathbf{n} , as depicted in Figure 1.3. The angle between the vectors \mathbf{p} and \mathbf{n} is given by γ which may be non-zero and is assumed constant. The propulsive force results in the cell swimming in the direction of \mathbf{p} , and the propulsive torque contributes to determining how the vector \mathbf{p} rotates.

The cell swims according to the following ordinary differential equations [6] where time is non-dimensionalized on a gravitational time scale $2B$

$$\frac{d\mathbf{x}}{dt} = \mathbf{V} + v\mathbf{p}, \quad (2.1)$$

$$\frac{d\mathbf{p}}{dt} = \boldsymbol{\Omega} \wedge \mathbf{p}, \quad (2.2)$$

$$\frac{d\mathbf{n}}{dt} = \boldsymbol{\Omega} \wedge \mathbf{n}, \quad (2.3)$$

where \mathbf{x} is the cell position, \mathbf{V} is the local fluid velocity and $v\mathbf{p}$ is the swimming velocity of the cell. The angular velocity $\boldsymbol{\Omega}$ is defined as

$$\boldsymbol{\Omega} = \mathbf{p} \wedge \mathbf{k} + \Theta\mathbf{n} + \Psi\boldsymbol{\omega}, \quad (2.4)$$

where $\Theta = 2BR$ and $\Psi = B|\boldsymbol{\omega}|$ are non-dimensional parameters representing the strength of the propulsive torque and viscous torque relative to the gravitational torque respectively. We assume that all parameters are positive and Ψ is assumed constant but shall consider non-constant Ψ in Section 2.3. The non-dimensional swimming speed of the cell is $\nu = \frac{2B\nu}{L}$ which is taken to be $\nu = 0.1$ in the simulations. The gravitational time scale is denoted by B and the width of the channel is $2L$.

For simplicity, we consider fluid flow constrained to be in the xz -plane so that the vorticity is given by $\boldsymbol{\omega} = \mathbf{j}$ where \mathbf{j} is a unit vector in the y -direction.

As discussed in Section 1.4, it is possible to convert the vector equations $\frac{d\mathbf{p}}{dt}$ and $\frac{d\mathbf{n}}{dt}$ into scalar equations for the variables $\theta_p, \phi_p, \theta_n$ and ϕ_n . These equations in non-dimensional form are given as

$$\frac{d\theta_p}{dt} = -\sin \theta_p + \Theta \sin \theta_n \sin(\phi_n - \phi_p) + \Psi \cos \phi_p, \quad (2.5)$$

$$\sin \theta_p \frac{d\phi_p}{dt} = -\Theta [\sin \theta_n \cos \theta_p \cos(\phi_n - \phi_p) - \cos \theta_n \sin \theta_p] - \Psi \cos \theta_p \sin \phi_p, \quad (2.6)$$

$$\frac{d\theta_n}{dt} = -\sin \theta_p \cos(\phi_p - \phi_n) + \Psi \cos \phi_n, \quad (2.7)$$

$$\sin \theta_n \frac{d\phi_n}{dt} = \sin \theta_p \cos \theta_n \sin(\phi_n - \phi_p) - \Psi \cos \theta_n \sin \phi_n. \quad (2.8)$$

In order that the cell dynamics be understood, we must first examine the equilibrium solutions $\mathbf{p} = \mathbf{p}^e$ and $\mathbf{n} = \mathbf{n}^e$ for constant vectors \mathbf{p}^e and \mathbf{n}^e . Assuming that \mathbf{p} and \mathbf{n} are not parallel and the angle between them is defined by

$$\cos \gamma = \mathbf{p} \cdot \mathbf{n} \quad (2.9)$$

In order to obtain the equilibrium orientation solution we should have $\boldsymbol{\Omega} \wedge \mathbf{p} = \mathbf{0}$ and $\boldsymbol{\Omega} \wedge \mathbf{n} = \mathbf{0}$ simultaneously. Because \mathbf{p} and \mathbf{n} are not parallel then we require $\boldsymbol{\Omega} = \mathbf{0}$. We take the dot product of angular velocity $\boldsymbol{\Omega} = \mathbf{0}$ with the unit basis vectors \mathbf{i}, \mathbf{j} , and \mathbf{k} as following

$$\boldsymbol{\Omega} \cdot \mathbf{i} = p_y^e + \Theta n_x^e = 0, \quad (2.10)$$

$$\boldsymbol{\Omega} \cdot \mathbf{j} = -p_x^e + \Theta n_y^e + \Psi = 0, \quad (2.11)$$

$$\boldsymbol{\Omega} \cdot \mathbf{k} = \Theta n_z^e = 0. \quad (2.12)$$

Multiplying Equation (2.10) by p_x^e and Equation (2.11) by p_y^e then adding them up, we get

$$\Theta(p_x^e n_x^e + p_y^e n_y^e) + \Psi p_y^e = 0. \quad (2.13)$$

Note that Equation (2.12) reduces Equation (2.9) to

$$\cos \gamma = p_x^e n_x^e + p_y^e n_y^e. \quad (2.14)$$

Inserting Equation (2.14) into Equation (2.13), gives

$$p_y^e = -\frac{\Theta}{\Psi} \cos \gamma. \quad (2.15)$$

Noting that \mathbf{n} is a unit vector, we obtain expression for n_x^e and n_y^e from Equations (2.10-2.11). From Equation (2.12) we can substitute these expressions in $n_x^{e2} + n_y^{e2} = 1$ to obtain

$$\frac{1}{\Psi^2} \cos^2 \gamma + \frac{1}{\Theta^2} (p_x^e - \Psi)^2 = 1. \quad (2.16)$$

Taking the square root, we get expression for p_x^e

$$p_x^e = \Psi \pm \Theta \sqrt{1 - \frac{1}{\Psi^2} \cos^2 \gamma}. \quad (2.17)$$

In [6], the stable equilibrium solution is identified as

$$p_x^e = \Psi - \Theta \sqrt{1 - \frac{1}{\Psi^2} \cos^2 \gamma}, \quad (2.18)$$

$$p_y^e = -\frac{\Theta}{\Psi} \cos \gamma, \quad (2.19)$$

$$p_z^e = \sqrt{1 - (p_x^e)^2 - (p_y^e)^2}. \quad (2.20)$$

In order to determine the feasibility region for the equilibrium solution in (Θ, Ψ) parameter space, we must ensure that the components of \mathbf{p} are real. Particularly for p_x^e to be a real value we require

$$\frac{\cos \gamma}{\Psi} \leq 1, \quad (2.21)$$

and when subsequently we substitute Equations (2.18-2.19) into the following

condition

$$(p_x^e)^2 + (p_y^e)^2 \leq 1,$$

which is obtained from Equation (2.20) to ensure p_z^e is a real value, we hence obtain the following quadratic inequality for Θ

$$\Psi^2 - 2\Theta\Psi\sqrt{1 - \left(\frac{\cos \gamma}{\Psi}\right)^2} + \Theta^2 \leq 1. \quad (2.22)$$

To determine the feasibility for the equilibrium solution in (Θ, Ψ) parameter space, the above inequality is solved for Θ to obtain

$$\Psi\sqrt{1 - \left(\frac{\cos \gamma}{\Psi}\right)^2} - \sin \gamma \leq \Theta \leq \Psi\sqrt{1 - \left(\frac{\cos \gamma}{\Psi}\right)^2} + \sin \gamma, \quad (2.23)$$

or in a similar way, this can be written as a constraint for Ψ

$$\sqrt{\Theta^2 - 2\Theta \sin \gamma + 1} \leq \Psi \leq \sqrt{\Theta^2 + 2\Theta \sin \gamma + 1}. \quad (2.24)$$

From Equation (2.9) we note that $\mathbf{p} \cdot \mathbf{n}$ is a constant and thus the angle γ should be understood as an initial constant not a constraint. To see this, remark that (using Equations (2.2–2.3))

$$\begin{aligned} \frac{d\mathbf{p} \cdot \mathbf{n}}{dt} &= \mathbf{p} \cdot \frac{d\mathbf{n}}{dt} + \frac{d\mathbf{p}}{dt} \cdot \mathbf{n} \\ &= \mathbf{p} \cdot (\boldsymbol{\Omega} \wedge \mathbf{n}) + (\boldsymbol{\Omega} \wedge \mathbf{p}) \cdot \mathbf{n} \\ &= -(\boldsymbol{\Omega} \wedge \mathbf{p}) \cdot \mathbf{n} + (\boldsymbol{\Omega} \wedge \mathbf{p}) \cdot \mathbf{n} \\ &= 0. \end{aligned} \quad (2.25)$$

In Figure (2.1), the outer boundary of the region in which equilibrium solutions exist is demarcated through the inequalities given by (2.21 and 2.23). It is important to notice that the singular behaviour for $\Theta = 0$ as the lower bound $\Psi \geq \cos \gamma$ need not be fulfilled for the existence of an equilibrium solution for

non-helical swimmers. This is due to the fact that it is possible to find an equilibrium solution for small shear rates, ($0 < \Psi < 1$), where the propulsive torque is not present, i.e $\Theta = 0$ and the equilibrium solution is thus the line segment $0 < \Psi < 1$. When the propulsive torque exists, $\Theta \neq 0$, at low shear rates, however, the cells lose equilibrium orientation as they undergo helical trajectories.

In view of the behaviour of cells outside the feasibility region, for non-helical swimmers, $\Theta = 0$, a strong enough vorticity, $\Psi > 1$ where the equilibrium is not feasible, cells tumble with period of oscillation given by $\tau = \frac{2\pi}{\sqrt{\Psi^2-1}}$. This expression is corrected by a factor of 2 from that given by [52] (referenced in Pedley and Kessler [83]). For non-helical swimmers, the average cell orientation during an oscillation period which is constrained to the xz -plane where $\phi_p = 0$ is given by

$$\begin{aligned}\bar{p}_x &= \frac{1}{T} \int_0^T \sin \theta(t) dt = \frac{1}{T} \int_0^{2\pi} \frac{\sin \theta}{\Psi - \sin \theta} d\theta \\ &= \Psi - \sqrt{\Psi^2 - 1}.\end{aligned}\tag{2.26}$$

It is worth mentioning that $\bar{p}_x = 1$ for $\Psi = 1$, is in concurrence with the equilibrium solution which from Equation (2.18) with $\Theta = 0$ is $p_x^e = \Psi$.

Figure 2.3 shows numerical computations of \bar{p}_x for different values for propulsive torque over a range of shear. In Figure 2.3(b)-(d), we note that when the shear is weak, the average value of p_x shows no difference for helical or non-helical swimmers. In other word, $\bar{p}_x = \Psi$. Figure 2.3c, though, shows that as the shear increases, it generates a new equilibrium solutions, the average value of p_x drops and becomes negative.

2.3 Cell trajectories in channel flow

In this section, the swimming trajectories of gyrotactic cells in Poiseuille flow in a vertical channel between two parallel walls that are separated by a distance of

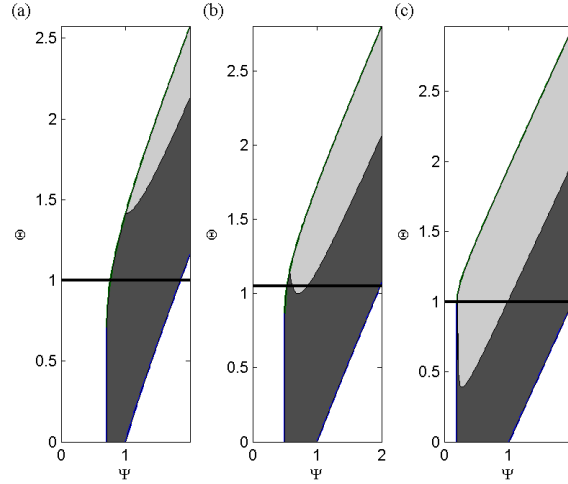


Figure 2.1: **Equilibrium feasibility region:** (a) $\gamma = \frac{\pi}{4}$, (b) $\gamma = \frac{\pi}{3}$, and (c) $\gamma = \frac{7\pi}{16}$. The shaded regions indicate where the equilibrium orientation is feasible, with lower and upper curved boundaries given by Equation (2.23) and left-hand vertical boundary given by Equation (2.21). Dark gray regions indicate that $p_x^e > 0$ while light gray regions indicate $p_x^e < 0$. The white region shows where equilibrium is not feasible. Solid horizontal lines indicate feasibility for (a) $\Theta = 1$, (b) $\Theta = 1.05$, and (c) $\Theta = 1$. The equilibrium solution for non-helical swimmers, $\Theta = 0$, is the line segment $0 < \Psi < 1$.

$2L$ will be examined (Figure 2.2). Poiseuille flow is given by

$$\mathbf{V} = \frac{U}{L^2}(x^2 - L^2)\mathbf{k}, \quad (2.27)$$

where U represents the flow speed at the centre and \mathbf{k} is a unit vector in the vertical direction. The vorticity of the flow is $\boldsymbol{\omega} = -\frac{2U}{L^2}x\mathbf{j}$. We non-dimensionalize length on L and time on $2B$, so we obtain an expression for Ψ which represents the non-dimensional measure of the viscous torque

$$\Psi = -\Psi_{max}x, \quad (2.28)$$

where $\Psi_{max} = \frac{2BU}{L}$. The governing equation for cell position, with regard to non-dimensional variables, is given by

$$\frac{d\mathbf{x}}{dt} = \Psi_{max}(x^2 - 1)\mathbf{k} + \nu\mathbf{p}. \quad (2.29)$$

The vector \mathbf{p} was initially chosen by randomly choose ϕ_p from the uniform

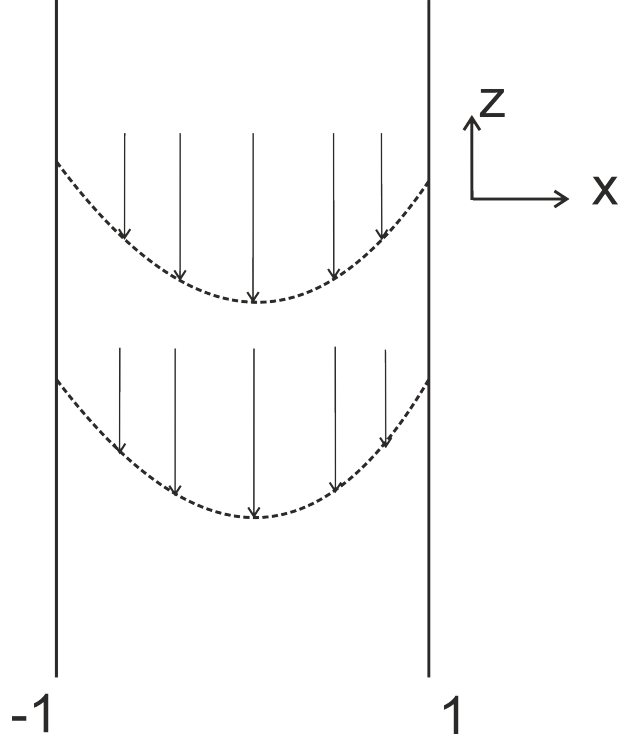


Figure 2.2: **Vertical channel flow:** The flow is described by Poiseuille flow between two walls located at $x = -1$ and $x = 1$. The distance between the walls is $2L$. We consider absorbing boundary conditions upon the the channel walls as to keep in place the cells that reach the walls.

distribution $U(0, 2\pi)$ and θ_p is $\cos^{-1} z$ where z is a random number chosen from $U(0, \pi)$. The vector \mathbf{n} was then initially chosen by defining a unit vector \mathbf{q} perpendicular to \mathbf{p} and then define \mathbf{n} by rotating \mathbf{p} around \mathbf{q} using Rodrigues' rotation formula

$$\mathbf{n} = \mathbf{p} \cos \gamma + (\mathbf{q} \wedge \mathbf{p}) \sin \gamma + \mathbf{q}(\mathbf{q} \cdot \mathbf{p})(1 - \cos \gamma). \quad (2.30)$$

Equations (2.5-2.8) and (2.29) were solved numerically using Runge-Kutta method [20] which is implemented in Matlab (we use Matlab 2014a) using ode45 solver with the default relative error tolerance 10^{-3} and absolute error tolerance 10^{-6} [95]. We computed the solution values within the time period $t = 0.1$. Equations (2.5-2.8) consist of four unknown variables with four equations. The solution to this system can be checked to satisfy the constraint (2.9). The shear parameter $\Psi(x)$ is given by Equation (2.28) in order to simulate the trajectories of cells swimming in Poiseuille flow. For simplicity, we impose absorbing boundary

conditions upon the channel boundaries so as to keep in place the cells that reach the walls.

For non-helical swimmers, $\Theta = 0$, cells accumulate in the centre of the channel as found previously by Kessler [64] and shown in Figures 2.4a and 2.5a. Such focusing of cells can be explained by considering $\overline{p_x}$ plotted in Figure 2.3 a if we assume that the average cell orientation, when taken as a function of its position, can be approximated by the average cell orientation for the shear rate at that position. The horizontal component of equilibrium swimming direction is $p_x^e = \Psi$ when $|\Psi| \leq 1$ where Ψ is given by Equation (2.28). The mean horizontal component of swimming direction for tumbling cells is given by Equation (2.26). When $|\Psi| < 1$, which corresponds to the inner region of the channel $|x| < \frac{1}{\Psi_{max}}$, cells swim towards the centre of the channel. Outside the feasibility region of equilibrium, $|\Psi| > 1$, cells are tumbling as shown in Figure 2.3a but the mean of horizontal swimming direction, $\overline{p_x}$, is positive for $\Psi > 1$ which indicates cells maintain swimming towards the centre of the channel.

We simulated 100 cells over time $T = 100$ in Figure 2.3 where the default error tolerances were assumed. The numerical and analytical average of p_x agree within the equilibrium feasibility region. However, there is a discrepancy between the numerical solution and analytical solution in Figure 2.3a when $\Psi > 1$. We test this discrepancy for different error tolerances. We compute the average of p_x numerically at $\Psi = 2$ at end time ($T = 100$ and 200) as shown in Table 2.1. The average of p_x ranges between $\overline{p_x} \approx 0.3$ and $\overline{p_x} \approx 0.4$ regardless of error tolerances with accuracy of two significant figures while the value of the analytical solution given by (2.26) at $\Psi = 2$ at the end time is $\overline{p_x} = 0.2534$. The discrepancy between the numerical and analytical solutions is still there regardless of error tolerances values. Note that regardless of tumbling near the walls we did not include cells that accumulate at the walls in the calculation of average of horizontal component of orientation.

For helical swimmers, $\Theta \neq 0$, three regions in the channel can be distinguished. It is important to note here that, once again, the assumption has been made that

CHAPTER 2. DETERMINISTIC MODEL FOR HELICAL GYROTACTIC SWIMMERS FOCUSSING IN CHANNELS

	$t = 100$ sim = 100	$t = 100$ sim = 100	$t = 100$ sim = 100	$t = 200$ sim = 1000
Absolute error tolerance	10^{-6}	10^{-4}	10^{-8}	10^{-6}
relative error tolerance	10^{-3}	10^{-2}	10^{-4}	10^{-3}
$\overline{p_x}$	0.3349	0.3542	0.3560	0.3491

Table 2.1: Numerical values for $\overline{p_x}$ for non-helical swimmers for different error tolerances where we use `ode45` to solve Equations (2.5–2.8). t denotes the duration of the simulations sim. Error tolerances in the first and last columns are the default error tolerances for `ode45`.

the cell orientation is determined by the local shear rate. Taking note of the fact that Ψ is proportional to x , Figure 2.3 can be interpreted as plotting the average value of p_x as a function of position x . In the central region, cells swim in helical trajectories due to the insufficiency of viscous torque to balance the propulsive torque and generate a stable equilibrium swimming orientation. As shown in Figure 2.1 and Equations (2.21) and (2.24) this happens when

$$|x| \leq \frac{1}{\Psi_{max}} \max\{\cos \gamma, \sqrt{\Theta^2 - 2\Theta \sin \gamma + 1}\}. \quad (2.31)$$

Outside this region, within $\Theta - \Psi$ parameter space in which equilibrium solutions are feasible, cells are able to attain equilibrium orientation as given by Equations (2.18-2.20). The third region is near the walls. When the shear is too strong, the vorticity torque causes cells to tumble. This occurs if

$$|x| \geq \frac{1}{\Psi_{max}} \sqrt{\Theta^2 + 2\Theta \sin \gamma + 1}. \quad (2.32)$$

To give such an example of this phenomena, for the parameters $\Psi_{max} = 2$, $\gamma = \pi/4$, $\Theta = 1$, we solve Equation (2.24) for $|x|$. We conclude that cells may attain equilibrium orientation if $0.382 \leq |x| \leq 0.923$. This is visible from the feasibility region in Figure 2.1a as, when nearer to the centre of the channel, cells maintain helical swimming trajectories, while when closer to the walls, cells begin to tumble. It should be mentioned, however, that in the case of these

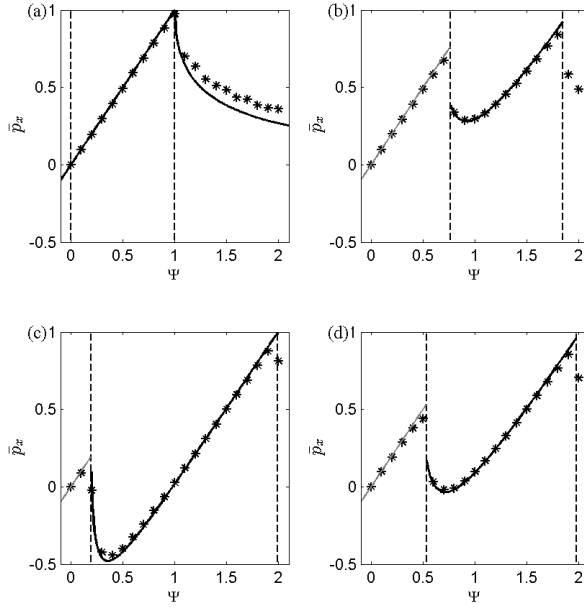


Figure 2.3: **Average value of p_x** : Stars indicate the average value for 100 simulations run for 100 time units. The vertical dashed lines are the boundaries of equilibrium feasibility. (a) $\Theta = 0$. (b) $\Theta = 1$, $\gamma = \frac{\pi}{4}$. (c) $\Theta = 1$, $\gamma = \frac{7\pi}{16}$. (d) $\Theta = 1.05$, $\gamma = \frac{\pi}{3}$. In (a) the solid line is the analytical average for $\Theta = 0$ given by Equation (2.26) for $\Psi > 1$ and the equilibrium value for $\Psi < 1$, given by $p_x^e = \Psi$. In (b-d) the black solid lines are the equilibrium value given by Equation (2.18) for values of Ψ where the equilibrium is feasible. The grey lines are the $\Theta = 0$ equilibrium value, $p_x^e = \Psi$. Taken from [4].

parameters, from Figure 2.3b, the average of horizontal component of swimming direction calculated for a fixed shear rate is towards the centre of the channel and we therefore see accumulation at the centreline of the channel as shown in Figures 2.4b and 2.5b.

The strength of the propulsive torque has a potential impact on the nature of the equilibrium solutions and we may find focussing away from the channel centre, Figures 2.4c and 2.5c. This is because there is a location away from the centre where $p_x = 0$ as shown in Figures 2.3 c and d. To quantify the impact of Θ on cell position, we solve Equation (2.18) for $p_x^e = 0$ to obtain (using Equation 2.28)

$$|x| = \frac{1}{\Psi_{max}} \sqrt{\frac{\Theta^2 \pm \Theta \sqrt{\Theta^2 - 4 \cos^2 \gamma}}{2}}. \quad (2.33)$$

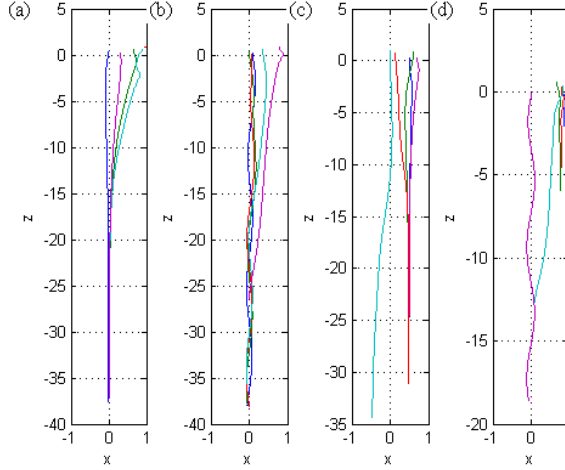


Figure 2.4: **Swimming trajectories in a vertical channel:** Example trajectories of duration 20 time units with parameters $\Psi_{max} = 2$ and (a) $\Theta = 0$, (b) $\Theta = 1$, $\gamma = \frac{\pi}{4}$, (c) $\Theta = 1$, $\gamma = \frac{7\pi}{16}$, and (d) $\Theta = 1.05$, $\gamma = \frac{\pi}{3}$. Taken from [4].

For instance, for the parameters $\Psi_{max} = 2$, $\gamma = 7\pi/16$, equilibrium solutions are feasible when $0.0980 < |x| < 0.9952$ and $p_x^e = 0$ when $|x| = 0.099$ and $|x| = 0.49$. In the case of the same parameters though, when $0.099 < |x| < 0.49$, the equilibrium orientation is away from the centre and when $0.49 < |x| < 0.995$, the equilibrium orientation is towards the centreline and subsequently cells accumulate at the interface $|x| = 0.49$ where the horizontal component of orientation is zero.

As another example, we consider the parameters $\Psi_{max} = 1$, $\gamma = \pi/3$, $\Theta = 1.05$ for which $p_x^e = 0$ are clearly differentiated from the feasibility boundaries as shown in Figures 2.1b and 2.3d. The equilibria are feasible when $0.53 \leq |x| \leq 1.98$ and $p_x^e = 0$ when $|x| = 0.61$ or $|x| = 0.84$. Cells located within the region $|x| < 0.61$ swim towards the centre of the channel while cells located beyond this region swim towards $|x| = 0.84$. Therefore, accumulation occurs at two locations, on the centreline and away from the centreline, as shown in Figures 2.4d and 2.5d. Figure 2.5d shows how cells that are originally located at $|x| < 0.61$ tends to focus in the centre as opposed to cells that are originally located closer to the walls accumulate around $|x| = 0.84$.

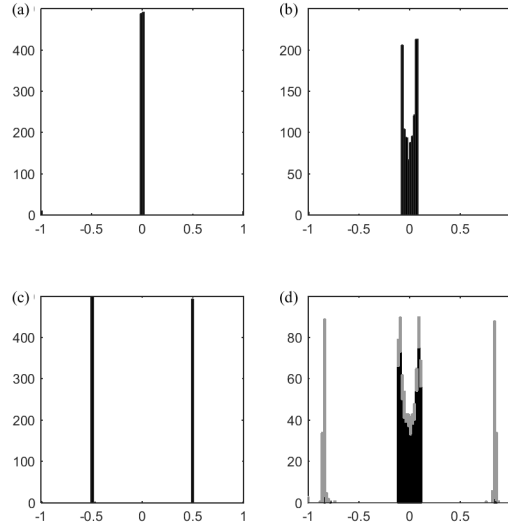


Figure 2.5: **Distribution of cells across the channel:** Horizontal position after 100 time units of 1000 cells initially uniformly distributed across the channel with parameters (a) $\Theta = 0, \Psi_{max} = 2$; (b) $\Theta = 1, \gamma = \frac{\pi}{4}, \Psi_{max} = 2$; (c) $\Theta = 1, \gamma = \frac{7\pi}{16}, \Psi_{max} = 2$; (d) $\Theta = 1.05, \gamma = \frac{\pi}{3}, \Psi_{max} = 1$. In (d) grey indicates cells which had initial position $|x| > 0.61$ and black indicates cells which had initial position $|x| < 0.61$. Taken from [4].

2.4 Cell orientation in terms of Euler angles

To describe the cell orientation in three-dimensional Euclidean space, three independent parameters are required. Euler angles (θ, ϕ, ψ) can be viewed as a prescription whereby the space fixed frame XYZ might be made to coincide with the body fixed frame xyz by performing three successive finite rotations. We choose a body fixed frame xyz such that \mathbf{p} is aligned with the z -axis and \mathbf{n} lies in xz -plane

$$\mathbf{p} = \mathbf{e}_3, \quad \mathbf{n} = \sin \gamma \mathbf{e}_1 + \cos \gamma \mathbf{e}_3. \quad (2.34)$$

where \mathbf{e}_i are orthonormal basis vectors for the body fixed axes. We next align the body fixed axes with the space axes XYZ . We move the body to its final

orientation using the rotational matrices

$$Z(\phi) = \begin{pmatrix} \cos \phi & -\sin \phi & 0 \\ \sin \phi & \cos \phi & 0 \\ 0 & 0 & 1 \end{pmatrix} \quad Y(\theta) = \begin{pmatrix} \cos \theta & 0 & \sin \theta \\ 0 & 1 & 0 \\ -\sin \theta & 0 & \cos \theta \end{pmatrix} \quad (2.35)$$

The course of rotation is successively done in the following order [38]:

- 1) $R_Z(\phi)$: Rotate the body with angle ϕ around Z axis and call the new position of body fixed axes (x_1, y_1, z_1) . The axis z_1 coincides with Z , Figure (2.6b). Define rotation vector

$$\hat{\mathbf{u}}_\phi = \mathbf{k} \quad (2.36)$$

- 2) $R_{y_1}(\theta)$: Rotate the body with angle θ around y_1 . Call the new position of the body fixed axes (x_2, y_2, z_2) . Remark that y_2 and y_1 coincide (Figure (2.6c)). Define the rotation vector $\hat{\mathbf{u}}_\theta$ as a vector in direction of y_1 axis

$$\hat{\mathbf{u}}_\theta = R_Z(\phi)\mathbf{j} \quad (2.37)$$

- 3) $R_{z_2}(\psi)$: Rotate with angle ψ around z_2 . Call the new position of the body fixed axes (x_3, y_3, z_3) where z_3 is identical to z_2 (Figure (2.6d)). Define the rotation vector $\hat{\mathbf{u}}_\psi$ as a vector in direction of z_2 axis

$$\hat{\mathbf{u}}_\psi = R_{y_1}(\theta)\mathbf{k} = \mathbf{e}_3 \quad (2.38)$$

It is worth mentioning that the rotation course given in Figure (2.6) is defined with respect to the frame of reference carried with the moving body. It is convenient in many applications; however, to refer to rotations with respect to the fixed frame X, Y, Z [38]. The composition of the three successive rotations is defined as $R_{z_2}(\psi)R_{y_1}(\theta)R_Z(\phi)$ where the rotations are ordered from right to left. The rotation $R_{y_1}(\theta)$ about the line of nodes is equivalent to the composition $R_Z(\phi)R_Y(\theta)R_Z(-\phi)$ of three successive rotations about axis Z, Y, Z .

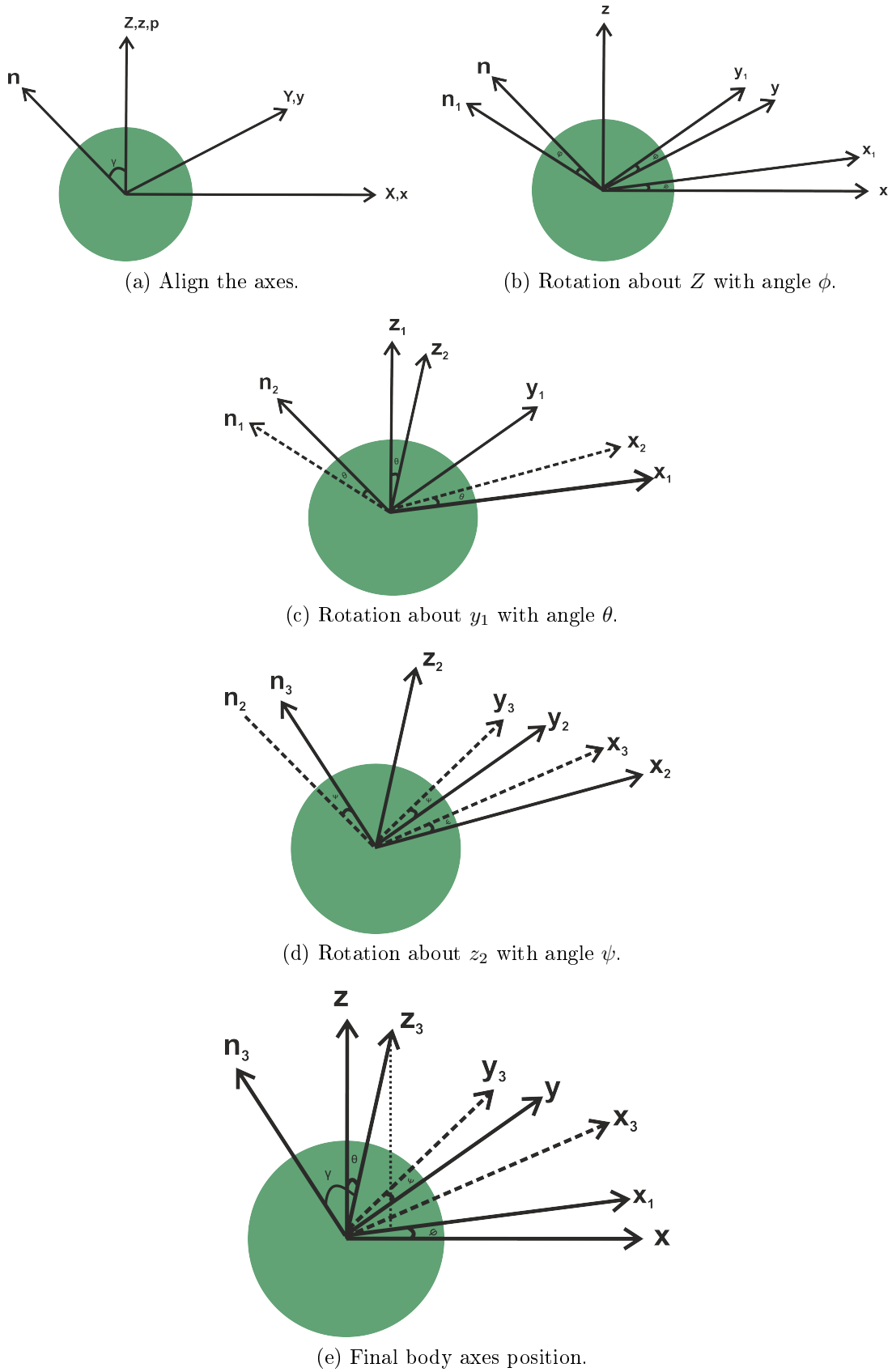


Figure 2.6: Rotation process

This equivalence is because of we first rotate the line of nodes y_1 about Y using the rotation $R_Z(-\phi)$, then rotating about Y -axis (which is the line of nodes axis at this point) with $R_Y(\theta)$ and finally rotating back to its original position with $R_Z(\phi)$. In a similar way, we have $R_{z_2}(\psi) = R_{y_1}(\theta)R_Z(\psi)R_{y_1}(-\theta)$. In conclusion, we can express the rotations course in Figure (2.6) in terms of the physical space axes by carrying out the following steps

- i) Rotation about Z by angle ψ .
- ii) Rotation about Y by angle θ .
- iii) Rotation about Z by angle ϕ .

To show that these two courses of rotation are equivalent, we remark first that two rotations about the same axis commute, therefore

$$\begin{aligned}
 R_{z_2}(\psi)R_{y_1}(\theta)R_Z(\phi) &= [R_{y_1}(\theta)R_Z(\psi)R_{y_1}(-\theta)]R_{y_1}(\theta)R_Z(\phi) \\
 &= R_{y_1}(\theta)R_Z(\psi)R_Z(\phi) \\
 &= [R_Z(\phi)R_Y(\theta)R_Z(-\phi)]R_Z(\psi)R_Z(\phi) \\
 &= R_Z(\phi)R_Y(\theta)R_Z(\psi)R_Z(-\phi)R_Z(\phi) \\
 &= R_Z(\phi)R_Y(\theta)R_Z(\psi). \tag{2.39}
 \end{aligned}$$

Noting that $R_Z = Z$ and $R_Y = Y$ as defined in (2.35), the body fixed basis

vectors given with respect to physical space coordinates as following

$$\mathbf{e}_1 = Z(\phi)Y(\theta)Z(\psi)\mathbf{i} = \begin{pmatrix} \cos \phi \cos \theta \cos \psi - \sin \phi \sin \psi \\ \sin \phi \cos \theta \cos \psi + \cos \phi \sin \psi \\ -\sin \theta \cos \psi \end{pmatrix}, \quad (2.40)$$

$$\mathbf{e}_2 = Z(\phi)Y(\theta)Z(\psi)\mathbf{j} = \begin{pmatrix} -\cos \phi \cos \theta \sin \psi - \sin \phi \cos \psi \\ -\sin \phi \cos \theta \sin \psi + \cos \phi \cos \psi \\ \sin \theta \sin \psi \end{pmatrix}, \quad (2.41)$$

$$\mathbf{e}_3 = \mathbf{p} = Z(\phi)Y(\theta)Z(\psi)\mathbf{k} = \begin{pmatrix} \cos \phi \sin \theta \\ \sin \theta \sin \phi \\ \cos \theta \end{pmatrix}. \quad (2.42)$$

where \mathbf{e}_i are orthonormal basis vectors for the body axes xyz and $\mathbf{i}, \mathbf{j}, \mathbf{k}$ are orthonormal basis vectors for the space axes XYZ . This rotation choice indicates that (θ, ϕ) corresponds to (θ_p, ϕ_p) defined previously in [6].

In Section 3.4.2, we will need to express $\hat{\mathbf{u}}_\phi$ and $\hat{\mathbf{u}}_\theta$ in terms of \mathbf{e}_1 , \mathbf{e}_2 , and \mathbf{e}_3 . We have that $\hat{\mathbf{u}}_\phi = \mathbf{k}$ which can be obtained as

$$\hat{\mathbf{u}}_\phi = \begin{pmatrix} 0 \\ 0 \\ 1 \end{pmatrix} = \mathbf{k} = -\sin \theta \cos \psi \mathbf{e}_1 + \sin \theta \sin \psi \mathbf{e}_2 + \cos \theta \mathbf{e}_3, \quad (2.43)$$

and we have that

$$\hat{\mathbf{u}}_\theta = R_Z(\phi)\mathbf{j} = \begin{pmatrix} -\sin \phi \\ \cos \phi \\ 0 \end{pmatrix} = \sin \psi \mathbf{e}_1 + \cos \psi \mathbf{e}_2. \quad (2.44)$$

For completeness, note that from (2.38) we have

$$\hat{\mathbf{u}}_\psi = \mathbf{e}_3. \quad (2.45)$$

The unit vectors that orient the cell, \mathbf{p} and \mathbf{n} , rotate at the angular velocity

according to the following ordinary differential equations [6]

$$\frac{d\mathbf{p}}{dt} = \boldsymbol{\Omega} \wedge \mathbf{p}, \quad (2.46)$$

$$\frac{d\mathbf{n}}{dt} = \boldsymbol{\Omega} \wedge \mathbf{n}, \quad (2.47)$$

where the angular velocity of the cell is expressed in terms of the body fixed vectors (see equation 2.4)

$$\boldsymbol{\Omega} = \mathbf{e}_3 \wedge \mathbf{k} + \Theta(\sin \gamma \mathbf{e}_1 + \cos \gamma \mathbf{e}_3) + \Psi \mathbf{j}. \quad (2.48)$$

To obtain a set of ordinary differential equations that describe the orientation of the cell in terms of Euler angles, we consider evolution equations for the body-fixed orthonormal vectors $\mathbf{e}_1, \mathbf{e}_2, \mathbf{e}_3$

$$\frac{d\mathbf{e}_3}{dt} = \boldsymbol{\Omega} \wedge \mathbf{e}_3 = \frac{d\theta}{dt} \frac{\partial \mathbf{e}_3}{\partial \theta} + \frac{d\phi}{dt} \frac{\partial \mathbf{e}_3}{\partial \phi} + \frac{d\psi}{dt} \frac{\partial \mathbf{e}_3}{\partial \psi} \quad (2.49)$$

and in similar way for $\frac{d\mathbf{e}_1}{dt}$ and $\frac{d\mathbf{e}_2}{dt}$. Computing the partial derivatives with respect to Euler angles in Equation (2.49) lead to

$$\frac{d\mathbf{e}_3}{dt} = \frac{d\theta}{dt} (\cos \psi \mathbf{e}_1 - \sin \psi \mathbf{e}_2) + \frac{d\phi}{dt} (\sin \theta \sin \psi \mathbf{e}_1 + \sin \theta \cos \psi \mathbf{e}_2). \quad (2.50)$$

This evolution equation represents the change in the unit vector \mathbf{e}_3 with respect to the change in Euler angles θ and ϕ in direction of \mathbf{e}_1 and \mathbf{e}_2 . Therefore, we take the dot product for both sides of

$$\frac{d\mathbf{e}_3}{dt} = \boldsymbol{\Omega} \wedge \mathbf{e}_3 \quad (2.51)$$

with the unit vectors \mathbf{e}_1 and \mathbf{e}_2 . to obtain

$$\frac{d\mathbf{e}_3}{dt} \cdot \mathbf{e}_1 = (\boldsymbol{\Omega} \wedge \mathbf{e}_3) \cdot \mathbf{e}_1, \quad (2.52)$$

$$\frac{d\mathbf{e}_3}{dt} \cdot \mathbf{e}_2 = (\boldsymbol{\Omega} \wedge \mathbf{e}_3) \cdot \mathbf{e}_2. \quad (2.53)$$

The right hand sides of Equation (2.52) and Equation (2.53) respectively are (using Equation(2.48))

$$(\boldsymbol{\Omega} \wedge \mathbf{e}_3) \cdot \mathbf{e}_1 = \boldsymbol{\Omega} \cdot \mathbf{e}_2 = -\sin \theta \cos \psi + \Psi \boldsymbol{\omega} \cdot \mathbf{e}_2, \quad (2.54)$$

$$(\boldsymbol{\Omega} \wedge \mathbf{e}_3) \cdot \mathbf{e}_2 = -\boldsymbol{\Omega} \cdot \mathbf{e}_1 = \sin \theta \sin \psi - \Theta \sin \gamma - \Psi \boldsymbol{\omega} \cdot \mathbf{e}_1. \quad (2.55)$$

Substitute back into equation (2.52) and equation (2.53) and note that the $\boldsymbol{\omega} = \mathbf{j}$, we have

$$\frac{d\theta}{dt} \cos \psi + \frac{d\phi}{dt} \sin \theta \sin \psi = -\sin \theta \cos \psi + \Psi (\cos \phi \cos \psi - \sin \phi \cos \theta \sin \psi) \quad (2.56)$$

$$-\frac{d\theta}{dt} \sin \psi + \frac{d\phi}{dt} \sin \theta \cos \psi = \sin \theta \sin \psi - \Theta \sin \gamma - \Psi (\sin \phi \cos \theta \cos \psi + \cos \phi \sin \psi). \quad (2.57)$$

Solving this system for $\frac{d\theta}{dt}$ and $\frac{d\phi}{dt}$ results in

$$\sin \theta \frac{d\phi}{dt} = -\Psi \sin \phi \cos \theta - \Theta \sin \gamma \cos \psi, \quad (2.58)$$

$$\frac{d\theta}{dt} = -\sin \theta + \Psi \cos \phi + \Theta \sin \gamma \sin \psi. \quad (2.59)$$

To obtain an equation for $\frac{d\psi}{dt}$, we solve

$$\frac{d\mathbf{e}_1}{dt} \cdot \mathbf{e}_2 = (\boldsymbol{\Omega} \wedge \mathbf{e}_1) \cdot \mathbf{e}_2 \quad (2.60)$$

to get

$$\frac{d\phi}{dt} \cos \theta + \frac{d\psi}{dt} = \Theta \cos \gamma + \Psi \sin \theta \sin \phi. \quad (2.61)$$

Multiply (2.61) by $\sin \theta$ and use (2.58), gives

$$\frac{d\psi}{dt} \sin \theta = \Psi \sin \phi + \Theta (\cos \gamma \sin \theta + \sin \gamma \cos \psi \cos \theta). \quad (2.62)$$

To summarize, the evolution equations lead to the following ordinary differential

equations that describe the cell orientation in terms of Euler angles

$$\frac{d\theta}{dt} = -\sin\theta + \Psi \cos\phi + \Theta \sin\gamma \sin\psi, \quad (2.63)$$

$$\sin\theta \frac{d\phi}{dt} = -\Psi \sin\phi \cos\theta - \Theta \sin\gamma \cos\psi, \quad (2.64)$$

$$\sin\theta \frac{d\psi}{dt} = \Psi \sin\phi + \Theta (\cos\gamma \sin\theta + \sin\gamma \cos\psi \cos\theta). \quad (2.65)$$

Note that when there is no propulsive torque, $\Theta = 0$, these equations reduce to

$$\frac{d\theta}{dt} = -\sin\theta + \Psi \cos\phi, \quad (2.66)$$

$$\sin\theta \frac{d\phi}{dt} = -\Psi \sin\phi \cos\theta \quad (2.67)$$

which describe the orientation of the non-helical swimmers as given for instance in [56].

2.5 Conclusion

The full constraints on the feasibility of the equilibrium of the cell orientation have been determined where the constraint on p_z was necessary to ensure that \mathbf{p} is a real vector of unit length. We have also extended the model presented in [6] to the case where the fluid vorticity is not constant but varies in space. We saw that the helical swimmers exhibit an accumulation in the centre of the channel as in the classical case of the non-helical swimmers and they also can accumulate away from the centre of the channel depending on the strength of propulsive torque and the angle between this torque and the propulsive force that pulls the cell through the flow.

Cells generally swim in a random way. To develop a Fokker–Planck equation for helical swimmers, we use the Euler angles as they describe the three degrees of freedom.

The next chapters are devoted to develop a Fokker–Planck equation that describes

the evolution of the cell through the fluid flow.

Chapter 3

Orientation distribution of gyrotactic helical swimmers

3.1 Introduction

Microorganisms do not generally swim in deterministic paths, instead they swim in random trajectories. Pedley and Kessler [82] proposed a Fokker–Planck equation to model this random behaviour in microorganism orientation. This equation is also known as a Forward Kolomogrov equation which describes the probability distribution of the random variable of interest at future time $s > t$ knowing the state of this variable at current time t .

While the Fokker–Planck equation gives information about the distribution, the underlying stochastic differential equations are useful for providing sample trajectories. The Fokker–Planck equation for probability density function $P(\mathbf{x}, t)$ of an n -dimensional random variable \mathbf{x} is given as [45]

$$\frac{\partial P(\mathbf{x}, t)}{\partial t} = - \sum_{i=1}^n \partial_i (A_i(\mathbf{x})P(\mathbf{x}, t)) + \frac{1}{2} \sum_{i=1}^n \sum_{j=1}^n \partial_i \partial_j (B_{ij}(\mathbf{x})P(\mathbf{x}, t)), \quad (3.1)$$

where $\mathbf{A}(\mathbf{x}, t)$ is the drift and $\mathbf{B}(\mathbf{x}, t)$ is the diffusion coefficient respectively. The

associated stochastic differential equation is

$$d\mathbf{x} = \mathbf{A}(\mathbf{x}, t)dt + \sqrt{\mathbf{B}(\mathbf{x}, t)}d\mathbf{W}(t), \quad (3.2)$$

where $d\mathbf{W}(t)$ is an n variable Wiener process. Additional information on the Wiener process, and the connection between Equation (3.1) and the stochastic differential equation (3.2) is provided in appendix A.

We start by describing the random walk on a unit sphere using spherical coordinates (θ, ϕ) . The distribution of this Brownian motion is the solution of the diffusion equation. This equation is then associated with a stochastic differential equation [22, 93] and in the later sections will be used as a generator for the diffusion term for non-helical gyrotactic swimmers.

To develop the Fokker–Planck equation for gyrotactic helical swimmers, we first express the Forward Kolomogrov equation in terms of the generators of infinitesimal rotation about the body fixed axes [76] and then using the relationship between these generators and Euler angles (θ, ϕ, ψ) , we obtain the required Fokker–Planck equation. By writing this equation in the standard form [45], we lastly derive its associated stochastic differential equation.

3.2 Random walk on a unit sphere

The probability distribution function for a random walk (Brownian motion) on a unit sphere is the solution of diffusion equation

$$\frac{\partial f}{\partial t} - d_r \nabla^2 f = 0, \quad (3.3)$$

where $\nabla^2 f$ is given in spherical coordinates (θ, ϕ)

$$\nabla^2 f = \left(\frac{1}{\sin \theta} \left(\frac{\partial}{\partial \theta} \sin \theta \frac{\partial}{\partial \theta} \right) + \frac{1}{\sin^2 \theta} \frac{\partial^2}{\partial \phi^2} \right) f, \quad (3.4)$$

and d_r can be interpreted as the rotational diffusion constant. Equation (3.3) is solved subject to the normalization condition

$$\int_{\phi=0}^{2\pi} \int_{\theta=0}^{\pi} f \sin \theta d\theta d\phi = 1. \quad (3.5)$$

Equation (3.3) is not in the standard form that can be associated with a stochastic differential equation. To write it in a standard form, we define the transformation

$$F = \sin \theta f, \quad (3.6)$$

which leads to the following standard diffusion equation [93]

$$\frac{\partial F}{\partial t} = -\frac{\partial}{\partial \theta} (d_r \cot \theta F) + \frac{\partial^2}{\partial \theta^2} d_r F + \frac{\partial^2}{\partial \phi^2} \frac{d_r}{\sin^2 \theta} F, \quad (3.7)$$

with normalization

$$\int_0^{2\pi} \int_0^{\pi} F d\theta d\phi = 1. \quad (3.8)$$

So as to compare with Fokker–Planck equation of the form given in Equation (3.1), we rewrite this equation as

$$\frac{\partial F}{\partial t} = -\frac{\partial}{\partial \theta} (d_r \cot \theta F) + \frac{1}{2} \left[\frac{\partial^2}{\partial \theta^2} 2d_r F + \frac{\partial^2}{\partial \phi^2} \frac{2d_r}{\sin^2 \theta} F \right]. \quad (3.9)$$

We can then see that the diffusion matrix in the Fokker–Planck equation (3.1) is given by

$$\mathbf{B} = \begin{bmatrix} 2d_r & 0 \\ 0 & \frac{2d_r}{\sin^2 \theta} \end{bmatrix}, \quad (3.10)$$

where $x_1 = \theta$ and $x_2 = \phi$ in Equation (3.1).

To associate Equation (3.9) with an Ito's stochastic differential equation, we need to compute the square root of \mathbf{B} . The square root of \mathbf{B} is simply obtained by

taking the square root of the diagonal entries

$$\mathbf{B}^{\frac{1}{2}} = \begin{bmatrix} \sqrt{2d_r} & 0 \\ 0 & \frac{\sqrt{2d_r}}{\sin \theta} \end{bmatrix}. \quad (3.11)$$

We conclude that Equation (3.9) can be associated with the following stochastic differential equations [22]

$$\begin{pmatrix} d\theta \\ d\phi \end{pmatrix} = \begin{pmatrix} d_r \cot \theta \\ 0 \end{pmatrix} dt + \begin{pmatrix} \sqrt{2d_r} & 0 \\ 0 & \frac{\sqrt{2d_r}}{\sin \theta} \end{pmatrix} \begin{pmatrix} dW_1(t) \\ dW_2(t) \end{pmatrix}, \quad (3.12)$$

where $dW_1(t)$ and $dW_2(t)$ are independent Wiener processes. The drift term is called spurious-drift [93].

To solve these stochastic differential equations, we use the Euler-Maruyama method which is described in Appendix A. This method is implemented in Matlab by using the built-in solver `simByEuler`. Example realizations of the solutions are shown in Figure 3.1. We run 5000 simulations of these stochastic differential equations over 10 time units with time step $dt = 0.01$ and $d_r = 1$. We sample the initial values of θ and ϕ from the uniform distributions $U(0, \pi)$ and $U(0, 2\pi)$ respectively. The ensemble average of these simulations are given by

$$\langle \theta(t) \rangle = \frac{1}{N} \sum_{i=1}^N \theta_i(t), \quad (3.13)$$

$$\langle \phi(t) \rangle = \frac{1}{N} \sum_{i=1}^N \phi_i(t), \quad (3.14)$$

where N is the number of cells.

In all simulations done in thesis we never have counter $\theta_0 = 0$ or $\theta_0 = \pi$. If at any point $\theta = 0$ or $\theta = \pi$ arise we subsequently reject the simulation, however, in practice we never counter $\theta = 0$ or $\theta = \pi$.

The equilibrium solution to equations (3.7-3.8) is given by

$$F(\theta, \phi) = \frac{1}{4\pi} \sin \theta. \quad (3.15)$$

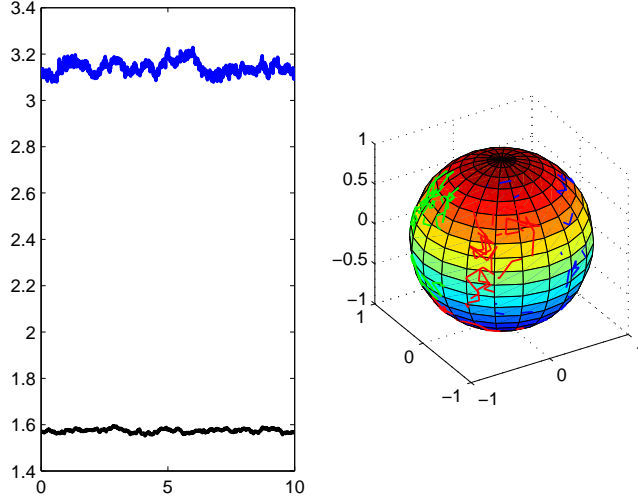


Figure 3.1: **Example realizations of the stochastic differential equation for Brownian motion.** The left panel shows the ensemble average of θ in black and ensemble average of ϕ in blue for 5000 realizations of Equation (3.12). The right panel shows three examples of random walk on unit sphere.

This function gives the marginal distribution of θ and ϕ as follows

$$g(\theta) = \int_0^{2\pi} F(\theta, \phi) d\phi = \frac{1}{2} \sin \theta, \quad h(\phi) = \int_0^\pi F(\theta, \phi) d\theta = \frac{1}{2\pi}, \quad (3.16)$$

as shown in Figure 3.2.

In Figure 3.3, we show three different realizations of the horizontal component of orientation

$$p_x = \sin \theta \cos \phi, \quad (3.17)$$

and the ensemble average of 5000 realizations for the stochastic model where $\langle p_x(t) \rangle = \langle \sin \theta \cos \phi \rangle$. Despite the unpredictable orientation of any single cell, for cells that orient themselves uniformly, they have zero horizontal component of orientation on average; $\langle p_x(t) \rangle = 0$.

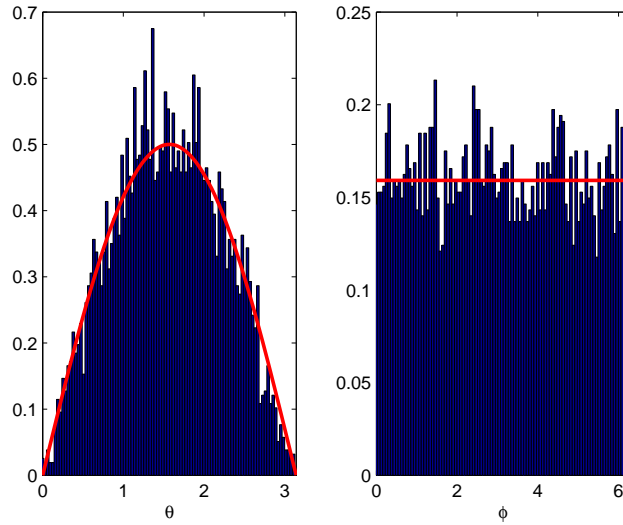


Figure 3.2: **Orientation distribution of Brownian motion on a sphere.** The histograms show 5000 realizations of the solutions of Equation (3.12) at the end time point. The red curves are the marginal distribution given by Equation (3.16).

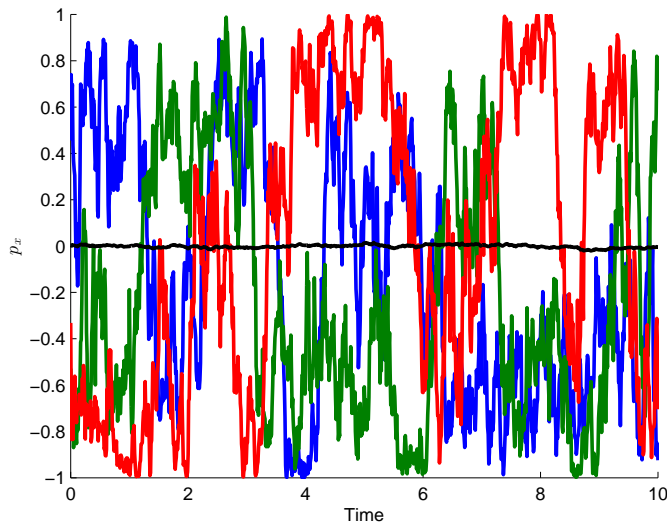


Figure 3.3: **Horizontal component of orientation p_x .** Three realizations (red, green, blue) of p_x are shown and the ensemble average $\langle p_x(t) \rangle$ of 5000 simulations is shown as black line.

3.3 Orientation distribution of non-helical swimmers

In the previous section, we presented pure Brownian motion on a unit sphere. In this section, we discuss the impact of gravitational and viscous torques on the orientation of a cell. The deterministic orientation of the cell is given by Equation (1.48)

$$\frac{d\mathbf{p}}{dt} = \boldsymbol{\Omega} \wedge \mathbf{p}, \quad (3.18)$$

where the angular velocity is given by

$$\boldsymbol{\Omega} = \mathbf{p} \wedge \mathbf{k} + \Psi \boldsymbol{\omega}, \quad (3.19)$$

and Ψ is the non-dimensional parameter representing the relative strength of the viscous torque compared to the gravitational torque.

As given by Equations (2.66-2.67) the orientation angles (θ, ϕ) are governed by

$$\frac{d\theta}{dt} = -\sin \theta + \Psi \cos \phi, \quad (3.20)$$

$$\sin \theta \frac{d\phi}{dt} = -\Psi \cos \theta \sin \phi. \quad (3.21)$$

The stable equilibrium solution for the deterministic model is

$$\sin \theta = \Psi, \quad \phi = 0. \quad (3.22)$$

To describe randomness associated with changes in cell orientation, we extend the Fokker–Planck equation of the previous section. That is we consider a Fokker–Planck equation given by [82,83]

$$\frac{\partial f}{\partial t} + \nabla \cdot (\mathbf{j}_d + \mathbf{j}_f) = 0, \quad (3.23)$$

where $\mathbf{j}_d = -D_r \nabla f$ and $\mathbf{j}_f = \dot{\mathbf{p}} f$ are the probability fluxes due to diffusion and the

field respectively, $\dot{\mathbf{p}}$ is given by Equation (3.18), and D_r is the non-dimensional rotational diffusion. To write this equation in scalar form, we first compute the contribution of the probability flux of the field. We know that [92]

$$\nabla \cdot (\dot{\mathbf{p}}f) = \frac{1}{\sin \theta} \frac{\partial}{\partial \theta} [\sin \theta (\dot{\mathbf{p}} \cdot \mathbf{e}_\theta) f] + \frac{1}{\sin \theta} \frac{\partial}{\partial \phi} [(\dot{\mathbf{p}} \cdot \mathbf{e}_\phi) f], \quad (3.24)$$

where

$$\dot{\mathbf{p}} = \mathbf{k} - (\mathbf{k} \cdot \mathbf{p})\mathbf{p} + \boldsymbol{\omega} \wedge \mathbf{p}, \quad (3.25)$$

$$\mathbf{e}_\theta = (\cos \theta \cos \phi, \cos \theta \sin \phi, -\sin \theta), \quad (3.26)$$

$$\mathbf{e}_\phi = (-\sin \phi, \cos \phi, 0). \quad (3.27)$$

Substituting Equations (3.25-3.27) into (3.24) and simplifying the result, we obtain

$$\nabla \cdot (\dot{\mathbf{p}}f) = - \left(\sin \theta \frac{\partial f}{\partial \theta} + 2 \cos \theta f \right) + \Psi \cos \phi \frac{\partial f}{\partial \theta} - \Psi \frac{\cos \theta \sin \phi}{\sin \theta} \frac{\partial f}{\partial \phi}, \quad (3.28)$$

Remark that Equation (3.28) can be related to $\dot{\theta}$ and $\dot{\phi}$ via

$$\nabla \cdot (\dot{\mathbf{p}}f) = \frac{1}{\sin \theta} \frac{\partial}{\partial \theta} (\dot{\theta} \sin \theta f) + \frac{\partial}{\partial \phi} (\dot{\phi} f). \quad (3.29)$$

Therefore, substituting Equation (3.4,3.28) into Equation (3.23) we obtain

$$\begin{aligned} & \frac{\partial f}{\partial t} - D_r \left(\frac{1}{\sin \theta} \frac{\partial}{\partial \theta} (\sin \theta \frac{\partial f}{\partial \theta}) + \frac{1}{\sin^2 \theta} \frac{\partial^2 f}{\partial \phi^2} \right) \\ & + \Psi \left(\cos \phi \frac{\partial f}{\partial \theta} - \frac{\cos \theta \sin \phi}{\sin \theta} \frac{\partial f}{\partial \phi} \right) - \left(\sin \theta \frac{\partial f}{\partial \theta} + 2 \cos \theta f \right) = 0, \end{aligned} \quad (3.30)$$

where $f(t, \theta, \phi)$ is the probability density function of finding a cell with orientation (θ, ϕ) at time t , which should be solved subject to

$$\int_0^{2\pi} \int_0^\pi f \sin \theta d\theta d\phi = 1. \quad (3.31)$$

This equation is not in the standard form that can be directly associated with a stochastic differential equation. Using the transformation given in Equation (3.6), the standard Fokker–Planck equation is

$$\begin{aligned} \frac{\partial F}{\partial t} = & -\frac{\partial}{\partial \theta} \left(-\sin \theta + \Psi \cos \phi + D_r \cot \theta \right) F - \frac{\partial}{\partial \phi} \left(-\Psi \cot \theta \sin \phi \right) F \\ & + \frac{1}{2} \left(\frac{\partial^2}{\partial \theta^2} 2D_r + \frac{\partial^2}{\partial \phi^2} \frac{2D_r}{\sin^2 \theta} \right) F, \end{aligned} \quad (3.32)$$

where $F(t, \theta, \phi)$ is the probability density function normalized such that

$$\int_0^{2\pi} \int_0^\pi F d\theta d\phi = 1. \quad (3.33)$$

Using Gardiner [45], we can associate the standard Fokker–Planck equation with the following stochastic differential equation

$$\begin{pmatrix} d\theta \\ d\phi \end{pmatrix} = \begin{pmatrix} -\sin \theta + \Psi \cos \phi + D_r \cot \theta \\ -\Psi \frac{\cos \theta \sin \phi}{\sin \theta} \end{pmatrix} dt + \begin{pmatrix} \sqrt{2D_r} & 0 \\ 0 & \frac{\sqrt{2D_r}}{\sin \theta} \end{pmatrix} \begin{pmatrix} dW_1(t) \\ dW_2(t) \end{pmatrix}, \quad (3.34)$$

where $dW_1(t)$ and $dW_2(t)$ are independent Brownian process. Note that we have simply added the deterministic drift given in Equations (3.20-3.21) to the spurious drift. The impact of gravitational and viscous torques are included in the drift term.

As in the previous section, we take the initial values of θ and ϕ to be sampled from the uniform distributions $U(0, \pi)$ and $U(0, 2\pi)$ respectively, and solve the equation using the built-in solver `simByEuler`. We compare our results with the deterministic model by considering the same set of initial conditions and computing the mean (averaged over the initial conditions) of the deterministic model.

We now study the cell orientation in the case of still fluid and then shear flow.

3.3.1 Gravitactic cells in still fluid

In the case of zero shear flow, $\Psi = 0$, from Equation (3.30) the steady orientation distribution satisfies

$$\frac{1}{\sin \theta} \left(\frac{\partial}{\partial \theta} \sin \theta \frac{\partial f}{\partial \theta} \right) + \frac{1}{\sin^2 \theta} \frac{\partial^2 f}{\partial \phi^2} = -\frac{1}{D_r} \left(\sin \theta \frac{\partial f}{\partial \theta} + 2 \cos \theta f \right), \quad (3.35)$$

Pedley and Kessler [83] solved this equation subject to the requirement that f is positive and finite, and tends to the isotropic solution $f = \frac{1}{4\pi}$ as $D_r \rightarrow \infty$, subject to normalization condition (3.31), so that the solution is the Fisher distribution obtained by Brenner and Weissman [21]

$$f = \frac{\lambda}{4\pi \sinh(\lambda)} \exp(\lambda \cos \theta), \quad (3.36)$$

where $\lambda = D_r^{-1}$.

The function $F = f \sin \theta$ is thus given by

$$F(\theta, \phi) = \frac{\lambda \sin \theta}{4\pi \sinh(\lambda)} \exp(\lambda \cos \theta). \quad (3.37)$$

In this zero shear flow case, the stochastic differential Equation (3.34) becomes

$$\begin{pmatrix} d\theta \\ d\phi \end{pmatrix} = \begin{pmatrix} -\sin \theta + D_r \cot \theta \\ 0 \end{pmatrix} dt + \begin{pmatrix} \sqrt{2D_r} & 0 \\ 0 & \frac{\sqrt{2D_r}}{\sin \theta} \end{pmatrix} \begin{pmatrix} dW_1(t) \\ dW_2(t) \end{pmatrix}. \quad (3.38)$$

The deterministic model displays that the cells swim against the gravity in the direction $\theta = 0$. To test the effect of rotational diffusion, we simulate 1000 cells over 10 time units with time step $dt = 0.01$, and take the rotational diffusion $D_r = 0.01$. As in the previous section, the ensemble average is given by Equations (3.13) and (3.14) and shown in Figure 3.4. The ensemble average of θ is less than the ensemble average of θ for pure Brownian motion. This is due to the

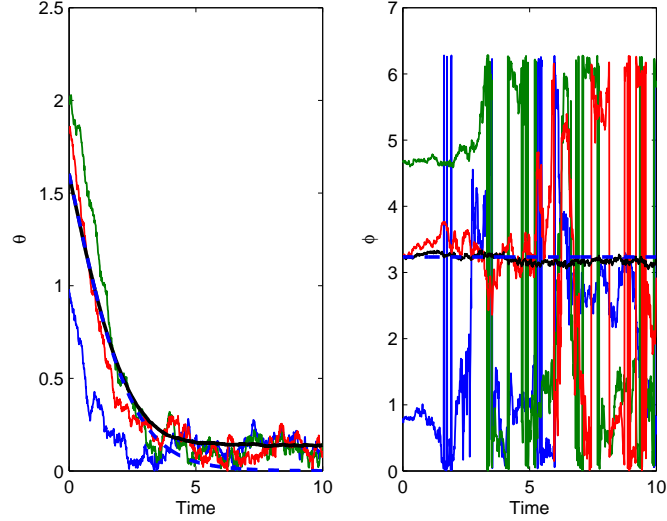


Figure 3.4: **Example realizations of the stochastic differential equation for gravitactic non-helical swimmers in still fluid.** The left panel shows three realizations (red, green, blue) of solutions of the first row of Equation (3.38) and the right panel shows three realizations of solution of the second row. The black line is the ensemble average of 1000 cells given by Equations (3.13) and (3.14) respectively. We fix rotational diffusion $D_r = 0.01$. The dashed blue is the mean of 1000 cells calculated using the deterministic Equations (3.20-3.21).

gravitational torque effect which causes cells to tend to swim upwards in the direction $\theta = 0$. The deterministic model shows that the mean of θ tends to zero. However, the ensemble average of θ for the stochastic differential equation, $\langle \theta \rangle = 0.13$, does not tend to zero because of the spurious drift presence.

In Figure 3.5, the orientation distribution of θ and ϕ are shown. The distribution of θ is given by Fisher distribution (3.37), and the distribution of ϕ is given by uniform distribution (3.16). The ensemble average of horizontal component of orientation, $\langle p_x(t) \rangle$ is close to what the deterministic model calculates (Figure 3.6).

Increasing the magnitude of the rotational diffusion, $D_r = 1$ result in divergence in the mean of θ . In Figure 3.7, it is noted that the ensemble average of θ of 5000 cells calculated using Equation (3.13) becomes closer to the ensemble average of θ for pure Brownian motion (see Figure 3.1). However the orientation distribution remains to be the Fisher distribution, Figure 3.8, and the ensemble average of horizontal component of orientation is zero as shown in Figure 3.9.

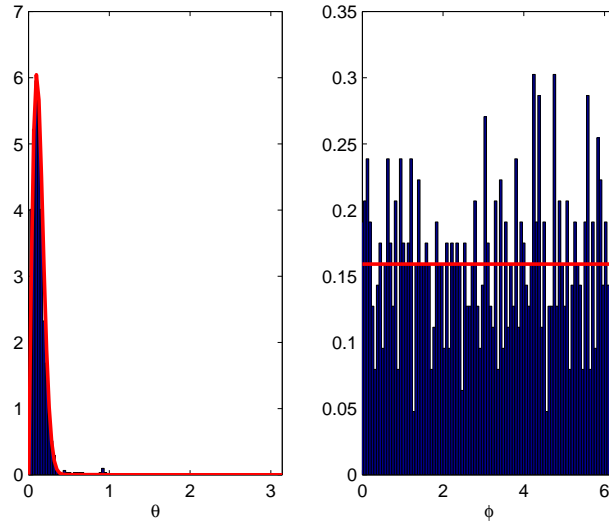


Figure 3.5: **Orientation distribution of gravitactic non-helical swimmers in still fluid.** The histograms show the realization of the solutions at the end time point. The left panel shows the realizations of the solution of the first row of Equation (3.38) at the end time point and the red curve is the distribution given by Equation (3.37). The right panel shows the realizations of the solution the second row of Equation (3.38) at the end time point and the red curve is the distribution given by Equation (3.16). We fix rotational diffusion $D_r = 0.01$.

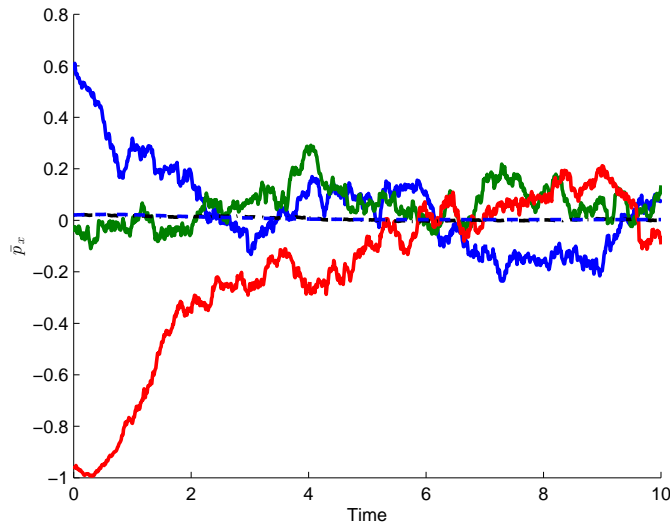


Figure 3.6: **Horizontal component of orientation p_x .** Three realizations (red, green, blue) of p_x are shown and the ensemble average $\langle p_x(t) \rangle$ of 1000 simulations is shown as black line. The dashed blue line is the average \bar{p}_x calculated using the deterministic model.

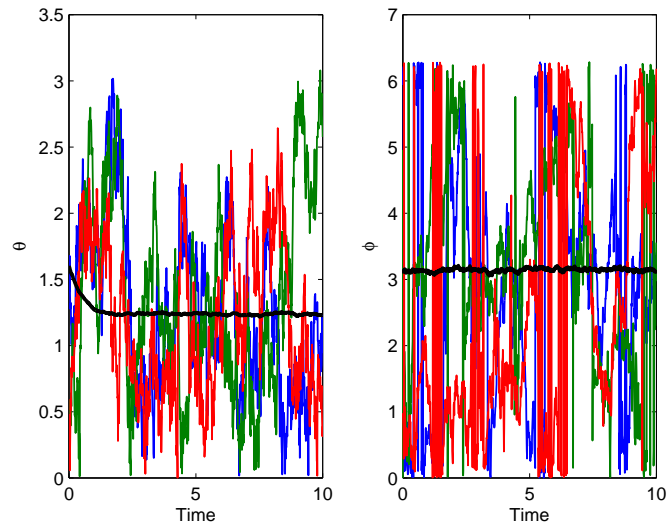


Figure 3.7: **Example realizations of the stochastic differential equation for gravitactic non-helical swimmers in still fluid.** As Figure 3.4 with $D_r = 1$ and 5000 cells simulated using Equation (3.38).

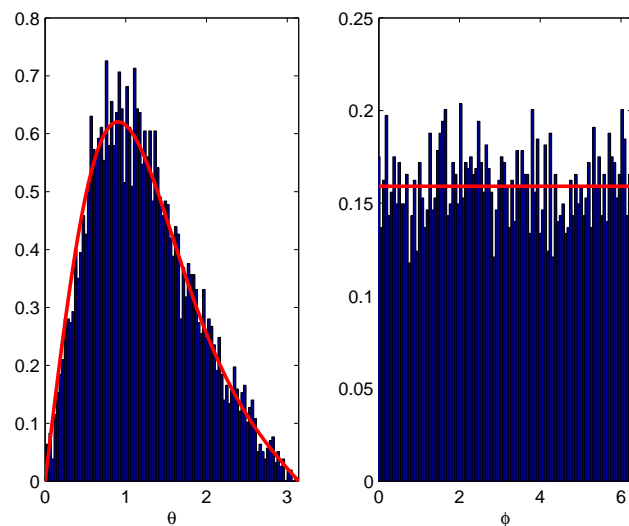


Figure 3.8: **Orientation distribution of gravitactic non-helical swimmers in still fluid.** As Figure 3.5 with $D_r = 1$ and 5000 cells simulated using Equation (3.38).

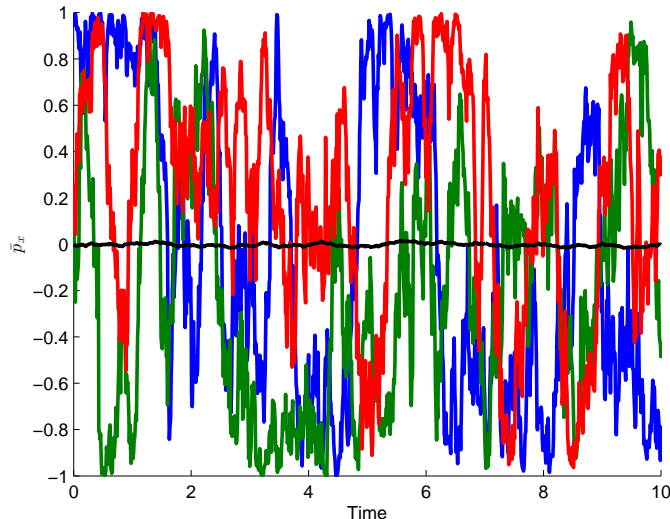


Figure 3.9: **Horizontal component of orientation p_x .** Three realizations (red, green, blue) of p_x are shown and the ensemble average $\langle p_x(t) \rangle$ of 5000 simulations is shown as black line.

3.3.2 Uniform shear flow

When the shear strength is not zero, we have the stochastic differential equation given in Equation (3.34).

Bees et al. [13] obtained a solution to the steady Fokker–Planck equation (3.30) using a spherical harmonic expansion in two dimensional flow as given in Equation (1.23). However, we do not compare their solution to the numerical solution we obtain here because of the complexity of their solution.

We here extend the case considered in Section 3.3.1 by adding the effect of shear flow to the drift term. We simulated 5000 cells in shear flow with magnitude $\Psi = 0.5$.

When the rotational diffusion is small, $D_r = 0.01$, the ensemble average of θ is $\langle \theta \rangle = 0.5310$. The mean of θ for deterministic model is $\bar{\theta} = 0.5233$. Both are close to the equilibrium solution $\theta^e = 0.5236$ as shown in Figure 3.10. The distribution of orientation angles are shown in Figure 3.11. Note that some cells have negative horizontal orientation component, thus we see a little peak at $\phi = \pi$. The ensemble average of the horizontal component of orientation, $\langle p_x(t) \rangle$, is

close to the mean expected from the deterministic model. This is shown in Figure 3.12.

To test the numerical method for stochastic differential equation (3.34) quantitatively, we run the code for different time step and different time duration and for different number of cells and rotational diffusion as shown in Table 3.1. As time step is decreased (Columns 2–3) the ensemble average of $\theta(t)$ is $\langle \theta(t) \rangle = 0.53$ to two decimal points differences but the ensemble average of $\cos \phi(t)$ is $\langle \cos \phi(t) \rangle = 0.9$ to only one decimal point difference. As time duration of simulations is increased (Columns 3–4) each of $\langle \theta(t) \rangle$ and $\langle \cos \phi(t) \rangle$ have the same ensemble average to two decimal points differences. Furthermore, increasing number of the cells (Columns 4–5) does not change the convergence of ensemble averages. However, as the rotational diffusion is increased (Columns 5–6) the ensemble average of $\theta(t)$, attains a new equilibrium $\langle \theta(t) \rangle$ while $\langle \cos \phi(t) \rangle$ does not yet attain the equilibrium over time interval of the simulation. In conclusion, once the equilibrium solution is attained for $D_r = 0.01$ the true value of $\langle \theta(t) \rangle$ and $\langle \cos \phi(t) \rangle$ are 0.53 and 0.97 respectively.

For the deterministic model given by Equations (3.20–3.21), as the time interval of the simulation is increased from $T = 10$ to $T = 20$, the average values of $\bar{\theta}$ and $\langle \cos \bar{\phi} \rangle$ attain the stable equilibrium solutions (θ^e and $\cos \phi^e$) given by (3.22) and shown in Table 3.2 where we assumed the default relative error tolerance 10^{-3} and the default absolute error tolerance 10^{-6} for the solver `ode45` [95].

For small time step $dt = 0.01$ and rotational diffusion $D_r = 0.01$, the absolute error in $\langle \theta(t) \rangle$ compared to the equilibrium solution θ^e is of order 10^{-2} .

When the rotational diffusion is strong, $D_r = 1$, the ensemble average of θ diverges from what the deterministic model expect and becomes close to the ensemble average for pure Brownian motion (see Figure 3.1). The orientation distribution for θ is indistinguishable from the case of still fluid, Figure 3.14. The ensemble average of horizontal component, $\langle p_x(t) \rangle$ is also indistinguishable from the still fluid value of zero, Figure 3.15.

	$T = 10$		$T = 20$		
	$dt = 0.1$	$dt = 0.01$	$dt = 0.01$	$dt = 0.01$	$dt = 0.01$
$\langle \theta \rangle$	0.5327	0.5310	0.5336	0.5345	0.6410
$\cos \langle \phi \rangle$	0.9182	0.9760	0.9714	0.9733	0.2454
	$D_r = 0.01$				$D_r = 0.1$
	sim= 1000		sim= 1000	sim= 2000	sim= 1000

Table 3.1: Convergence and accuracy of `simByEuler` used to solve stochastic model (Equation (3.34)). $\langle \theta \rangle$ and $\cos \langle \phi \rangle$ are the ensemble averages. Duration of time for simulations is denoted by T and time step is dt . Number of simulated cells is denoted by `sim` and rotational diffusion is D_r . Figures are given in Appendix C.

	$T = 10$	$T = 20$
$\bar{\theta}$	0.5233	0.5236
θ^e	0.5236	0.5236
$\cos \bar{\phi}$	0.9999	1.0000
$\cos \phi^e$	1.0000	1.0000

Table 3.2: Convergence and accuracy of `ode45` solver used to solve deterministic model (Equations (3.20–3.21)). The average of orientation angles are $\bar{\theta}$ and $\bar{\phi}$. θ^e and $\cos \phi^e$ are the equilibrium solutions. Number of simulated cells is 1000. Figures are given in Appendix C.

The difference between the ensemble averages and the mean of the deterministic model as rotational diffusion becomes large is due to the fact that we are dealing with nonlinear stochastic differential equations which their expectation does not preserve the additive property. It only preserves the monotonicity property and also preserves the expectation of constant property [27, 84]. More information about the expectation of stochastic differential equation is provided in the Appendix A. It is important to note that

$$\langle p_x(t) \rangle = \langle \sin \theta(t) \cos \phi(t) \rangle \neq \sin \langle \theta(t) \rangle \cos \langle \phi(t) \rangle. \quad (3.39)$$

This inequality is shown for instance in Figure 3.12.

3.4 Fokker–Planck Equation for helical swimmers

In the previous section, we studied the orientation of non-helical swimmers where the propulsive torque and force are parallel and the orientation is determined by

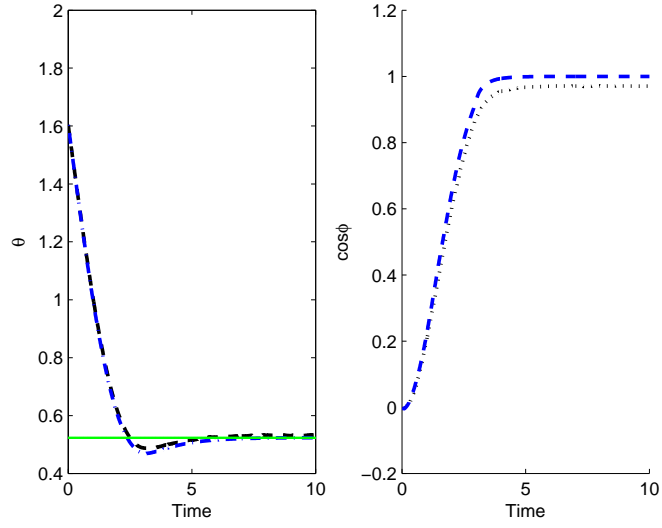


Figure 3.10: **Example realizations of the stochastic differential equation for non-helical swimmers in uniform shear flow.** The left panel shows the ensemble average given by Equations (3.13) of solutions of Equation (3.34) and the right panel shows $\cos \langle \phi(t) \rangle$. The blue dashed curves are the average calculated using the deterministic model, and the green line in the left panel is the equilibrium solution for deterministic model. We simulated 1000 cells where we fix $\Psi = 0.5$ and $D_r = 0.01$. Time step is $dt = 0.01$.

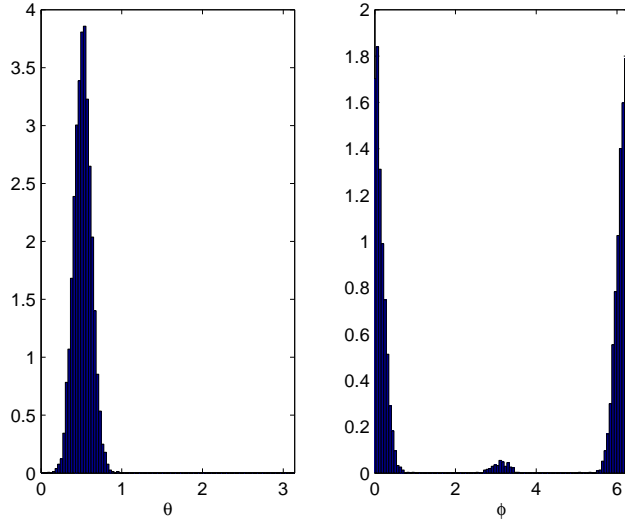


Figure 3.11: **Orientation distribution of non-helical swimmers in uniform shear flow.** The histograms show the realization of the solutions at the end time point. The left panel shows the realizations of the solution of the first row of Equation 3.34 at the end time point. The right panel shows the realizations of the solution of the second row of Equation 3.34 at the end time point. We fix $\Psi = 0.5$ and $D_r = 0.01$.

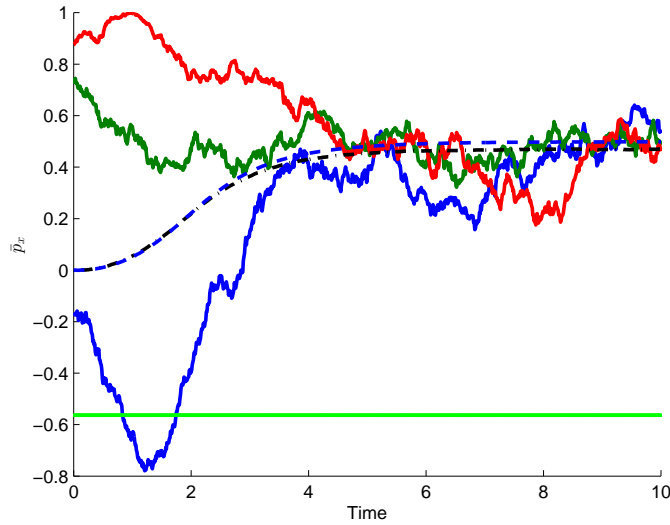


Figure 3.12: **Horizontal component of orientation p_x .** Three realizations of p_x are shown and the ensemble average $\langle p_x(t) \rangle$ of 5000 simulations is shown as black dashed line. The dashed blue line is the mean calculated using the deterministic model. The green line is $\sin \langle \theta(t) \rangle \cos \langle \phi(t) \rangle$. We fix $\Psi = 0.5$ and $D_r = 0.01$.

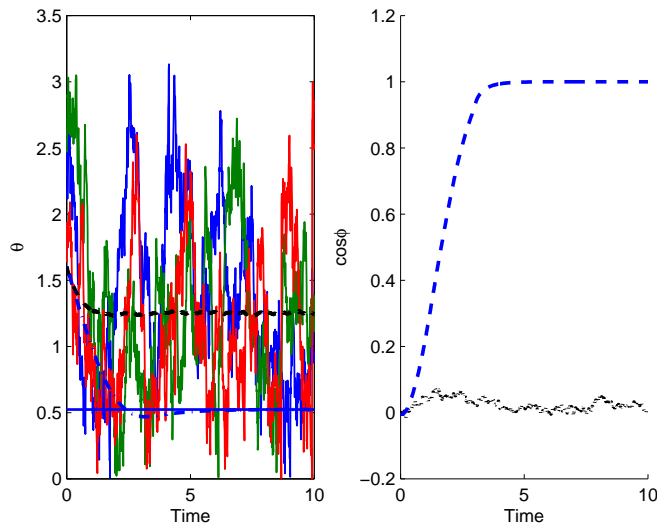


Figure 3.13: **Example realizations of the stochastic differential equation for non-helical swimmers in uniform shear flow.** The left panel shows three realizations (red, green, blue) of solutions of Equation (3.34). The ensemble average given by Equations (3.13). The right panel shows $\cos \langle \phi(t) \rangle$. The blue dashed curves are the average calculated using the deterministic model, and the blue line in the left panel is the equilibrium solution for deterministic model. We simulated 1000 cells where we fix $\Psi = 0.5$ and $D_r = 1$. Time step is $dt = 0.01$.

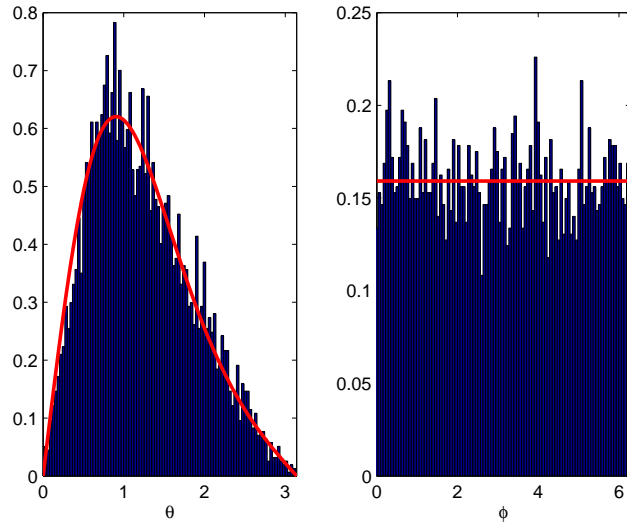


Figure 3.14: **Orientation distribution of non-helical swimmers in uniform shear flow.** As Figure 3.11. The red curve in the left panel is Fisher distribution (3.37) and the red line in the left panel is the uniform distribution. We fix $\Psi = 0.5$ and $D_r = 1$.

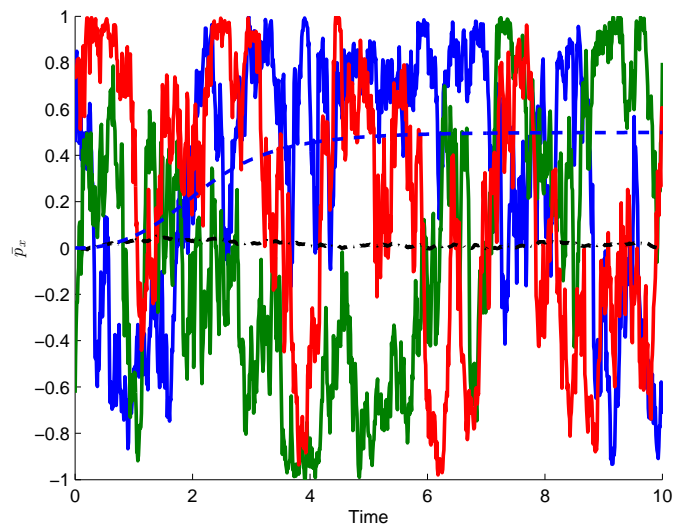


Figure 3.15: **Horizontal component of orientation p_x .** As Figure 3.12 with $\Psi = 0.5$ and $D_r = 1$.

spherical angles (θ, ϕ) . When the torque and force are not parallel, an additional angle is needed to describe the cells orientation as we have seen in Section 2.4. The orientation of the cell can be described using Euler angles (θ, ϕ, ψ) , see Equations (2.63-2.65).

To write Fokker–Planck equation in terms of the orientation angles (θ, ϕ, ψ) , we need to convert between infinitesimal rotations associated with these angles and those associated with rotations of angles η_i about the body fixed axes.

3.4.1 Infinitesimal rotation

To derive the relationship between Euler angles and the generators of infinitesimal rotations about the body fixed axes, we start by explaining the nature of infinitesimal rotation.

Consider an angle of rotation α about a unit vector \mathbf{u} . For small α , the infinitesimal matrix is given by

$$\mathbf{R} = \begin{pmatrix} 1 & -u_3\alpha & u_2\alpha \\ u_3\alpha & 1 & -u_1\alpha \\ -u_2\alpha & u_1\alpha & 1 \end{pmatrix} \quad (3.40)$$

A vector $\mathbf{x} = (x, y, z)^T$ will be rotated to $\mathbf{x}' = \mathbf{R}(\mathbf{x}) = \mathbf{x} + \alpha \mathbf{u} \wedge \mathbf{x}$. Consider a differentiable function $F(\mathbf{x})$ and use a Taylor expansion to obtain [61]

$$F(\mathbf{x}') = F(\mathbf{x}) + \alpha \mathbf{u} \wedge \mathbf{x} \cdot \nabla F. \quad (3.41)$$

Therefore we can associate this rotation with the following infinitesimal rotation operator

$$\frac{\partial}{\partial \alpha} = \mathbf{u} \wedge \mathbf{x} \cdot \nabla. \quad (3.42)$$

We note that if the vector \mathbf{u} is expressed in terms of the body-fixed basis vectors

$$\mathbf{u} = c_1 \mathbf{e}_1 + c_2 \mathbf{e}_2 + c_3 \mathbf{e}_3, \quad (3.43)$$

and $\frac{\partial}{\partial \eta_i}$ represents infinitesimal rotation about the axis \mathbf{e}_i

$$\frac{\partial}{\partial \eta_i} = \mathbf{e}_i \wedge \mathbf{x} \cdot \nabla, \quad (3.44)$$

then we have the relationship

$$\begin{aligned} \frac{\partial}{\partial \alpha} &= (c_1 \mathbf{e}_1 + c_2 \mathbf{e}_2 + c_3 \mathbf{e}_3) \wedge \mathbf{x} \cdot \nabla \\ &= c_1 \frac{\partial}{\partial \eta_1} + c_2 \frac{\partial}{\partial \eta_2} + c_3 \frac{\partial}{\partial \eta_3}. \end{aligned} \quad (3.45)$$

3.4.2 Infinitesimal rotation generators

To find the relationship between the rotation vectors given by Equations (2.40-2.42) for body fixed axes and the infinitesimal rotations associated with Euler angles, we have (Equations 2.43-2.45)

$$\hat{\mathbf{u}}_\phi = -\sin \theta \cos \psi \mathbf{e}_1 + \sin \theta \sin \psi \mathbf{e}_2 + \cos \theta \mathbf{e}_3, \quad (3.46)$$

$$\hat{\mathbf{u}}_\theta = \sin \psi \mathbf{e}_1 + \cos \psi \mathbf{e}_2, \quad (3.47)$$

$$\hat{\mathbf{u}}_\psi = \mathbf{e}_3. \quad (3.48)$$

Remark that Euler angles are rotation angles that play the role of α in Equation (3.45). So we have

$$\frac{\partial}{\partial \phi} = -\sin \theta \cos \psi \frac{\partial}{\partial \eta_1} + \sin \theta \sin \psi \frac{\partial}{\partial \eta_2} + \cos \theta \frac{\partial}{\partial \eta_3}, \quad (3.49)$$

$$\frac{\partial}{\partial \theta} = \sin \psi \frac{\partial}{\partial \eta_1} + \cos \psi \frac{\partial}{\partial \eta_2}, \quad (3.50)$$

$$\frac{\partial}{\partial \psi} = \frac{\partial}{\partial \eta_3}. \quad (3.51)$$

Therefore, the required relationship between the generators of infinitesimal

rotations about the body fixed axes xyz and infinitesimal rotations about $\hat{\mathbf{u}}_\phi$, $\hat{\mathbf{u}}_\theta$, and $\hat{\mathbf{u}}_\psi$ respectively is given by

$$\begin{pmatrix} \frac{\partial}{\partial \phi} \\ \frac{\partial}{\partial \theta} \\ \frac{\partial}{\partial \psi} \end{pmatrix} = \begin{pmatrix} -\cos \psi \sin \theta & \sin \theta \sin \psi & \cos \theta \\ \sin \psi & \cos \psi & 0 \\ 0 & 0 & 1 \end{pmatrix} \begin{pmatrix} \frac{\partial}{\partial \eta_1} \\ \frac{\partial}{\partial \eta_2} \\ \frac{\partial}{\partial \eta_3} \end{pmatrix}, \quad (3.52)$$

and taking the inverse, we obtain [76]

$$\begin{pmatrix} \frac{\partial}{\partial \eta_1} \\ \frac{\partial}{\partial \eta_2} \\ \frac{\partial}{\partial \eta_3} \end{pmatrix} = \begin{pmatrix} -\frac{\cos \psi}{\sin \theta} & \sin \psi & \cos \psi \cot \theta \\ \frac{\sin \psi}{\sin \theta} & \cos \psi & -\sin \psi \cot \theta \\ 0 & 0 & 1 \end{pmatrix} \begin{pmatrix} \frac{\partial}{\partial \phi} \\ \frac{\partial}{\partial \theta} \\ \frac{\partial}{\partial \psi} \end{pmatrix}, \quad (3.53)$$

which gives the relationship between the generators of infinitesimal rotations and Euler angles as stated in [76].

3.4.3 Fokker–Planck equation

Extending the definition of Equation (3.23) to account for the orientation due to Euler angles, we have Fokker–Planck equation [76]

$$\frac{\partial f}{\partial t} + \nabla \cdot (\mathbf{j}_d + \mathbf{j}_f) = 0 \quad (3.54)$$

where $\mathbf{j}_d = -D_r \nabla f$ and $\mathbf{j}_f = \dot{\boldsymbol{\eta}}_i f$ are the probability densities functions due to diffusion and due to the field respectively where $\dot{\boldsymbol{\eta}}_i$ is expression for the rate of the change of the angles of rotation θ , ϕ , and ψ about the body fixed axes for $i = 1, 2, 3$.

To write $\dot{\boldsymbol{\eta}}_i$ in term of Euler angles, we compute the dot product of the angular

velocity with the body fixed vectors

$$\dot{\eta}_1 = \mathbf{\Omega} \cdot \mathbf{e}_1 = -\sin \theta \sin \psi + \Theta \sin \gamma + \Psi [\sin \phi \cos \theta \cos \psi + \cos \phi \sin \psi], \quad (3.55)$$

$$\dot{\eta}_2 = \mathbf{\Omega} \cdot \mathbf{e}_2 = -\sin \theta \cos \psi + \Psi [\cos \phi \cos \psi - \sin \phi \cos \theta \sin \psi], \quad (3.56)$$

$$\dot{\eta}_3 = \mathbf{\Omega} \cdot \mathbf{e}_3 = \Theta \cos \gamma + \Psi \sin \phi \sin \theta, \quad (3.57)$$

where \mathbf{e}_i are orthogonal basis vectors for the body axes xyz given by Equations (2.40–2.42) and $\mathbf{\Omega}$ is the angular velocity given by Equation (2.48). Note that ∇ is now defined in three dimensional orientation space.

Choosing the body fixed axes to be the standard axes of the rotational diffusion coefficient tensor, the Fokker–Planck equation is then given by

$$\frac{\partial f}{\partial t} = \sum_{i=1}^3 D_{r_i} \frac{\partial^2 f}{\partial \eta_i^2} - \frac{\partial}{\partial \eta_i} (\dot{\eta}_i f). \quad (3.58)$$

The variables η_i are not convenient as they express the change in Euler angles relative to the body fixed axes [76]; therefore, we need variables that describe the orientation of the cell relative to the space fixed axes. These variables are Euler angles. Since we are considering spherical cells, we are assuming the diffusion is isotropic so that $D_{r_i} = D_r$ for $i = 1, 2, 3$.

Using the matrix relationship given in (3.53), we obtain the diffusion in terms of Euler angles

$$D_r \sum_{i=1}^3 \frac{\partial}{\partial \eta_i} \left(\frac{\partial f}{\partial \eta_i} \right) = D_r \left(\frac{1}{\sin \theta} \left(\frac{\partial}{\partial \theta} \sin \theta \frac{\partial}{\partial \theta} \right) + \frac{1}{\sin^2 \theta} \frac{\partial^2}{\partial \phi^2} + \frac{1}{\sin^2 \theta} \frac{\partial^2}{\partial \psi^2} - 2 \frac{\cos \theta}{\sin^2 \theta} \frac{\partial^2}{\partial \phi \partial \psi} \right) f. \quad (3.59)$$

Substituting Equations (3.55-3.57) and (3.59) into Equation (3.58) gives

$$\begin{aligned}
 & \frac{\partial f}{\partial t} - D_r \left(\frac{\partial^2}{\partial \theta^2} + \cot \theta \frac{\partial}{\partial \theta} + \frac{1}{\sin^2 \theta} \frac{\partial^2}{\partial \phi^2} + \frac{1}{\sin^2 \theta} \frac{\partial^2}{\partial \psi^2} - 2 \frac{\cos \theta}{\sin^2 \theta} \frac{\partial^2}{\partial \phi \partial \psi} \right) f \\
 & - \Psi \left(\cos \phi \frac{\partial f}{\partial \theta} - \cot \theta \sin \phi \frac{\partial f}{\partial \phi} + \frac{\sin \phi}{\sin \theta} \frac{\partial f}{\partial \psi} \right) \\
 & + \left(\sin \theta \frac{\partial f}{\partial \theta} + 2 \cos \theta f \right) \\
 & - \Theta \left(\sin \psi \sin \gamma \frac{\partial f}{\partial \theta} - \frac{\cos \psi}{\sin \theta} \sin \gamma \frac{\partial f}{\partial \phi} + (\cos \gamma + \cot \theta \sin \gamma \cos \psi) \frac{\partial f}{\partial \psi} \right) = 0.
 \end{aligned} \tag{3.60}$$

The second term in the first line is the diffusion term and the last three lines are the drift term in the Fokker–Planck equation where the term multiplied by Ψ represents the contribution of vorticity torque, the third line is due to the gravitational torque and the last line is the contribution of propulsive torque.

Note that if there is no propulsive torque acting on the cell, $\Theta = 0$, and we assume f is independent of ψ , we have that

$$\begin{aligned}
 & \frac{\partial f}{\partial t} - D_r \left(\frac{\partial^2}{\partial \theta^2} + \cot \theta \frac{\partial}{\partial \theta} + \frac{1}{\sin^2 \theta} \frac{\partial^2}{\partial \phi^2} \right) \\
 & - \Psi \left(\cos \phi \frac{\partial f}{\partial \theta} - \cot \theta \sin \phi \frac{\partial f}{\partial \phi} \right) + \left(\sin \theta \frac{\partial f}{\partial \theta} + 2 \cos \theta f \right) = 0.
 \end{aligned} \tag{3.61}$$

which is Fokker–Planck equation (3.30).

3.4.4 Derivation of stochastic differential equation for gyrotactic helical swimmers

We follow the same approach to write Fokker–Planck equation (3.32) in the standard form. Using the transformation (3.6), we can write Equation (3.60)

as

$$\begin{aligned}
 \frac{\partial F}{\partial t} = & -\frac{\partial}{\partial \theta} \left((-\sin \theta + \Theta \sin \gamma \sin \psi + \Psi \cos \phi + D_r \cot \theta) F \right) \\
 & -\frac{\partial}{\partial \phi} \left(\left(-\Theta \frac{\sin \gamma \cos \psi}{\sin \theta} - \Psi \frac{\sin \phi \cos \theta}{\sin \theta} \right) F \right) \\
 & -\frac{\partial}{\partial \psi} \left(\left(\Theta (\cot \theta \cos \psi \sin \gamma + \cos \gamma) + \Psi \frac{\sin \phi}{\sin \theta} \right) F \right) \\
 & + \frac{1}{2} \left[\frac{\partial^2}{\partial \theta^2} (2D_r F) + \frac{\partial^2}{\partial \phi^2} \left(\frac{2D_r}{\sin^2 \theta} F \right) + \frac{\partial^2}{\partial \psi^2} \left(\frac{2D_r}{\sin^2 \theta} F \right) + \frac{\partial^2}{\partial \phi \partial \psi} \left(\frac{-4D_r \cos \theta}{\sin^2 \theta} F \right) \right].
 \end{aligned} \tag{3.62}$$

Both forms of Fokker–Planck equation (3.60 and 3.62) are equivalent.

To associate the standard Fokker–Planck equation (3.62) with a stochastic differential equation, we first need to compute the square root of the diffusion matrix

$$\mathbf{B} = \begin{bmatrix} 2D_r & 0 & 0 \\ 0 & \frac{2D_r}{\sin^2 \theta} & -\frac{2D_r \cos \theta}{\sin^2 \theta} \\ 0 & -\frac{2D_r \cos \theta}{\sin^2 \theta} & \frac{2D_r}{\sin^2 \theta} \end{bmatrix}. \tag{3.63}$$

We compute the eigenvalues and eigenvectors and then use the diagonalization method to calculate the square root.

We start by solving the characteristic equation

$$0 = \det |\mathbf{B} - \lambda \mathbf{I}| = \begin{vmatrix} 2D_r - \lambda & 0 & 0 \\ 0 & \frac{2D_r}{\sin^2 \theta} - \lambda & -2D_r \frac{\cos \theta}{\sin^2 \theta} \\ 0 & -2D_r \frac{\cos \theta}{\sin^2 \theta} & \frac{2D_r}{\sin^2 \theta} - \lambda \end{vmatrix} \tag{3.64}$$

$$= (2D_r - \lambda) \left[\left(\frac{2D_r}{\sin^2 \theta} - \lambda \right)^2 - 4D_r^2 \frac{\cos^2 \theta}{\sin^4 \theta} \right]. \tag{3.65}$$

Solving for λ , we obtain the following eigenvalues

$$\lambda_1 = 2D_r, \quad \lambda_2 = \frac{2D_r(1 + \cos \theta)}{\sin^2 \theta}, \quad \lambda_3 = \frac{2D_r(1 - \cos \theta)}{\sin^2 \theta}. \tag{3.66}$$

The associated eigenvectors are

$$\mathbf{v}_1 = (1, -1, 0), \quad \mathbf{v}_2 = (0, 0, 1), \quad \mathbf{v}_3 = (1, 1, 0), \quad (3.67)$$

which form a basis for the null space of matrix \mathbf{B} . Since they are linearly independent, \mathbf{B} is diagonalizable. Therefore, the square root of \mathbf{B} is given by

$$\mathbf{B}^{\frac{1}{2}} = \mathbf{V}\mathbf{\Lambda}^{\frac{1}{2}}\mathbf{V}^{-1}, \quad (3.68)$$

where \mathbf{V} is a square matrix whose columns are the eigenvectors and $\mathbf{\Lambda}$ is a diagonal matrix whose diagonal consists of the eigenvalues. So, we have

$$\mathbf{V} = \begin{pmatrix} 1 & 0 & 1 \\ -1 & 0 & 1 \\ 0 & 1 & 0 \end{pmatrix}, \quad \mathbf{V}^{-1} = \begin{pmatrix} \frac{1}{2} & -\frac{1}{2} & 0 \\ 0 & 0 & 1 \\ \frac{1}{2} & \frac{1}{2} & 0 \end{pmatrix}, \quad \mathbf{\Lambda}^{\frac{1}{2}} = \begin{pmatrix} \sqrt{2D_r} & 0 & 0 \\ 0 & \frac{\sqrt{2D_r(1+\cos\theta)}}{\sin\theta} & 0 \\ 0 & 0 & \frac{\sqrt{2D_r(1-\cos\theta)}}{\sin\theta} \end{pmatrix}. \quad (3.69)$$

Substitute in Equation (3.68) and simplify the result, we obtain

$$\mathbf{B}^{\frac{1}{2}} = \begin{pmatrix} \sqrt{2D_r} & 0 & 0 \\ 0 & \frac{\sqrt{2D_r(1+\cos\theta)} + \sqrt{2D_r(1-\cos\theta)}}{2\sin\theta} & \frac{\sqrt{2D_r(1-\cos\theta)} - \sqrt{2D_r(1+\cos\theta)}}{2\sin\theta} \\ 0 & \frac{\sqrt{2D_r(1-\cos\theta)} - \sqrt{2D_r(1+\cos\theta)}}{2\sin\theta} & \frac{\sqrt{2D_r(1+\cos\theta)} + \sqrt{2D_r(1-\cos\theta)}}{2\sin\theta} \end{pmatrix}. \quad (3.70)$$

The standard Fokker–Planck equation (3.62) thus can be associated with the following stochastic differential equation

$$\begin{pmatrix} d\theta \\ d\phi \\ d\psi \end{pmatrix} = \begin{pmatrix} -\sin\theta + \Theta \sin\gamma \sin\psi + \Psi \cos\phi + D_r \cot\theta \\ -\Theta \frac{\sin\gamma \cos\psi}{\sin\theta} - \Psi \frac{\sin\phi \cos\theta}{\sin\theta} \\ \Theta(\cot\theta \cos\psi \sin\gamma + \cos\gamma) + \Psi \frac{\sin\phi}{\sin\theta} \end{pmatrix} dt + \begin{pmatrix} \sqrt{2D_r} & 0 & 0 \\ 0 & \frac{\sqrt{2D_r(1+\cos\theta)} + \sqrt{2D_r(1-\cos\theta)}}{2\sin\theta} & \frac{\sqrt{2D_r(1-\cos\theta)} - \sqrt{2D_r(1+\cos\theta)}}{2\sin\theta} \\ 0 & \frac{\sqrt{2D_r(1-\cos\theta)} - \sqrt{2D_r(1+\cos\theta)}}{2\sin\theta} & \frac{\sqrt{2D_r(1+\cos\theta)} + \sqrt{2D_r(1-\cos\theta)}}{2\sin\theta} \end{pmatrix} \begin{pmatrix} dW_1(t) \\ dW_2(t) \\ dW_3(t) \end{pmatrix}. \quad (3.71)$$

3.5 Numerical simulation of stochastic differential equation for gyrotactic helical swimmers

In this section we undertake a numerical simulation for the stochastic differential Equation (3.71). We first consider the case where this equation is reduced numerically to that for the non-helical swimmers. We will then discuss simulations of the full system (3.71) for helical swimmers, first in still fluid and then in uniform flow.

The ensemble average of the simulations given by

$$\langle \theta(t) \rangle = \frac{1}{N} \sum_{i=1}^N \theta_i(t), \quad \langle \phi(t) \rangle = \frac{1}{N} \sum_{i=1}^N \phi_i(t), \quad \langle \psi(t) \rangle = \frac{1}{N} \sum_{i=1}^N \psi_i(t), \quad (3.72)$$

where N is the number of cells.

When either $\Theta = 0$ or $\gamma = 0$, or both are zero, the helical model should reduce to the non-helical model. To test this case, we simulated 1000 cells in uniform shear flow with magnitude $\Psi = 0.5$ and rotational diffusion $D_r = 0.01$. For example, when $\Theta = 0$ and $\gamma = \frac{\pi}{4}$, the ensemble average of θ agrees with the mean computed for the non-helical model as shown in Figure 3.16. The equilibrium solution for the non-helical is given in equation (3.22) and is attained in this example. Furthermore, the orientation of Euler angles are shown in Figure 3.17 where the orientations of θ and ϕ are indistinguishable from the case of the non-helical model (see Figure 3.11), and the orientation of ψ appears to be uniform distribution as it depends only on the initial condition which is assumed to be uniform $U(0, 2\pi)$. The ensemble average of the horizontal component, $\langle p_x(t) \rangle$, is also indistinguishable from the mean calculated for the deterministic model, Figure 3.18. Another example where the helical model should reduce to the non-helical model is shown in Figures 3.19–3.21 for $\Theta = 1$ and $\gamma = 0$ and the same argument as in the previous example holds here too.

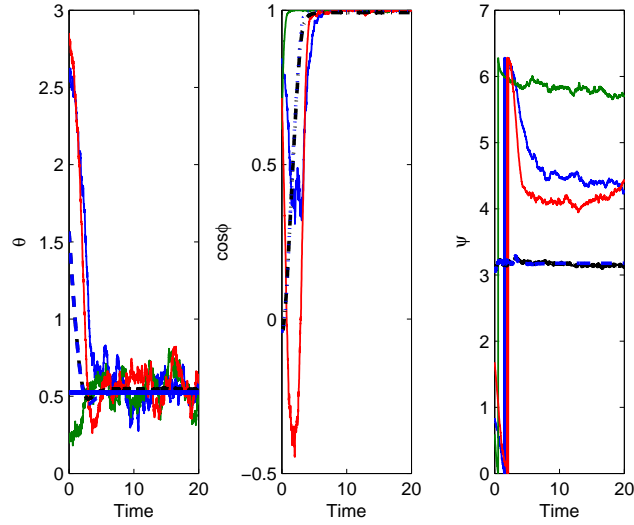


Figure 3.16: **Example realizations to the stochastic differential equation for helical swimmers in uniform shear flow.** Three realization of solution of Equation (3.71) are shown. The black dashed curves are the ensemble average of Euler angles which is calculated by using Equations (3.72) respectively. The blue dashed curve is the mean of orientation angles calculated using the deterministic model. We fix $\Theta = 0$, $\gamma = \frac{\pi}{4}$, $D_r = 0.01$ and $\Psi = 0.5$.

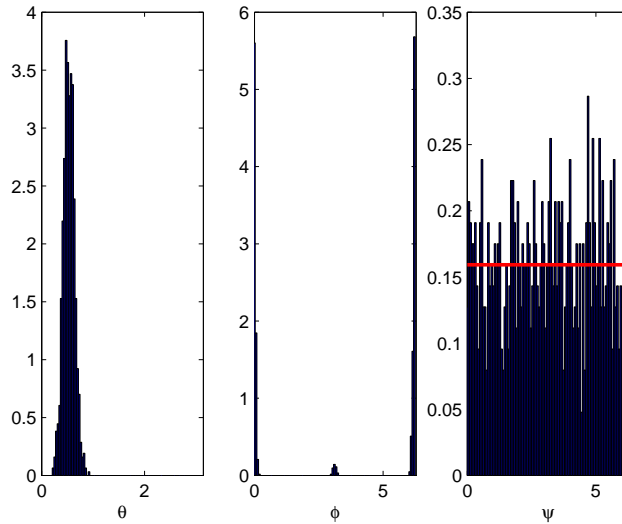


Figure 3.17: **Orientation distribution of helical swimmers in uniform shear flow.** The histograms show the realization of the solutions at the end time point. The left panel shows the realizations of the solution of the first row of Equation (3.71) at the end time point. The middle and right panels show the realizations of the solution the second and third rows of Equation (3.71) respectively at the end time point. The red line in the right panel is the uniform distribution. We fix $\Theta = 0$, $\gamma = \frac{\pi}{4}$, $D_r = 0.01$ and $\Psi = 0.5$.

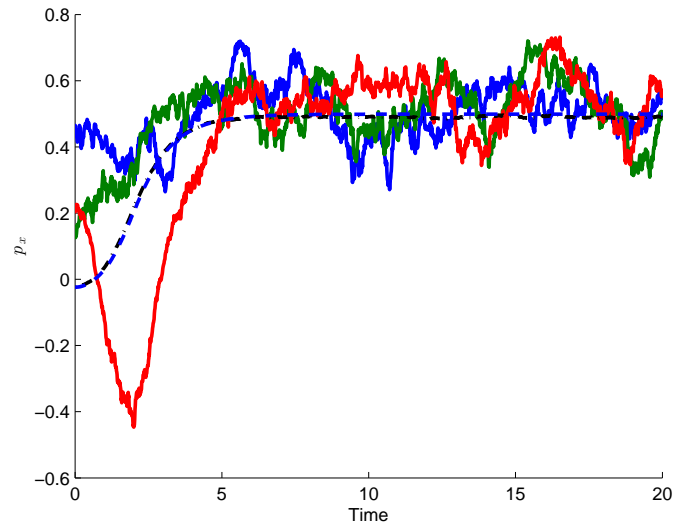


Figure 3.18: **Horizontal component of orientation p_x** : Three realizations of p_x are shown and the ensemble average $\langle p_x \rangle$ of 5000 simulations is shown as black line. We fix $\Theta = 0$, $\gamma = \frac{\pi}{4}$, $\Psi = 0.5$ and $D_r = 0.01$.

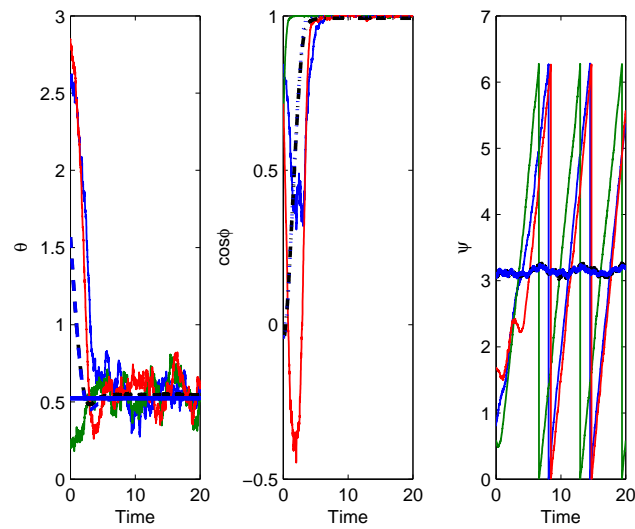


Figure 3.19: **Example realizations to the stochastic differential equation for helical swimmers in uniform shear flow.** As of Figure 3.16. We fix $\Theta = 1$, $\gamma = 0$, $D_r = 0.01$ and $\Psi = 0.5$.

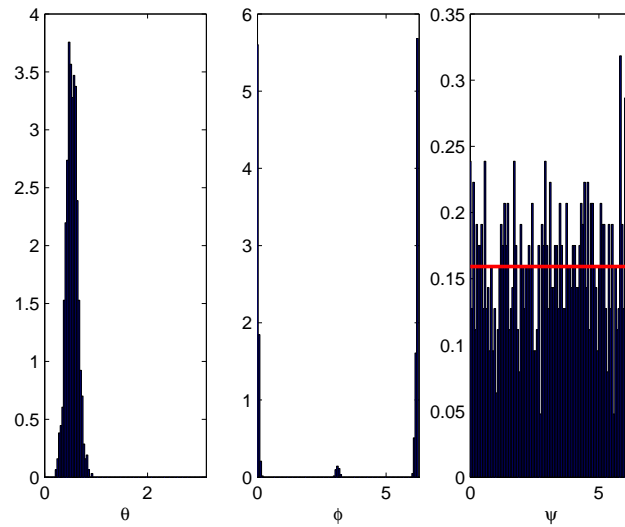


Figure 3.20: **Orientation distribution of helical swimmers in uniform shear flow.** As of Figure 3.17. We fix $\Theta = 1$, $\gamma = 0$, $D_r = 0.01$ and $\Psi = 0.5$.

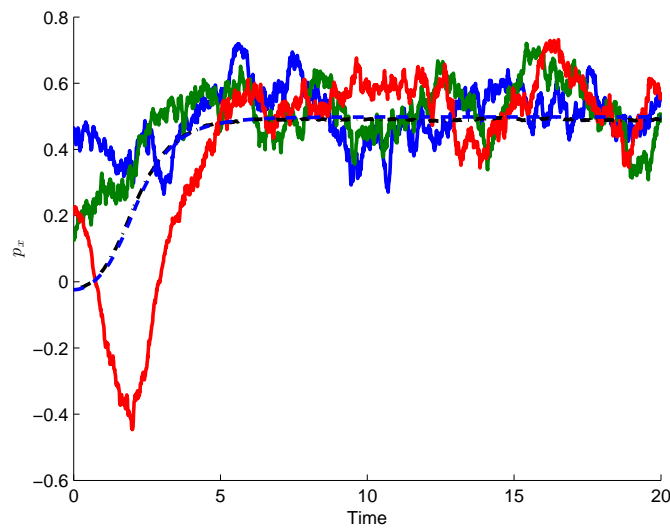


Figure 3.21: **Horizontal component of orientation p_x :** As of Figure 3.18. We fix $\Theta = 1$, $\gamma = 0$, $\Psi = 0.5$ and $D_r = 0.01$.

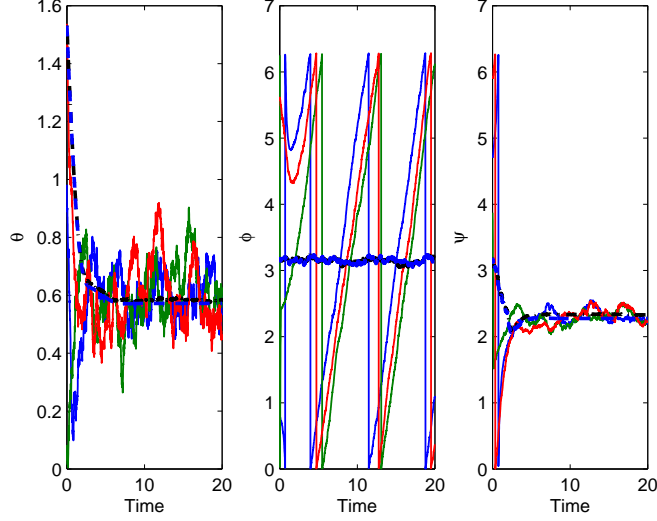


Figure 3.22: **Example realizations to the stochastic differential equation for helical swimmers in still fluid.** Three realizations of solutions of Equation (3.73) are shown in red, green and blue. The black dashed curves are the ensemble average of Euler angles which is calculated by using Equations (3.72) respectively. Blue dashed curve is the mean of orientation angles calculated using the deterministic model. We fix $\Theta = 1$, $\gamma = \frac{\pi}{4}$ and $D_r = 0.01$.

3.5.1 Gyrotactic bias of helical swimmers in still fluid

When the shear strength is zero, $\Psi = 0$, Equation (3.71) reduces to

$$\begin{pmatrix} d\theta \\ d\phi \\ d\psi \end{pmatrix} = \begin{pmatrix} -\sin\theta + \Theta \sin\gamma \sin\psi + D_r \cot\theta \\ -\Theta \frac{\sin\gamma \cos\psi}{\sin\theta} \\ \Theta(\cot\theta \cos\psi \sin\gamma + \cos\gamma) \end{pmatrix} dt + \begin{pmatrix} \sqrt{2D_r} & 0 & 0 \\ 0 & \frac{\sqrt{2D_r(1+\cos\theta)} + \sqrt{2D_r(1-\cos\theta)}}{2\sin\theta} & \frac{\sqrt{2D_r(1-\cos\theta)} - \sqrt{2D_r(1+\cos\theta)}}{2\sin\theta} \\ 0 & \frac{\sqrt{2D_r(1-\cos\theta)} - \sqrt{2D_r(1+\cos\theta)}}{2\sin\theta} & \frac{\sqrt{2D_r(1+\cos\theta)} + \sqrt{2D_r(1-\cos\theta)}}{2\sin\theta} \end{pmatrix} \begin{pmatrix} dW_1(t) \\ dW_2(t) \\ dW_3(t) \end{pmatrix}, \quad (3.73)$$

To test the effect of small rotational diffusion, we simulate 1000 realisations of the stochastic differential Equation (3.73) over 20 time units with time step $dt = 0.01$, taking the rotational diffusion $D_r = 0.01$. As in the previous section, the ensemble average is given by Equations (3.72) and shown in Figure 3.22. The ensemble average, $\langle \theta(t) \rangle$ is indistinguishable of what is expected from the

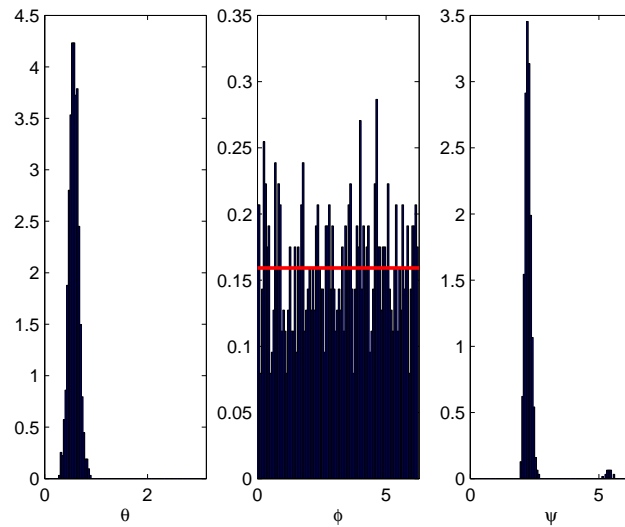


Figure 3.23: **Orientation distribution of helical swimmers in still fluid.** The histograms show the realization of the solutions at the end time point of Equation (3.73). The red line in the middle panel is the uniform distribution. We fix $\Theta = 1$, $\gamma = \frac{\pi}{4}$ and $D_r = 0.01$.

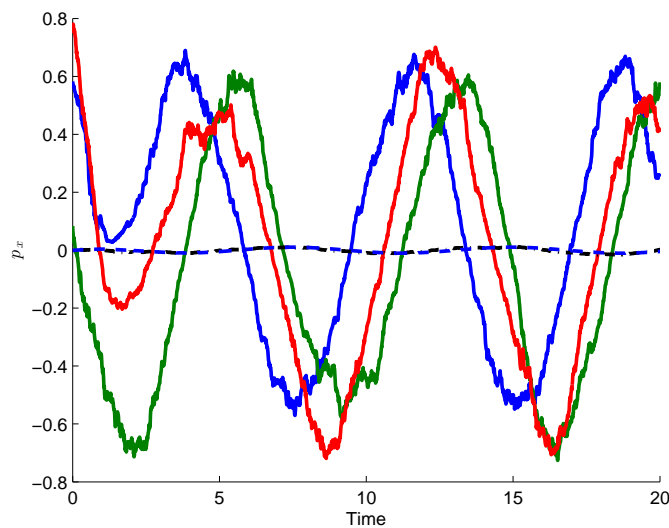


Figure 3.24: **Horizontal component of orientation p_x of helical swimmers in still fluid.** Three realizations of p_x are shown and the ensemble average $\langle p_x \rangle$ of 1000 simulations is shown as black line. We fix $\Theta = 1$, $\gamma = \frac{\pi}{4}$ and $D_r = 0.01$.

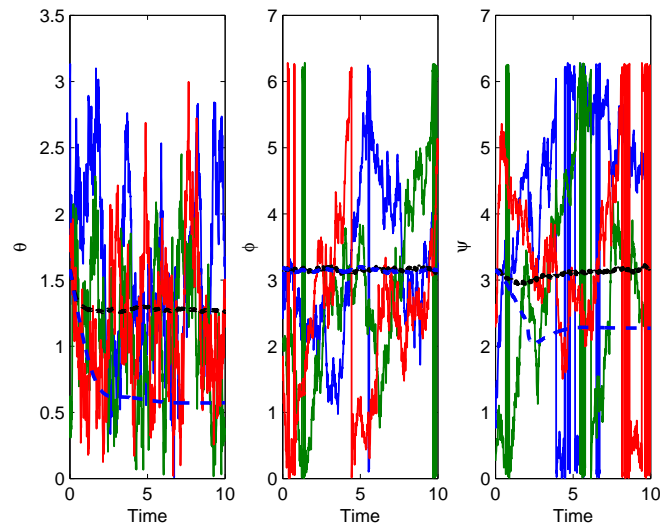


Figure 3.25: **Example realizations to the stochastic differential equation for helical swimmers in still fluid.** As of Figure 3.22. We fix $\Theta = 1$, $\gamma = \frac{\pi}{4}$ and $D_r = 1$.

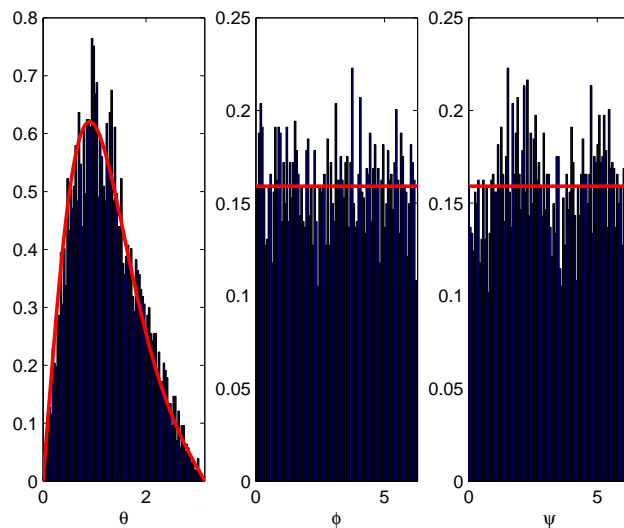


Figure 3.26: **Orientation distribution of helical swimmers in still fluid.** As of Figure 3.23. We fix $\Theta = 1$, $\gamma = \frac{\pi}{4}$ and $D_r = 1$.

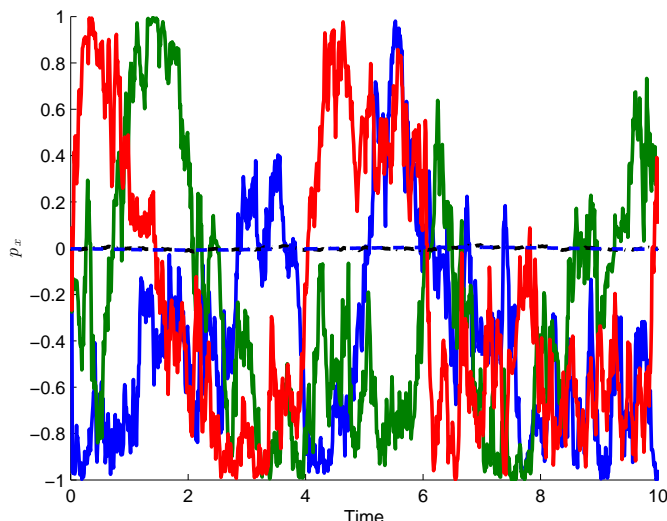


Figure 3.27: **Horizontal component of orientation p_x of helical swimmers in still fluid.** As of Figure 3.24. We fix $\Theta = 1$, $\gamma = \frac{\pi}{4}$ and $D_r = 1$.

deterministic model. In the case of zero shear flow, the cells swim in helical trajectories upwards as will be shown in the next chapter. The angle ϕ oscillate between 0 and 2π with ensemble average π which is indistinguishable from the mean expected from the deterministic model. The effect of the propulsive torque is seen in the ensemble average of ψ angle where it is initially assumed to be uniform $U(0, 2\pi)$. We note that the ensemble average of ψ attain the equilibrium ($\langle \psi \rangle = 2.32$) which is close to the equilibrium that is calculated using the deterministic model, $\bar{\psi} = 2.27$. The orientation distribution of Euler angles is shown in Figure 3.23. The ensemble average of horizontal component is shown in Figure 3.24 where the example realization of $p_x(t)$ oscillates around $\langle p_x(t) \rangle$ which is indistinguishable from the mean expected from the deterministic model.

As we have seen in Section 3.3, the magnitude of the rotational diffusion has an important impact on the nature of the orientation distribution, and the ensemble average of the horizontal component of orientation. To test this effect, we simulated 5000 realizations of the stochastic differential equation (3.73) over 10 time units with time step $dt = 0.01$. We fix $D_r = 1$. The ensemble average of Euler angles given by Equations (3.72) is shown in Figure 3.25. The ensemble average $\langle \theta(t) \rangle$ diverges from the mean expected from the deterministic model and becomes close to that of Brownian motion on unit sphere (see Figure 3.1).

In Figure 3.26, the orientation distribution of Euler angles are shown. The orientation distribution of θ is indistinguishable from Fisher distribution, Equation (3.37). The distribution of ϕ and ψ appears to be uniform.

The ensemble average of the horizontal component of orientation, $\langle p_x(t) \rangle$, is zero as expected from the deterministic model.

3.5.2 Uniform flow

In this section we add the shear strength to the stochastic differential equation to see how it will impact the the swimming orientation distribution. In this case we simulate Equation (3.71).

To compare with the non-helical model in uniform flow (Figures 3.10–3.12), with the aid of the equilibrium feasibility diagram (Figure 2.1) we consider $\Theta = 0.2$ and $\gamma = \frac{7\pi}{16}$ and shear strength $\psi = 0.5$. We simulate 1000 realizations of the stochastic differential equation (3.71) over 100 time units. We fix the rotational diffusion $D_r = 0.01$. The ensemble average of θ is slightly below the ensemble average for θ in the non-helical case. This is due to the existence of the propulsive torque. The ensemble averages for the Euler angles are shown in Figure 3.28. The orientation distribution shown in Figure 3.29. In Figure 3.30 the ensemble average of the horizontal component is distinguishable from the case of the non-helical model. Specifically, in the non-helical model, $\overline{p_x} = 0.5$ whilst for the helical model, this is reduced to $\overline{p_x} = 0.316$.

In Chapter 2, we discussed the impact of the propulsive torque strength, Θ , on the nature of the equilibrium feasibility. We will consider a pair of Θ and γ which have feasibility equilibrium for specific shear strength (see Figure 2.1). We first consider $\Theta = 1$, $\gamma = \frac{\pi}{4}$ and shear strength $\Psi = 1$. With these parameter values, the equilibrium is feasible and cells swim downwards in uniform flow. We fix rotational diffusion $D_r = 0.01$. We simulate 1000 realizations of the stochastic differential equation (3.71). The ensemble average of Euler angles attain equilibrium and is indistinguishable from the mean calculated using the

3.5. NUMERICAL SIMULATION OF STOCHASTIC DIFFERENTIAL EQUATION FOR GYROTACTIC HELICAL SWIMMERS

deterministic model as shown in Figure 3.31. The orientation distribution is shown in Figure 3.32. The ensemble average of the horizontal component, $\langle p_x(t) \rangle$ is indistinguishable from the mean expected from the deterministic model, Figure 3.33.

As another example to show the effect of the propulsive torque on the equilibrium feasibility we fix $\Theta = 1$ and $\gamma = \frac{7\pi}{16}$. When shear strength, $\Psi = 0.5$, the cells swim upwards with negative equilibrium horizontal component, $p_x^e < 0$ as expected from the deterministic model (see Figure 2.1c). We fix the rotational diffusion $D_r = 0.01$. The ensemble average of Euler angles are shown in Figure 3.34. The ensemble average of θ , ϕ , and ψ are indistinguishable from the mean expected from the deterministic model. The orientation distribution is shown in Figure 3.35. The ensemble average of horizontal component, $\langle p_x(t) \rangle$, is negative and indistinguishable from the mean expected from the deterministic model, Figure 3.36. When $\Psi = 1.5$, cells swim downwards in uniform flow (see Figure 2.1c). Again, the ensemble average of Euler angles are indistinguishable from the mean expected from the deterministic model for each angle as shown in Figure 3.37. Their orientation distribution is shown in Figure 3.38. The ensemble average becomes positive and is indistinguishable from the mean expected from the deterministic model Figure 3.39.

The above example shows also the effect of shear strength on orientation distribution. To compare the orientation distribution of ψ , we note that the peak of the histogram is on the far left when $\Psi = 0.5$, see Figure 3.35, and on the far right when $\Psi = 1.5$, see Figure 3.38.

As we have seen in Section 3.5.1, the magnitude of rotational diffusion has a potential impact on the nature of the swimming behaviour. We examine the stochastic differential equation for large rotational diffusion, $D_r = 1$. For example, when $\Theta = 1$ and $\gamma = \frac{\pi}{4}$, the ensemble average of Euler angles which reach equilibrium is indistinguishable from the case when the shear flow is zero, Figure 3.40. Also, the orientation distribution shown in Figure 3.41 and the ensemble average of horizontal component are indistinguishable from the case of

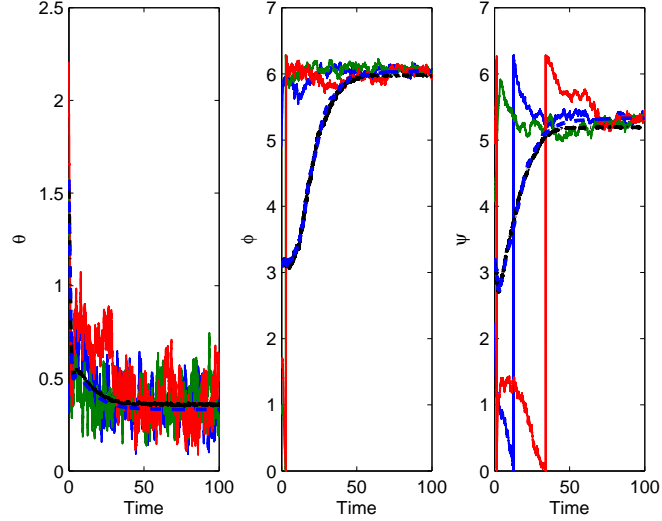


Figure 3.28: **Example realizations to the stochastic differential equation for helical swimmers in shear flow.** Three realizations of solutions of Equation (3.71) are shown in red, green and blue. The black dashed curves are the ensemble average of Euler angles which is calculated by using Equations (3.72) respectively. Blue dashed curve is the mean of orientation angles calculated using the deterministic model. We fix $\Theta = 0.2$, $\gamma = \frac{7\pi}{16}$, $D_r = 0.01$ and $\Psi = 0.5$.

still fluid, Figure 3.42. Another example is shown in Figures 3.43-3.45 for $\Theta = 1$ and $\gamma = \frac{7\pi}{16}$. These two examples show the effect of strength of rotational diffusion on cell orientation.

To test the case when the equilibrium expected from the deterministic model is not feasible, we choose $\Theta = 1$, $\gamma = \frac{\pi}{4}$, $\Psi = 0.5$. We simulate 1000 realizations of the stochastic differential equation (3.71) with rotational diffusion $D_r = 0.01$ over 20 time units. The ensemble average of θ and ψ are indistinguishable from the expected mean of the deterministic model as shown in Figure 3.46. The orientation distribution is shown in Figure 3.47. The ensemble average, $\langle p_x(t) \rangle$, oscillates over time, Figure 3.48.

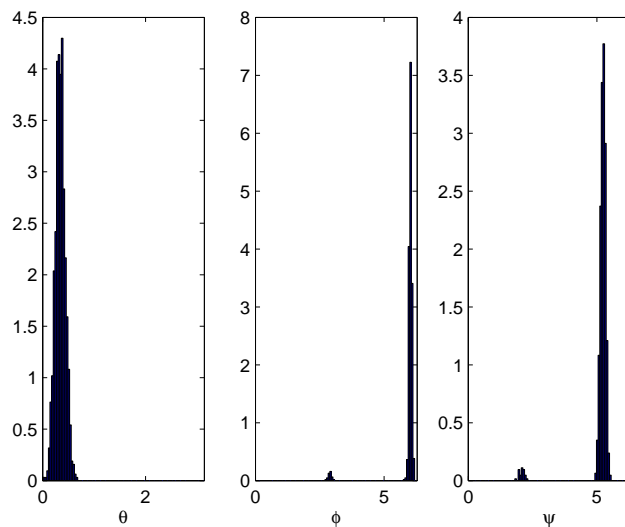


Figure 3.29: **Orientation distribution of helical swimmers in shear flow.** The histograms show the realization of the solutions at the end time point of Equation (3.71). We fix $\Theta = 0.2$, $\gamma = \frac{7\pi}{16}$, $D_r = 0.01$ and $\Psi = 0.5$.

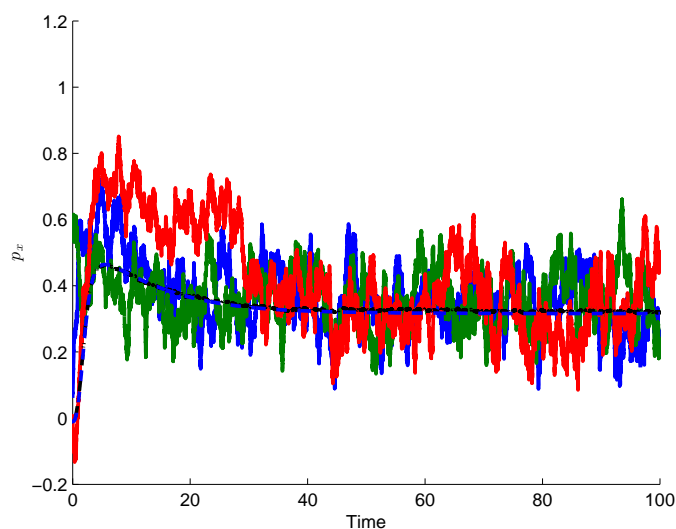


Figure 3.30: **Horizontal component of orientation p_x in shear flow for helical swimmers.** Three realizations of p_x are shown and the ensemble average $\langle p_x \rangle$ is shown as dash-dot black curve. The dashed blue curve is the mean computed from the deterministic model. We fix $\Theta = 0.2$, $\gamma = \frac{7\pi}{16}$, $D_r = 0.01$ and $\Psi = 0.5$.

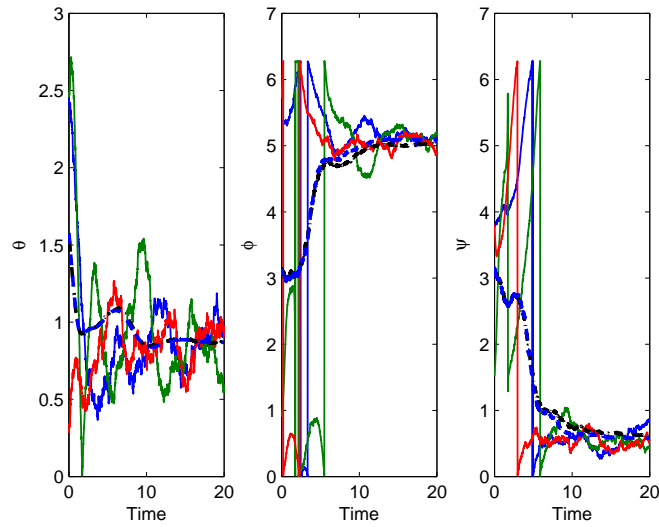


Figure 3.31: **Example realizations to the stochastic differential equation for helical swimmers in shear flow.** As of Figure 3.28. We fix $\Theta = 1$ and $\gamma = \frac{\pi}{4} D_r = 0.01 \Psi = 1$.

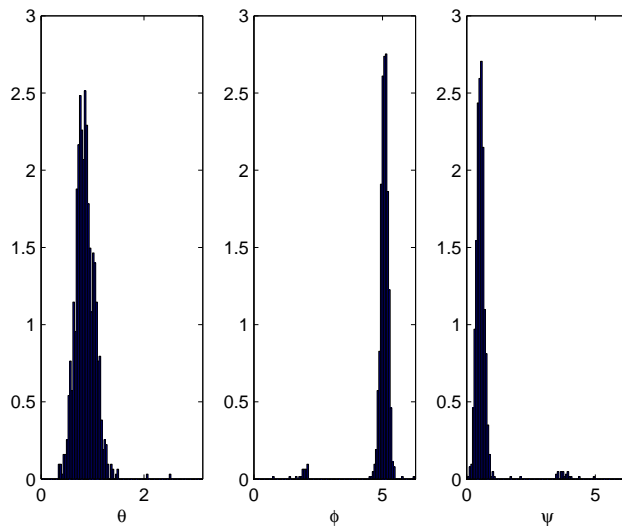


Figure 3.32: **Orientation distribution of helical swimmers in shear flow.** As of Figure 3.29. We fix $\Theta = 1$ and $\gamma = \frac{\pi}{4} D_r = 0.01 \Psi = 1$.

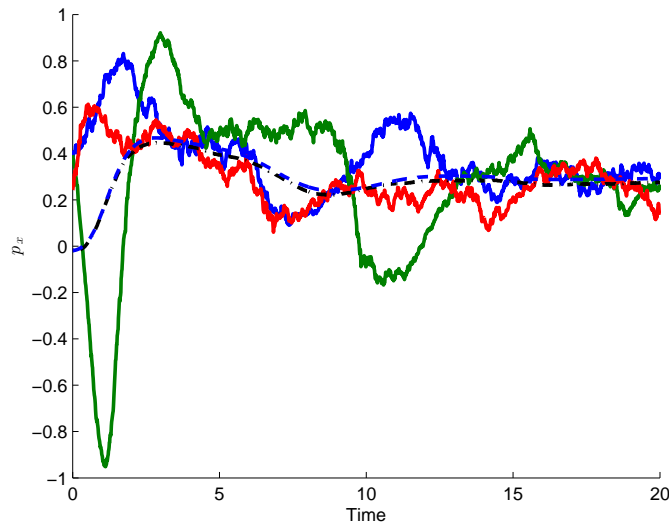


Figure 3.33: **Horizontal component of orientation p_x in shear flow for helical swimmers.** As of Figure 3.30. We fix $\Theta = 1$ and $\gamma = \frac{\pi}{4}$ $D_r = 0.01$ $\Psi = 1$.

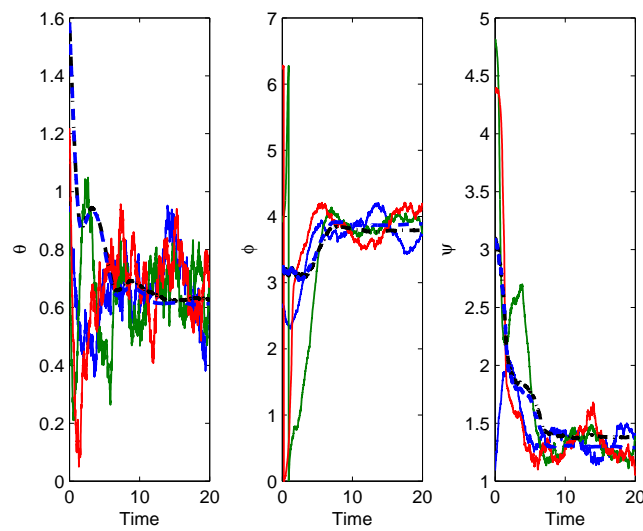


Figure 3.34: **Example realizations to the stochastic differential equation for helical swimmers in shear flow.** As of Figure 3.28. We fix $\Theta = 1$, $\gamma = \frac{7\pi}{16}$ $D_r = 0.01$ and $\Psi = 0.5$.

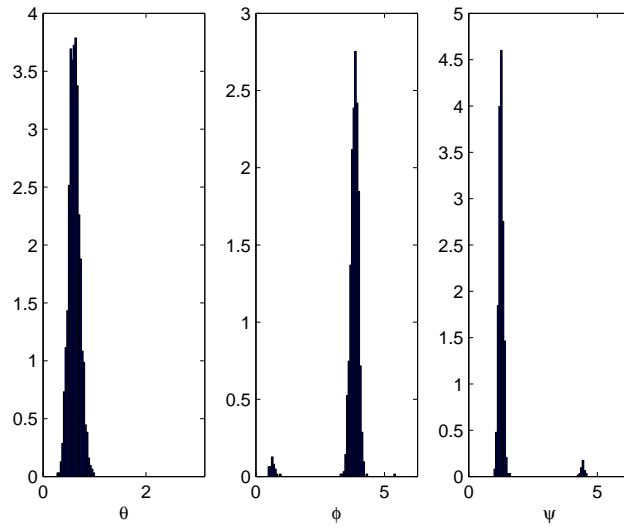


Figure 3.35: **Orientation distribution of helical swimmers in shear flow.** As of Figure 3.29. We fix $\Theta = 1$, $\gamma = \frac{7\pi}{16}$, $D_r = 0.01$ and $\Psi = 0.5$.

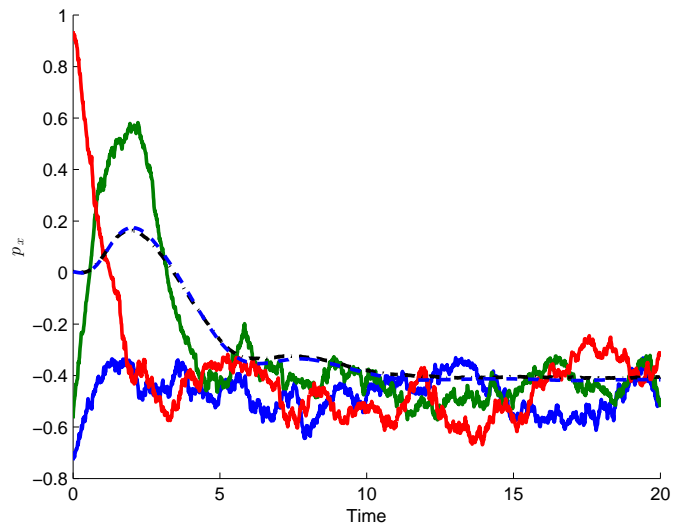


Figure 3.36: **Horizontal component of orientation p_x in shear flow for helical swimmers.** As of Figure 3.30. We fix $\Theta = 1$, $\gamma = \frac{7\pi}{16}$, $D_r = 0.01$ and $\Psi = 0.5$.

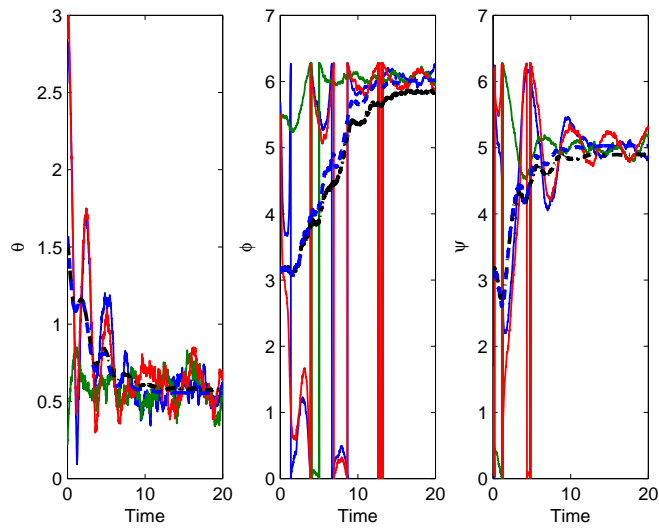


Figure 3.37: **Example realizations to the stochastic differential equation for helical swimmers in shear flow.** As of Figure 3.28. We fix $\Theta = 1$, $\gamma = \frac{7\pi}{16}$ $D_r = 0.01$ and $\Psi = 1.5$.

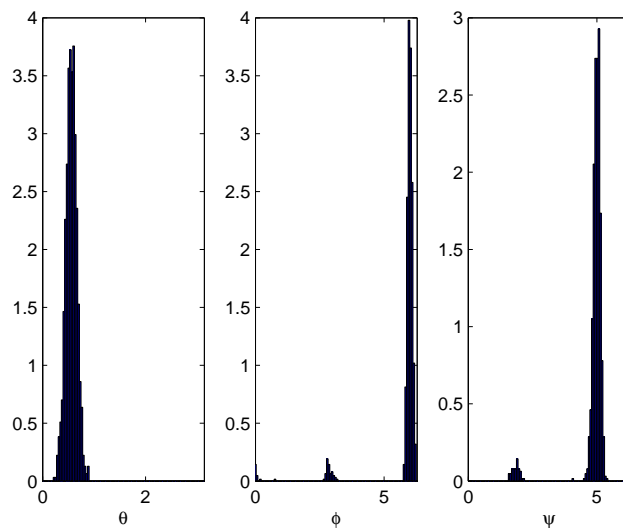


Figure 3.38: **Orientation distribution of helical swimmers in shear flow.** As of Figure 3.29. We fix $\Theta = 1$, $\gamma = \frac{7\pi}{16}$ $D_r = 0.01$ and $\Psi = 1.5$.

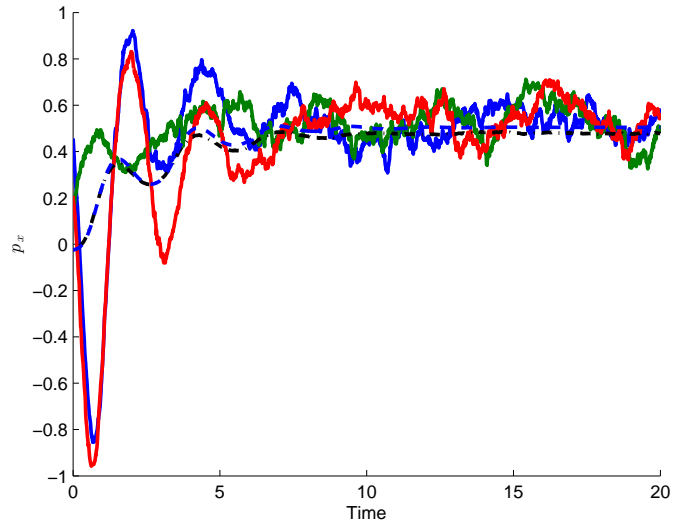


Figure 3.39: **Horizontal component of orientation p_x in shear flow for helical swimmers.** As of Figure 3.30. We fix $\Theta = 1$, $\gamma = \frac{7\pi}{16}$, $D_r = 0.01$ and $\Psi = 1.5$.

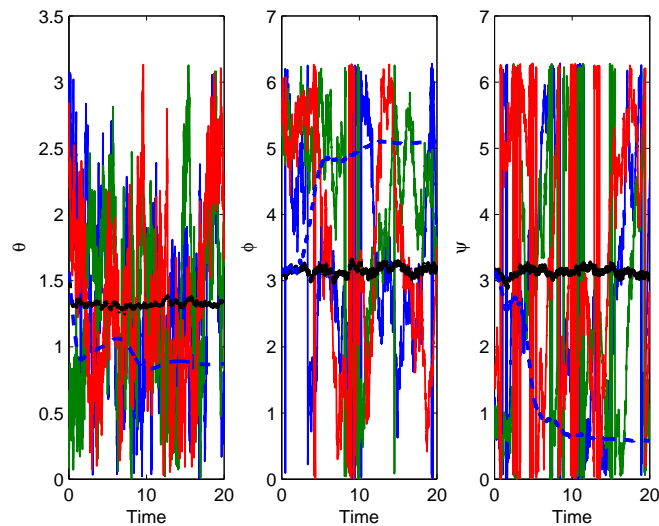


Figure 3.40: **Example realizations to the stochastic differential equation for helical swimmers in shear flow.** As of Figure 3.28. We fix $\Theta = 1$, $\gamma = \frac{\pi}{4}$, $\Psi = 1$ and $D_r = 1$. 1000 cells is simulated.

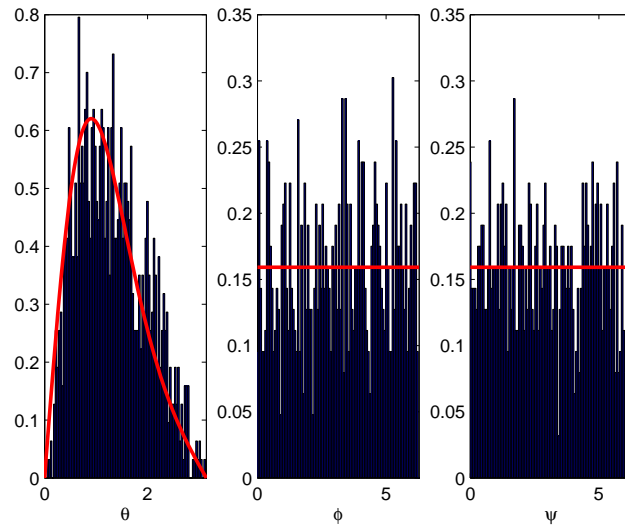


Figure 3.41: **Orientation distribution of helical swimmers in shear flow.** As of Figure 3.29. The red curve in the left panel is Fisher distribution (3.37). The red line is the uniform distribution. We fix $\Theta = 1$, $\gamma = \frac{\pi}{4}$ and $D_r = 1$ $\Psi = 1$.

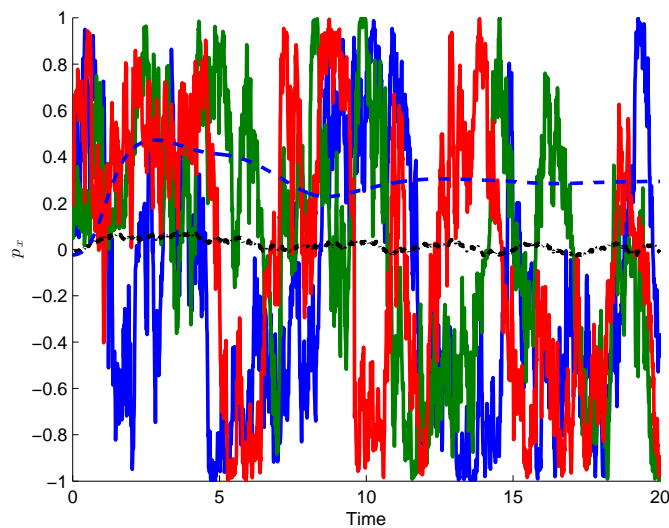


Figure 3.42: **Horizontal component of orientation p_x in shear flow for helical swimmers.** As of Figure 3.30. We fix $\Theta = 1$, $\gamma = \frac{\pi}{4}$ and $D_r = 1$ $\Psi = 1$. 1000 cells simulated.

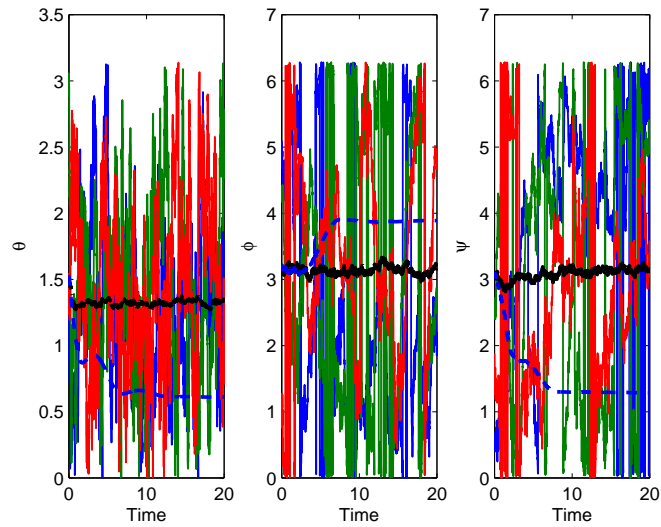


Figure 3.43: **Example realizations to the stochastic differential equation for helical swimmers in shear flow.** As of Figure 3.28. We fix $\Theta = 1$, $\gamma = \frac{7\pi}{16}$, $D_r = 1$ and $\Psi = 0.5$.

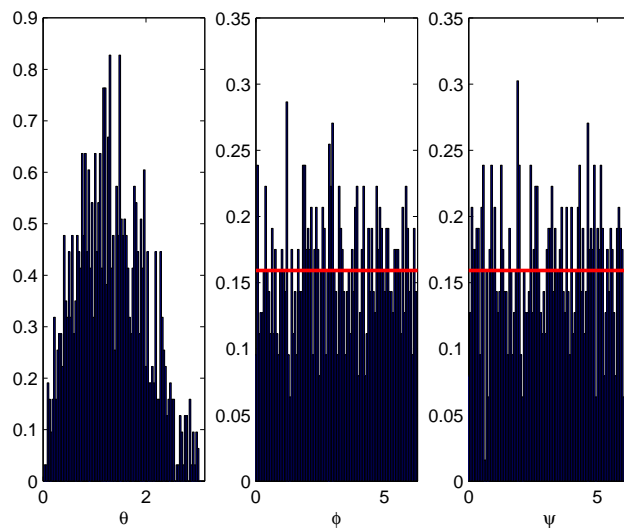


Figure 3.44: **Orientation distribution of helical swimmers in shear flow.** As of Figure 3.29. The red line is the uniform distribution. We fix $\Theta = 1$, $\gamma = \frac{7\pi}{16}$, $D_r = 1$ and $\Psi = 0.5$.

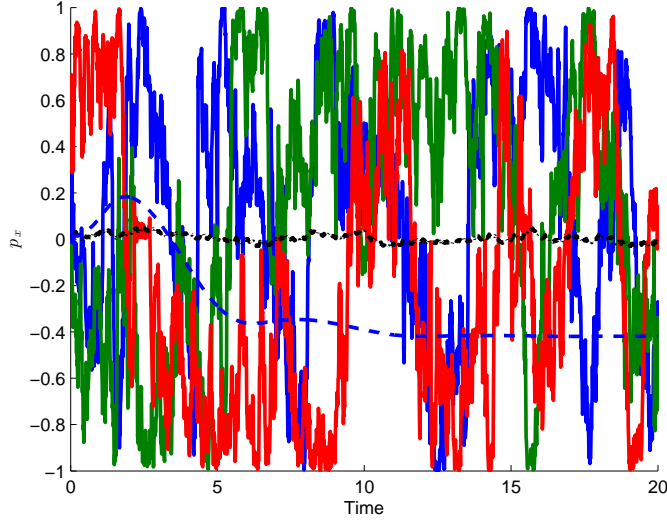


Figure 3.45: **Horizontal component of orientation p_x in shear flow for helical swimmers.** As of Figure 3.30. We fix $\Theta = 1$, $\gamma = \frac{7\pi}{16}$, $D_r = 1$ and $\Psi = 0.5$.

To test the stochastic differential equation for a rotational diffusion between $D_r = 0.01$ and $D_r = 1$ we show two examples with $D_r = 0.1$ and $D_r = 0.5$ for non-helical swimmers. For instance when $D_r = 0.1$, the ensemble average $\langle \theta \rangle$ attains equilibrium that is not the same as the equilibrium of the mean computed using the deterministic model, see Figure 3.49. The effect of increasing randomness becomes noticeable in the ensemble average of ϕ where $\langle \phi \rangle$ decreases rapidly to fluctuate around zero. The orientation distribution is shown in Figure 3.50 where we note that ϕ forms three peaks: two at the boundaries of the interval and one in the middle as there are some cells swim with negative horizontal component, p_x . The ensemble average of the horizontal component of the cell orientation, however, decreases to attain zero over the time considered as shown in Figure 3.51. When the rotational diffusion $D_r = 0.5$, the mean of θ attains the equilibrium $\theta^e = 0.5$ but the ensemble average $\langle \theta \rangle$ attains equilibrium that is double that obtained using the deterministic model, Figure 3.52. Furthermore $\langle \theta \rangle$ is not close to the ensemble average for purely Brownian motion (see Figure 3.1). Moreover, the orientation distribution is indistinguishable from the Fisher distribution as shown in Figure 3.53. The ensemble average for p_x however attains an equilibrium of zero, Figure 3.54.

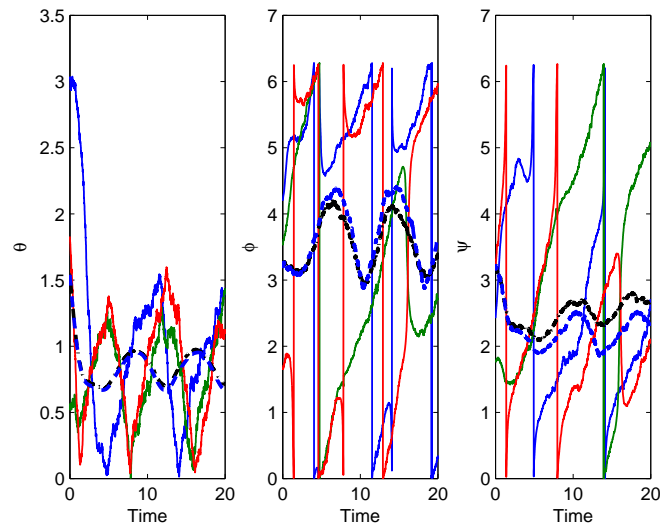


Figure 3.46: **Example realizations to the stochastic differential equation for helical swimmers in shear flow.** As of Figure 3.28. We fix $\Theta = 1$, $\gamma = \frac{\pi}{4}$ $D_r = 0.01$ and $\Psi = 0.5$.

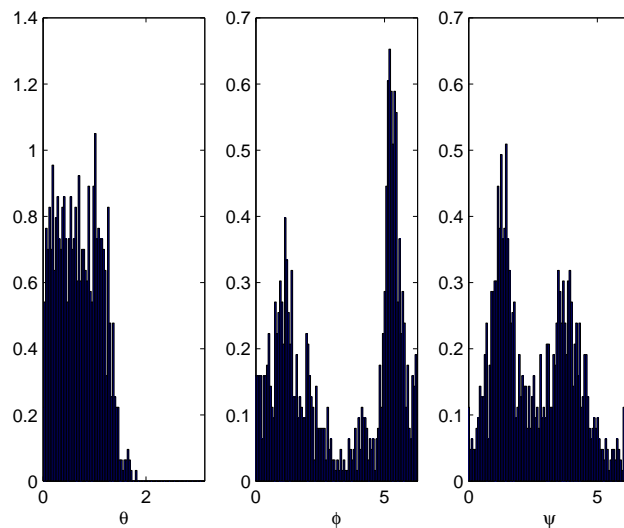


Figure 3.47: **Orientation distribution of helical swimmers in shear flow.** As of Figure 3.29. We fix $\Theta = 1$, $\gamma = \frac{\pi}{4}$ $D_r = 0.01$ and $\Psi = 0.5$.

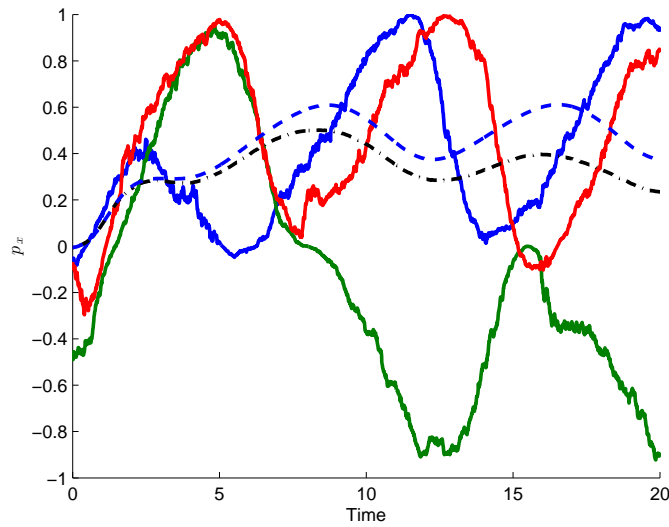


Figure 3.48: **Horizontal component of orientation p_x in shear flow for helical swimmers.** As of Figure 3.30. We fix $\Theta = 1$, $\gamma = \frac{\pi}{4}$, $D_r = 0.01$ and $\Psi = 0.5$.

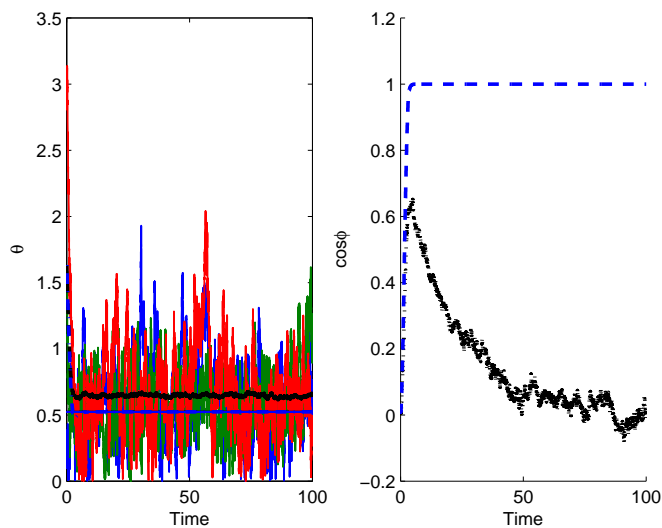


Figure 3.49: **Example realizations of the stochastic differential equation for non-helical swimmers in uniform shear flow.** As Figure 3.10 with $\Psi = 0.5$ and $D_r = 0.1$. We do not plot realization for $\cos \phi$ to aid visualization.

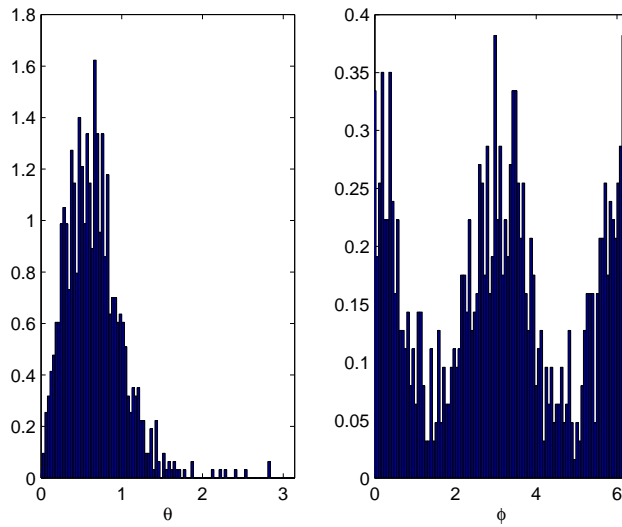


Figure 3.50: **Orientation distribution of non-helical swimmers in uniform shear flow.** As Figure 3.11. The red curve in the left panel is Fisher distribution (3.37) and the red line in the left panel is the uniform distribution. We fix $\Psi = 0.5$ and $D_r = 0.1$.

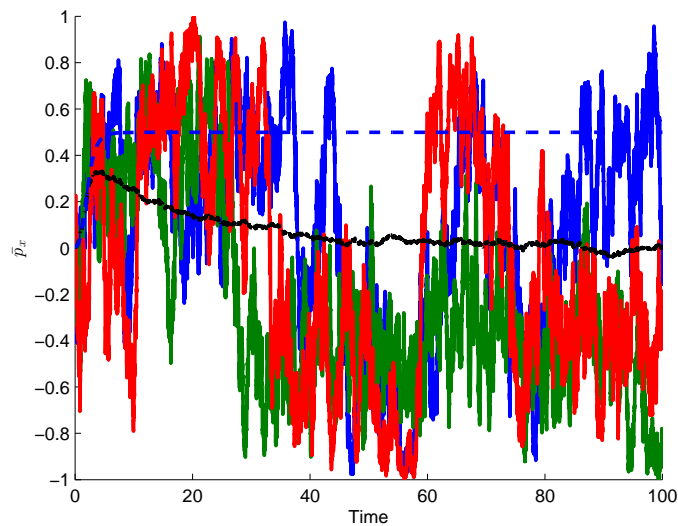


Figure 3.51: **Horizontal component of orientation p_x .** As Figure 3.12 with $\Psi = 0.5$ and $D_r = 0.1$.

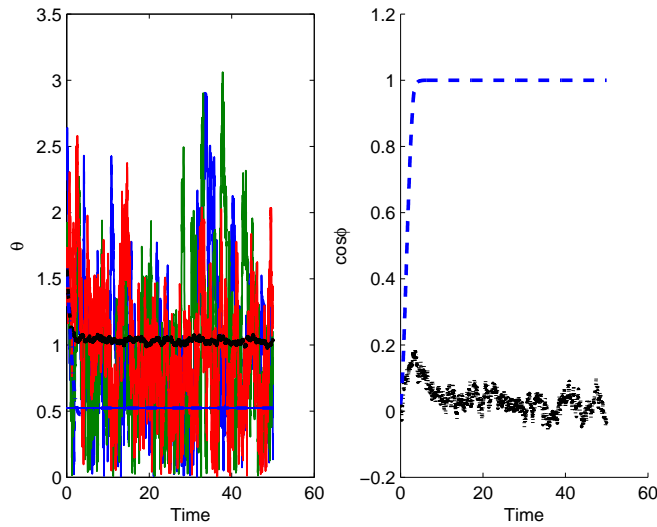


Figure 3.52: **Example realizations of the stochastic differential equation for non-helical swimmers in uniform shear flow.** As Figure 3.10 with $\Psi = 0.5$ and $D_r = 0.5$.

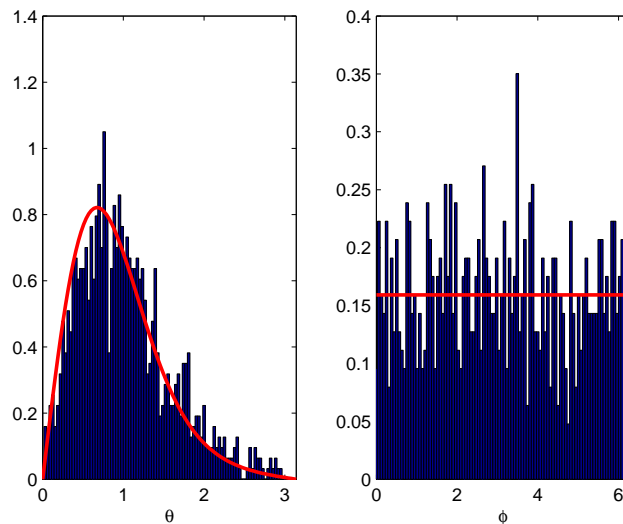


Figure 3.53: **Orientation distribution of non-helical swimmers in uniform shear flow.** As Figure 3.11. The red curve in the left panel is Fisher distribution (3.37) and the red line in the left panel is the uniform distribution. We fix $\Psi = 0.5$ and $D_r = 0.5$.

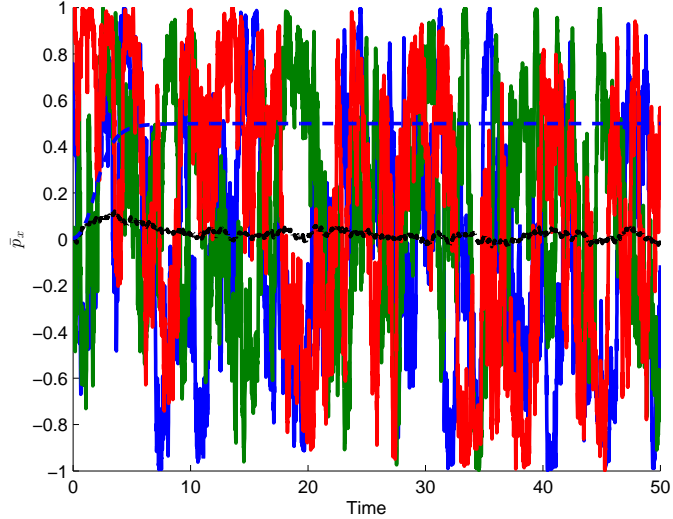


Figure 3.54: **Horizontal component of orientation p_x .** As Figure 3.12 with $\Psi = 0.5$ and $D_r = 0.5$.

3.6 Conclusion

In this chapter, we developed the Fokker–Planck equation for helical swimmers and discussed the randomness effect on the orientation of swimmers. We also derived the stochastic differential equations for both non-helical and helical swimmers.

When the rotational diffusion is small, in still fluid we note the effect of the spurious drift term on the average ensemble for orientation angle θ for the non-helical swimmers. This term leads to divergence between $\langle \theta \rangle$ and the mean of θ computed using the deterministic model. In uniform shear flow, however, $\langle \theta \rangle$ is indistinguishable from the mean predicted from the deterministic model.

The helical model should reduce to the non-helical model for either $\Theta = 0, \gamma = 0$ or $\Theta = \gamma = 0$. When $\Theta = 0$ and γ varies, the model can be used to describe the orientation of a cell where its swimming direction makes angle γ with the eye spot, for instance. On the other hand when $\gamma = 0$ and Θ varies the model can be used to describe the orientation of a cell where the propulsive torque and force are parallel.

For the helical swimmers, when the rotational diffusion is small, $D_r = 0.01$,

the ensemble averages of orientation angles are indistinguishable from the mean obtained from the deterministic model.

For both non-helical swimmers and helical swimmers, when the rotational diffusion is quite large the ensemble averages and the orientation distribution in shear flow is similar to the orientation distribution in still fluid.

Pedley and Kessler [83] gave an estimate for rotational diffusion $d_r = 0.067\text{s}^{-1}$ which if we non-dimensionalize on $2B$ give estimate $D_r = 0.45$ where $B = 3.4\text{s}$. Recently, Croze et al [31] reported an experimental value $d_r = 0.23\text{s}^{-1}$ and $B = 10.5\text{s}$. So, we hypothesise that a moderate rotational diffusion $D_r < 1$ is biologically realistic.

The next chapter is devoted to studying the spatial-temporal distribution. We will study the impact of randomness with chosen $D_r < 1$.

Chapter 4

Spatial distribution of stochastic gyrotactic helical swimmers

4.1 Introduction

In this chapter, we consider the Fokker–Planck equation for the spatial-orientation distribution which is an extension of the Fokker–Planck equation discussed in the previous chapter. The probability density function, $P(\mathbf{p}, \mathbf{x}, t)$, of finding a cell with orientation \mathbf{p} at position $\mathbf{x} = (x, y, z)$ at time t satisfies

$$\frac{\partial P}{\partial t} + \nabla_{\mathbf{x}} \cdot \mathbf{J} + \nabla_{\mathbf{p}} \cdot \mathbf{j} = 0, \quad (4.1)$$

as described in Hill and Bees [56] and Manela and Frankel [75]. The probability current densities are given by

$$\mathbf{j} = \dot{\mathbf{p}}P - D_r \nabla_{\mathbf{p}} P, \quad \text{orientation space flux density,} \quad (4.2)$$

$$\mathbf{J} = \dot{\mathbf{x}}P - D_t \nabla_{\mathbf{x}} P, \quad \text{physical space flux density,} \quad (4.3)$$

where $\dot{\mathbf{x}}$ is the deterministic change in cell position \mathbf{x} due to advection by the local fluid \mathbf{V} , the cell swimming velocity $\nu \mathbf{p}$ is given by Equation (1.47), and $\dot{\mathbf{p}}$ is the deterministic change in cell orientation \mathbf{p} as given by Equation (1.48). The

translational diffusion and rotational diffusion are D_t and D_r , respectively.

The probability density function, $P(\mathbf{p}, \mathbf{x}, t)$ is also assumed to satisfy

$$\int_{R_\infty} \int_{S_2} P d^2\mathbf{p} d^3\mathbf{x} = 1 \quad \text{for all } t > 0 \quad (4.4)$$

where R_∞ is the whole Euclidean space and S_2 is the unit sphere [56]. We impose the initial condition

$$P(\mathbf{p}, \mathbf{x}, 0) = \delta(\mathbf{x} - \mathbf{x}')\delta(\mathbf{p} - \mathbf{p}'), \quad (4.5)$$

where $\delta(\cdot)$ is the delta function. Therefore the initial position and initial orientation are specified as \mathbf{x}' and \mathbf{p}' . However, for long time the stochastic time series are independent of the initial orientation conditions.

We define the cell concentration $n(\mathbf{x}, t) = \int_\Omega P d\mathbf{p}$ where Ω is the space of all possible orientations \mathbf{p} [9]. By considering moments of the distribution function P , for homogeneous shear flow on long time compared to $\frac{1}{D_r}$, the cell density satisfies the following advection–diffusion equation

$$\frac{\partial n}{\partial t} + \nabla_{\mathbf{x}} \cdot \left[\nu \mathbf{q} n - \left(D_t \mathbf{I} + \frac{\nu^2}{D_r} \mathbf{D} \right) \cdot \nabla_{\mathbf{x}} n \right] = 0, \quad (4.6)$$

where \mathbf{q} , \mathbf{D} , and \mathbf{I} are the average swimming direction, diffusion tensor, and identity tensor respectively. The mean swimming direction \mathbf{q} and the non-dimensional diffusion tensor are given respectively by [7, 10]

$$\mathbf{q} = \int_{\mathbf{p}} \mathbf{p} f d\mathbf{p}, \quad (4.7)$$

$$\mathbf{D} = \int_{\mathbf{p}} \left[\mathbf{b}\mathbf{p} + \frac{\Psi}{f(\mathbf{p})} \mathbf{b}\mathbf{b} \cdot \hat{\mathbf{G}} \right]^{sym} d\mathbf{p}, \quad (4.8)$$

where Ψ is the shear strength and \mathbf{b} satisfies Equation (1.38). The equilibrium

orientation $f(\mathbf{p})$ and vector $\mathbf{b}(\mathbf{p})$ satisfy [7, 10]

$$\mathcal{L}f = 0, \quad (4.9)$$

$$\mathcal{L}\mathbf{b} - \Psi\mathbf{b} \cdot \hat{\mathbf{G}} = f(\mathbf{p})(\mathbf{p} - \mathbf{q}), \quad (4.10)$$

subject to

$$\int_{\mathbf{p}} f d\mathbf{p} = 1, \quad \int_{\mathbf{p}} \mathbf{b} d\mathbf{p} = 0, \quad (4.11)$$

where $\hat{\mathbf{G}} = (\nabla\mathbf{V})^T$ is the transpose of the non-dimensional fluid velocity gradient and the linear operator \mathcal{L} is defined in orientation space for gravitactic spherical cells as

$$\mathcal{L}f = \nabla_{\mathbf{p}} \cdot [(\mathbf{k} - (\mathbf{k} \cdot \mathbf{p})\mathbf{p} - \Psi\mathbf{j} \wedge \mathbf{p})f - \nabla_{\mathbf{p}}f]. \quad (4.12)$$

Equation (4.6) will be used to obtain the mean square displacement of unbiased diffusion motion in still fluid and compared numerically with the results obtained from the stochastic differential equation. It will also be used to quantify the relationship of the variance in the horizontal position of non-helical swimmers across the channel and effect of changing the shear strength and rotational diffusion strength.

We first consider the case where there is no gravitactic or propulsive torques acting on the spherical swimmers in still fluid. Then we consider the case of spherical swimmers in uniform shear flow and discuss the deterministic model [6] compared with the stochastic model to see how the rotational diffusion modifies the swimming trajectories for different shear strength and different rotational diffusion values. For the helical swimmers, we consider the stochastic differential equation associated with Equation (4.1) where the cell orientation is given in terms of Euler angles by Equation (3.62). We will examine the effect of propulsive torque strength for different rotational diffusion. Lastly, we consider the case where the shear is a function of the cell's position. This section is an extension of the deterministic model presented in Chapter 2. Moreover, we will discuss

the effect of shear strength on the accumulation of the non-helical swimmers across the channel and the effect of the propulsive torque strength and shear strength on the accumulation of helical swimmers for different value of rotational diffusion. We then examine the stochastic model for the recent experiment for the non-helical swimmer alga *Dunaliella salina* where the Fokker–Planck model and generalized Taylor dispersion theory were examined in a pipe [31]. However, due to time constraint we consider their data for a channel and examine the stochastic differential equations associated with the Fokker–Planck equation for an individual-based model.

4.2 Unbiased diffusion motion in still fluid

We consider an unbiased swimmer whose probability density function P of finding the swimmer at position \mathbf{x} with orientation \mathbf{p} at time t satisfies

$$\frac{\partial P}{\partial t} + \nabla_{\mathbf{x}} \cdot (\nu \mathbf{p} P - D_t \nabla_{\mathbf{x}} P) - D_r \nabla_{\mathbf{p}}^2 P = 0, \quad (4.13)$$

subject to constraint given by (4.4) and initial condition (4.5) where $\nu \mathbf{p}$ is the swimming velocity and D_t and D_r are translational and rotational diffusion constants respectively. This equation is a special case of Equation (4.1) where the particles swim in still fluid and there is no acting torques that affect the swimming paths. Remark also that the linear operator defined in Equation (4.12) is reduced here to $\mathcal{L}P = -\nabla_{\mathbf{p}}^2 P$.

The cell concentration $n(\mathbf{x}, t)$ satisfies Equation (4.6). Hill and Bees [56] called \mathbf{q} and \mathbf{D} the drift velocity and effective diffusion respectively which are given from Equations (4.7-4.8) as

$$\mathbf{q} = \int_{\mathbf{p}} \mathbf{p} f d\mathbf{p}, \quad (4.14)$$

$$\mathbf{D} = \int_{\mathbf{p}} [\mathbf{b}\mathbf{p}]^{sym} d\mathbf{p}. \quad (4.15)$$

The following are the governing equations for the equilibrium orientation $f(\mathbf{p})$

and vector $\mathbf{b}(\mathbf{p})$

$$-\nabla_{\mathbf{p}}^2 f = 0, \quad (4.16)$$

$$-\nabla_{\mathbf{p}}^2 \mathbf{b} = f(\mathbf{p})(\mathbf{p} - \mathbf{q}), \quad (4.17)$$

subject to the normalization conditions

$$\int_{\mathbf{p}} f(\mathbf{p}) d\mathbf{p} = 1 \quad \text{and} \quad \int_{\mathbf{p}} \mathbf{b} d\mathbf{p} = 0. \quad (4.18)$$

Equations (4.16) and (4.17) are special cases of Equations (4.9) and (4.10) respectively with $\Psi = 0$. The solution to Equation (4.16) subject to the normalization condition (4.18a) is [7]

$$f(\mathbf{p}) = \frac{1}{4\pi}. \quad (4.19)$$

Setting

$$\mathbf{p} = (\sin \theta \cos \phi, \sin \theta \sin \phi, \cos \theta),$$

we can compute

$$\mathbf{q} = \frac{1}{4\pi} \int_0^{2\pi} \int_0^\pi \begin{bmatrix} \sin \theta \cos \phi \\ \sin \theta \sin \phi \\ \cos \theta \end{bmatrix} \sin \theta d\theta d\phi = \mathbf{0}, \quad (4.20)$$

as expected for unbiased cells that swim randomly in still fluid. We next solve Equation (4.17)

$$-\nabla_{\mathbf{p}}^2 \mathbf{b} = \frac{1}{4\pi} \mathbf{p}, \quad (4.21)$$

which has solution [7]

$$\mathbf{b} = \frac{1}{8\pi} \mathbf{p}. \quad (4.22)$$

To evaluate the effective diffusion given by (4.15), we need to compute

$$\begin{aligned}
 \mathbf{b}\mathbf{p} &= \frac{1}{8\pi} \begin{bmatrix} \sin \theta \cos \phi \\ \sin \theta \sin \phi \\ \cos \theta \end{bmatrix} \begin{bmatrix} \sin \theta \cos \phi \\ \sin \theta \sin \phi \\ \cos \theta \end{bmatrix}^T \\
 &= \frac{1}{8\pi} \begin{bmatrix} \sin^2 \theta \cos^2 \phi & \sin^2 \theta \cos \phi \sin \phi & \sin \theta \cos \phi \cos \theta \\ \sin^2 \theta \sin \phi \cos \phi & \sin^2 \theta \sin^2 \phi & \sin \theta \sin \phi \cos \theta \\ \cos \theta \sin \theta \cos \phi & \cos \theta \sin \theta \sin \phi & \cos^2 \theta \end{bmatrix}. \quad (4.23)
 \end{aligned}$$

Therefore,

$$\mathbf{D} = \frac{1}{8\pi} \begin{bmatrix} \frac{4\pi}{3} & 0 & 0 \\ 0 & \frac{4\pi}{3} & 0 \\ 0 & 0 & \frac{4\pi}{3} \end{bmatrix} = \frac{1}{6} \mathbf{I}. \quad (4.24)$$

On substituting for \mathbf{q} and \mathbf{D} in Equation (4.6), the cell concentration satisfies

$$\frac{\partial n}{\partial t} = \left(D_t + \frac{\nu^2}{6D_r} \right) \nabla_{\mathbf{x}}^2 n. \quad (4.25)$$

4.2.1 Stochastic differential equation

We expand the Fokker–Planck equation (4.13) to components in Cartesian coordinates for cell position and to components in spherical coordinates for cell orientation and noting that in still fluid the cell position is only advected by the cell swimming velocity $\nu\mathbf{p}$, we have

$$\begin{aligned}
 \frac{\partial P}{\partial t} &= - \left[\frac{\partial}{\partial x} \nu \sin \theta \cos \phi + \frac{\partial}{\partial y} \nu \sin \theta \sin \phi + \frac{\partial}{\partial z} \nu \cos \theta + \frac{\partial}{\partial \theta} D_r \cot \theta \right] P \\
 &+ \frac{1}{2} \left[\frac{\partial^2}{\partial x^2} 2D_t + \frac{\partial^2}{\partial y^2} 2D_t + \frac{\partial^2}{\partial z^2} 2D_t + \frac{\partial^2}{\partial \theta^2} 2D_r + \frac{\partial^2}{\partial \phi^2} \frac{2D_r}{\sin^2 \theta} \right] P, \quad (4.26)
 \end{aligned}$$

which can be associated with the following stochastic differential equation

$$\begin{bmatrix} dx \\ dy \\ dz \\ d\theta \\ d\phi \end{bmatrix} = \mathbf{A}dt + \sqrt{\mathbf{B}}d\mathbf{W}(t), \quad (4.27)$$

where the drift and diffusion terms are

$$\mathbf{A} = \begin{bmatrix} \nu \sin \theta \cos \phi \\ \nu \sin \theta \sin \phi \\ \nu \cos \theta \\ D_r \cot \theta \\ 0 \end{bmatrix}, \quad \sqrt{\mathbf{B}} = \begin{bmatrix} \sqrt{2D_t} & 0 & 0 & 0 & 0 \\ 0 & \sqrt{2D_t} & 0 & 0 & 0 \\ 0 & 0 & \sqrt{2D_t} & 0 & 0 \\ 0 & 0 & 0 & \sqrt{2D_r} & 0 \\ 0 & 0 & 0 & 0 & \frac{\sqrt{2D_r}}{\sin \theta} \end{bmatrix}, \quad (4.28)$$

respectively, and Brownian motion column vector $d\mathbf{W}(t)$. The derivation of this equation is presented in Appendix B. We use Euler–Maruyama approximation method to solve stochastic differential equation (4.27).

In Figure 4.1, we demonstrate trajectories in case of zero translational diffusion, $D_t = 0$. When the swimming speed is fixed, Figure 4.1 (left to right panel), as the rotational diffusion, D_r , is reduced the cells have larger net displacement. When rotational diffusion is fixed and swimming speed is increased (top to bottom panel) the net displacement of cell increases.

4.2.2 Linear relationship

To examine the effect of diffusivity of unbiased swimmers, we compute the mean square displacement. To do this we consider Equation (4.25). That is

$$\frac{\partial n}{\partial t} = D\nabla_{\mathbf{x}}^2 n, \quad (4.29)$$

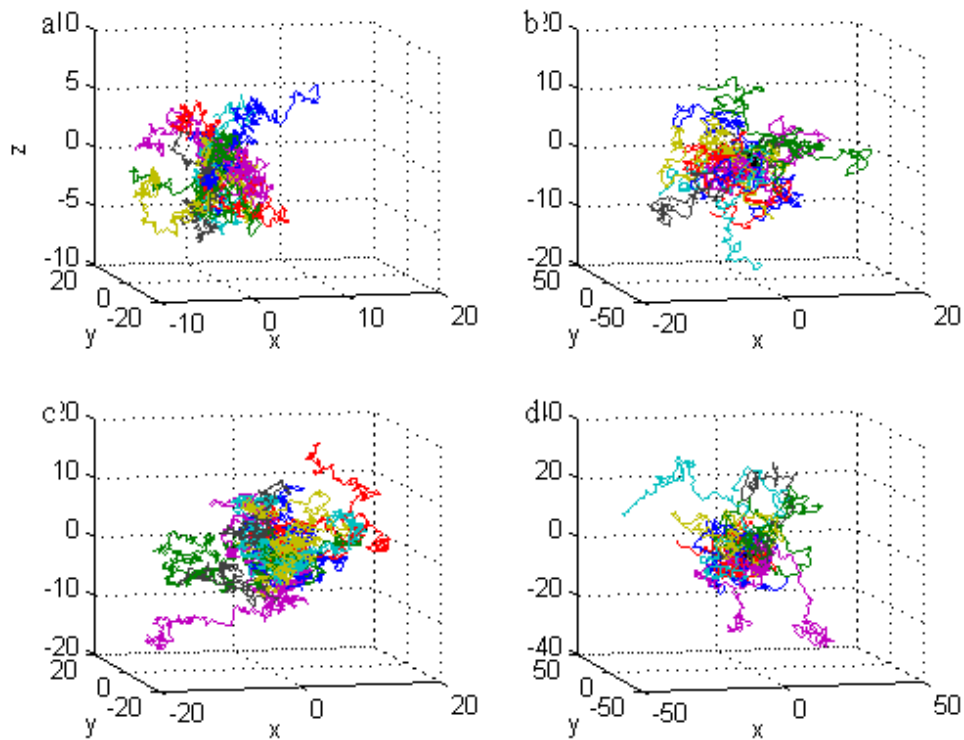


Figure 4.1: **Example trajectories:** We plot 20 trajectories corresponding to second linearity relationship, i.e when $D_t = 0$. We fix time step $dt = 0.1$ on time interval $[0, 100]$. The simulation is run for different values for the pair (D_r, ν) . (a) $(2, 1)$ (b) $(0.5, 1)$ (c) $(2, 2)$ and (d) $(0.5, 2)$. the effective diffusion $D = \frac{\nu^2}{D_r}$ in Equation (4.29) is: (a) $D = 0.5$ (b) $D = 2$ (c) $D = 2$ (d) $D = 8$.

where $D = D_t + \frac{\nu^2}{6D_r}$. The fundamental solution of this equation, with initial condition

$$n(\mathbf{x}, 0) = \delta(\mathbf{x}), \quad (4.30)$$

where we assume the concentration is conserved, i.e

$$\int n(\mathbf{x}, t) d\mathbf{x} = 1, \quad (4.31)$$

is given by

$$n(\mathbf{x}, t) = \frac{1}{2\sqrt{\pi Dt}} \exp\left(-\frac{|\mathbf{x}|^2}{4Dt}\right). \quad (4.32)$$

The mean square of displacement is then given by [14]

$$\langle |\mathbf{x}(t)|^2 \rangle = \int |\mathbf{x}|^2 n(\mathbf{x}, t) d\mathbf{x} = 6Dt. \quad (4.33)$$

When the translational diffusion is not zero, $D_t \neq 0$, and the cell is not swimming $\nu = 0$, the mean square displacement therefore becomes

$$\langle |\mathbf{x}(t)|^2 \rangle = 6D_t t. \quad (4.34)$$

Furthermore, when the cell is swimming and $D_t = 0$ then

$$\langle |\mathbf{x}(t)|^2 \rangle = \frac{\nu^2}{D_r} t. \quad (4.35)$$

These linear relationships can be summarized as follows

$$\langle |\mathbf{x}(t)|^2 \rangle \sim 6D_t t, \quad \text{if } \nu = 0, D_t \neq 0, \quad (4.36)$$

$$\langle |\mathbf{x}(t)|^2 \rangle \sim \frac{\nu^2}{D_r} t, \quad \text{if } \nu \neq 0, D_t = 0. \quad (4.37)$$

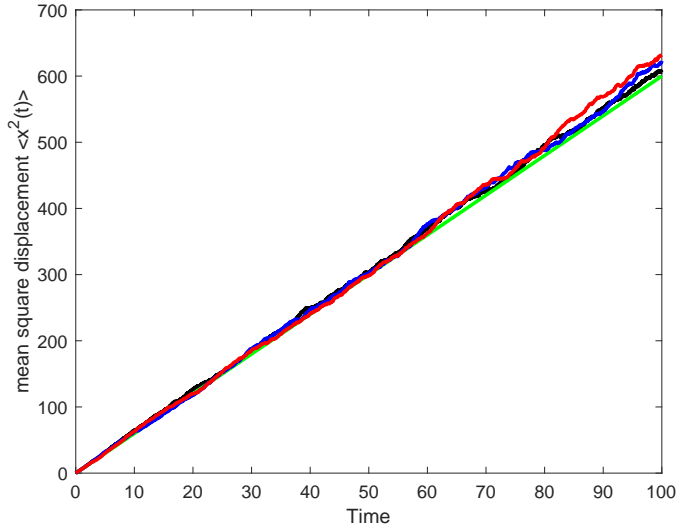


Figure 4.2: **Mean square displacement.** The mean square of the displacement of the solution of SDE (4.27) with time step $dt = 0.01$ (black), $dt = 0.05$ (blue), and $dt = 0.1$ (red). The green line is the function $g(t) = 6D_t t$. We fix $\nu = 0$, $D_t = 1$.

To test these relationships, We ran 100 simulations of stochastic differential equation (4.27) for different time step and time interval of simulation then we computed the mean square of the displacement $\langle |\mathbf{x}(t)|^2 \rangle$.

In Figures 4.2–4.3 and 4.6–4.7, we demonstrate these linearity relationships. The mean square displacement is computed for different time step dt . As the time step is decreased the best fit we have. This is understandable since `simByEuler` gives a discrete-time approximation to the underlying continuous-time process and as $dt \rightarrow 0$, the method approximates well the continuous time process [1]. The mean displacement, $\langle \mathbf{x}(t) \rangle$ should be zero as $t \rightarrow \infty$. In Figures 4.8–4.9 we demonstrate the mean displacement for different time step dt for 500 realizations of the solution of Equation (4.27) averaged over time t . Because of small number of realizations the mean displacement diverges from zero with small error. Despite that the Gaussian distribution given by (4.32) fits the histograms well as shown in Figures 4.4–4.5 and 4.10–4.11.

To compare the impact of translational and rotational diffusion parameters for active swimmers such as *Chlamydomonas nivalis* which has diameter $10\mu m$ and swimming speed $\nu = 50\mu m s^{-1}$ [83], we consider dynamic viscosity of fluid $\mu =$

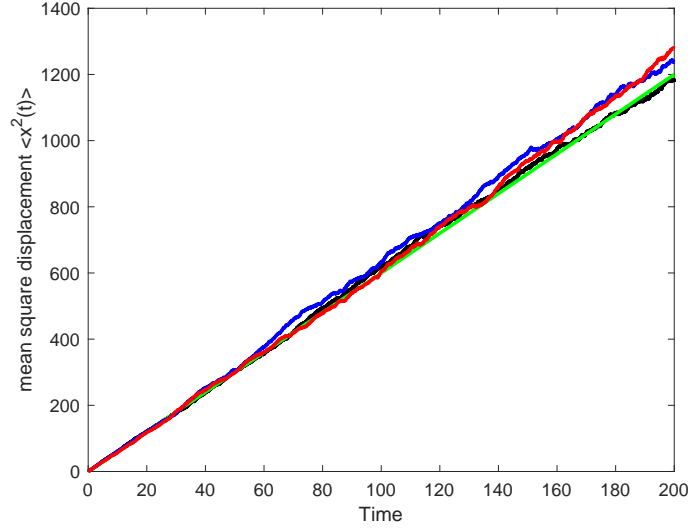


Figure 4.3: **Mean square displacement.** The mean square of the displacement of the solution of SDE (4.27) with time step $dt = 0.01$ (black), $dt = 0.05$ (blue), and $dt = 0.1$ (red). The green line is the function $g(t) = 6D_t t$. We fix $\nu = 0$, $D_t = 1$.

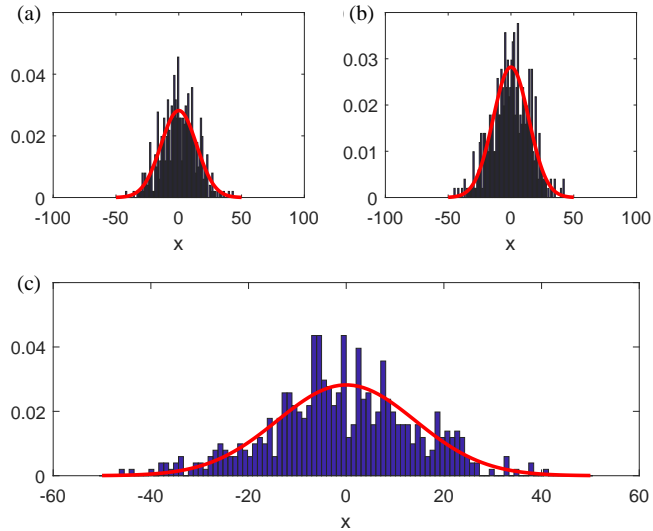


Figure 4.4: **Histogram of horizontal component of position.** We run 500 realizations of Equation (4.27) over $t = 100$ with time step (a) $dt = 0.01$, (b) $dt = 0.05$, and (c) $dt = 0.1$. The red curve is the Gaussian distribution given by Equation (4.32). We fix $\nu = 0$, $D_t = 1$.

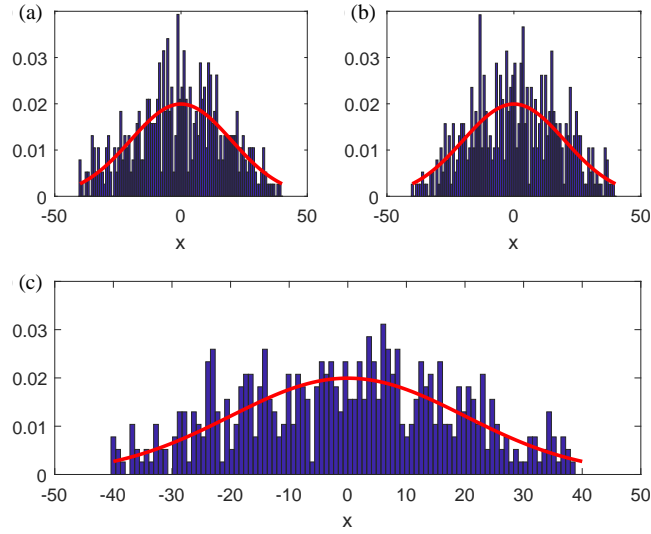


Figure 4.5: **Histogram of horizontal component of position.** We run 500 realizations of Equation (4.27) over $t = 200$ with time step (a) $dt = 0.01$, (b) $dt = 0.05$, and (c) $dt = 0.1$. The red curve is the Gaussian distribution given by Equation (4.32). We fix $\nu = 0, D_t = 1$.

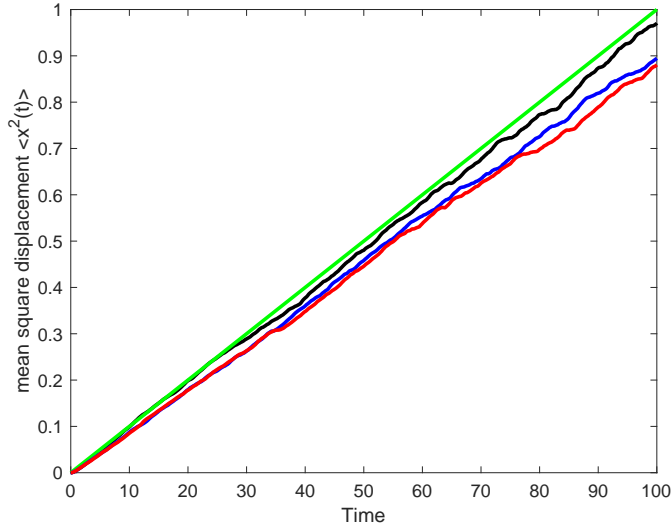


Figure 4.6: **Mean square displacement.** The mean square of the displacement of the solution of SDE (4.27) with time step $dt = 0.01$ (black), $dt = 0.05$ (blue), and $dt = 0.1$ (red). The green line is the function $g(t) = \frac{\nu^2}{D_r} t$. We fix $\nu = 0.1, D_t = 0$.

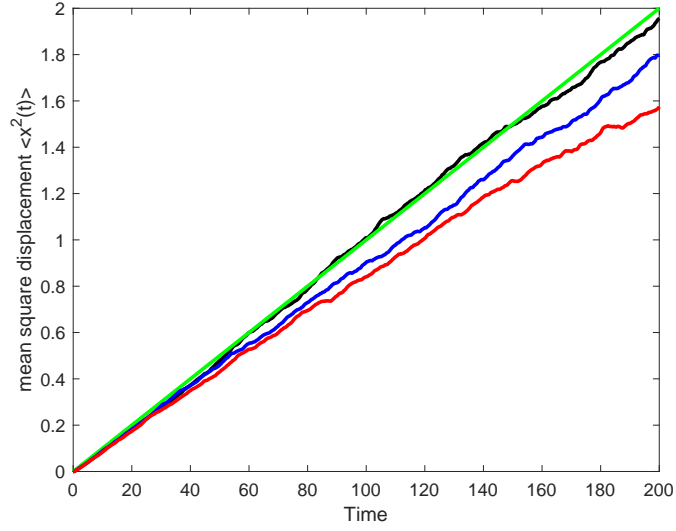


Figure 4.7: **Mean square displacement.** The mean square of the displacement of the solution of SDE (4.27) with time step $dt = 0.01$ (black), $dt = 0.05$ (blue), and $dt = 0.1$ (red). The green line is the function $g(t) = \frac{\nu^2}{D_r} t$. We fix $\nu = 0.1, D_t = 0$.

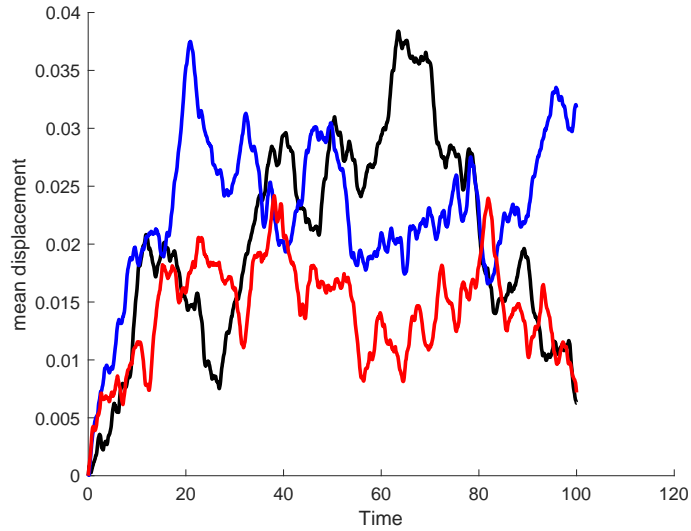


Figure 4.8: **Mean displacement.** We compute the mean displacement for 500 simulations for different time step over time duration $T = 100$. The black is the mean displacement with $dt = 0.01$, blue with $dt = 0.05$ and red with $dt = 0.1$. We fix $\nu = 0.1, D_t = 0$.

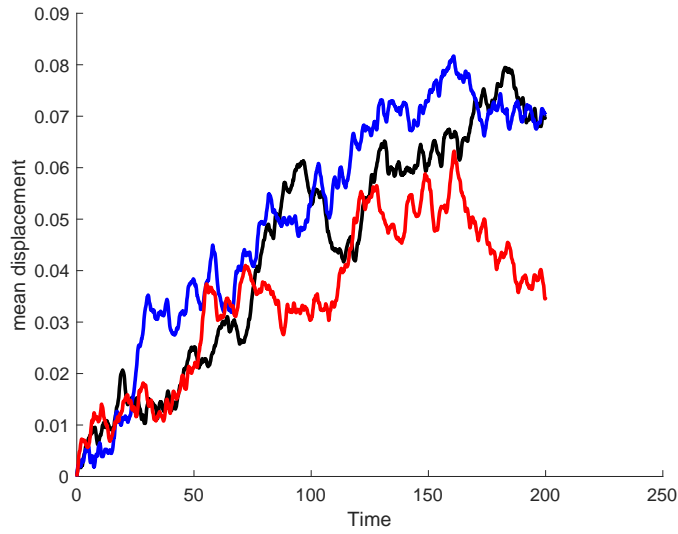


Figure 4.9: **Mean displacement.** We compute the mean displacement for 500 simulations for different time step over time duration $T = 200$. The black is the mean displacement with $dt = 0.01$, blue with $dt = 0.05$ and red with $dt = 0.1$. We fix $\nu = 0.1, D_t = 0$.

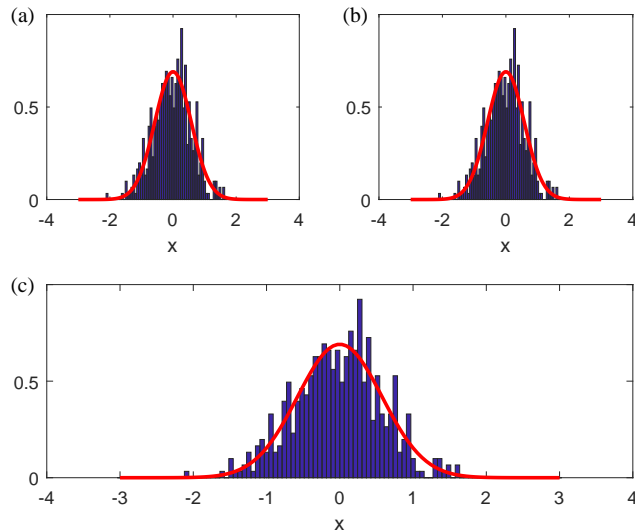


Figure 4.10: **Histogram of horizontal component of position.** We run 500 realizations of Equation (4.27) over $t = 100$ with time step (a) $dt = 0.01$, (b) $dt = 0.05$, and (c) $dt = 0.1$. The red curve is the Gaussian distribution given by Equation (4.32). We fix $\nu = 0.1, D_t = 0$.

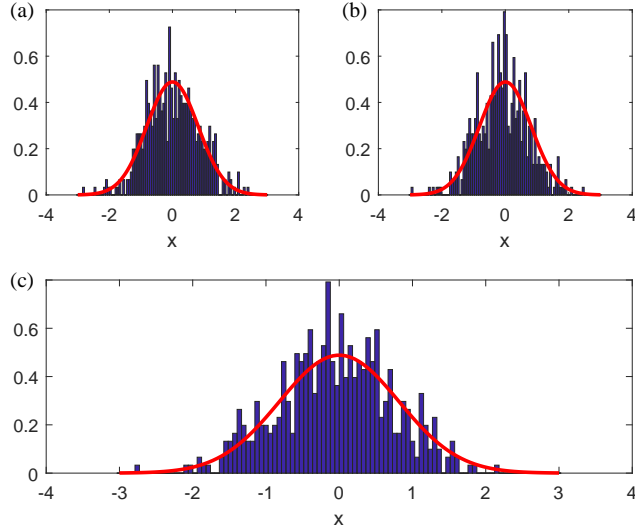


Figure 4.11: **Histogram of horizontal component of position.** We run 500 realizations of Equation (4.27) over $t = 200$ with time step (a) $dt = 0.01$, (b) $dt = 0.05$, and (c) $dt = 0.1$. The red curve is the Gaussian distribution given by Equation (4.32). We fix $\nu = 0.1$, $D_t = 0$.

$9 \times 10^{-3} \text{ g cm}^{-1} \text{ s}^{-1}$ [85] at room temperature $T = 298.15 \text{ K}$. The estimation of the effective rotational diffusion which captures intrinsic randomness in swimming behaviour is $D_r = 0.067 \text{ s}^{-1}$ [83]. In contrast an estimate for Brownian rotational diffusion is $1.3 \times 10^{-3} \text{ s}^{-1}$ [83]. Thus cells swim with effective spatial diffusion parameter $\frac{\nu^2}{6D_r} = 6.21 \times 10^3 \mu\text{m}^2 \text{ s}^{-1}$. On the other hand, the translational diffusion is estimated using Equation (1.11). It is given by $D_t = 4.85 \times 10^{-11} \mu\text{m}^2 \text{ s}^{-1}$. From this comparison, we see that translational diffusion is too small compared to cell's diameter and hence has no significant impact on cells swimming [56]. Therefore, we set $D_t = 0$ in the simulation of the remaining sections.

4.3 Uniform shear flow

We discuss the swimming trajectories of swimmers in the case where the shear strength Ψ is constant. This section is an extension of the deterministic model presented in [6]. We consider the Fokker–Planck equation (4.1) where the cell is advected at the fluid flow velocity \mathbf{V} in addition to the swimming velocity $\nu\mathbf{p}$.

In vertical uniform shear downwards flow, the flow velocity is [6]

$$\mathbf{V} = -\Psi x \mathbf{k}, \quad (4.38)$$

where Ψ is the non-dimensional shear strength and \mathbf{k} is unit vector in the vertical direction. The non-dimensional swimming speed is taken as $\nu = 0.1$ in the remaining simulations of this chapter.

4.3.1 Spatial-orientation model for non-helical gravitactic swimmers

We can follow the derivation of the stochastic differential equation of the previous section to derive the stochastic differential equation (4.27) for non-helical gravitactic swimmers with the drift term given by

$$\mathbf{A} = \begin{pmatrix} \nu \sin \theta \cos \phi \\ \nu \sin \theta \sin \phi \\ -\Psi x + \nu \cos \theta \\ -\sin \theta + \Psi \cos \phi + D_r \cot \theta \\ -\Psi \frac{\cos \theta \sin \phi}{\sin \theta} \end{pmatrix}. \quad (4.39)$$

When the shear strength is zero, cells swim upwards as shown in Figure 4.12a. As D_r is increased from zero, cells continue to swim upwards but in random paths as shown in Figures 4.13a, 4.14a, 4.15a. For small rotational diffusion ($D_r = 0.01$), the behaviour is only slightly altered from that in the deterministic model. As D_r is increased further, the vertical displacement is reduced.

As we increase the shear strength, $\Psi = 0.5$, cells swim towards downwards flow, Figure 4.12 b. As rotational diffusion is increased from zero, cells maintain downwards swimming in random trajectories, Figures 4.13-4.15b. For strong rotational diffusion ($D_r = 0.5$) the vertical displacement is reduced. Increasing shear strength further, $\Psi = 1.5$, cells maintain swimming downwards. Moreover, as D_r is increased, the reduction in the vertical displacement becomes more

obvious.

To understand how the rotational diffusion affects the vertical displacement, in Figure 4.16 we computed the average vertical displacement as a function of shear strength for different rotational diffusion. We simulated 100 cells that start at origin with random initial orientation over 100 time units. Within the feasibility region of the equilibrium of the horizontal component of the orientation, $\Psi \leq 1$, the deterministic model predicts that the cells swim downwards. For weak and intermediate rotational diffusion, $D_r = 0.01$ and $D_r = 0.1$ the cells maintain swimming downwards and the ensemble average of vertical transport is indistinguishable from the vertical mean expected from the deterministic model. For large $D_r = 0.5$ and within $\Psi \leq 1$ the cells maintain swimming downwards, though the ensemble average of the vertical transport diverges from the deterministic vertical mean. In Chapter 3, we see that for sufficiently large D_r , the ensemble average of horizontal component of orientation becomes zero. Therefore, we expect the ensemble average of vertical displacement becomes zero too for sufficiently large D_r .

When the equilibrium of horizontal component of orientation is infeasible, i.e when $\Psi > 1$ the cells maintain swimming downwards. Moreover, for strong shear strength and for sufficiently small D_r and intermediate D_r , the ensemble average is indistinguishable from the vertical mean predicted from the deterministic model. When $D_r = 0.5$, the ensemble average increase further. Therefore for sufficiently large D_r we expect the vertical displacement average becomes zero.

4.3.2 Spatio-orientation model for helical gravitactic swimmers

In this section we extend the deterministic model for helical swimmers given in [6] where we consider the deterministic model in terms of Euler angles (θ, ϕ, ψ) that we derived in Chapter 2 for cell orientation (see Equations (2.63-2.65)). The physical flux is added to the stochastic differential equation that describes the

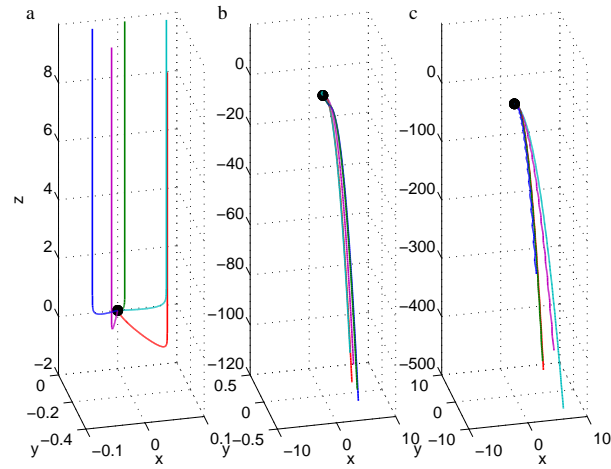


Figure 4.12: **Deterministic trajectories:** Example trajectories of duration 100 non-dimensionalized on $2B$ for different values of flow shear: (a) $\Psi = 0$, (b) $\Psi = 0.5$, and (c) $\Psi = 1.5$.

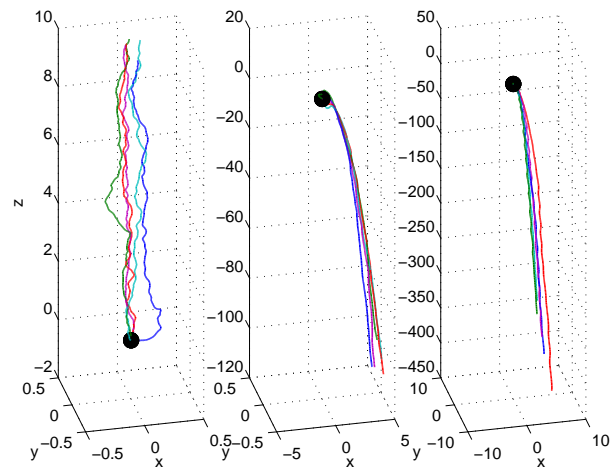


Figure 4.13: **Stochastic trajectories:** Example trajectories of duration 100 non-dimensionalized on $2B$ for different values of flow shear: (a) $\Psi = 0$, (b) $\Psi = 0.5$, and (c) $\Psi = 1.5$. We fix $D_r = 0.01$.

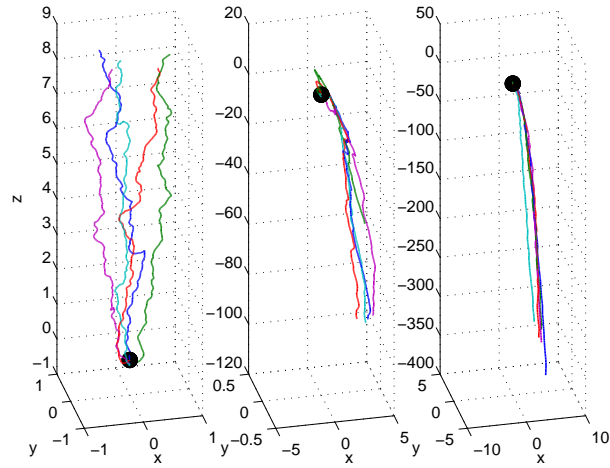


Figure 4.14: **Stochastic trajectories:** As of Figure 4.13 with fixed $D_r = 0.1$.

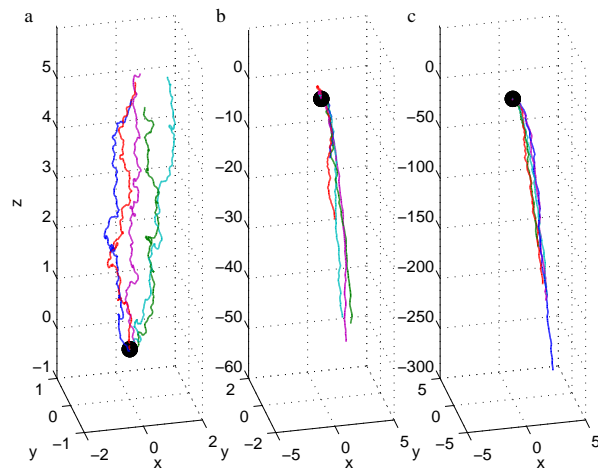


Figure 4.15: **Stochastic trajectories:** As of Figure 4.13 with fixed $D_r = 0.5$.

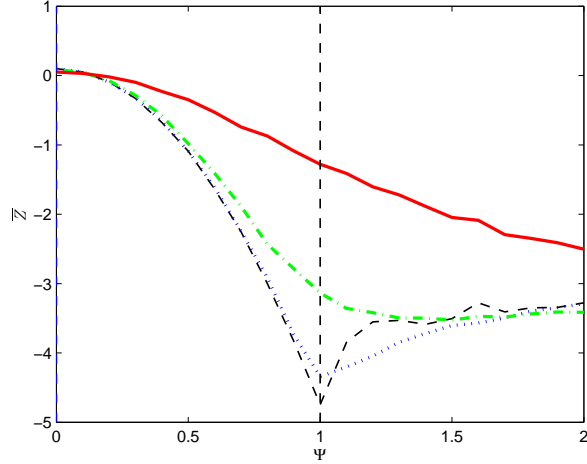


Figure 4.16: **Mean vertical transport for non-helical swimmers:** Average vertical displacement of 100 cells of duration 100 time units as a function of shear, Ψ . The black dashed is the average vertical transport using the deterministic model. Blue, green, red are the average vertical transport for the stochastic model for $D_r = 0.01, 0.1, 0.5$ respectively. The vertical dashed black line is $\Psi = 1$ where when $\Psi \leq 1$ the equilibrium solution for the horizontal component of orientation is feasible and when $\Psi > 1$ the equilibrium is infeasible.

cells orientation (Equation (3.71)) so that we have the following equation that describes the spatial-orientation distribution of a helical swimmer in uniform flow

$$\begin{pmatrix} dx \\ dy \\ dz \\ d\theta \\ d\phi \\ d\psi \end{pmatrix} = \mathbf{A}dt + \mathbf{B}d\mathbf{W}(t), \quad (4.40)$$

where

$$\mathbf{A} = \begin{pmatrix} \nu \sin \theta \cos \phi \\ \nu \sin \theta \sin \phi \\ -\Psi x + \nu \cos \theta \\ -\sin \theta + \Theta \sin \gamma \sin \psi + \Psi \cos \phi + D_r \cot \theta \\ -\Theta \frac{\sin \gamma \cos \psi}{\sin \theta} - \Psi \frac{\sin \phi \cos \theta}{\sin \theta} \\ \Theta(\cot \theta \cos \psi \sin \gamma + \cos \gamma) + \Psi \frac{\sin \phi}{\sin \theta} \end{pmatrix}, \quad (4.41)$$

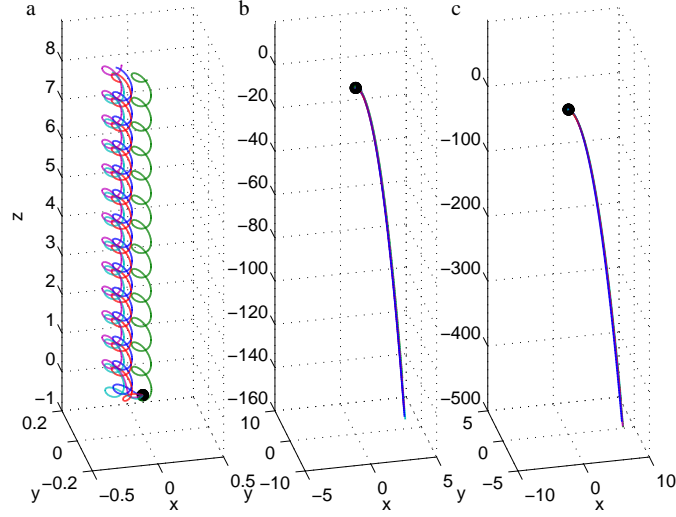


Figure 4.17: **Deterministic trajectories:** Example trajectories of duration 100 non-dimensionalized on $2B$ for different values of flow shear: (a) $\Psi = 0$, (b) $\Psi = 1$, and (c) $\Psi = 1.5$ and for fixed $\Theta = 1$, and $\gamma = \frac{\pi}{4}$.

$$\mathbf{B} = \begin{pmatrix} \sqrt{2D_t} & 0 & 0 & 0 & 0 & 0 \\ 0 & \sqrt{2D_t} & 0 & 0 & 0 & 0 \\ 0 & 0 & \sqrt{2D_t} & 0 & 0 & 0 \\ 0 & 0 & 0 & \sqrt{2D_r} & 0 & 0 \\ 0 & 0 & 0 & 0 & \frac{\sqrt{2D_r(1+\cos\theta)} + \sqrt{2D_r(1-\cos\theta)}}{2\sin\theta} & \frac{\sqrt{2D_r(1-\cos\theta)} - \sqrt{2D_r(1+\cos\theta)}}{2\sin\theta} \\ 0 & 0 & 0 & 0 & \frac{\sqrt{2D_r(1-\cos\theta)} - \sqrt{2D_r(1+\cos\theta)}}{2\sin\theta} & \frac{\sqrt{2D_r(1+\cos\theta)} + \sqrt{2D_r(1-\cos\theta)}}{2\sin\theta} \end{pmatrix} \quad (4.42)$$

In the case of no flow, cells swim upwards in helical path [6] as shown in Figure 4.17 a. For small rotational diffusion, $D_r = 0.01$ the swimming trajectories are only slightly altered from that of the deterministic model as shown in Figure 4.18a. Increasing D_r further ($D_r = 0.1$) cells hardly maintain swimming in helical paths as shown in Figure 4.19a. Furthermore, the vertical displacement is reduced. For large rotational diffusion, $D_r = 0.5$ cells swim randomly upwards and the vertical displacement is decreased further, Figure 4.20a.

To study the effect of randomness on swimming trajectories in shear flow, we will

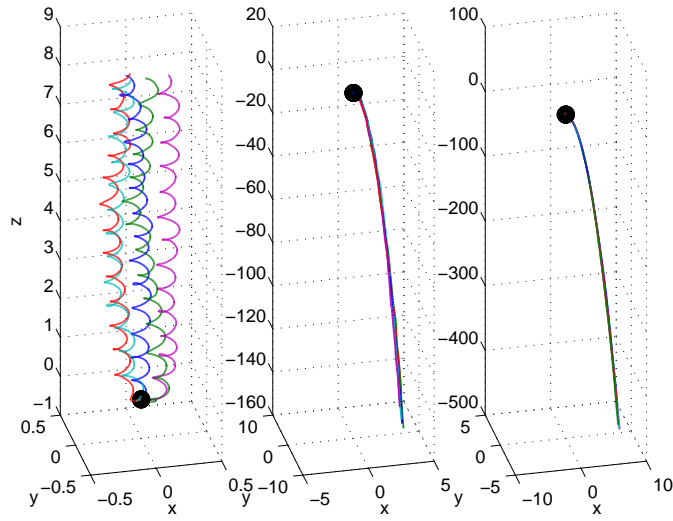


Figure 4.18: **Stochastic trajectories:** Example trajectories of duration 100 non-dimensionalized on $2B$ for different values of flow shear: (a) $\Psi = 0$, (b) $\Psi = 1$, and (c) $\Psi = 1.5$ and for fixed $\Theta = 1$, $\gamma = \frac{\pi}{4}$, and $D_r = 0.01$.

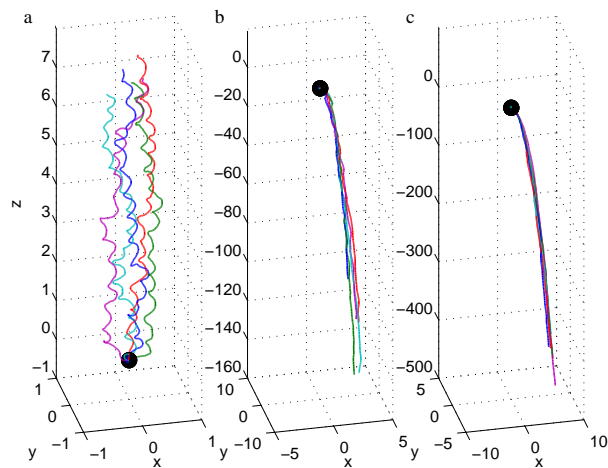


Figure 4.19: **Stochastic trajectories:** As of Figure 4.18 where we fix $D_r = 0.1$.

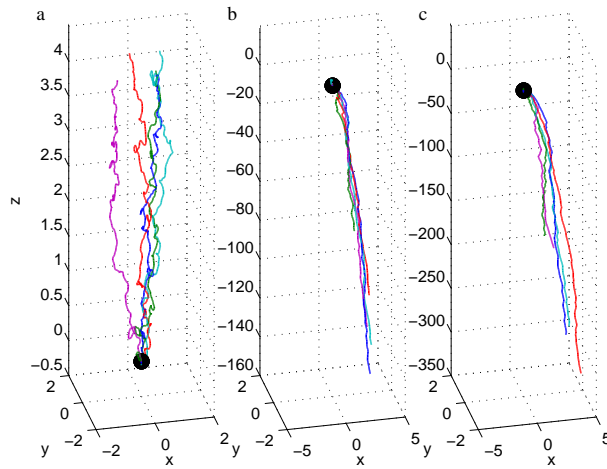


Figure 4.20: **Stochastic trajectories:** As of Figure 4.18 where we fix $D_r = 0.5$.

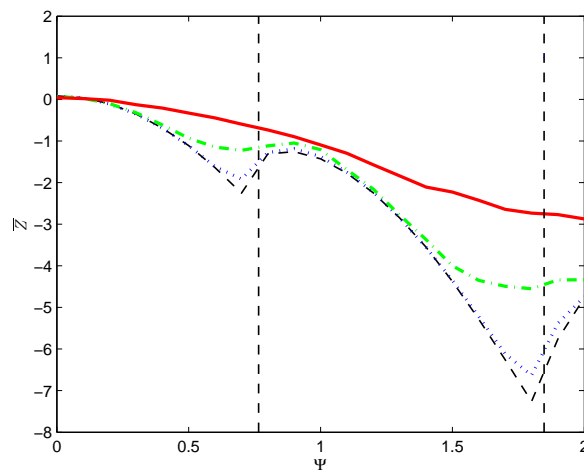


Figure 4.21: **Mean vertical transport:** As of Figure 4.16 but for helical swimmers with parameters $\Theta = 1$, and $\gamma = \frac{\pi}{4}$. The equilibrium of horizontal component of orientation is feasible within the vertical black dashed lines.

consider a selection of parameter sets which will illustrate the possible dynamics. Specifically, we first consider $\Theta = 1$ and $\gamma = \frac{\pi}{4}$ and then $\gamma = \frac{7\pi}{16}$ for different values of Θ .

When $\Theta = 1$, and $\gamma = \frac{\pi}{4}$, the deterministic model predicts that the equilibrium solution of the cells orientation is feasible when $0.76 \leq \Psi \leq 1.85$ (see Figure 2.1). Within this shear range, cells swim towards downwards flow as predicted in the deterministic model [6] and shown in Figure 4.17 b,c, because the average value of horizontal component of orientation is positive as shown in Figure 2.3. When $\Psi = 1$, as D_r is increased the randomness in cells trajectories becomes clear (Figures 4.18b–4.20b) compared with the deterministic model, Figure 4.17b. However, the magnitude of the vertical displacement is the same. When $\Psi = 1.5$, for small rotational diffusion, $D_r = 0.01$, the behaviour is indistinguishable from that of the deterministic model as shown in Figure 4.18c. Increasing D_r further, the randomness in the swimming trajectories is notable, Figure 4.20c and the vertical displacement is reduced.

In Figure 4.21 we computed the average of vertical displacement. The deterministic model (black dashed curve) predicts that the mean vertical transport is negative. Within the equilibrium feasibility of the orientation, the mean vertical displacement decreases as the shear strength increases. For small rotational diffusion, $D_r = 0.01$, within equilibrium feasibility, the average of vertical displacement is indistinguishable from that predicted of the deterministic model (blue dashed curve). As the rotational diffusion increases, $D_r = 0.5$ the mean vertical displacement diverges from that predicted from the deterministic model. For sufficiently large D_r , we saw in the previous chapter that the average ensemble of horizontal component of orientation becomes zero and thus we expect the mean of vertical displacement is zero.

Helical swimmers may exhibit different swimming trajectories pattern (upwards or downwards) in uniform shear vertical flow [6]. To examine such behaviour, we consider $\gamma = \frac{7\pi}{16}$ for different propulsive strength, Θ , and different rotational diffusion, D_r .

When $\Theta = 0.2$ the deterministic model predicts that the equilibrium of horizontal component of the orientation is feasible when $0.8 \leq \Psi \leq 1.19$. Within this range, cells swim downwards as shown in Figure 4.22a. As rotational diffusion is increased, cells maintain swimming downwards as shown in Figure 4.23a–4.25a.

When $\Theta = 1$, the deterministic model predicts that the equilibrium of horizontal component of the orientation is feasible when $0.196 \leq \Psi \leq 1.98$ and $p_x^e = 0$ when $\Psi = 0.19$ or $\Psi = 0.98$. Within this shear range, cells display two distinct swimming behaviours. Within $0.196 \leq \Psi \leq 0.98$, cells swim upwards and within $0.98 \leq \Psi \leq 1.98$ cells swim downwards. We choose $\Psi = 1$ in the simulation of Figures 4.22b–4.25b. In Figure 4.22b, cells will swim downwards if the simulation runs for longer time. This is quantified in Figure 4.27 where the vertical displacement is negative. Note that the zero of $p_x^e = 0$ is close to $\Psi = 1$ where the cells transform swimming from upwards towards downwards. For small rotational diffusion cells maintain swimming downwards, Figure 4.23b. As rotational diffusion is increased, cells swim randomly downwards and the vertical displacement is reduced, Figure 4.24b. Increasing the rotational diffusion further, cells undergoes more complex trajectories, Figure 4.25b. This is because of the non-linearity in the stochastic differential equation as we saw in Chapter 3.

When $\Theta = 1.5$, the deterministic model predicts that the equilibrium of horizontal component of the orientation is feasible when $0.55 \leq \Psi \leq 2.48$ and $p_x^e = 0$ when $\Psi = 1.48$. The shear strength we choose in the simulation, $\Psi = 1$ is within the range $0.55 \leq \Psi \leq 1.48$ where the cells swim upwards Figures 4.22c–4.25c. For small rotational diffusion cells maintain swimming upwards, Figure 4.23c. As rotational diffusion is increased, cells swim upwards, Figure 4.24c. Increasing the rotational diffusion further, cells undergo more complex trajectories but maintain upwards swimming, Figure 4.25c and the vertical displacement is reduced.

For the non-helical swimmers, we saw that when $\Psi \leq 1$, cells swim downwards. However, the helical swimmers may display another phenomena as we have seen in Figures 4.22c–4.25c. To show this more clearly we consider $\Theta = 1$ and $\gamma = \frac{7\pi}{16}$

for shear strength $\Psi = 0.5$ and rotational diffusion as shown in Figure 4.26. The deterministic model predicts that the cells swim upwards (Figure 4.26a). Moreover, as the rotational diffusion is increased the cells maintain swimming upwards and the average of vertical displacement decreases. For strongly enough rotational diffusion, $D_r = 0.5$, cells can not maintain the upwards swimming pattern and start downwards swimming as shown in Figure 4.26d.

To test this behaviour, we simulate 100 realizations over 100 time units and evaluate the average of the vertical displacement as a function of the shear strength as shown in Figure 4.27. Within the feasibility region of the horizontal component, the equilibrium of the horizontal component of orientation is zero when $\Psi = 1.005$. The cells swim upwards when $0.196 \leq \Psi \leq 1.005$ then change to swimming downwards within $1.005 \leq \Psi \leq 1.99$. For $D_r = 0.01$ and $D_r = 0.1$ the ensemble average of vertical transport is similar to the vertical mean expected from the deterministic model. Increasing rotational diffusion, $D_r = 0.5$, the ensemble average fluctuates around zero so that the cells are not able to maintain swimming upwards within $0.196 \leq \Psi \leq 1.005$ and becomes negative within $1.005 \leq \Psi \leq 1.99$. Furthermore it becomes more distinguishable from the vertical mean expected from the deterministic model.

In Figure 4.28, we depict the mean vertical transport as a function of the propulsive torque strength. We fix $\gamma = \frac{7\pi}{16}$, $\Psi = 1$ and simulate 100 cells over 100 time unit. Within the feasibility region of the horizontal component of orientation, the deterministic model predicts that the mean vertical displacement increases as the propulsive torque strength increases. For small rotational diffusion, $D_r = 0.01$, the ensemble average indistinguishable from the mean vertical predicted from the deterministic model. As D_r is increased, the ensemble average reduces. Outside the feasibility region, $\Theta \geq 1.96$, the mean vertical transport decreases to reach zero. As the rotational diffusion increases, also the ensemble average become zero.

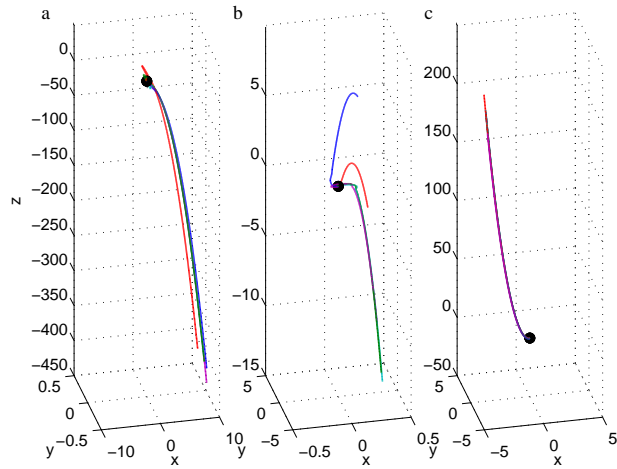


Figure 4.22: **Effect of propulsive torque strength on deterministic trajectories:** Example trajectories of duration 100 non-dimensionalized on $2B$ for different values of propulsive torque: (a) $\Theta = 0.2$, (b) $\Theta = 1$, and (c) $\Theta = 1.5$ and for fixed $\Psi = 1$, $\gamma = \frac{7\pi}{16}$.

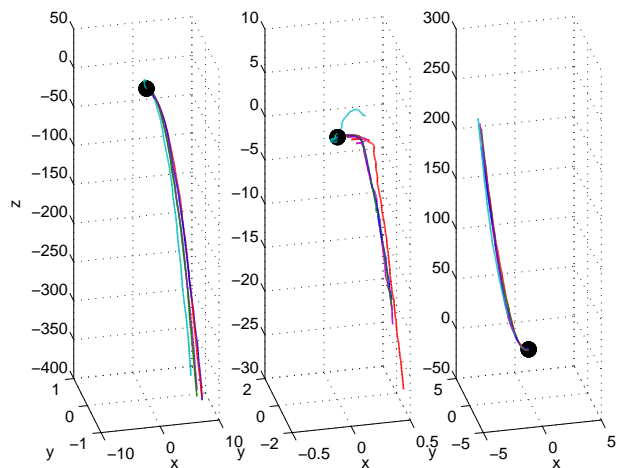


Figure 4.23: **Effect of propulsive torque strength on stochastic trajectories:** Example trajectories of duration 100 non-dimensionalized on $2B$ for different values of propulsive torque: (a) $\Theta = 0.2$, (b) $\Theta = 1$, and (c) $\Theta = 1.5$ and for fixed $\Psi = 1$, $\gamma = \frac{7\pi}{16}$, and $D_r = 0.01$.

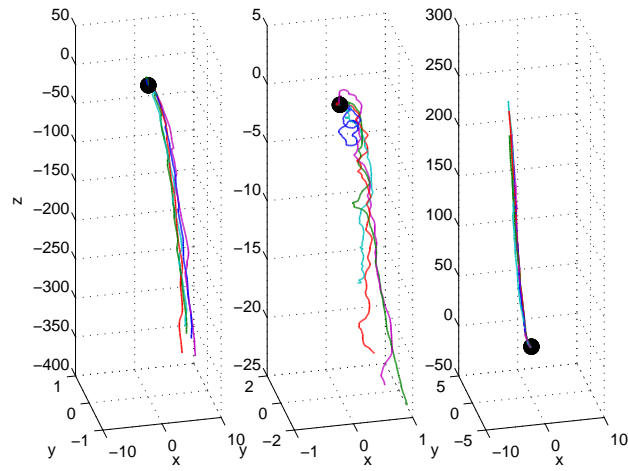


Figure 4.24: **Effect of propulsive torque strength on stochastic trajectories:** As of Figure 4.23 where we fixed $D_r = 0.1$.

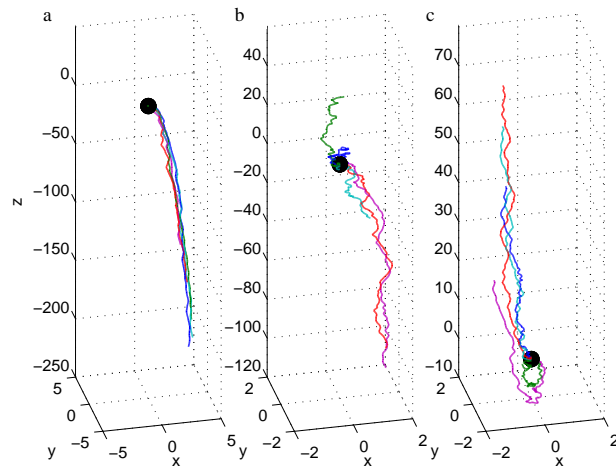


Figure 4.25: **Effect of propulsive torque strength on stochastic trajectories:** As of Figure 4.23 where we fix $D_r = 0.5$.

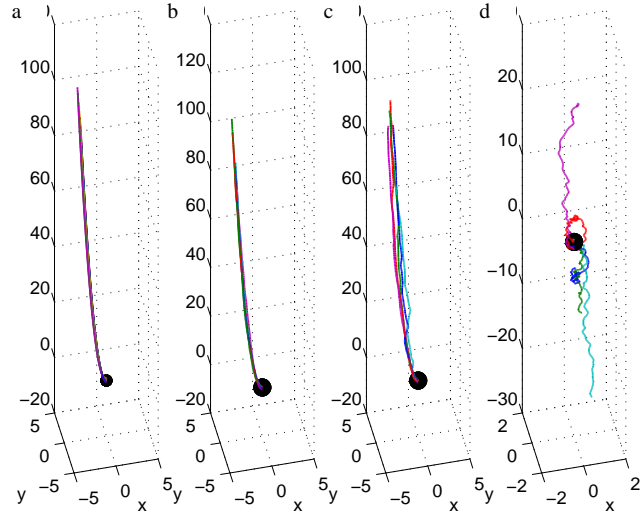


Figure 4.26: **Example trajectories:** Example trajectories of duration 100 non-dimensionalized on $2B$. (a) deterministic trajectories, and (b-d) stochastic trajectories for rotational diffusion (b) $D_r = 0.01$, (c) $D_r = 0.1$, and (d) $D_r = 0.5$. We fixed $\Theta = 1$, $\gamma = \frac{7\pi}{16}$, and shear strength $\Psi = 0.5$.

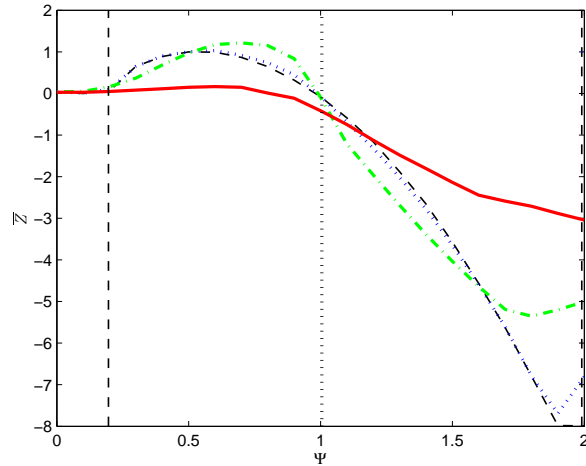


Figure 4.27: **Mean vertical transport:** As of Figure 4.16 but for helical swimmers with parameters $\Theta = 1$, and $\gamma = \frac{7\pi}{16}$. The vertical dotted line shows the zero of the horizontal component of orientation, p_x^e .

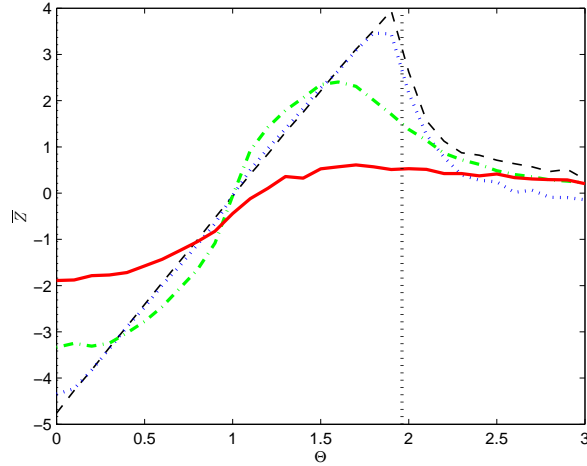


Figure 4.28: **Mean vertical transport:** vertical displacement of 100 cells of duration 100 time units as a function of propulsive torque strength, Θ for $\gamma = \frac{7\pi}{16}$ and fixed shear strength $\Psi = 1$. Black dashed curve is the average of vertical transport using the deterministic model. Blue, green, red curves are the average of vertical transport using the stochastic model for $D_r = 0.01$, $D_r = 0.1$, and $D_r = 0.5$ respectively. The equilibrium of horizontal component of orientation is feasible to left of the vertical black dashed line.

4.4 Non-uniform shear flow

4.4.1 Spatio-orientation model for non-helical gyrotactic swimmers

In this section, we extend the results of Section 2.3 to discuss the impact of rotational diffusion on swimming trajectories. We therefore consider the stochastic differential equation (4.27) in channel flow given by

$$\mathbf{V} = \Psi_{max}(x^2 - 1)\mathbf{k}, \quad (4.43)$$

where Ψ_{max} is the shear strength and \mathbf{k} is a unit vector in the vertical direction. The drift term in Equation (4.27) is thus given by

$$\mathbf{A} = \begin{pmatrix} \nu \sin \theta \cos \phi \\ \nu \sin \theta \sin \phi \\ \Psi_{max}(x^2 - 1) + \nu \cos \theta \\ -\sin \theta - \Psi_{max}x \cos \phi + D_r \cot \theta \\ \Psi_{max}x \frac{\sin \phi \cos \theta}{\sin \theta} \end{pmatrix}. \quad (4.44)$$

The rate of change of orientation, \mathbf{p} , is now a function of cell position.

The deterministic model predicts that the gyrotactic cells accumulate at the centre of the channel [64] as we showed in Chapter 2. Here we examine the effect of the D_r on the cell accumulation. That is, we are solving the stochastic differential equation (4.27) with drift term given by (4.44). We consider 1000 cells initially distributed uniformly across the channel with uniform orientation and with swimming speed $\nu = 0.1$ in downwards channel flow. We impose absorbing boundary conditions at the walls so that cells that initially start at walls or swim towards the wall will stay there. The cells swim for 100 time units with time step $dt = 0.01$.

In Figure 4.29, we see that cells accumulate and spread around the centre of the channel. Moreover, as rotational diffusion increase, there is more variation in the horizontal component of cell position. This variation in cell position as a function time for different values of rotational diffusion is shown in Figure 4.30. We see that by $t = 100$, an equilibrium is attained. This means that the mean swimming towards the centre of the channel is balanced by the diffusion away from the centre. In addition, in Figure 4.31 we compute the variance at the end time and we note that the variance in the cell position increases as the rotational diffusion is increased.

The absorbing boundary condition imposed during the simulations plays an important role in the value of the variation of the cells across the channel. In

Figure 4.32 we compute the variation of cell position at the end time excluding the cells that accumulate at the walls. Comparing with Figure 4.31, we see that the value of the variance decreases but the variance in cell position still increases as D_r is increased.

In order to understand the spatial distribution of cells, we recall that Equation (4.6) describes the cell concentration. Following [75], we assume that cells satisfy Equation (4.6), with $D_t = 0$, even though the channel has variable shear. The horizontal component of cell concentration satisfies

$$\frac{\partial n}{\partial t} = -\frac{\partial}{\partial x} \left[\nu q^x n - \frac{\nu^2}{D_r} D^{xx} \frac{\partial n}{\partial x} \right], \quad (4.45)$$

where q^x and D^{xx} are the x -component of mean swimming direction and effective diffusion tensor, respectively. We seek an equilibrium ($\frac{\partial n}{\partial t} = 0$) solution for this equation. Integrating both sides with respect to x , we get

$$c = -\nu q^x n - \frac{\nu^2}{D_r} D^{xx} \frac{\partial n}{\partial x}, \quad (4.46)$$

where c is a constant to be determined. Imposing no flux condition at the walls $x = \pm 1$

$$\nu q^x n - \frac{\nu^2}{D_r} D^{xx} \frac{\partial n}{\partial x} = 0, \quad (4.47)$$

we have $c = 0$. This condition means that swimming towards the channel centre is balanced by diffusion towards the walls [83]. Integrating once more, we obtain the equilibrium solution

$$n = n_0 \exp \left(\int_0^x \frac{D_r}{\nu} \frac{q^x}{D^{xx}} dx \right), \quad (4.48)$$

where $n(0) = n_0$ is the normalization constant. To obtain an estimate for $\frac{q^x}{D^{xx}}$, we use results from Bearon et. al. [10] where they obtained the estimate for two dimensional flow as

$$\frac{q^x}{D^{xx}} = -\frac{1}{2} \text{Pr} \kappa \quad (4.49)$$

valid in the limit of both $\text{Pr} \rightarrow 0$ and $\text{Pr} \rightarrow \infty$. They defined the non-dimensional shear as $\text{Pr} = \frac{G}{d_r}$ where $G = |\hat{\mathbf{G}}|$ is dimensional measure of the magnitude of fluid velocity gradient, and d_r is the dimensional rotational diffusion. The parameter $\kappa = \frac{1}{2Bd_r}$ is the non-dimensional parameter representing the bias due to gravitaxis.

To interpret this estimate in terms of our parameters, we note that $\kappa = \frac{1}{D_r}$ and $\text{Pr} = \Psi\kappa$. Therefore

$$\frac{q^x}{D^{xx}} = -\frac{1}{2} \frac{\Psi}{D_r^2}. \quad (4.50)$$

For non-uniform shear, we replace Ψ by $\Psi_{max}x$. Thus we have

$$n = n_0 \exp\left(\int_0^x -\frac{1}{2\nu} \frac{\Psi_{max}x}{D_r} dx\right), \quad (4.51)$$

which gives the equilibrium distribution

$$n = n_0 \exp\left(-\frac{\Psi_{max}}{4\nu D_r} x^2\right). \quad (4.52)$$

The variance in the cell concentration is inversely proportional to shear strength and proportional to rotational diffusion. In Figure 4.33, we see that when the variation, as a function of rotational diffusion, attains the equilibrium, the variance in cell position across the channel decreases as the shear strength is increased. This agrees with the results for two dimensional flow [10] and for a pipe flow [7]. Furthermore, from Equation (4.52), the variance increases as rotational diffusion is increased. This agrees with the results we found in Figure 4.31.

We further investigate the case of no shear, $\Psi_{max} = 0$. The only torque that acts on cells is the gravity torque. Therefore, cells swim upwards against gravity and uniformly across the channel. So that, the variance will be one when the cell variation as a function of D_r attains equilibrium.

Because of the absorbing boundary conditions, cells accumulate at walls as shown

in Figure D.4.

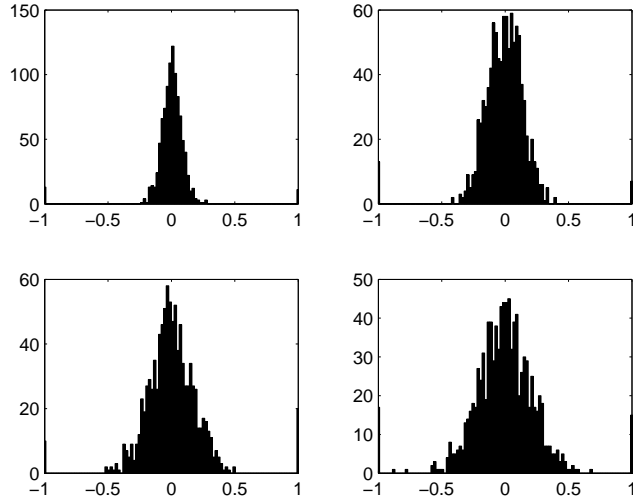


Figure 4.29: **Histogram of horizontal position across the channel for stochastic non-helical swimmers:** We run 1000 realizations of Equation (4.27) with drift term given by (4.44) with initial random horizontal component between the channel walls and with random orientation for different value for rotational diffusion: (a) $D_r = 0.1$, (b) $D_r = 0.3$ and (c) $D_r = 0.5$ and (d) $D_r = 0.7$. Shear strength is $\Psi_{max} = 2$. Histogram is at time $t = 100$. Accumulation at the walls are due to the absorbing boundary conditions.

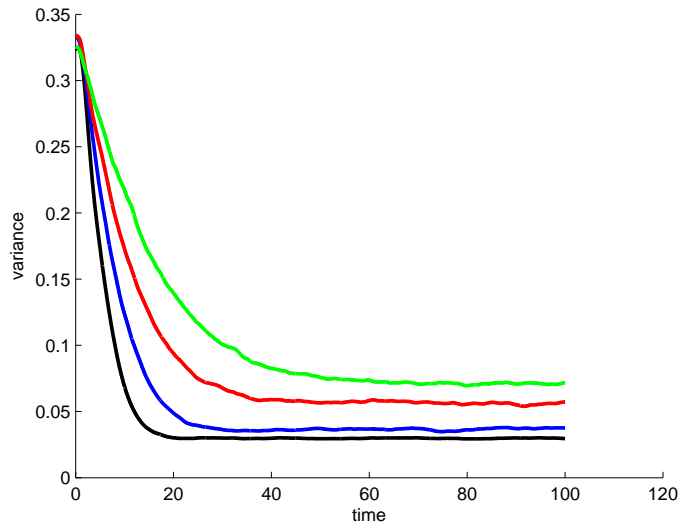


Figure 4.30: **Variation in horizontal component of position as function of time:** Simulations as Figure 4.29. Black curve corresponds to $D_r = 0.1$, blue curve corresponds to $D_r = 0.3$, red curve corresponds to $D_r = 0.5$, and green curve corresponds to $D_r = 0.7$. The shear strength is fixed $\Psi_{max} = 2$.

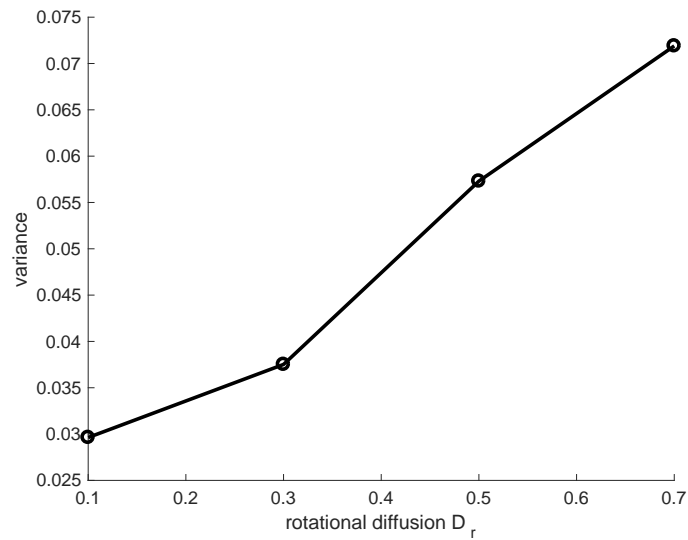


Figure 4.31: **Variance in horizontal position as function of D_r at time $t = 100$:** Variance from Figures 4.29 and 4.30 at end point $t = 100$ plotted as a function of D_r .

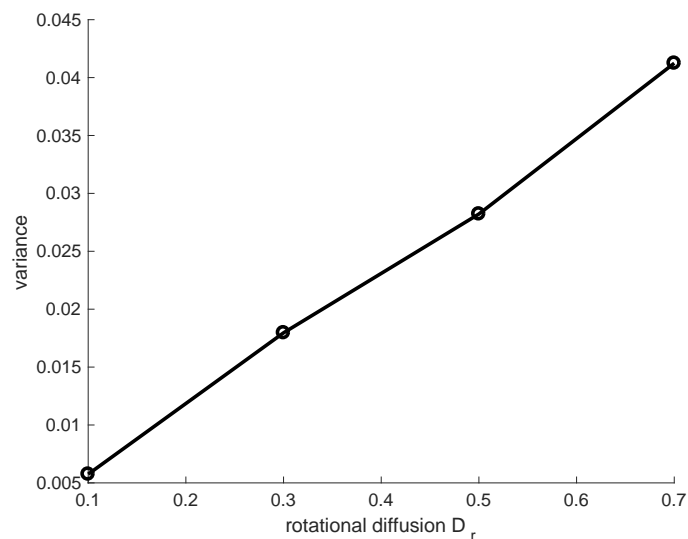


Figure 4.32: **Variance in horizontal position as function of D_r :** As Figure 4.31, excluding cells that accumulate at walls.

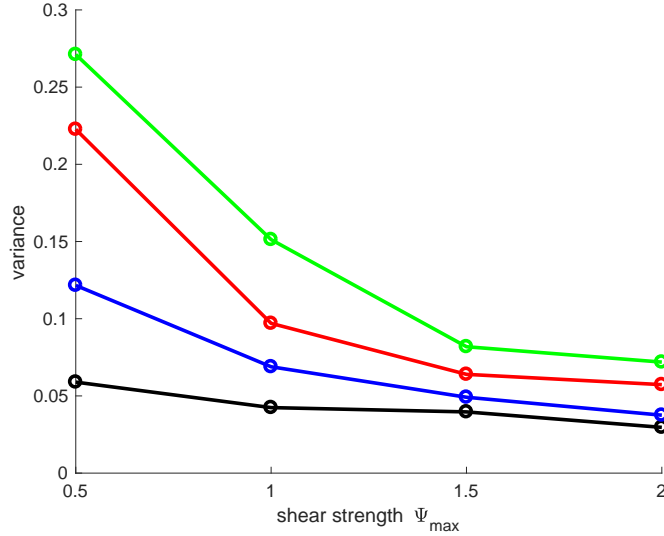


Figure 4.33: **Variance in horizontal position as function of Ψ_{max} :** Simulations as Figure 4.29 for range of Ψ_{max} indicated by circles. Variance computed at $t = 100$. Black line correspond to $D_r = 0.1$, blue line correspond to $D_r = 0.3$, red line correspond to $D_r = 0.5$, and green line correspond to $D_r = 0.7$.

4.4.2 Spatio-orientation model for helical gyrotactic swimmers

As in the previous section, we now extend the stochastic differential equation for helical swimmers to describe non-uniform shear flow, hence in Equation (4.40) the drift becomes

$$\mathbf{A} = \begin{pmatrix} \nu \sin \theta \cos \phi \\ \nu \sin \theta \sin \phi \\ \Psi_{max}(x^2 - 1) + \nu \cos \theta \\ -\sin \theta + \Theta \sin \gamma \sin \psi - \Psi_{max}x \cos \phi + D_r \cot \theta \\ -\Theta \frac{\sin \gamma \cos \psi}{\sin \theta} + \Psi_{max}x \frac{\sin \phi \cos \theta}{\sin \theta} \\ \Theta(\cot \theta \cos \psi \sin \gamma + \cos \gamma) - \Psi_{max}x \frac{\sin \phi}{\sin \theta} \end{pmatrix}. \quad (4.53)$$

We simulate 1000 cells over 100 time units for Equation (4.40) with the drift given above. We also impose the absorbing boundary condition as we did in the previous section. The deterministic model in Chapter 2 concludes that the accumulation of cells across the channel depends on the propulsive torque strength Θ and

the angle between the propulsive force and torque. To investigate the impact of randomness on swimming trajectories, we consider two distinct examples. Firstly, we consider $\Theta = 1$ and $\gamma = \frac{\pi}{4}$ and then $\Theta = 1$ and $\gamma = \frac{7\pi}{16}$.

When $\Theta = 1, \gamma = \frac{\pi}{4}$, and the shear strength $\Psi_{max} = 2$, the equilibrium horizontal component of orientation p_x^e is feasible when $0.382 \leq |x| \leq 0.923$ which is equivalent to $0.764 \leq \Psi \leq 1.846$ in shear range. Within this feasibility region $p_x^e > 0$ thus cells swim towards the centre of the channel. Outside the feasibility region, $p_x^e < 0$ (see Figure 2.3 b) and thus cells maintain swimming towards the centre.

As in the case of non-helical swimmers, we note that when there is randomness in the orientation of cells, the spread of cells focusing at the centre of the channel increases as the rotational diffusion, D_r , is increased as shown in Figure 4.34. The variation in the horizontal component of cells attains equilibrium over the time interval of the simulation as shown in Figure 4.35. At equilibrium there is a balance between swimming inwards to the centre of the channel and diffusion outwards. At the end time, we evaluate the variance as a function of rotational diffusion. The variation increases as D_r increased, Figure 4.36. In Figure 4.37, we exclude the cells that accumulate at the walls from the calculation of variation in horizontal position across the channel. We note that, as in the case of non-helical swimmers, on excluding cells that accumulate at the walls, the variance reduces but the trend of increasing variance with increasing D_r is maintained.

As the shear strength is increased, the variation in horizontal component of cell position decreases as shown in Figure 4.38. This behaviour is similar to the case of non-helical swimmers. However, the magnitude of the variation in helical swimmers is greater than the magnitude of the variation of non-helical swimmers due to the propulsive torque existence. When $\Psi_{max} = 0.5$, for small rotational diffusion ($D_r = 0.1, D_r = 0.3$) within the timescale of the simulation, we see that an equilibrium spatial distribution is attained as represented by an equilibrium value of the variance, Figure D.5. This occurs when the diffusive flux away from the centre balances the directed swimming towards the centre. For strong

rotational diffusion ($D_r = 0.5$ and $D_r = 0.7$), the variation in horizontal position does not attain an equilibrium value within the timescale of the simulation. As shear strength is increased further, $\Psi_{max} = 1$, the horizontal component of the cells position attains equilibrium. Furthermore, the equilibrium is maintained as rotational diffusion is increased (Figures D.6–D.7 and Figure 4.35). When we exclude the cells that accumulate at the walls from the calculation of the cells spread across the channel, we see that the value of the variation decreases and the variation in the horizontal component decreases as the shear strength is increased as shown in Figure 4.39.

The variation in cell position across the channel can be expressed as a function of the propulsive torque strength, Θ , as shown in Figure 4.40. The variation is increasing as the propulsive torque strength is increased. When $\Theta = 2$, cells maintain swimming towards the centre of the channel as shown in Figure 4.41. However, the equilibrium of cells spread across the channel is not attained over the timescale of the simulation, Figure 4.42. For this value of Θ , the deterministic model reveals that the equilibrium of the horizontal component of cells orientation is feasible when $1.474 \leq \Psi \leq 2.798$ (see right panel in Figure 4.42) which is equivalent to $0.737 \leq |x| \leq 1.39$ and the horizontal component of orientation is zero, $p_x^e = 0$, when $\Psi = 1.848$ as shown in Figure 4.42. Therefore when $1.474 \leq \Psi \leq 1.84$ cells swim towards the walls and when $1.84 \leq \Psi \leq 2.798$ cells swim towards the centre. The choice of the shear strength $\Psi_{max} = 2$ is in the interval $(1.848, 2.798)$ where the cells swim towards the channel centreline. Furthermore, it is close to the point where the horizontal component of orientation is zero. The cells accumulate at the centre because they swim into the centre when p_x^e is not feasible (white region in the right panel of Figure 4.42) and also swim towards the centre when p_x^e is feasible over the shear range $1.84 \leq \Psi \leq 2.798$. For small randomness, $D_r = 0.1$, the variation in the horizontal component of the cells position does not attain the equilibrium (black curve in Figure 4.42). This is because the cells are swimming outwards towards a point close to the wall then D_r spreads the distribution around this point causing accumulate at the walls. As D_r is increased ($D_r = 0.3$ and $D_r = 0.5$) the variation in the horizontal component of the cells position attains the equilibrium. For strong rotational

diffusion, $D_r = 0.7$, the variation in the horizontal component of the cells position does not attain the equilibrium but cells maintain swimming towards the centre. Note that as D_r is increased the number of cells that accumulate at the walls decreases (see Figure 4.41).

The impact of the absorbing boundary conditions is remarkable in the case of variation as a function of the propulsive torque strength as shown in Figure 4.43. For $\Theta = 0.5$ and $\Theta = 1$, where the cells swim towards the centre of the channel, for small rotational diffusion ($D_r = 0.1$ and $D_r = 0.3$) the variation in the horizontal component of cell position decreases as the propulsive torque strength is increased from $\Theta = 0.5$ to $\Theta = 1$ and increases for $D_r = 0.5$ and $D_r = 0.7$. When $\Theta = 2$, as we see above cells maintain to swim towards the centre of the channel but these cells that accumulate at the walls have an impact in the value of the cells variation across the channel. Comparing Figures 4.40 and 4.43 we note that when we exclude the cells accumulate at the walls, the value of the variation of cells across the channel decreases with increasing D_r for each fixed Θ .

As expected in Chapter 2, the helical swimmers may show accumulation away from the centre of the channel. As an example, we consider $\Theta = 1, \gamma = \frac{7\pi}{16}, \Psi_{max} = 2$. The deterministic model reveals that the equilibrium of horizontal component of the cells orientation is feasible when $0.196 \leq \Psi \leq 1.99$ and the equilibrium of horizontal component of orientation is zero when $\Psi = 0.199$ or $\Psi = 0.98$. Cells swim towards the walls when $0.199 \leq \Psi \leq 0.98$ and swim into the centre of the channel when $0.98 \leq \Psi \leq 1.99$, therefore accumulation of cells at the interface where $\Psi = 0.98$. In Figure 4.44, we see that as the rotational diffusion is increased, the spread of the cells around the interface, where the orientation horizontal component, p_x^e , is zero, increases. Some cells accumulate at walls. This is because of the random behaviour of cells close to the wall and once they hit the wall, they stay there because of the absorbing boundary condition imposed on the flow.

Because of the symmetric peaks of cells about the centre of the channel (Figure 2.5c), we calculate the variance using the absolute value. In other words, we

evaluate the variation of cells spread around the interface where the orientation horizontal component is zero. The variation attains its equilibrium as a function of time as shown in Figure 4.45 for each rotational diffusion value. At the end time, we compute the variance of horizontal component of cell position as a function of rotational diffusion as shown in Figure 4.46. As in the previous example, the variation increases as D_r increased. When we exclude the cells that accumulate at the walls from the calculation of the cells variation across the channel, we see that the value of the variance decreases as shown in Figure 4.47 compared with Figure 4.46.

Within shear strength range, cells display two distinct behaviours. For $\Theta = 1$ and $\gamma = \frac{7\pi}{16}$ when the shear strength $\Psi_{max} \leq 1$ cells swim towards the walls as shown in Figures D.8-D.9. Although, the equilibrium has not been attained over the timescale of the simulation except at $\Psi_{max} = 1$ for $D_r = 0.1$ (see Figures D.10-D.11), the variation decreases as the shear strength is increased from $\Psi_{max} = 0.5$ to $\Psi_{max} = 1$. Furthermore, when the shear strength $\Psi_{max} > 1$ cells swim towards the centre of the channel. The increasing in the variance as shear strength is increased from $\Psi_{max} = 1$ to $\Psi_{max} = 1.5$, Figure 4.48, is due to the fact that the variance in cell horizontal position does not attain the equilibrium at $\Psi_{max} = 1$ for all D_r except $D_r = 0.1$ but the variance does attain the equilibrium at $\Psi_{max} = 1.5$ for $D_r = 0.1$ and $D_r = 0.3$ only. When we exclude the cells that accumulate at the walls, the value of the variance decreases with increasing D_r for each fixed shear strength Ψ_{max} , Figure 4.49.

The variation over the propulsive torque strength range, Θ , is shown in Figure 4.50. For weak rotational diffusion, $D_r = 0.1$ the variation decreases as Θ increases from $\Theta = 0.5$ to $\Theta = 1.5$. For the other values of D_r , the variation of the cells across the channel increases as Θ increases. This is because cells swim towards the centre of the channel (see Figure 2.1c). When $\Theta = 2$, the deterministic model predicts that the equilibrium of the horizontal component of cells orientation is feasible when $1.037 \leq \Psi \leq 2.987$ and $p_x^e = 0$ when $\Psi = 1.99$ as shown in Figure 4.51. The value of the shear strength $\Psi_{max} = 2$ is too close to the point where the cells re-orient themselves from swimming towards the walls

to swimming into the centre. As the rotational diffusion is increased, the cells swim towards the walls. Moreover, the variation in the cells position across the channel does not attain the equilibrium over the time interval considered in the simulation as shown in the left panel of Figure 4.51. When we exclude the cells that accumulate at the walls, the value of the variance increases as the propulsive torque strength increases, see Figure 4.52.

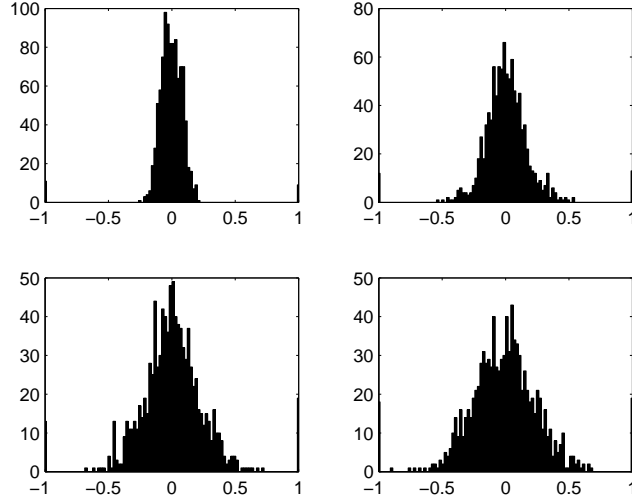


Figure 4.34: **Histogram of horizontal position across the channel for stochastic helical swimmers:** As of Figure 4.29 where we simulate Equation (4.40) with drift term given by (4.53) with shear strength $\Psi_{max} = 2$ and propulsive torque strength $\Theta = 1$ for $\gamma = \frac{\pi}{4}$ at $t = 100$.

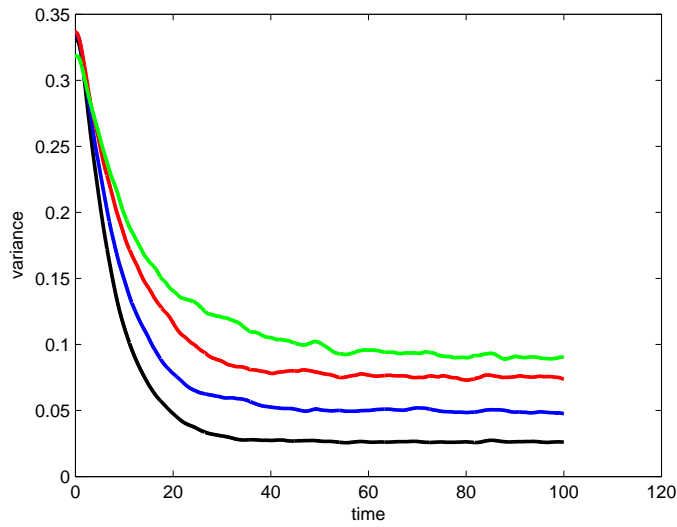


Figure 4.35: **variation in horizontal position as function of time for helical swimmers:** As of Figure 4.30 where we simulate realization of Equation (4.40) with drift given by (4.53). The shear strength is fixed $\Psi_{max} = 2$ and propulsive torque strength $\Theta = 1$ for $\gamma = \frac{\pi}{4}$.

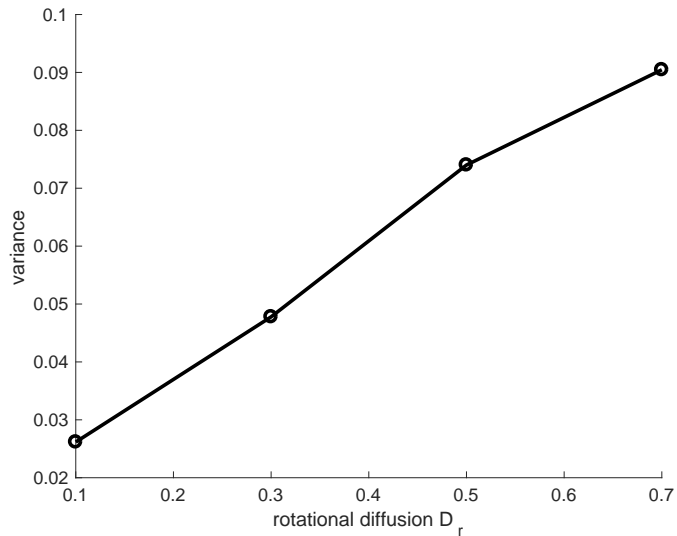


Figure 4.36: **variation in horizontal position as function of D_r for helical swimmers:** As of Figure 4.31 where we simulate Equation (4.40) with drift term given by (4.53) for helical swimmers with $\Theta = 1$, $\gamma = \frac{\pi}{4}$ and $\Psi_{max} = 2$.

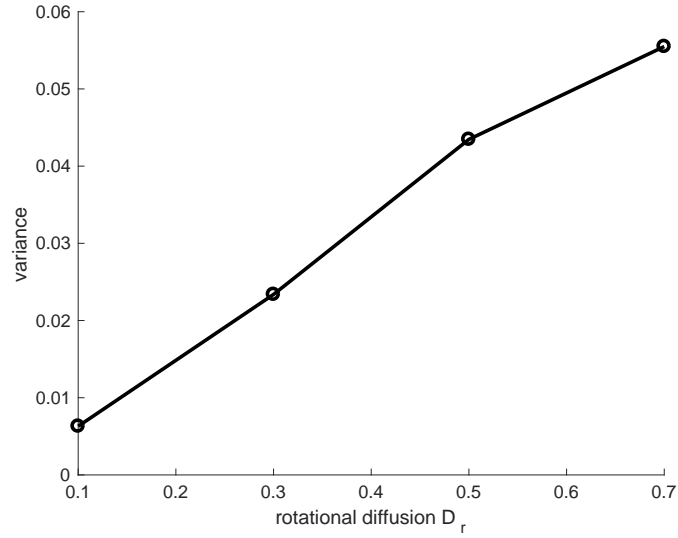


Figure 4.37: **variation in horizontal position as function of D_r for helical swimmers:** As of Figure 4.31 where we simulate Equation (4.40) with drift term given by (4.53) for helical swimmers with $\Theta = 1$, $\gamma = \frac{\pi}{4}$ and $\Psi_{max} = 2$. Excluding cells accumulate at walls.

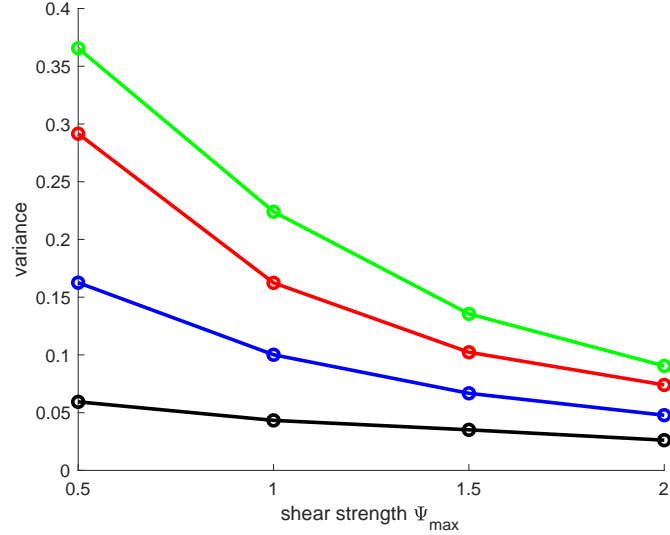


Figure 4.38: **variation in horizontal position as function of shear strength Ψ_{max} for helical swimmers:** We simulate realizations of Equation (4.40) with drift given by (4.53) for range of Ψ_{max} indicated by circles. Variance computed at $t = 100$. Black line corresponds to $D_r = 0.1$, blue line corresponds to $D_r = 0.3$, red line corresponds to $D_r = 0.5$, and green line corresponds to $D_r = 0.7$. We fix $\Theta = 1$ and $\gamma = \frac{\pi}{4}$. Including cells accumulate at walls.

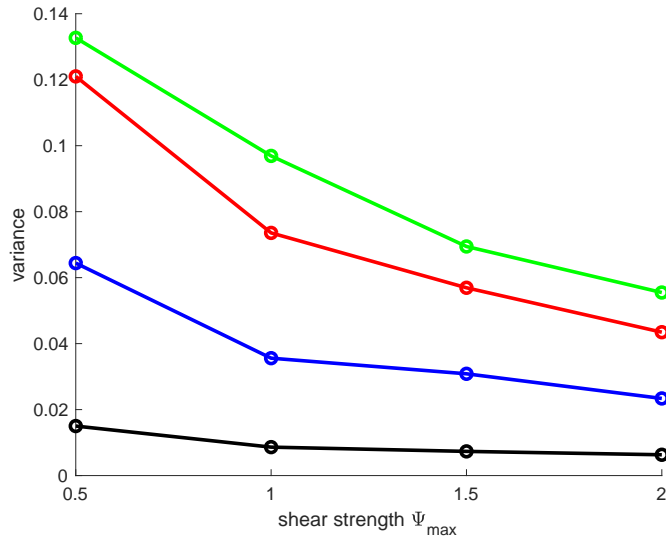


Figure 4.39: **variation in horizontal position as function of Ψ_{max} for helical swimmers:** As of Figure 4.38 where we simulate realizations of Equation (4.40) with drift given by (4.53) for different values of shear strength, Ψ_{max} , indicated by circles. We fix $\Theta = 1$ and $\gamma = \frac{\pi}{4}$. Excluding cells accumulate at walls.

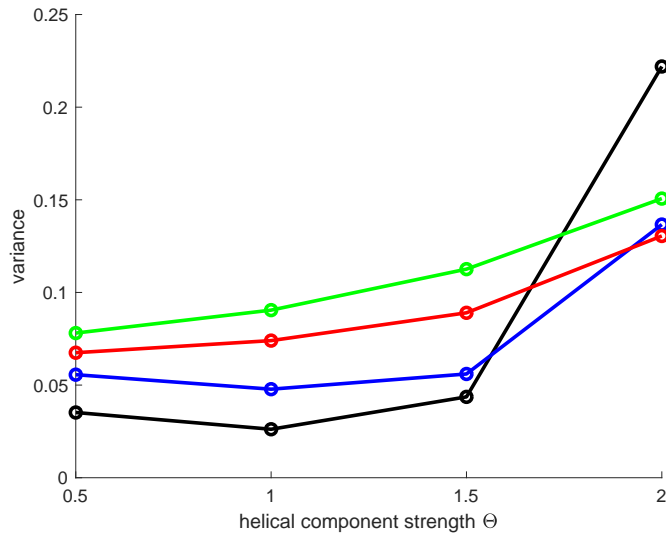


Figure 4.40: **variation in horizontal position as function of Θ for helical swimmers:** We run 1000 realizations of of Equation (4.40) with drift given by (4.53) for 100 time units for different values of propulsive strength, Θ , indicated by circles and computed at $t = 100$. We fix $\gamma = \frac{\pi}{4}$ and $\Psi_{max} = 2$. Green line corresponds to rotational diffusion $D_r = 0.7$, red line corresponds to rotational diffusion $D_r = 0.5$, blue line corresponds to rotational diffusion $D_r = 0.3$, and black line corresponds to rotational diffusion $D_r = 0.1$.

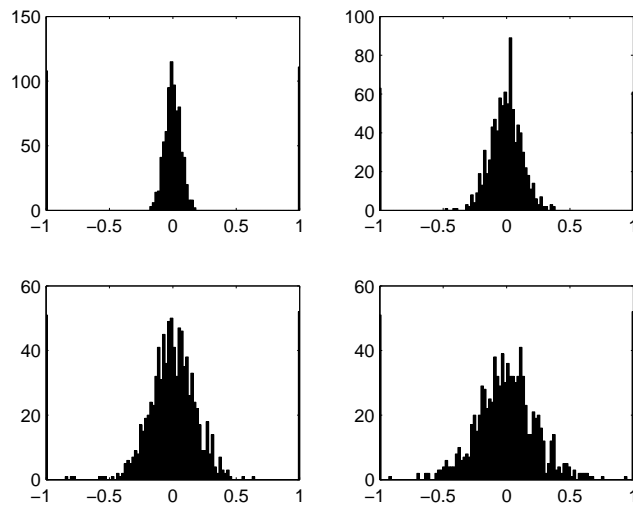


Figure 4.41: **Histogram of horizontal position across the channel for stochastic helical swimmers:** As of Figure 4.29 where we simulate Equation (4.40) with drift term given by (4.53) with shear strength is $\Psi_{max} = 2$ and propulsive torque strength $\Theta = 2$ for $\gamma = \frac{\pi}{4}$. Accumulation at the walls are due to the absorbing boundary conditions.

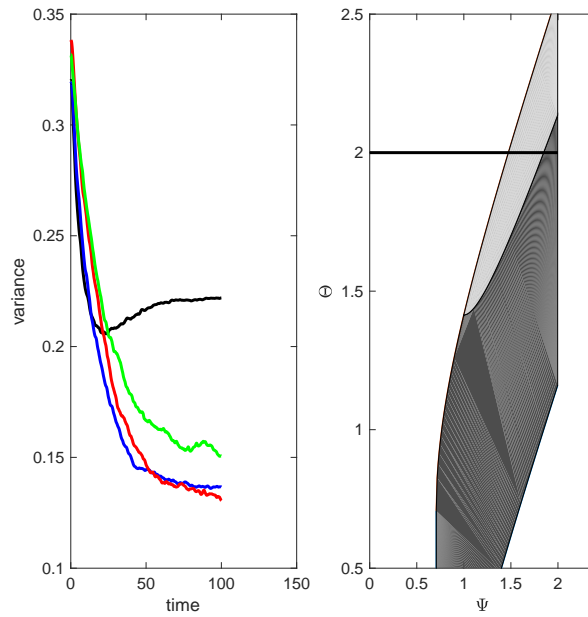


Figure 4.42: **variation in horizontal position as function of time and equilibrium feasibility for helical swimmers:** The left panel is the variance in cells position across the channel as function of time. We simulate realizations of Equation (4.40) with drift given by (4.53). The shear strength is fixed $\Psi_{max} = 2$ and propulsive torque strength $\Theta = 2$ for $\gamma = \frac{\pi}{4}$. The right panel is the equilibrium feasibility region for these values obtained from the deterministic model.

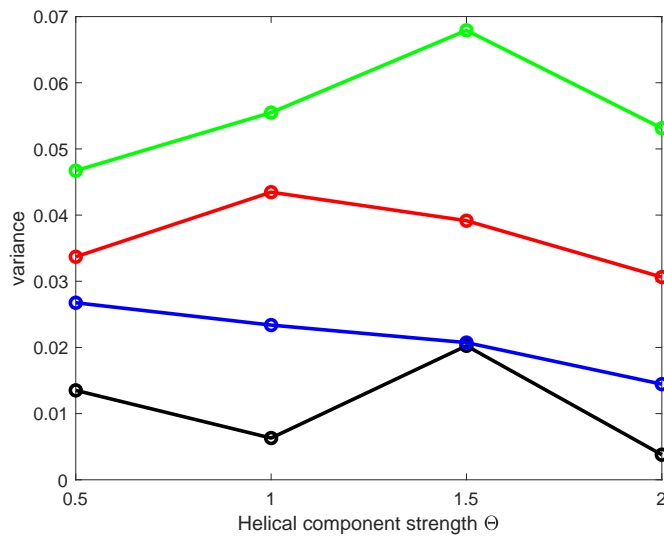


Figure 4.43: **variation in horizontal position as function of Θ for helical swimmers:** As of Figure 4.40. Excluding cells that accumulate at the walls.

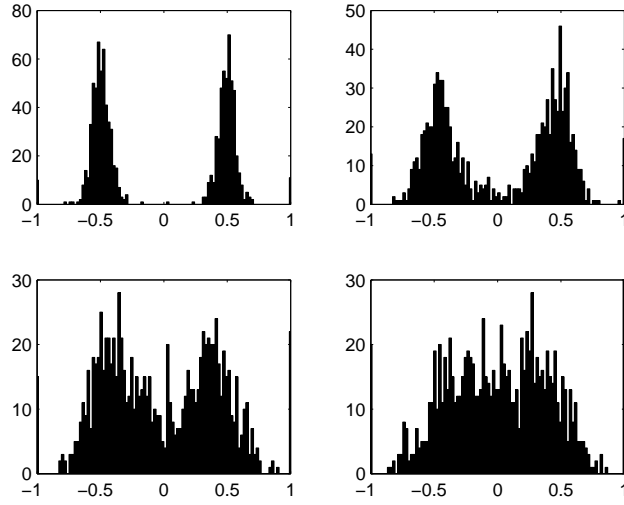


Figure 4.44: **Histogram of horizontal position across the channel for stochastic helical swimmers:** As of Figure 4.29 where we simulate Equation (4.40) with drift term given by (4.53) with shear strength is $\Psi_{max} = 2$ and propulsive torque strength $\Theta = 1$ for $\gamma = \frac{7\pi}{16}$ at $t = 100$.

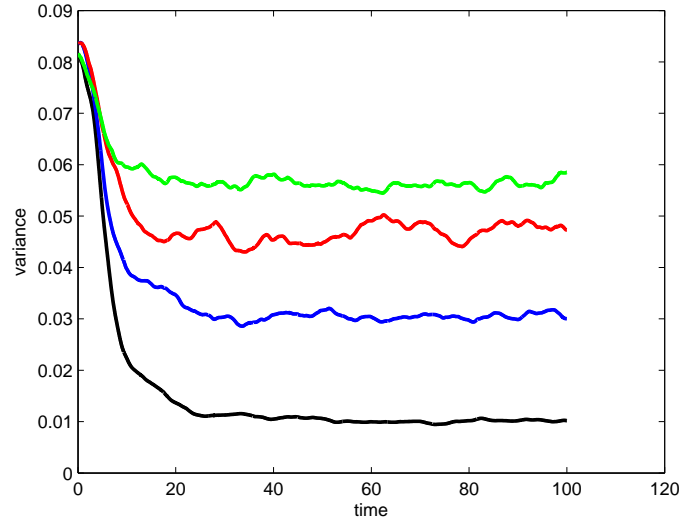


Figure 4.45: **variation in horizontal position as function of time for helical swimmers:** As of Figure 4.30 where we simulate realizations of Equation (4.40) with drift given by (4.53). The shear strength is fixed $\Psi_{max} = 2$ and propulsive torque strength $\Theta = 1$ for $\gamma = \frac{7\pi}{16}$. The variance reach equilibrium over time.

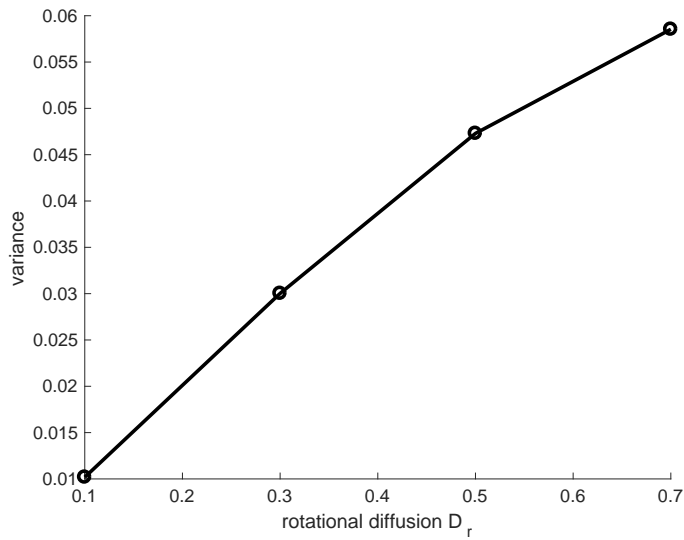


Figure 4.46: **variation in horizontal position as function of D_r for helical swimmers:** As of Figure 4.31 where we simulate Equation (4.40) with drift term given by (4.53) for helical swimmers with $\Theta = 1, \gamma = \frac{7\pi}{16}$. Shear strength $\Psi_{max} = 2$.

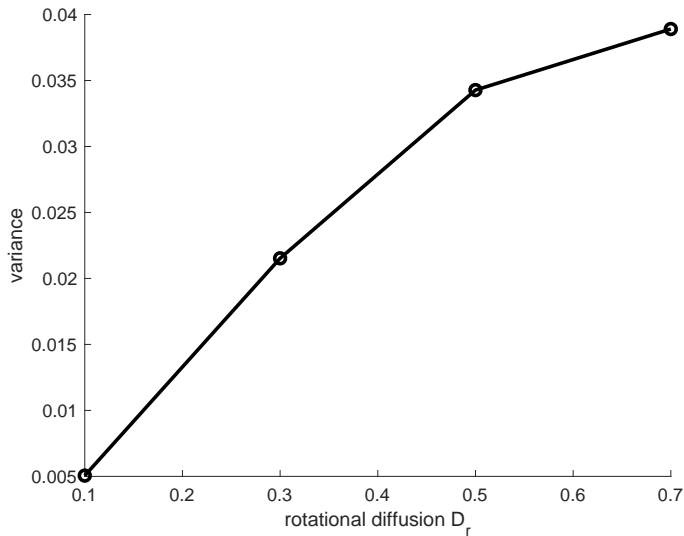


Figure 4.47: **variation in horizontal position as function of D_r for helical swimmers:** As of Figure 4.31 where we simulate Equation (4.40) with drift term given by (4.53) for helical swimmers with $\Theta = 1, \gamma = \frac{7\pi}{16}$. Shear strength $\Psi_{max} = 2$. Excluding cells at walls.

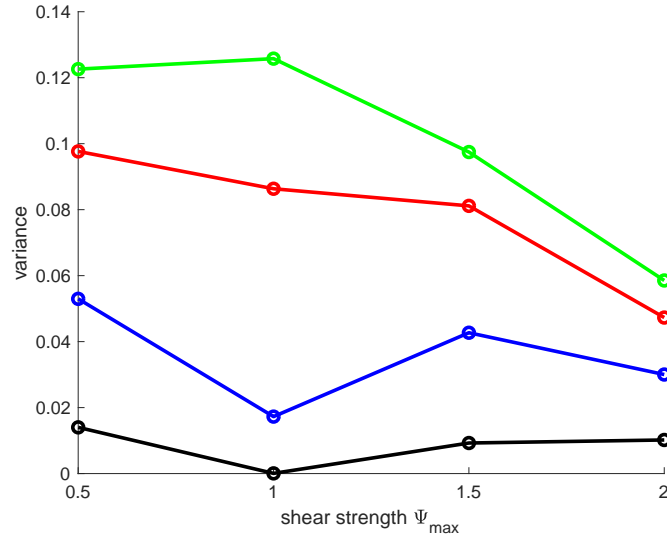


Figure 4.48: **variation in horizontal position as function of Ψ_{max} for helical swimmers:** We simulate realizations of Equation (4.40) with drift given by (4.53) for range of Ψ_{max} indicated by circles. Variance computed at $t = 100$. Black line corresponds to $D_r = 0.1$, blue line corresponds to $D_r = 0.3$, red line corresponds to $D_r = 0.5$, and green line corresponds to $D_r = 0.7$. We fix $\Theta = 1$ and $\gamma = \frac{7\pi}{16}$. Including cells accumulate at walls.

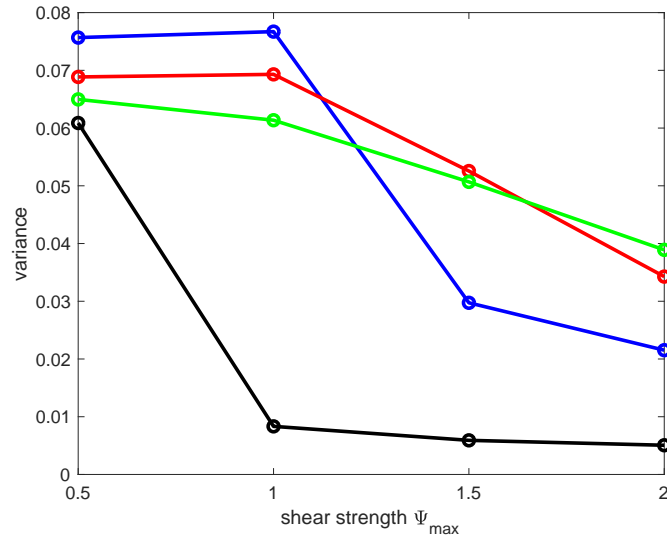


Figure 4.49: **variation in horizontal position as function of Ψ_{max} for helical swimmers:** We simulate realizations of Equation (4.40) with drift given by (4.53) for range of Ψ_{max} indicated by circles. Variance computed at $t = 100$. Black line corresponds to $D_r = 0.1$, blue line corresponds to $D_r = 0.3$, red line corresponds to $D_r = 0.5$, and green line corresponds to $D_r = 0.7$. We fix $\Theta = 1$ and $\gamma = \frac{7\pi}{16}$. Excluding cells accumulate at walls.

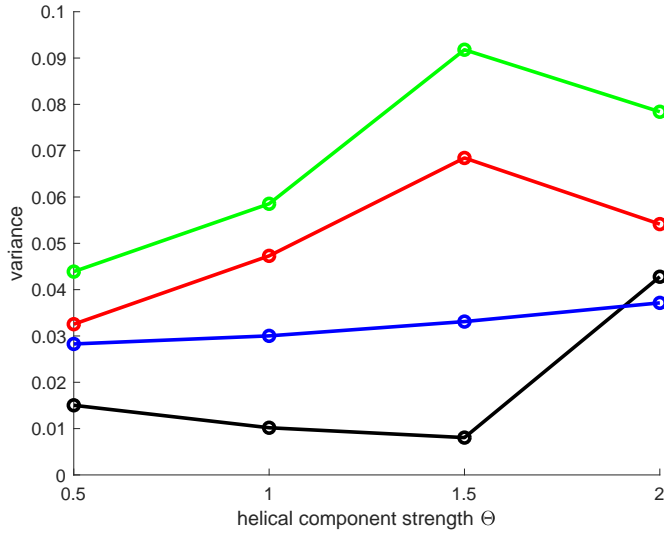


Figure 4.50: **variation in horizontal position as function of Θ for helical swimmers:** We simulate realizations of Equation (4.40) with drift given by (4.53) for range of Θ indicated by circles. Variance computed at $t = 100$. Black line corresponds to $D_r = 0.1$, blue line corresponds to $D_r = 0.3$, red line corresponds to $D_r = 0.5$, and green line corresponds to $D_r = 0.7$. We fix $\gamma = \frac{7\pi}{16}$ and $\Psi_{max} = 2$. Including cells that accumulate at the walls.

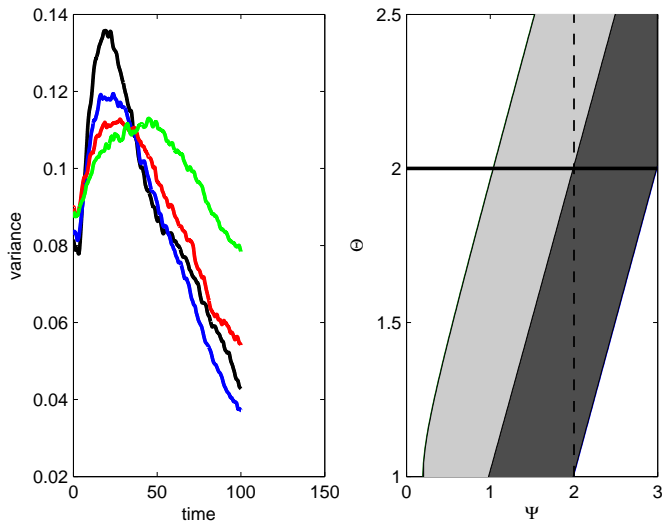


Figure 4.51: **variation in horizontal position as function of time and equilibrium feasibility for helical swimmers:** The left panel is the variance in cells position across the channel as function of time. We simulate realizations of Equation (4.40) with drift given by (4.53). The shear strength is fixed $\Psi_{max} = 2$ and propulsive torque strength $\Theta = 2$ for $\gamma = \frac{7\pi}{16}$. The right panel is the equilibrium feasibility region for these values obtained from the deterministic model. The vertical dashed line is $\Psi_{max} = 2$. The axis scales in the left panel is chosen to aid visualization.

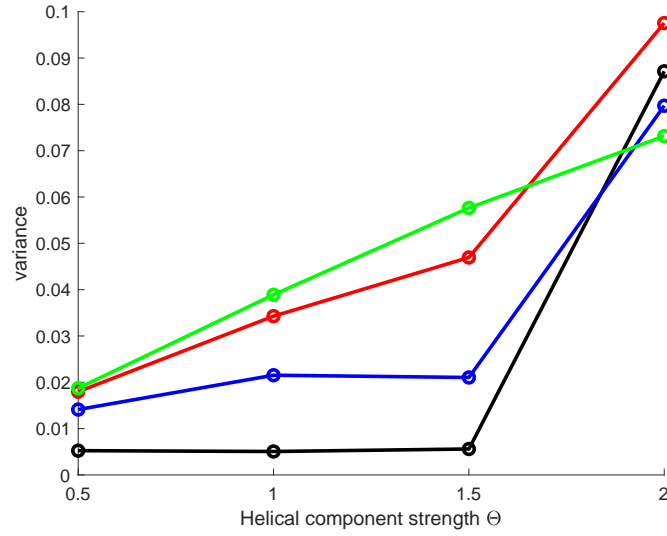


Figure 4.52: **variation in horizontal position as function of Θ for helical swimmers:** As of Figure 4.50. Excluding cells at walls.

4.4.3 Testing stochastic differential equation for non-helical swimmers

Croze et al [31] provided experimental data for alga *Dunaliella salina* dispersing in a pipe flow. They used fluorescently stained slug of the alga and recorded the downwards flow. The cell has a radius $r \approx 10^{-4}$ cm. The estimation of the thermal rotational diffusion at room temperature ($T = 298.15K$) using Equation (1.12) is

$$d_r = \frac{1.38 \times 10^{-16} \times 298.15}{8\pi \times 9 \times 10^{-3} \times (10^{-4})^3} = 0.18 \text{ s}^{-1},$$

which is quite large compared to the thermal diffusion for *Chlamydomonas nivalis* given in [83] by $1.3 \times 10^{-3} \text{ s}^{-1}$. This is due to the fact that the radius of *Dunaliella Salina* ($r = 1\mu\text{m}$) is smaller than the cell radius of *Chlamydomonas nivalis* ($r = 5\mu\text{m}$). The estimate of the rotational diffusion in the experiment is $d_r = 0.23 \text{ s}^{-1}$ [31].

We used their data to examine the stochastic differential equations of non-helical

swimmers in a channel. However, the experiment was conducted using a pipe. Therefore, our results here is an approximation of the experiment.

We non-dimensionalize length on the half-width of the channel, L and time on $\frac{L}{U}$ where U is the flow speed at the centre as given in Croze et. al. [32]. This choice of non-dimensionalizing was made because non-dimensionalizing the parameters based on “cell-based” rescaling is not appropriate for numerical simulations [32] as it results in a large value of rotational diffusion. For instance if we use the non-dimensionalization method as we did earlier, the non-dimensional rotational diffusion is $D_r = 2Bd_r = 4.8$ where the estimate of gravitational time scale $B = 10.5$ s [31].

The flow speed, U , at the centre is double the average flow speed, U_{av} , where $0.07\text{cms}^{-1} \leq U_{av} \leq 0.29\text{cms}^{-1}$ as given in [31].

We have defined time $t = \frac{\tau}{2B}$ in Chapter 2. The new non-dimensional time is defined as $t^* = \frac{U}{L}\tau$. Therefore $t = \xi t^*$ where $\xi = \frac{L}{2BU}$ is the ratio of gravitational time scale to flow time scale. The shear strength of Poiseuille flow given in Chapter 2 is thus $\Psi_{max} = 2$. The swimming speed of cell and rotational diffusion are non-dimensionalized as $\nu^* = \frac{\nu}{U}$ and $D_r^* = \frac{d_r L}{U}$ respectively where the estimate for swimming speed is given by $\nu = 6.26 \times 10^{-3}\text{cm s}^{-1}$ and the estimate for rotational diffusion is $d_r = 0.23 \text{ s}^{-1}$ [31] where d_r was estimated by the dimensionless parameter $\lambda = \frac{1}{2Bd_r}$ which measures the relative strength of random reorientation due to the rotational diffusion to the reorientation due to the gravitactic torque at time rate $\frac{1}{2B}$. The estimate of gravitational time scale $B = 10.5$ s [31].

For each flow rate considered in Figure 3 in [31], we computed the non-dimensional parameters in table 4.1. The ratio of rotational time scale to flow scale is defined as $\beta = \frac{1}{D_r^*}$. The Péclet number that measures the rates of transport by flow and swimming diffusion can be defined by $\text{Pe} = \frac{D_r^*}{\nu^{*2}} = \frac{ULD_r}{\nu^2}$.

As in the previous two sections, we simulate 1000 realizations of the stochastic

differential equation (4.27) with the drift term

$$\mathbf{A} = \begin{pmatrix} \nu^* \sin \theta \cos \phi \\ \nu^* \sin \theta \sin \phi \\ 2(x^2 - 1) + \nu^* \cos \theta \\ -\xi \sin \theta - 2x \cos \phi + D_r^* \cot \theta \\ 2x \frac{\sin \phi \cos \theta}{\sin \theta} \end{pmatrix}. \quad (4.54)$$

For each set of parameters in table 4.1, the time to attain equilibrium increases. In other words, as Péclet number increases, i.e the flow rate increase, the time to attain equilibrium increases as shown in Figure 4.53. When $Pe = 1183.64$ the equilibrium is not attained over the time interval considered in the simulation

In Figure 4.54, the accumulation of cells across the channel is shown. As Péclet number increases, the accumulation in the centre becomes tight. The variation in the horizontal component of cells decreases as a function of Péclet number is shown in Figure 4.55.

To calculate the channel length needed to attain the equilibrium of the accumulation, we first compute the dimensional time taken for the first three flows. Within these three flows, the equilibrium of the variation of cells accumulation is attained. Noting that t^* is the time at which the equilibrium of variation in cells accumulation is attained in the simulation, restore the dimensional time, $\tau = \frac{L}{U}t^*$. The time taken to attain the equilibrium is 2000 s, 1958 s, and 2592 s for the first three flows respectively. The channel length is calculated by multiplying the dimensional time and the maximum flow speed. Therefore, the length of the channel would be 280 cm, 559 cm, and 1119 cm, for the first flow respectively. The experiment was conducted for different cell concentration (see Figure 3 in [31]).

	Flow rate (cm^3h^{-1})	Flow speed at the centre (cms^{-1})	ν^*	D_r^*	ξ	Pe
a	100	0.14	0.0448	0.575	0.119	286.69
b	200	0.286	0.0219	0.281	0.0583	585.6
c	300	0.432	0.0145	0.163	0.0386	884.66
d	400	0.578	0.0108	0.139	0.0288	1183.64

Table 4.1: Fluid flow parameters from Croze et. al. [31] experiment for *D. salina* algae and non-dimensional parameters for spatial-orientation problem. Flow rates are chosen to test Figure (3) in [31].

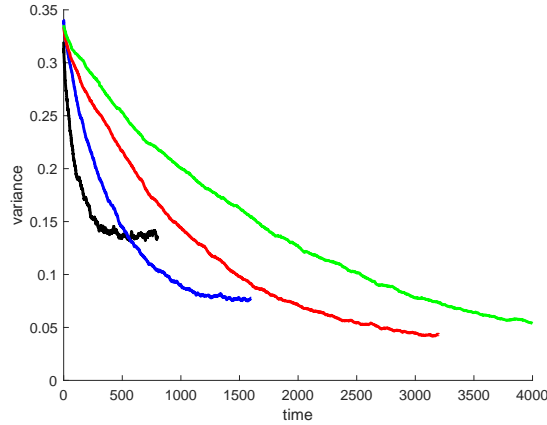


Figure 4.53: **Variation in horizontal position as a function of time:** variance of horizontal component of cell position across the channel. We run 1000 simulations of cells with initial random horizontal component between the channel walls with random orientation with time step $dt = 0.1$. The non-dimensional parameters are (ν^*, D_r^*, ξ) . The black curve corresponds to flow rate (a), blue curve corresponds to flow rate (b), red curve corresponds to flow rate (c), and green curve corresponds to flow rate (d) in Table 4.1 over time interval 800 for flow (a), over 1600 for flow (b), over 3200 for flow (c), and over 4000 for flow (d).

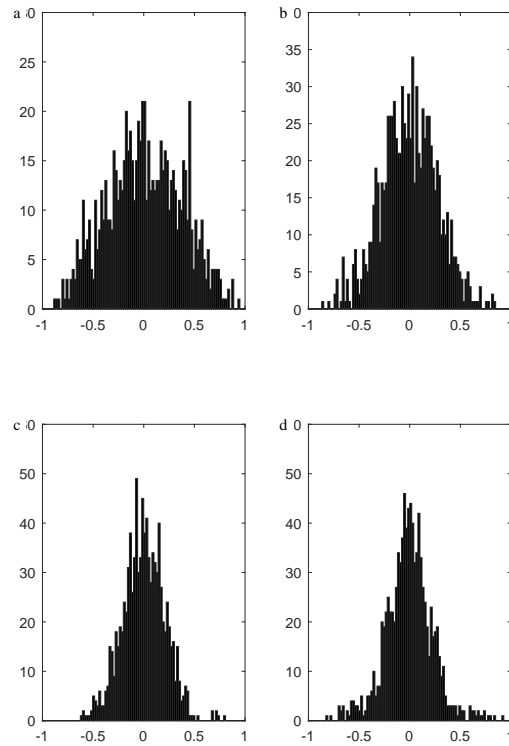


Figure 4.54: **Distribution across the channel for *D. salina*:** We run 1000 simulations for different flow rates. Parameter values for each flow rate are given in table 4.1. Time step is $dt = 0.1$ and time duration T for (a) is $T = 800$, for (b) is $T = 1600$, for (c) is $T = 3200$ and for (d) is $T = 4000$ time units using the non-dimensional parameters given in table (4.1) where the cells are initially distributed uniformly across the channel with uniform orientation. All flows attain their equilibrium over the time interval considered except flow (d).

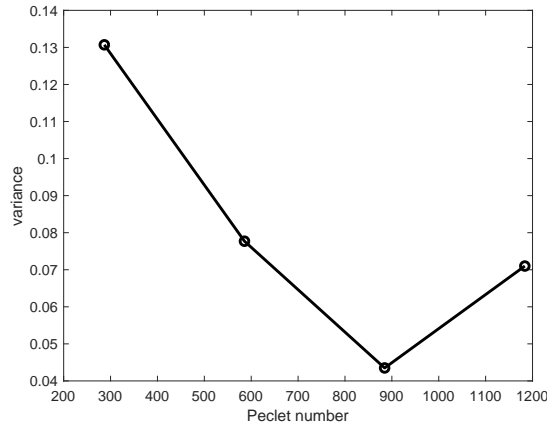


Figure 4.55: **Variance in horizontal component as function of Péclet number:** We run 1000 simulations for different flow rates as given in table 4.1. Flow (a) $T = 800$, (b) $T = 1600$ (c) $T = 3200$, and (d) $T = 4000$. Dots indicate the variance value for four different Péclet numbers Pe at the end time point.

4.5 Conclusion

In this chapter, we have extended the spatial-temporal model that describes cell swimming behaviour in uniform flow and in the channel flow by adding randomness to the cell orientation. In uniform flow where the shear strength is zero, the non-helical swimmers maintain swimming upwards randomly. The helical swimmers also maintain swimming upwards in helical trajectories for small and intermediate rotational diffusion value, but for strong rotational diffusion cells swim in more complicated trajectories. The vertical ensemble average for small and intermediate rotational diffusion are indistinguishable from the mean expected from the deterministic model for both non-helical and helical swimmers within the equilibrium feasibility region. For strong rotational diffusion, the ensemble average of vertical transport diverges from the mean expected from the deterministic model but maintains the expected behaviour of swimming behaviour (upwards or downwards) as expected from the deterministic model. To compare the behaviour of helical swimmers and non-helical swimmers, we presented an example where $\Psi = 0.5$. The helical swimmers ($\Theta = 1$ and $\gamma = \frac{7\pi}{16}$) swim upwards in contrast to the non-helical swimmers.

In the case where the cell orientation is a function of cell position, the variation in the accumulation of non-helical swimmers in the centre of the channel increases as the randomness in the cells orientation increases. In contrast, as the shear strength increases, the variation in the cells distribution across the channel decreases.

For helical swimmers, we have presented two distinct examples of the cells distribution across the channel. The cells may accumulate at the centre of the channel ($\gamma = \frac{\pi}{4}$ and $\Theta = 1$) and the variation of their distribution is similar to the case of non-helical swimmers. They also may accumulate away from the centre. This means they accumulate at the interface where the equilibrium of horizontal component is zero. To show that we consider $\gamma = \frac{7\pi}{16}$ and $\Theta = 1$. In this case the variation in their distribution is measured by considering the distance from horizontal position where $p_x^e = 0$. The variation increases as a function of the randomness in cells orientation while it decreases as the shear strength increases. The variation in the horizontal position as a function of the propulsive torque strength ($\Theta = 0.5 - 1.5$) decreases for weak rotational diffusion ($D_r = 0.1$) and increases for the other values of D_r . In contrast, for $\gamma = \frac{\pi}{4}$ the variation is increasing as the propulsive torque is increased for all values of the rotational diffusion.

To test the stochastic differential equation for non-helical swimmers, we used the data of Croze's experiment. We apply this data on a channel flow while the experiment was developed using a pipe flow. Our results are an approximation to their experiment. We note that when the distribution across the channel attain equilibrium, the variation of the cells across the channel decreases as the Péclet number is increased. This results agrees with their experiment. However the time taken to attain the equilibrium is relatively high compared with the time that the experiment took.

Chapter 5

Conclusions

5.1 Summary of thesis

A deterministic model for gyrotactic helical swimmers where the propulsive force and propulsive torque are not parallel was developed by Bearon [6] based on the alga *Heterosigma akashiwa* where uniform shear flow was assumed. In Chapter 2 we extended the deterministic model to the case where the cell orientation is a function of variable vorticity. Specifically, we considered channel flow where the vorticity depends on cell position. For this, we analyzed the accumulation of the helical swimmers across the channel. We concluded that the helical swimmers may exhibit accumulation away from the center of the channel depending on the strength of the propulsive torque in contrast to the non-helical swimmers that accumulate in the center, as discussed for instance in [10, 32, 64, 65, 82, 83].

However, cells generally swim in random paths. To describe the impact of randomness, Pedley and Kessler [82] proposed a Fokker–Planck equation in two dimensions θ and ϕ in orientation space. This equation describes the orientation distribution for non-helical swimmers. We have extended this equation in Chapter 3 to describe the orientation of helical swimmers in three dimensions in orientation space using Euler angles θ, ϕ, ψ . We also developed stochastic differential equations associated with the Fokker-Planck equations for

both non-helical and helical swimmers. The stochastic differential equations enable us to generate sample trajectories and to quantify the effect of rotational diffusion on the orientation of the cell. For a small value of rotational diffusion, orientation behaviour can be approximated using the deterministic model. For strong rotational diffusion, though, the ensemble averages and the orientation distribution in shear flow is similar to the orientation distribution in still fluid. We also presented two examples where the helical model should reduce to the non-helical model for either $\Theta = 0, \gamma = 0$ or $\Theta = \gamma = 0$. When $\Theta = 0$ and γ varies, the model can be used to describe the orientation of a cell where its swimming direction makes angle γ with the eye spot, for instance. On the other hand when $\gamma = 0$ and Θ varies, the model can be used to describe the orientation of a cell where the propulsive torque and force are parallel.

In Chapter 4 we extended the stochastic differential equation to discuss the spatial-temporal distribution in uniform flow and non-uniform flow. We also presented an example where the translational diffusion, D_t , is too small to affect swimming trajectories; therefore we focus on the randomness in the cell orientation which is described by rotational diffusion, D_r .

In downward uniform shear flow, Bearon [6] showed that helical swimmers may swim either towards down flow regions or up-flow regions depending on the choice of parameters. This is important for microorganisms seeking optimal light conditions for photosynthesis. We extended the model in this case by adding randomness to the cell orientation. For non-helical swimmers, the ensemble average of vertical transport is negative as expected from the deterministic model when the equilibrium of the horizontal component of orientation is feasible, $\Psi \leq 1$. When the shear strength $\Psi > 1$, the cells maintain swimming downwards and for weak and intermediate rotational diffusion, the ensemble average is indistinguishable from the vertical mean predicted from the deterministic model. For strong rotational diffusion the ensemble average of vertical displacement becomes zero. The mean vertical transport for helical swimmers depends on the model parameters. For $\gamma = \frac{\pi}{4}$ and $\Theta = 1$, within the equilibrium feasibility region of the horizontal component of orientation the mean vertical transport is negative

as predicted from the deterministic model. For weak and intermediate rotational diffusion, the ensemble average of vertical transport is negative and for sufficiently strong rotational diffusion the ensemble average is reduced and becomes zero as in the case of non-helical swimmers. Outside the feasibility region, the ensemble average is negative and thus cells maintain swimming downwards. For $\gamma = \frac{7\pi}{16}$ and $\Theta = 1$, on the other hand, within the equilibrium feasibility region of the horizontal component of orientation, the mean vertical transport can be positive as expected from the deterministic model. For weak and intermediate rotational diffusion, the ensemble average of vertical transport is positive and for sufficiently strong rotational diffusion the ensemble average is reduced and becomes zero. Outside the feasibility region, however, the deterministic model predicts that the mean vertical transport is negative and the stochastic model also predicts the ensemble average is negative for weak and intermediate rotational diffusion. For sufficiently strong rotational diffusion the ensemble average is reduced and becomes zero.

When the vorticity is a function of the position of the cell, we extended the model presented in Chapter 2 by adding randomness to the cell orientation where the orientation is expressed in terms of Euler angles. For non-helical swimmers, we noted that as rotational diffusion is increased, the variation in cell position increases. Furthermore, as the shear strength is increased, the variation in cell position decreases. These results are in agreement with the population model given in Bearon et. al. [10] where we express their parameters in terms of our model's parameters. For helical swimmers, as rotational diffusion is increased, the variation in cell position across the channel increases. This is in agreement with the non-helical swimmers. When the shear strength is increased, depending on the accumulation centre relative to the channel centre, the variation in cell position increases (accumulate at the centre of the channel) or decreases (accumulate away from the channel's centre). When the propulsive strength is increased, the variation in cell position increases. We have seen in chapter 2 that the accumulation is entirely dependant on the value of the model's parameters.

We impose the absorbing boundary conditions on cells across the channel for

both deterministic and stochastic model where we assumed that the cells that are initially starts at the walls remain there. These boundary conditions have an impact in calculations of the variation in the cells accumulation across the channel. We have noted that when we ignore the cells which accumulate at the walls the magnitude of the variation decreases.

A summary of key results is provided in Table 5.1.

Table 5.1: Key results of thesis.

Chapter	Key Results	Reference
2	Determining the equilibrium feasibility constraints for helical swimmers.	Equation (2.23).
	Helical swimmers may display the classical accumulation in the centre of the channel or display a new accumulation region away from the centre.	Figures 2.4b-d.
	Deriving ODEs that describe the orientation of helical swimmers in terms of independent Euler angles.	Section 2.4.
3	Deriving a Fokker–Planck equation for helical swimmers and its associated SDE.	Section 3.4.
	Numerical simulations of stochastic differential equations for non-helical and helical swimmers.	Sections 3.3 and 3.5.
4	Extending SDEs to include spatial distribution for non-helical and helical swimmers.	Sections 4.3–4.4.
	Examining spatial distribution in uniform flow and non-uniform flow and make comparison with previous numerical solution and experiments.	Sections 4.3–4.4.

5.2 Discussion

The results presented in thesis are relevant to the studies of bioconvection patterns. Previous studies focussed on the patterns formed by non-helical swimmers at higher volume fraction [58, 59, 83] could be extended to study the pattern form of helical swimmers. The results are relevant to the studies of employing microorganism swimming behaviour in biotechnological applications [12]. For example, phytoplankton can provide different renewable resources of energy [25]. It also relevant to photobioreactors design. For instance, Croze et. al. [32] study the accumulation of non-helical swimmers in air-lift flat bioreactor (vertical channel) where rising bubbles generate flow and provide mixing and aeration.

Attraction of the cells to solid walls plays an important role in biological processes. Li and Tang [74] observed a wall accumulation using kinematic model. Their model was based on the bacterium *C. crescentus*. They found that the cells swim parallel to the solid surface after hitting the surface and Brownian motion then changes the direction of swimming. The combination of swimming parallel to the surface and Brownian motion effect leads to an accumulation at the surface. Kaya and Koser [63] observed that accumulation of *E. coli* near a solid surface was due to the hydrodynamic interactions. They deduce that the local shear rates close to the wall determines the motility mode. Their argument as following: at low shear rates, cells swim in circular trajectories while at high shear rates, cells swim upwards in response to the shear flow. Such response is called rheotaxis [83]. *Chlamydomonas* interact with the surface through flagella contact and leave the walls with an angle that can be determined based on the flagellar wave geometry [46].

Bearon et al [10] used the reflective boundary conditions for position and orientation of the cells at solid boundaries. These boundary conditions are expressed as when a cell is outside the solid boundaries, it is reflected back to be within the domain between the solid boundaries and the cell orientation, θ is replaced by $-\theta$ on encountering a vertical solid boundaries and replaced by

$\pi - \theta$ on encountering horizontal solid walls. In our simulations, the reflective boundary for orientation could be imposed instead of assuming the cells stay at walls when they encounter the wall.

Brumley et. al [23] carried out an experiment using Nikon TE2000-U inverted microscope to record videos and to study the synchronization of the flagella of *Volvox carteri*. This microorganism forms spherical colonies which are composed of many cells. They found that the magnitude and direction of the flow alters during the beating cycle. Furthermore, the force generated by a flagellum varies continuously along the cycle. Wan and Goldstein [107] recently studied the coordination of beating flagella and concluded that not only can hydrodynamic interaction between flagella generate synchrony in unicellular cells such as *Chlamydomonas* but it also depends on the physiology of intracellular coupling of the flagella. It is of interest to study the role of synchronization of flagella in cell locomotion and how this impacts the total propulsive force and torque.

The beating of flagella generate a flow field that can be described in terms of the geometry of force distribution [23]. For one flagellum, the time averaged flow can be determined by the flow at a force point applied at appropriate average location on the flagellum [23]. Drescher et. al. [35] used three Stokeslet model to study the flow field around *Chlamydomonas* cells. In the model, they assign one Stokeslet to each flagellum and one Stokeslet to the cell body. They found that the flow around the cell can be modelled as a puller stresslet at a distance that is approximately seven times the radius of the cell, where the velocity of the fluid is $\leq 1\%$ of the swimming speed. Furthermore, close to the cell, the topology of the flow impacts the flagella and body forces. The time averaged flow field for *Chlamydomonas* is analogous to the three Stokeslet model [35]. This idea of a Stokeslet model can be used to understand and analyse the force that the cell and its flagella have on the fluid flow as we will see in the next section. We assumed for simplicity that the angle between the propulsive force and the propulsive torque is a constant. However, as the cell swims within the field, the flagella-beat pattern generates certain force and torque distribution. This hypothesis is of interest to

investigate the effect of the change in the angle and how this would modify the feasibility of the equilibrium and as a consequence change the spatial -temporal distribution.

Throughout the thesis, we assumed the swimming speed is constant. However, cells can change their instantaneous speed in response to an external field. For instance, bacteria adjust their swimming speed when exposed to a chemical concentration field [106]. Takatori et. al [101] analyzed the variation in swimming speed as a response to an external field such as gravity. This could be extended to investigate the effect of the change in swimming speed on the swimming trajectories for gyrotactic swimmers by expressing the swimming speed as a function of the cell orientation.

We presented a non-dimensional model for helical swimmers where we non-dimensionalize time on gravitational time scale $2B$ and the length on the channel width, L . Consequently the shear strength $\Psi_{max} = \frac{2BU}{L}$ and the propulsive torque strength is $\Theta = 2BR$ where $R = \frac{T}{8\pi\mu a^3}$, T is the dimensional magnitude of propulsive torque and a is the radius of the cell. In the examples we provided, we considered $\Psi_{max} = 2$ and $\Theta = 1$. We can give approximation of dimensional measure of the magnitude of fluid velocity gradient $G = \frac{U}{L}$ and propulsive torque magnitude T by assuming the gravitational time scale $B = 3.4 \text{ s}$ [83]. Therefore $G = 0.1471 \text{ s}^{-1}$ and $T = 0.0013 - 0.0037 \text{ s}$ which can be tested experimentally.

The interaction between cells was neglected in this thesis. Such interaction is crucial for biological processes and the rheological properties of a suspension of microorganisms. For instance, if we consider two cells then the interaction between them affects the flow field close to a cell [70]. This is because the velocity gradient for the first cell interrupts the flow near the second cell. It also impacts the reorientation of the two cells as a result of the gradient velocity of each cell [70]. Such interactions become noticeable when the volume fraction of cells is $\ll 1$ [70]. The interaction between the cells is important in biofilm studies. Biofilm generated by suspension of bacteria or algae is useful in bioreactor design

[72] or producing biofuels [12].

The helical swimmers model leads to some results that can be tested experimentally. For instance the helical swimmers show accumulation away from the center of the channel and the variance in horizontal position across the channel is more than for non-helical swimmers.

5.3 Potential future work

The work presented here can be extended and it opens new avenues for further research. For instances:

1. In this work we assumed spherical cells. This can be developed to include the non-spherical cell. This can be done by considering the swimming direction given by

$$\frac{d\mathbf{p}}{dt} = \frac{1}{2B}(\mathbf{k} - (\mathbf{k} \cdot \mathbf{k})\mathbf{p}) + \frac{1}{2}\boldsymbol{\omega} \wedge \mathbf{p} + \alpha_0 \mathbf{p} \cdot \mathbf{E} \cdot (\mathbf{I} - \mathbf{p}\mathbf{p}) \quad (5.1)$$

where $\mathbf{E} = \frac{1}{2}[\nabla_{\mathbf{x}}\mathbf{V} + (\nabla_{\mathbf{x}}\mathbf{V})^T]$ is the rate of strain and $\alpha_0 = \frac{r^2-1}{r^2+1}$ is the measure of the eccentricity of the spheroid where r is the ratio of polar and equatorial radii [82]. We can investigate the effect of the rate of the strain on the feasibility of the orientation equilibrium and the effect on the helical swimmers behaviour and their accumulation on the channel. It has been shown [10] that for the non-helical swimmer when $\alpha_0 \neq 0$ a more flattened distribution in downward Poiseuille flow is observed compared to the distribution when $\alpha_0 = 0$. Furthermore, Bearon and Hazel [9] observed reduced accumulation at the centre of the channel for slender bacteria.

2. An investigation of how the changing in the angle between the propulsive force and torque could modify the feasibility of the orientation equilibrium and hence the swimming behaviour in uniform flow or the distribution of the

cells across the channel. Farthing et. al. [41] recently demonstrate the use of digital holographic microscopy (DHM) in imaging long flexible flagellum of microorganism *Leishmania mexicana*. This can be done by taking many images and then compare the angle between the propulsive force and torque in each frame to obtain estimate for the angle between them.

3. Investigate the force and the torque that a cell exerts on the fluid. The fluid flow is governed by [77]

$$\begin{aligned}\mu\nabla^2\mathbf{u} - \nabla p + \mathbf{F} &= \mathbf{0} \\ \nabla \cdot \mathbf{u} &= 0,\end{aligned}\tag{5.2}$$

where μ is the viscosity of the flow, \mathbf{u} is the flow velocity, p is the pressure, and \mathbf{F} is the body force acting on the fluid. The force that a cell exerts on the fluid flow is unknown but it can be approximated using the method of regularized stokeslets which is given in [77] and briefly described as following: Consider a one dimensional filament of length L and centreline parametrization $\hat{\mathbf{x}}(s, t)$. The force exerted by the filament is given by [77]

$$\mathbf{F}(\mathbf{x}, t) = \delta(\mathbf{x}, \hat{\mathbf{x}})\mathbf{f}(s, t),\tag{5.3}$$

where $\mathbf{f}(s, t)$ is the force per unit length, and $\delta(\mathbf{x}, \hat{\mathbf{x}})$ is Dirac delta distribution function centered at $\hat{\mathbf{x}}$. The velocity solution corresponding to this fundamental singularity is

$$u_i(\mathbf{x}) = \frac{1}{8\pi\mu} \left(\frac{\delta_{ij}}{r} + \frac{r_i r_j}{r^3} \right) f_j(\hat{\mathbf{x}}) = S_{ij}(\mathbf{x}, \hat{\mathbf{x}}) f_j(\hat{\mathbf{x}}),\tag{5.4}$$

where S_{ij} is the Stokeslet tensor.

To get a regular solution that contains singularity distribution, Cortez [28] developed a regularized Stokeslets method and used in [77] to approximate the unknown stress distribution $\psi_j(\hat{\mathbf{x}}, t)$ and force per unit length distribution $f_j(s, t)$ for each time step including a beat cycle. A regularized Stokeslets is assumed as it is an exact solution for equation (5.2) where \mathbf{F} is now defined as a smooth point-force $\mathbf{F} = \mathbf{f}\psi^\epsilon(\mathbf{x} - \hat{\mathbf{x}})$ where

ψ^ϵ is a truncation function with regularization parameter ϵ [77]. Then the velocity in an infinite domain is defined as

$$u_i = S_{ij}^\epsilon f_j, \quad (5.5)$$

where [28]

$$S_{ij}^\epsilon = \frac{(r^2 + 2\epsilon^2)S_{ij} + r_i r_j}{8\pi r_\epsilon^3}. \quad (5.6)$$

Discretize the flagella to N points and using the no-slip condition at each point and the surface mesh, and using a boundary element constant force discretization, we can obtain an approximation for unknown stress distribution ψ_j and the unknown force f_j [77] by solving $\mathbf{u} = \mathbf{S}^\epsilon \mathbf{f}$ at the collocation point where the Stokeslet is known. Once the force is known, we can calculate the flow at any point in the domain.

Montenegro et. al. [78] used the method to study the shear-thinning rheology effect on squirmer and monoflagellate pushers. They found that the effect on swimmer is extremely delicate to the swimming stroke. Furthermore, the velocity of the squirmer is interrupted by the shear-thinning.

O'Malley and Bees [80] employed the method of regularized Stokeslets coupled with the cell force and torque balance and no-slip boundary condition to obtain approximation of fluid flow around *C. reinhardtii* and their swimming speeds and rotation rates. They also examined the reorientation of gravitactic swimmers resulting from either bottom-heaviness, sedimentation torque or a combination of both mechanisms and found that both torques act accordingly on the cell. Also the beat pattern of flagella in no flow case has the best rates of reorientation.

Recently, Desai and Ardekani [34], proposed an equation for a puller

swimmer based on a stresslet

$$\Sigma^s = Fl\left(\mathbf{p}\mathbf{p} - \frac{1}{3}\mathbf{I}\right), \quad (5.7)$$

where $F = |\mathbf{F}|$, l is the distance between the propulsive force and the drag force which for simplicity can be assumed the diameter of the cell, \mathbf{p} is the swimming direction, and \mathbf{I} is the identity tensor.

Once we know the swimming stress, we can evaluate the torque exerted by the cell using

$$L = \int_S \mathbf{x} \wedge (\Sigma^s \cdot \mathbf{n}) dS \quad (5.8)$$

where \mathbf{x} is the centre of the cell, \mathbf{n} is the cell surface normal vector, and S is the surface area of the cell. This equation can be used to evaluate the propulsive torque \mathbf{n} in equation (1.51).

4. Develop a population model for the helical swimmers. The population model for non-helical swimmers was developed based on the model and results of Frankel and Brenner [43, 44]. For instance, Hill and Bees [56] and Manela and Frankel [75] used the results of Frankel and Brenner to develop Fokker-Planck equation in spatial-temporal space: for three dimensions to describe the physical space, (x, y, z) , and two dimensions to describe the orientation space, (θ, ϕ) . We note that the original model presented [43, 44] was in six dimensions: three dimensions (using Euler angles) to describe the orientation space and three dimensions to describe the physical space. Hill and Bees [56] and Manela and Frankel [75] computed the average swimming velocity and effective diffusion for cells swim in a homogeneous shear. These two quantities are important in the advection-diffusion equation that describes the concentration of cells (see equation 4.1). To obtain these two quantities for helical swimmers, one should use the results of Frankel and Brenner for the full six dimensional problem. Once such quantities are obtained, we can test the advection-diffusion equation against the spatial-temporal results presented in Section 4.4.2 obtained through

simulation of the stochastic differential equation for the spatial–temporal distribution.

Appendix A

Stochastic differential equations

In this appendix we explain the connection between the Fokker-Planck equation and the stochastic differential equation. We also present the Euler-Maruyama method which we use to solve the stochastic differential equation numerically. We lastly give the definition of the expectation of a non-linear stochastic differential equation.

The Fokker-Planck equation for the probability density function $f(x, t)$ of random variable X_t in one dimension is given as [45]

$$\frac{\partial f(x, t)}{\partial t} = -\frac{\partial}{\partial x} [A(x, t)f(x, t)] + \frac{1}{2} \frac{\partial^2}{\partial x^2} [B^2(x, t)f(x, t)], \quad (\text{A.1})$$

where $A(x, t)$ is the drift and $B^2(x, t)$ is the diffusion coefficient respectively. This equation is valid for conditional probability by choosing $f(x, t) = p(x, t|x_0, t_0)$ for any initial x_0, t_0 and with the initial condition

$$p(x, t_0|x_0, t_0) = \delta(x - x_0). \quad (\text{A.2})$$

The associated Ito stochastic differential equation of equation (A.1) is [45]

$$dx(t) = A(x, t)dt + B(x, t)dW(t), t \quad (\text{A.3})$$

where $W(t)$ is Wiener process which has the properties given in the following definition:

Definition 1. [45, 49, 68] *Standard Wiener process (also called Brownian motion) is a stochastic process $W = \{W(t), t \geq 0\}$ which has the following properties*

- 1 $W(0) = 0$.
- 2 $W(t)$ is continuous in t with probability 1.
- 3 *Expectation:* $E[W(t)] = 0$.
- 5 *Independent increments:* for $0 \leq s \leq t \leq T$, the random variable given by the increment $W(t) - W(s)$ is normally distributed with mean zero and variance $t - s$. i.e $W(t) - W(s) \sim \sqrt{t - s}N(0, 1)$.
- 6 *Interpret* $dW(t) = W(t + dt) - W(t)$.

A.1 Connection between Fokker-Planck equation and stochastic differential equation

The Ito's formula, which provides a tool to prove the connection between Fokker-Planck equation and stochastic differential equation, is stated as following [45]:

Theorem 1. *Consider a stochastic quantity $x(t)$ which obeys an Ito stochastic differential equation given by A.3. Then a function $f(x(t))$ obeys the stochastic differential equation*

$$df = \left[\frac{\partial f}{\partial x} A(x, t) + \frac{1}{2} \frac{\partial^2 f}{\partial x^2} B^2(x, t) \right] dt + \frac{\partial f}{\partial x} B(x, t) dW(t). \quad (\text{A.4})$$

The proof of this theorem can be found in [45, 79] for example. We now provide the connection between the Fokker-Planck equation (A.1) and the stochastic differential equation (A.3) which can be found in [45, 97].

A.1. CONNECTION BETWEEN FOKKER-PLANCK EQUATION AND
STOCHASTIC DIFFERENTIAL EQUATION

Let $\phi(x)$ be an arbitrary twice differentiable function. Ito's formula gives

$$d\phi = \frac{\partial\phi}{\partial x}A(x, t) + \frac{1}{2}\frac{\partial^2\phi}{\partial x^2}B^2(x, t)dt + \frac{\partial\phi}{\partial x}B(x, t)dW(t). \quad (\text{A.5})$$

Take the expectation for both side with respect to x and divide by dt

$$\frac{dE[\phi]}{dt} = E\left[\frac{\partial\phi}{\partial x}A(x, t)\right] + \frac{1}{2}E\left[\frac{\partial^2\phi}{\partial x^2}B^2(x, t)\right]. \quad (\text{A.6})$$

Remark that the expectation of the last term on the right is zero following from the definition (1). The left hand side of (A.6) can be written as

$$\frac{dE[\phi]}{dt} = \frac{d}{dt} \int \phi(x)f(x, t)dx = \int \phi(x)\frac{\partial f}{\partial t}dx. \quad (\text{A.7})$$

We use integration by parts to obtain

$$E\left[\frac{\partial\phi}{\partial x}A(x, t)\right] = \int \frac{\partial\phi}{\partial x}A(x, t)f(x, t)dx = - \int \phi\frac{\partial}{\partial x}(A(x, t)f(x, t))dx. \quad (\text{A.8})$$

The second term on the right hand side of (A.6), becomes

$$\begin{aligned} E\left[\frac{\partial^2\phi}{\partial x^2}B^2(x, t)\right] &= \int \frac{\partial^2\phi}{\partial x^2}B^2(x, t)f(x, t)dx = - \int \left(\frac{\partial\phi}{\partial x}\right)\frac{\partial}{\partial x}(B^2(x, t)f(x, t))dx \\ &= \int \phi\frac{\partial^2}{\partial x^2}(B^2(x, t)f(x, t))dx \end{aligned} \quad (\text{A.9})$$

where we use integration by parts twice. Substitute (A.7-A.9) in (A.6) and rearrange to obtain

$$\int \phi(x)\left[\frac{\partial f}{\partial t} - \frac{\partial}{\partial x}(A(x, t)f(x, t)) + \frac{1}{2}\frac{\partial^2}{\partial x^2}(B^2(x, t)f(x, t))\right]dx = 0. \quad (\text{A.10})$$

Therefore

$$\frac{\partial f}{\partial t} = -\frac{\partial}{\partial x}(A(x, t)f(x, t)) + \frac{1}{2}\frac{\partial^2}{\partial x^2}(B^2(x, t)f(x, t)) \quad (\text{A.11})$$

which is Fokker-Planck equation given in A.1.

A.2 Euler–Maruyama method

In analogy to the Euler method for ordinary differential equations, the Euler–Maruyama (EM) method is used to solve stochastic differential equations numerically. This method is explained in the literature, for example [55, 68, 97]. We give a brief overview of the method in this section.

Consider a stochastic differential equation for the random variable X_t

$$dX_t = a(t, X_t)dt + b(t, X_t)dW_t, \quad (\text{A.12})$$

with initial value

$$X_{t_0} = x_0, \quad (\text{A.13})$$

on the time interval $[t_0, T]$. To develop Euler approximation, we discretize the interval $[t_0, T]$

$$t_0 = \tau_0 < \tau_1 < \dots < \tau_n < \dots < \tau_N = T. \quad (\text{A.14})$$

Euler approximation $Y = Y(t), t_0 \leq t \leq T$ satisfies the iterative scheme [68]

$$Y_{n+1} = Y_n + a(\tau_n, Y_n)\Delta_n + b(\tau_n, Y_n)\Delta W_n, \quad (\text{A.15})$$

for $n = 0, 1, \dots, N - 1$ with initial value

$$Y_0 = X_0 = x_0, \quad (\text{A.16})$$

and we denoted $Y(\tau_n)$ by Y_n . The increments Δ_n and ΔW_n are defined as following

$$\Delta_n = \tau_{n+1} - \tau_n, \quad (\text{A.17})$$

$$\Delta W_n = W_{\tau_{n+1}} - W_{\tau_n}, \quad (\text{A.18})$$

for $n = 0, 1, \dots, N - 1$ of Weiner process $W = W(t), t \geq 0$.

To model Brownian motion ΔW_i , we know that ΔW_n are independent Gaussian random variables with mean

$$E[\Delta W_n] = 0, \tag{A.19}$$

and variance

$$E[(\Delta W_n)^2] = \Delta_n. \tag{A.20}$$

We define $N(0, 1)$ to be the standard normal distribution and consider ω_n be a random variable such that $\omega_n \sim N(0, 1)$. Then each random number ΔW_n is computed as

$$\Delta W_n = \sqrt{\Delta_n} \omega_n \tag{A.21}$$

We can summarize Euler approximation in the following algorithm:

For a given time interval $[t_0, T]$ and a positive integer number N

Let $\Delta t = \frac{T}{N}$

- set $Y_0 = X_0 = x_0$.
- For $i = 0$ to $N - 1$
 - simulate $\omega_i \sim N(0, 1)$
 - set

$$\Delta W_i = \sqrt{\Delta t} \omega_i \tag{A.22}$$

$$Y_{i+1} = Y_i + a(i, Y_i) \Delta t + b(i, Y_i) \Delta W_i \tag{A.23}$$

Remark that each set $\{Y_n, n = 0, \dots, N - 1\}$ of Euler method is an approximation realization of the solution $X(t)$ which depends on the random numbers ω_i that are chosen.

Higham [55] provides Matlab codes in one dimension that one can use to generate Brownian motion and more importantly solving stochastic differential equations numerically. Euler-Maruyama method was introduced in Matlab in version R2008a under the solver `simByEuler`.

A.3 Expectation of non-linear stochastic differential equation

Peng [84] and Coquet et. al [27] gave the following definition for non-linear expectation. Consider A be a given set and a vector lattice \mathcal{H} be a linear space of real functions such that if a random variable $X \in \mathcal{H}$ then $|X| \in \mathcal{H}$. The non-linear expectation $\mathbb{E} : \mathcal{H} \rightarrow \mathbb{R}$ has the following properties

- If $X \geq Y$ then $\mathbb{E}[X] \geq \mathbb{E}[Y]$ (monotonicity property).
- $\mathbb{E}[c] = c$ (constant preserving),

where $X, Y \in \mathcal{H}$.

Appendix B

Derivation of stochastic differential equation 4.27

To derive eq.(4.27), we start with the pure (rotational) diffusion equation

$$\frac{\partial P}{\partial t} = D_r \nabla_{\mathbf{p}}^2 P \quad (\text{B.1})$$

where $\nabla_{\mathbf{p}}^2 P$ is Laplace operator given in spherical coordinates

$$D_r \nabla_{\mathbf{p}}^2 P = D_r \left(\frac{1}{\sin \theta} \left(\frac{\partial}{\partial \theta} \sin \theta \frac{\partial}{\partial \theta} \right) + \frac{1}{\sin^2 \theta} \frac{\partial^2}{\partial \phi^2} \right) P, \quad (\text{B.2})$$

where P is the probability density on the surface of unit sphere. Define the probability density F of θ and ϕ coordinates we have [93]

$$F = P \sin \theta, \quad (\text{B.3})$$

subject to integral constraints

$$\int_0^{2\pi} \int_0^\pi F d\theta d\phi = 1, \quad (\text{B.4})$$

we can write the diffusion equation (B.2) in the following standard form [93]

$$\frac{\partial F}{\partial t} = \frac{\partial}{\partial \theta} (D_r \cot \theta F) + \frac{\partial^2}{\partial \theta^2} D_r F + \frac{\partial^2}{\partial \phi^2} \frac{D_r}{\sin^2 \theta} F \quad (\text{B.5})$$

Now we turn attention to the spatial part of equation (4.13), namely

$$\frac{\partial P}{\partial t} + \nabla_{\mathbf{x}} \cdot (\nu \mathbf{p}) P = D_t \nabla_{\mathbf{x}}^2 P. \quad (\text{B.6})$$

The drift term can be written in scalar form as

$$\nabla_{\mathbf{x}} \cdot (\nu \mathbf{p}) P = \left(\frac{\partial}{\partial x} \nu \sin \theta \cos \phi + \frac{\partial}{\partial y} \nu \sin \theta \sin \phi + \frac{\partial}{\partial z} \nu \cos \theta \right) P, \quad (\text{B.7})$$

and the translational diffusion becomes

$$D_t \nabla_{\mathbf{x}}^2 P = D_t \left(\frac{\partial^2}{\partial x^2} + \frac{\partial^2}{\partial y^2} + \frac{\partial^2}{\partial z^2} \right) P \quad (\text{B.8})$$

$$= \left(\frac{\partial^2}{\partial x^2} + \frac{\partial^2}{\partial y^2} + \frac{\partial^2}{\partial z^2} \right) D_t P. \quad (\text{B.9})$$

Remark that we do not need any transformation in this diffusion as it only depends on a constant parameter, and the functions in the drift part are independent of the variable we take the derivative with respect to. So that we can interchange the functions (assume they are constants) with the derivatives. Also, using transformation (B.3), we can write eq.B.7 and eq.B.9 for F

$$\nabla_{\mathbf{x}} \cdot (\nu \mathbf{p}) F = \left(\frac{\partial}{\partial x} \nu \sin \theta \cos \phi + \frac{\partial}{\partial y} \nu \sin \theta \sin \phi + \frac{\partial}{\partial z} \nu \cos \theta \right) F, \quad (\text{B.10})$$

and

$$D_t \nabla_{\mathbf{x}}^2 F = \left(\frac{\partial^2}{\partial x^2} + \frac{\partial^2}{\partial y^2} + \frac{\partial^2}{\partial z^2} \right) D_t F. \quad (\text{B.11})$$

The last two equations are obtained by multiplying through eq B.7 and eq.B.9 by $\sin \theta$ and take in account the above remark.

Substitute (B.5),(B.10), and (B.11) into (4.13), we obtain

$$\begin{aligned}
\frac{\partial F}{\partial t} &= -\left(\frac{\partial}{\partial x}\nu \sin \theta \cos \phi + \frac{\partial}{\partial y}\nu \sin \theta \sin \phi + \frac{\partial}{\partial z}\nu \cos \theta\right)F \\
&+ \left(\frac{\partial^2 D_t}{\partial x^2} + \frac{\partial^2 D_t}{\partial y^2} + \frac{\partial^2 D_t}{\partial z^2}\right)F + \frac{\partial}{\partial \theta}(D_r \cot \theta F) + \frac{\partial^2}{\partial \theta^2}D_r F + \frac{\partial^2}{\partial \phi^2}\frac{D_r}{\sin^2 \theta}F \\
&= -\left(\frac{\partial}{\partial x}\nu \sin \theta \cos \phi + \frac{\partial}{\partial y}\nu \sin \theta \sin \phi + \frac{\partial}{\partial z}\nu \cos \theta\right)F + \frac{\partial}{\partial \theta}(D_r \cot \theta F) \\
&+ \left(\frac{\partial^2 D_t}{\partial x^2} + \frac{\partial^2 D_t}{\partial y^2} + \frac{\partial^2 D_t}{\partial z^2}\right)F + \frac{\partial^2}{\partial \theta^2}D_r F + \frac{\partial^2}{\partial \phi^2}\frac{D_r}{\sin^2 \theta}F. \tag{B.12}
\end{aligned}$$

Comparing with Fokker-Planck equation as given in Gardiner [45], equation (B.12) can be written in the standard Fokker-Planck equation

$$\begin{aligned}
\frac{\partial F}{\partial t} &= -\left(\frac{\partial}{\partial x}\nu \sin \theta \cos \phi + \frac{\partial}{\partial y}\nu \sin \theta \sin \phi + \frac{\partial}{\partial z}\nu \cos \theta + \frac{\partial}{\partial \theta}D_r \cot \theta\right)F \\
&+ \frac{1}{2}\left(\frac{\partial^2 2D_t}{\partial x^2} + \frac{\partial^2 2D_t}{\partial y^2} + \frac{\partial^2 2D_t}{\partial z^2} + \frac{\partial^2}{\partial \theta^2}2D_r + \frac{\partial^2}{\partial \phi^2}\frac{2D_r}{\sin^2 \theta}\right)F, \tag{B.13}
\end{aligned}$$

which can be associated with the following Ito's stochastic differential equation

$$\begin{aligned}
\begin{bmatrix} dx \\ dy \\ dz \\ d\theta \\ d\phi \end{bmatrix} &= \begin{bmatrix} \nu \sin \theta \cos \phi \\ \nu \sin \theta \sin \phi \\ \nu \cos \theta \\ D_r \cot \theta \\ 0 \end{bmatrix} dt + \begin{bmatrix} \sqrt{2D_t} & 0 & 0 & 0 & 0 \\ 0 & \sqrt{2D_t} & 0 & 0 & 0 \\ 0 & 0 & \sqrt{2D_t} & 0 & 0 \\ 0 & 0 & 0 & \sqrt{2D_r} & 0 \\ 0 & 0 & 0 & 0 & \frac{\sqrt{2D_r}}{\sin \theta} \end{bmatrix} \begin{bmatrix} dW_1(t) \\ dW_2(t) \\ dW_3(t) \\ dW_4(t) \\ dW_5(t) \end{bmatrix}. \tag{B.14}
\end{aligned}$$

Appendix C

Additional figures to Chapter 3

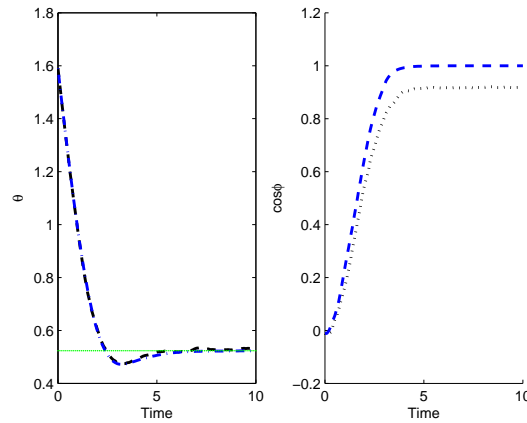


Figure C.1: **Example realizations of the stochastic differential equation for non-helical swimmers in uniform shear flow.** The left panel shows the ensemble average given by Equations (3.13) of solutions of Equation (3.34) and the right panel shows $\cos \langle \phi(t) \rangle$. The blue dashed curves are the average calculated using the deterministic model, and the green line in the left panel is the equilibrium solution for deterministic model. We simulated 1000 cells where we fix $\Psi = 0.5$ and $D_r = 0.01$. Time step is $dt = 0.1$.

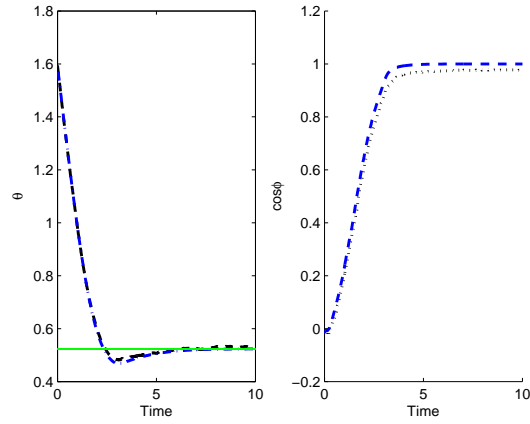


Figure C.2: **Example realizations of the stochastic differential equation for non-helical swimmers in uniform shear flow.** The left panel shows the ensemble average given by Equations (3.13) of solutions of Equation (3.34) and the right panel shows $\cos \langle \phi(t) \rangle$. The blue dashed curves are the average calculated using the deterministic model, and the green line in the left panel is the equilibrium solution for deterministic model. We simulated 1000 cells where we fix $\Psi = 0.5$ and $D_r = 0.01$. Time step is $dt = 0.01$.

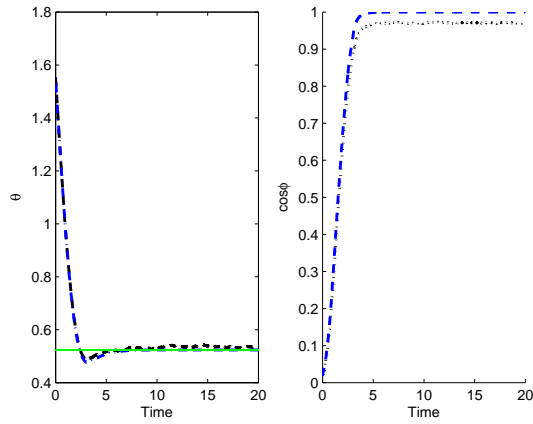


Figure C.3: **Example realizations of the stochastic differential equation for non-helical swimmers in uniform shear flow.** The left panel shows the ensemble average given by Equations (3.13) of solutions of Equation (3.34) and the right panel shows $\cos \langle \phi(t) \rangle$. The blue dashed curves are the average calculated using the deterministic model, and the green line in the left panel is the equilibrium solution for deterministic model. We simulated 1000 cells where we fix $\Psi = 0.5$ and $D_r = 0.01$. Time step is $dt = 0.01$.

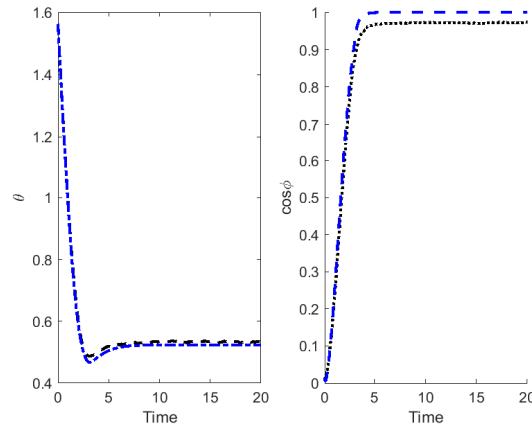


Figure C.4: **Example realizations of the stochastic differential equation for non-helical swimmers in uniform shear flow.** The left panel shows the ensemble average given by Equations (3.13) of solutions of Equation (3.34) and the right panel shows $\cos \langle \phi(t) \rangle$. The blue dashed curves are the average calculated using the deterministic model. We simulated 2000 cells where we fix $\Psi = 0.5$ and $D_r = 0.01$. Time step is $dt = 0.01$.

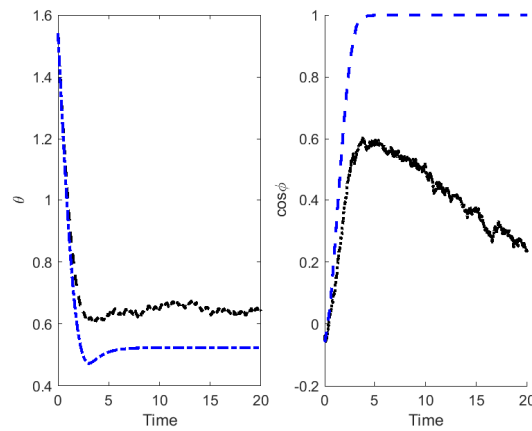


Figure C.5: **Example realizations of the stochastic differential equation for non-helical swimmers in uniform shear flow.** The left panel shows the ensemble average given by Equations (3.13) of solutions of Equation (3.34) and the right panel shows $\cos \langle \phi(t) \rangle$. The blue dashed curves are the average calculated using the deterministic model. We simulated 1000 cells where we fix $\Psi = 0.5$ and $D_r = 0.1$. Time step is $dt = 0.01$.

Appendix D

Additional figures to Chapter 4

D.1 Non-helical swimmers

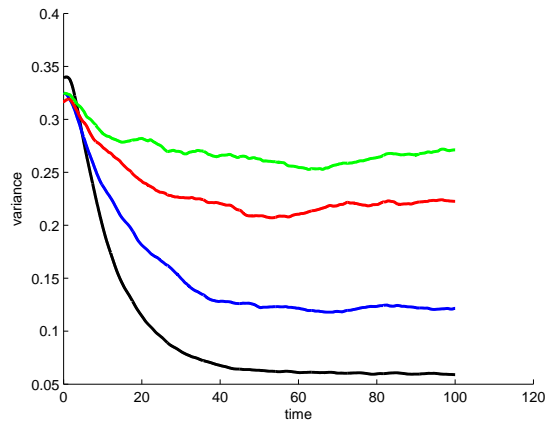


Figure D.1: **Variation in horizontal component of position as function of time:** We run 1000 realization of equation (4.27) with drift term given by (4.44) with initial random horizontal component between the channel walls and with random orientation. Black curve corresponds to $D_r = 0.1$, blue curve corresponds to $D_r = 0.3$, red curve corresponds to $D_r = 0.5$, and green curve corresponds to $D_r = 0.7$. The shear strength is fixed $\Psi_{max} = 0.5$.

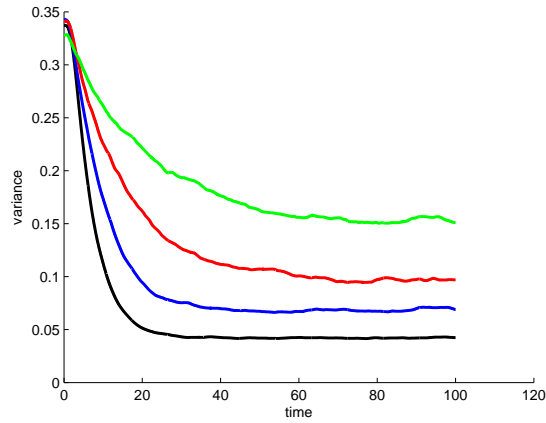


Figure D.2: **Variation in horizontal component of position as function of time:** As of figure D.1 where the shear strength is $\Psi_{max} = 1$.

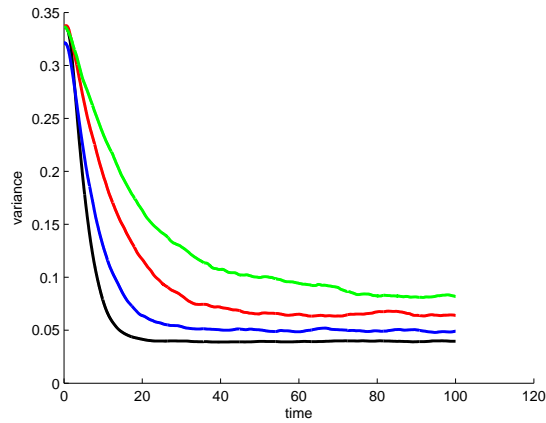


Figure D.3: **Variation in horizontal component of position as function of time:** As of figure D.1 where the shear strength is $\Psi_{max} = 1.5$.

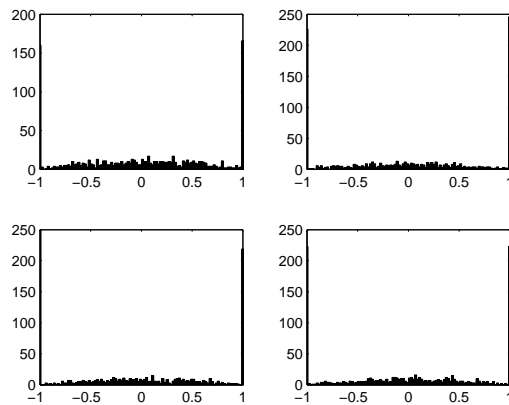


Figure D.4: **Histogram of horizontal position across the channel for stochastic non-helical swimmers:** As of figure 4.29 with shear strength is $\Psi_{max} = 0$.

D.2 Helical swimmers

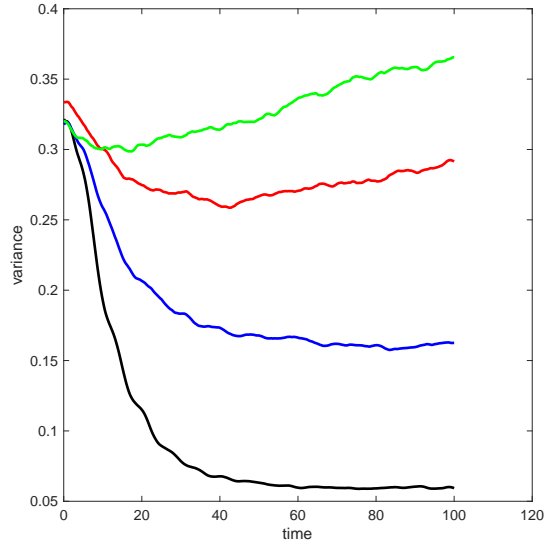


Figure D.5: **variation in horizontal component as function of D_r for helical swimmers:** variance of horizontal component of cell position across the channel. We run 1000 simulations of cells with initial random horizontal component between the channel walls with random orientation. Black line corresponds to $D_r = 0.1$, blue line corresponds to $D_r = 0.3$, red line corresponds to $D_r = 0.5$, and green line corresponds to $D_r = 0.7$. The shear strength is fixed $\Psi_{max} = 0.5$ and propulsive torque strength $\Theta = 1$ for $\gamma = \frac{\pi}{4}$. The variance reach equilibrium over time.

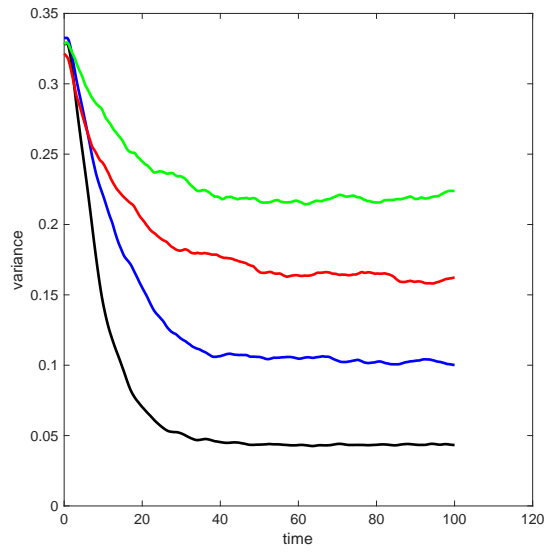


Figure D.6: **variation in horizontal component as function of D_r for helical swimmers:** As of figure D.5 with $\Psi_{max} = 1$.

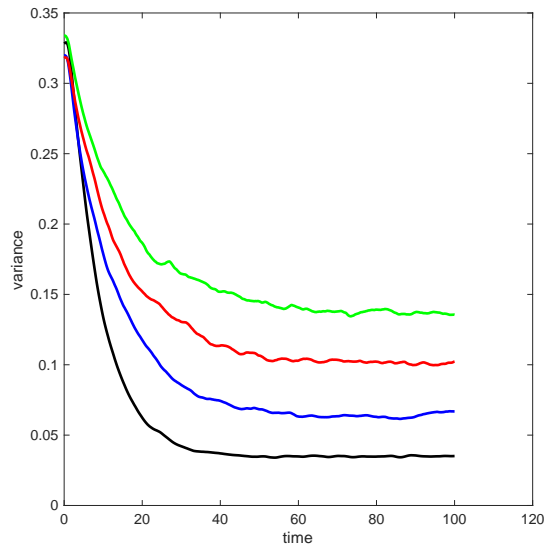


Figure D.7: **variation in horizontal component as function of D_r for helical swimmers:** As of figure D.5 with $\Psi_{max} = 1.5$.

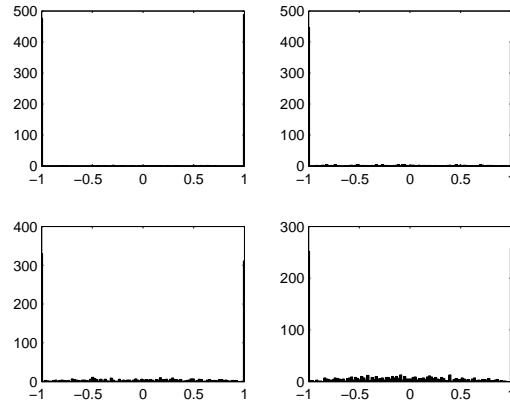


Figure D.8: **Histogram of horizontal position across the channel for stochastic helical swimmers:** (a) $D_r = 0.1$, (b) $D_r = 0.3$ and (c) $D_r = 0.5$ and (d) $D_r = 0.7$. Shear strength is $\Psi_{max} = 2$ and propulsive torque strength $\Theta = 1$ for $\gamma = \frac{7\pi}{16}$ at $t = 100$. Spread measure is shown in figure 4.46. Accumulation at the walls are due to the absorbing boundary conditions. Including cells accumulate at walls. We fix $\Theta = 1$, $\gamma = \frac{7\pi}{16}$ and $\Psi_{max} = 0.5$.

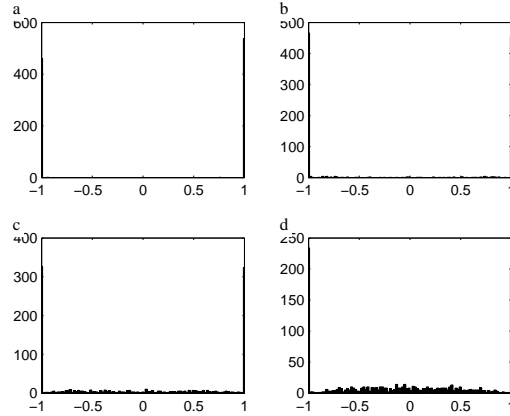


Figure D.9: **Histogram of horizontal position across the channel for stochastic helical swimmers:** As of figure D.8. We fix $\Theta = 1$, $\gamma = \frac{7\pi}{16}$ and $\Psi_{max} = 1$.

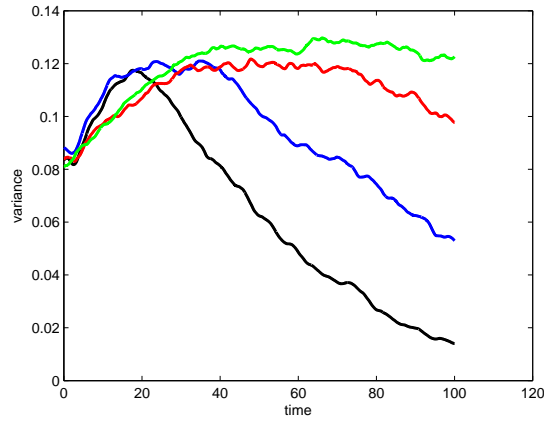


Figure D.10: **variation in horizontal component as function of D_r for helical swimmers:** As of figure 4.30 where we simulate realizations of equation (4.40) with drift given by (4.53). We fix $\Psi = 0.5$, $\Theta = 1$ and $\gamma = \frac{7\pi}{16}$.

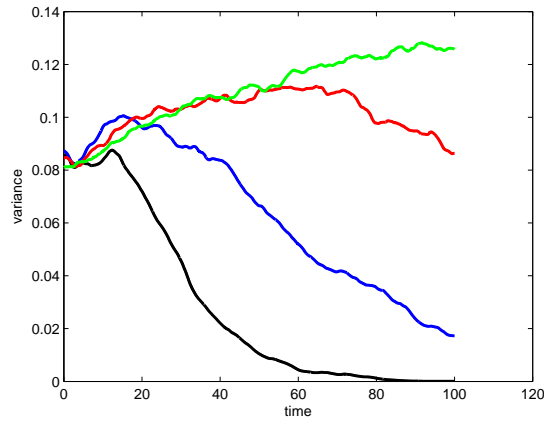


Figure D.11: **variation in horizontal component as function of D_r for helical swimmers:** As of figure 4.30 where we simulate realizations of equation (4.40) with drift given by (4.53). We fix $\Psi = 1$, $\Theta = 1$ and $\gamma = \frac{7\pi}{16}$.

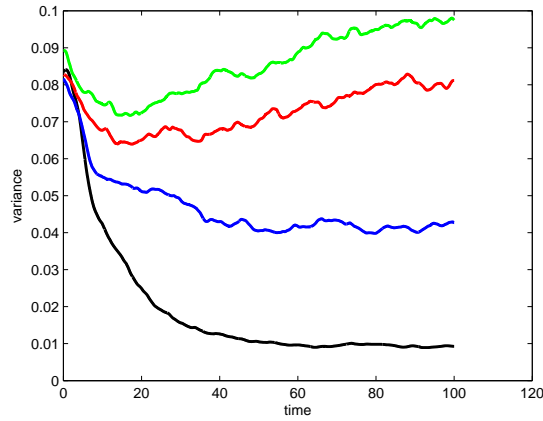


Figure D.12: **variation in horizontal component as function of D_r for helical swimmers:** As of figure 4.30 where we simulate realizations of equation (4.40) with drift given by (4.53). We fix $\Psi = 1.5$, $\Theta = 1$ and $\gamma = \frac{7\pi}{16}$.

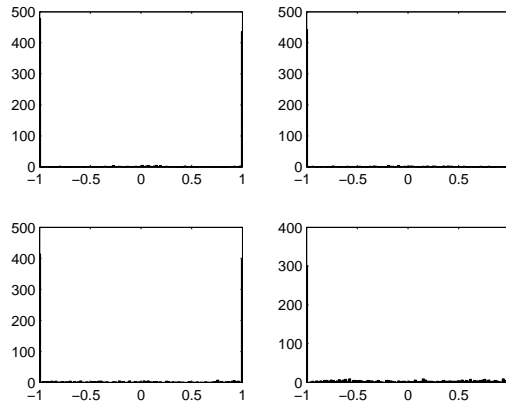


Figure D.13: **Stochastic distribution across the channel for helical swimmers:** (a) $D_r = 0.1$, (b) $D_r = 0.3$ and (c) $D_r = 0.5$ and (d) $D_r = 0.7$. Shear strength is $\Psi_{max} = 2$ and propulsive torque strength $\Theta = 2$ and $\gamma = \frac{7\pi}{16}$. Accumulation at the walls are due to the absorbing boundary conditions.

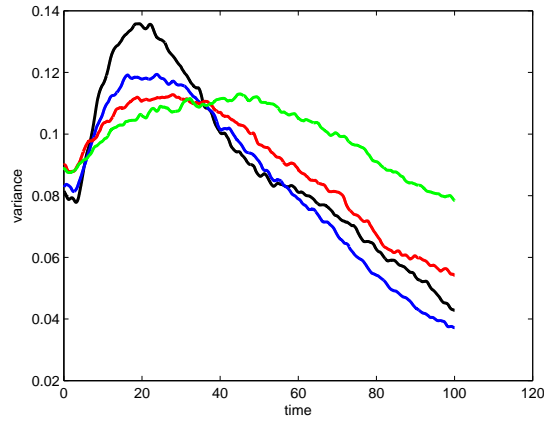


Figure D.14: **Variance over time for helical swimmers:** We run 1000 simulations for 100 time units. We fix $\Psi = 2$, $\Theta = 2$ and $\gamma = \frac{7\pi}{16}$. Green line corresponds to rotational diffusion $D_r = 0.7$, red line corresponds to rotational diffusion $D_r = 0.5$, blue line corresponds to rotational diffusion $D_r = 0.3$, and black line corresponds to rotational diffusion $D_r = 0.1$. $(D_r, \text{var}) = (0.1, 0.0428), (0.3, 0.0372), (0.5, 0.0542), (0.7, 0.0785)$.

Appendix E

Matlab codes

E.1 Matlab codes for Chapter 2

```
% -----  
%% Plot the equilibrium feasibility in Theta-Psi parameteric space  
% -----  
%% ---Clear memory, close figure windows  
clear all  
close all  
f1 = figure('PaperSize',[17.5 25],'PaperPosition',[1 1 16 8]);  
%% Specify fixed parameters  
params.Psi_max=2; %shear strength  
gamma_range=[pi/4,pi/3,7*pi/16];  
Theta_range=[1,1.05,1];  
  
for nplot=1:3  
sph(nplot)=subplot(1,3,nplot);  
params.gamma=gamma_range(nplot);  
params.Theta=Theta_range(nplot);  
  
Psi=[cos(params.gamma):0.01:params.Psi_max];  
Thmin=Psi.*sqrt(1-(cos(params.gamma)./Psi).^2)-sin(params.gamma);
```

```

Thmax=Thmin+2*sin(params.gamma);
plot(Psi,Thmin,Psi,Thmax);
hold on
line([Psi(1), Psi(1)], [Thmin(1),Thmax(1)])

Thzero=Psi./sqrt(1-(cos(params.gamma)./Psi).^2);
%find intersection
index=find(abs(Thmax-Thzero)==min(abs(Thmax-Thzero)));
%plot patch where p_x feasible & less than zero
x=[Psi(1), Psi,fliplr(Psi)];
y = [Thmin(1), Thmax(1:index),Thzero(index+1:end),fliplr(Thmin) ];
patch(x,y,[.3 .3 .3])
%plot patch where p_x feasible & less than zero
x=[Psi(index), Psi(index:end),fliplr(Psi(index:end))];
y = [Thmax(index), Thmax(index:end),fliplr(Thzero(index:end)) ];
patch(x,y,[.8 .8 .8])

h=line([0,params.Psi_max],[params.Theta,params.Theta]);
set(h,'LineWidth',2,'Color','k')
axis([0,params.Psi_max,0,params.Psi_max])
xlabel('\Psi');
ylabel('\Theta');
end

```

```

% -----
%% Plot average of p_x
% -----
%% ---Clear memory, close figure windows
clear all
close all
%% -----

```

```
xaxismin=-0.1;
xaxismax=2.1;

f1 = figure('PaperSize',[17.5 25],'PaperPosition',[1 1 16 16]);
%% -----
m=2; n=2;

load('Mean_px.mat')

h(1)=subplot(m,n,1);
plot(Psi_range,average_px(1,:), 'k*');
xlabel('\Psi')
ylabel('\bar p_x$', 'interpreter', 'latex');
hold on

hold all

%%calculat the px average when Theta=0
y=[1:0.01:xaxismax];
px_bar=y-sqrt(y.^2-1);
plot(y,px_bar,'Linewidth',1.5,'color','k');
y=[xaxismin:0.01:1];
px_bar=y;
plot(y,px_bar,'Linewidth',1.5,'color','k');

plot([0,0],[-0.5,1], 'color','k','Linestyle','--')
plot([1,1],[-0.5,1], 'color','k','Linestyle','--')
axis([xaxismin,xaxismax,-0.5,1])

%% -----

for nplot=2:4
```

```
params.Theta=Theta_range(nplot);
params.gamma=Gamma_range(nplot);

h(nplot)=subplot(m,n,nplot);
plot(Psi_range,average_px(nplot,:),'k*');
xlabel('\Psi')
ylabel('$\bar{p}_x$', 'interpreter', 'latex');
hold on
if params.Psi>cos(params.gamma)
Psimin=sqrt(params.Theta^2-2*params.Theta*sin(params.gamma)+1);
Psimax=sqrt(params.Theta^2+2*params.Theta*sin(params.gamma)+1);
xmin=Psimin/params.Psimax;
xmax=Psimax/params.Psimax;

plot([Psimin,Psimin],[-0.5,1], 'color', 'k', 'Linestyle', '--')
plot([Psimax,Psimax],[-0.5,1], 'color', 'k', 'Linestyle', '--')

z=[Psimin:0.01:Psimax];
pxe=z-params.Theta*sqrt(1-(cos(params.gamma)./z).^2);
plot(z,pxe, 'Linewidth', 1.5, 'color', 'k');
end
y=[xaxismin:0.01:Psimin];
px_bar=y;
plot(y,px_bar, 'Linewidth', 1, 'color', [0.5 0.5 0.5]);
axis([xaxismin,xaxismax,-0.5,1])
end

return
```

```
% -----
% Simulation to loop over variable parameters
% and output mean values
% it generate mat file for average p_x
% -----
%% ---Clear memory, close figure windows
```

```

clear all
close all
%% Specify fixed parameters
params.Psimax = 2; %vorticity
params.v =0.1;    %swimming speed; non-dimensionalise speed on this
params.t0 = 0;    % start time of simulation
params.tend = 100; % end time
params.dt =0.1;
params.sim = 100; %number simulation
%% Specify parameter ranges for variable parameters
Psi_range = [0:0.1:2];
Theta_range=[0,1,1,1.05];
Gamma_range=[pi/4,pi/4,7*pi/16,pi/3];
average_px=zeros(4,length(Psi_range));
%% Loop over parameter sets

for nplot=1:4
params.Theta=Theta_range(nplot);
params.gamma=Gamma_range(nplot);
%% Loop over different Psi values
for i=1:length(Psi_range)
params.Psi=Psi_range(i);
mean_px=zeros(1,params.sim);

%loop over the 100 simulations
for nsim=1:params.sim
params.x0=0;
params.y0=0;
params.z0=0;
[params.theta_p0,params.phi_p0,params.theta_n0,params.phi_n0]= generate_initial_orientation(params);
mean_px(nsim)=calc_vert_transport(params);
end
average_px(nplot,i)=mean(mean_px);
end
subplot(2,2,nplot)
plot(Psi_range,average_px(nplot,:))
end
fname=['Mean_px.mat'];
save(fname)

```

```

function [th_p,ph_p,th_n,ph_n]=generate_initial_orientation(params)
% -----
%% generate random initial condition such that p.n=cos(gamma)
%randomly choose p direction uniformly on sphere

```

```

% -----
ph_p=2*pi*rand(1);
z=2*rand(1)-1;
th_p=acos(z);
[p_vec(1),p_vec(2),p_vec(3)]=sph2cart(ph_p ,pi/2-th_p,1);

%construct random unit vector, q, perpendicular to p
vtemp=2*rand(1,3)-1;
q=cross(vtemp,p_vec);
q=q./norm(q);

%constuct n vector by rotating p by angle gamma around axis q using
%Rodrigues formula

n_vec=p_vec*cos(params.gamma)+cross(q,p_vec)*sin(params.gamma)...
+q*(dot(q,p_vec))*(1-cos(params.gamma));
[TH,PHI,Psi] = cart2sph(n_vec(1),n_vec(2),n_vec(3));
ph_n=TH;
th_n=pi/2-PHI;

end

```

```

function mean_px = calc_vert_transport(params)
% -----
% calculate mean p_x
% -----
%%Specify initial conditions
% cell position
y0(1) = params.x0;
y0(2) = params.y0;
y0(3) = params.z0;
%swimming direction specified by theta_p, phi_p

```

```
y0(4)=params.theta_p0;
y0(5)=params.phi_p0;
%intrinsic torque direction specified by theta_n, phi_n
y0(6)=params.theta_n0 ;
y0(7)=params.phi_n0;
%% ----- Run simulation ----- %
tspan = [params.t0:params.dt:params.tend];

%solve differential equations specified by function p_n_model
options = [];
[T,Y]=ode45(@p_n_model,tspan,y0,options,params);

px=sin(Y(:,4)).*cos(Y(:,5));
mean_px=mean(px);
end
```

```
function dydt=p_n_model(t,y,p)
% -----
%function specifying differential equations
% -----
xpos = y(1);
ypos = y(2);
zpos = y(3);
theta_p = y(4);
phi_p = y(5);
theta_n = y(6);
phi_n = y (7);

%parameters
Psi=p.Psi;
v=p.v;
%omega=p.omega;
```

```
ux=0;
uy=0;
uz=-Psi*xpos;

%
dydt=[...
ux+v*cos(phi_p)*sin(theta_p)%dx/dt
uy+v*sin(phi_p)*sin(theta_p)%dy/dt
uz+v*cos(theta_p)%dz/dt
theta_dot(phi_p,theta_n,phi_n,theta_p,phi_p,p) % dtheta_p/dt
phi_dot(theta_p,phi_p,theta_n,phi_n,theta_p,phi_p,p); %dphi_p/dt
theta_dot(phi_n,theta_n,phi_n,theta_p,phi_p,p) % dtheta_n/dt
phi_dot(theta_n,phi_n,theta_n,phi_n,theta_p,phi_p,p); %dphi_n/dt
];

function soln=theta_dot(phi_u,theta_n,phi_n,theta_p,phi_p,p)
%parameters
Theta=p.Theta;
Psi=p.Psi;

soln=-sin(theta_p)*cos(phi_p-phi_u)...
+Theta*sin(theta_n)*sin(phi_n-phi_u)...
+Psi*cos(phi_u);

function soln=phi_dot(theta_u,phi_u,theta_n,phi_n,theta_p,phi_p,p)
%parameters
Theta=p.Theta;
Psi=p.Psi;

soln=(...
(cos(theta_u)*sin(theta_p)*sin(phi_u-phi_p))...
-Theta*(sin(theta_n)*cos(theta_u)*cos(phi_n-phi_u)-cos(theta_n)*sin(theta_u))...
+Psi*sin(phi_u));
```

```
-Psi*cos(theta_u)*sin(phi_u)...
)./sin(theta_u);
```

```
% -----
% Plot example trajectories in weak vertical shear
% for non-helical and helical swimmers (Figure 2.4)
% -----
%% ---Clear memory, close figure windows
clear all
close all

f1 = figure('PaperSize',[17.5 25],'PaperPosition',[1 1 16 23]);
%% Specify fixed parameters
params.v = 0.1; %swimming speed
params.t0 = 0; % start time of simulation
params.tend = 20; % end time
params.dt = 0.01;
params.sim = 5; %number of simulations
params.m=1; params.n=4; %subplot
%% Specify parameter ranges for variable parameters
Theta_range=[0,1,1,1.05];
Gamma_range=[pi/4,pi/4,7*pi/16,pi/3];
Psimax_range=[2,2,2,1];

for nplot=1:4
params.Theta=Theta_range(nplot);
params.gamma=Gamma_range(nplot);
params.Psi_max=Psimax_range(nplot);

%loop over the params.simsimulations
for nsim=1:params.sim

%take random initial orientation
[params.theta_p0,params.phi_p0,params.theta_n0,params.phi_n0]=generate_initial_orientation(params);

%%specify random initial positions
params.x0=rand(1);
params.y0=rand(1);
params.z0=rand(1);

[T,Y] =calc_trajectory(params);

index=find(Y(:,1)>1);
```

```

for in=index
Y(in,1)=1;
end

index=find(Y(:,1)<-1);
for in=index
Y(in,1)=-1;
end

sph(nplot)=subplot(params.m,params.n,nplot);

plot(Y(:,1),Y(:,3))
xlabel('x')
ylabel('z')
grid on
hold on
hold all
end
end

```

```

function [T,Y] = calc_trajectory(params)
% -----
% Calculate vertical transport
% -----
%%Specify initial conditions
% cell initially away from the origin
y0(1) = params.x0;
y0(2)=params.y0;
y0(3)=params.z0;
%swimming direction specified by theta_p, phi_p
y0(4)=params.theta_p0;
y0(5)=params.phi_p0;
%intrinsic torque direction specified by theta_n, phi_n
y0(6)=params.theta_n0 ;
y0(7)=params.phi_n0;

%% ----- Run simulation ----- %
tspan = [params.t0:params.dt:params.tend];

```

```
%solve differential equations specified by function p_n_model
options = [];
[T,Y]=ode45(@p_n_poiseuille_model,tspan,y0,options,params);
```

```
function dydt=p_n_poiseuille_model(t,y,p)
% -----
% Function specifying differential equation
% -----

xpos = y(1);
ypos = y(2);
zpos = y(3);
theta_p = y(4);
phi_p = y(5);
theta_n = y(6);
phi_n = y (7);

%parameters
v=p.v;
%Fix this with correct flow field
ux=0;
uy=0;

%ensure no vertical advection when outside pipe
if abs(xpos)<1
uz=p.Psi_max*(xpos^2-1);    %Poiseuille flow
p.Psi=-p.Psi_max*xpos;
else
uz=0;
p.Psi=0;
end
```

```

%-----
%
dydt=[...
ux+v*cos(phi_p)*sin(theta_p)%dx/dt
uy+v*sin(phi_p)*sin(theta_p)%dy/dt
uz+v*cos(theta_p)%dz/dt
theta_dot(phi_p,theta_n,phi_n,theta_p,phi_p,p) % dtheta_p/dt
phi_dot(theta_p,phi_p,theta_n,phi_n,theta_p,phi_p,p) %dphi_p/dt
theta_dot(phi_n,theta_n,phi_n,theta_p,phi_p,p) % dtheta_n/dt
phi_dot(theta_n,phi_n,theta_n,phi_n,theta_p,phi_p,p) %dphi_n/dt
];

function soln=theta_dot(phi_u,theta_n,phi_n,theta_p,phi_p,p)
%parameters
Theta=p.Theta;
Psi=p.Psi;

soln=-sin(theta_p)*cos(phi_p-phi_u)...
+Theta*sin(theta_n)*sin(phi_n-phi_u)...
+Psi*cos(phi_u);

function soln=phi_dot(theta_u,phi_u,theta_n,phi_n,theta_p,phi_p,p)
%parameters
Theta=p.Theta;
Psi=p.Psi;

soln=(...
(cos(theta_u)*sin(theta_p)*sin(phi_u-phi_p))...
-Theta*(sin(theta_n)*cos(theta_u)*cos(phi_n-phi_u)-cos(theta_n)*sin(theta_u))...
-Psi*cos(theta_u)*sin(phi_u)...
)./sin(theta_u);

```

```
% -----  
% Plotting figure 5  
% histograms of final position  
% -----  
%% ---Clear memory, close figure windows  
clear all  
close all  
  
fname=['final_horizontal_pos.mat'];  
load(fname)  
  
f1 = figure('PaperSize',[17.5 25],'PaperPosition',[1 1 16 16]);  
%% Loop over parameter sets  
bincentre=linspace(-1,1);  
  
for nplot=1:4  
sph(nplot)=subplot(2,2,nplot);  
if nplot==4  
  
for nsim=1:params.sim  
x0(nsim)=2*(nsim/params.sim)-1;  
end  
  
index=find(abs(x0)<0.61);  
H1=hist(horpos(nplot,index),bincentre);  
index=find(abs(x0)>0.61);  
H2=hist(horpos(nplot,index),bincentre);  
bar(bincentre,[H1' H2'],1,'stacked');  
mymap=[[0,0,0];[0.6,0.6,0.6]];  
colormap(mymap)  
else
```

```

hist(horpos(nplot,:),bincentre);
end
set(gca,'xlim',[-1, 1])
end

```

```

% -----
% Simulation to loop over variable parameters
% and generate mat file to plot histogram
% -----
%% ---Clear memory, close figure windows
clear all
close all

set(0,'defaultaxesfontname','Arial')
set(0,'defaulttextfontname','Arial')
set(0,'defaulttextfontsize',10)
set(0,'defaultlinelinewidth',1)

f1 = figure('PaperSize',[17.5 25],'PaperPosition',[1 1 16 23]);
%% Specify fixed parameters
params.v = 0.1;    %swimming speed; non-dimensionalise speed on this
params.t0 = 0;    % start time of simulation
params.tend = 100; % end time
params.dt = 0.1;
params.sim = 100000; %number of simulation
%% Specify parameter ranges for variable parameters

Theta_range=[0,1,1,1.05];
Gamma_range=[pi/4,pi/4,7*pi/16,pi/3];
Psimax_range=[2,2,2,1];
%% Loop over parameter sets
horpos=zeros(4, params.sim);

for nplot=1:4
params.Theta=Theta_range(nplot);
params.gamma=Gamma_range(nplot);
params.Psi_max=Psimax_range(nplot);
%loop over the params.simsimulations
for nsim=1:params.sim
params.x0=2*(nsim/params.sim)-1;
params.y0=0;
params.z0=0;
[params.theta_p0,params.phi_p0,params.theta_n0,params.phi_n0]=generate_initial_orientation(params);

```

```
horpos(nplot,nsim)=calc_final_horizontal_pos(params);

end

sph(nplot)=subplot(2,2,nplot);
hist(horpos(nplot,:))
set(gca,'xlim',[-1, 1])
end

fname=['final_horizontal_pos.mat'];
save(fname)
```

```
function horpos= calc_final_horizontal_pos(params)
% -----
% Calculate vertical transport
% -----
%%Specify initial conditions
% cell position
y0(1) =params.x0;
y0(2) = params.y0;
y0(3) = params.z0;
%swimming direction specified by theta_p, phi_p
y0(4)=params.theta_p0;
y0(5)=params.phi_p0;
%intrinsic torque direction specified by theta_n, phi_n
y0(6)=params.theta_n0 ;
y0(7)=params.phi_n0;
%% ----- Run simulation ----- %
tspan = [params.t0:params.dt:params.tend];
%solve differential equations specified by function p_n_poiseuille_model
options = [];
[T,Y]=ode45(@p_n_poiseuille_model,tspan,y0,options,params);

horpos=Y(end,1);
end
```

E.2 Matlab codes for Chapter 3

Simulations in this chapter are similar. The difference between them is the values considered for the parameters, duration of simulation, or the time step. We present Matlab code examples for each section in this chapter.

Matlab codes to simulate and plot random walks on sphere

```
% -----  
% Plot example trajectories and ensemble averages for  
% random walk on sphere  
% -----  
  
%% ---Clear memory, close figure windows  
clear all  
close all  
%% -----  
%load mat file  
fname=['Random_walk_RD1_dt0,01_nperiods10000_sim5000.mat'];  
load(fname)  
  
f1 = figure('PaperSize',[17.5 25],'PaperPosition',[1 1 16 16]);  
%% -----  
% comput the mean over all time points  
for tp = 1:length(T)  
theta_stoch=pi-abs(pi-(mod(S(tp,1,:),2*pi)));  
phi_stoch=2*pi-abs(2*pi-mod(S(tp,2,:),2*pi));  
calc_mean_theta(tp)=mean(theta_stoch);  
calc_mean_phi(tp)=mean(phi_stoch);  
end
```

```
%% -----  
figure(1)  
subplot(1,2,1)  
plot (T,calc_mean_theta,'k','linewidth',2);  
hold on  
plot (T,calc_mean_phi,'b','linewidth',2);  
subplot(1,2,2)  
% First random walk  
Wx=sin(theta_ss(:,1)).*cos(phi_ss(:,1));%  
Wy=sin(theta_ss(:,1)).*sin(phi_ss(:,1));  
Wz=cos(theta_ss(:,1));  
W_vec=[Wx;Wy;Wz];  
% Second random walk  
Wx2=sin(theta_ss(:,2)).*cos(phi_ss(:,2));  
Wy2=sin(theta_ss(:,2)).*sin(phi_ss(:,2));  
Wz2=cos(theta_ss(:,2));  
W2_vec=[Wx2;Wy2;Wz2];  
% Third random walk  
Wx3=sin(theta_ss(:,3)).*cos(phi_ss(:,3));  
Wy3=sin(theta_ss(:,3)).*sin(phi_ss(:,3));  
Wz3=cos(theta_ss(:,3));  
W3_vec=[Wx3;Wy3;Wz3];  
% plot  
Npts=100;  
sphere  
hold on  
plot3(Wx(1:Npts),Wy(1:Npts),Wz(1:Npts),'color','b')%  
hold on  
plot3(Wx(1),Wy(1),Wz(1),'b.','MarkerSize',10)%  
plot3(Wx2(1:Npts),Wy2(1:Npts),Wz2(1:Npts),'color','r')%  
hold on  
plot3(Wx3(1:Npts),Wy3(1:Npts),Wz3(1:Npts),'color','g')%  
hold on
```

```
axis equal
grid on
%% -----
% px
theta_S=theta_ss;
phi_S=phi_ss;
px_stcoh=sin(theta_S).*cos(phi_S);
% compute mean over sim
mean_px_stoch=mean(px_stcoh,2);
figure(2)
hold on
plot (T,px_stcoh(:,1:3),'linewidth',2);
hold on
plot (T,mean_px_stoch,'k','linewidth',2);
xlabel('Time')
ylabel('$p_x$', 'interpreter', 'latex');
hold off
%% -----
% plot histogram
binCenters=linspace(0,pi);
theta_mod2p=pi-abs(pi-(mod(theta_s,2*pi)));
binCount= histc(theta_mod2p,binCenters);
probScale = sum(binCount)*pi/100;
hold on
hold all
x = binCenters;
% distribution function
y=(1./2).*sin(x);
%%-----
binCenters_phi=linspace(0,2*pi);
phi_mod2p=2*pi-abs(2*pi-(mod(phi_s,2*pi)));
binCount_phi= histc(phi_mod2p,binCenters_phi);
probScale_phi= sum(binCount_phi)*2*pi/100;
hold on
```

```
x_phi = binCenters_phi;

figure(3)
subplot(1,2,1)
histHandle = bar(binCenters,binCount/probScale,'hist');
hold on
plot(x,y,'r-','linewidth',2);
xlim([0 pi]);
xlabel('\theta');

subplot(1,2,2)
histHandle = bar(binCenters_phi,binCount_phi/probScale_phi,'hist');
pd1 = makedist('Uniform','lower',0,'upper',2*pi);
pdf1 = pdf(pd1,x_phi);
hold on
stairs(x_phi,pdf1,'r','LineWidth',2);
xlim([0 2*pi]);
xlabel('\phi');
```

```
% -----
% Simulation to generate mat file for random walk on sphere
% SDE solved using simByEuler
% -----
%% ---Clear memory, close figure windows
clear all
close all
%% Specify fixed parameters
params.t0= 0;           % start time of simulation
params.dt =0.01;       % time increment
params.RD=1;           % rotational diffusion
nPeriods=1000;        % number of simulated observations
params.tend = nPeriods*params.dt ;   % end time
```

```

params.nsim=5000;                % number of simulations
%% preallocate of stochastic matrix S and its column vectors theta and phi
S = zeros(1001,2,params.nsim);%preallocate S
theta_s=zeros(1,params.nsim);
phi_s=zeros(1,params.nsim);
theta_stoch=zeros(nPeriods+1,1,params.nsim);
phi_stoch=zeros(nPeriods+1,1,params.nsim);
%% Simulation
for k = 1:params.nsim
params.theta0=pi*rand(1);
params.phi0=2*pi*rand(1);
% stochastic model -----
RWS=Random_walk_sphere(params);
[S(:, :, k), T]=simByEuler(RWS, nPeriods, 'DeltaTime', params.dt);
theta_stoch(:)=pi-abs(pi-(mod(S(:, 1, :), 2*pi)));
phi_stoch(:)=2*pi-abs(2*pi-mod(S(:, 2, :), 2*pi));
theta_s(:)=S(end, 1, :);
phi_s(:)=S(end, 2, :);
end
%% to be used in evaluating mean_px
theta_ss=squeeze(theta_stoch);
phi_ss=squeeze(phi_stoch);
%-----
mean_theta_stoch = mean(squeeze(theta_stoch), 2);
mean_phi_stoch = mean(squeeze(phi_stoch), 2);
%% -----
% save file
fname=['Random_walk_RD1_dt0,01_nperiods10000_sim5000.mat'];
save(fname)

```

```

% -----
%% Random Walk on sphere

```

```

% SDE in 2D solved using simByEuler
% -----
function RWS=Random_walk_sphere(params)

%p(1)=theta;
%p(2)=phi;

% Drift term
F = @(t,p)[params.RD.*cot(p(1));...
0];

%Diffusion term
G=@(t,p)[sqrt(2.*params.RD) 0 ;...
0 sqrt(2.*params.RD)./sin(p(1)) ];

RWS = sde(F,G,'StartState', [params.theta0;params.phi0], 'StartTime',params.t0);
end

```

Matlab codes to simulate and plot ensemble averages using SDE and mean of orientation angles using the deterministic model for non-helical swimmers.

```

% -----
% Plotting ensembl averages and histogram for nonhelical swimmers
% -----
%% ---Clear memory, close figure windows
clear all
close all
%% -----
% still fluid Psi=0, mat file is
fname=['Nonhelical_still_fluid_Dr0,01.mat'];
load(fname)
f1 = figure('PaperSize',[17.5 25], 'PaperPosition',[1 1 16 16]);

```

```

%% -----
for tp = 1:length(T)
theta_stoch=pi-abs(pi-(mod(S(tp,4,:),2*pi)));
phi_stoch=2*pi-abs(2*pi-mod(S(tp,5,:),2*pi));
calc_mean_theta(tp)=mean(theta_stoch);
calc_mean_phi(tp)=mean(phi_stoch);
end
%% -----
% Plot the average of simulation, deterministic \theta, drift term for
theta_DET=mean_theta_D_old;%from ODE no spurious term
phi_DET=mean_phi_D_old;%from ODE no spurious term
stoch_theta_av=mean(calc_mean_theta);% form SDE
stoch_phi_av=mean(calc_mean_phi); % form SDE
%plot theta and phi
theta_eq=asin(0.5);
phi_eq=0;
figure(1)
subplot(1,2,1)
plot(T,theta_ss(:,1:3),'linewidth',1)
hold on
plot (T,calc_mean_theta,'k','linewidth',2);
hold on
plot (T,theta_DET,'b--','linewidth',2);
xlabel('Time')
ylabel('\theta')
subplot(1,2,2)
plot(T,phi_ss(:,1:3),'linewidth',1)
hold on
plot (T,calc_mean_phi,'k','linewidth',1);
hold on
plot (T,phi_DET,'b--','linewidth',2);
xlabel('Time')
ylabel('\phi')
%% -----

```

```
% px
theta_S=theta_ss;% compute average wrt sim
phi_S=phi_ss; % compute average wrt sim
theta_D=theta_dd_old;%from ODE
phi_D=phi_dd_old;%from ODE
px_stcoh=sin(theta_S).*cos(phi_S);
px_det=sin(theta_D).*cos(phi_D);
% compute mean over sim
mean_px_stoch=mean(px_stcoh,2);
mean_px_det=mean(px_det,2);
px_av=mean(mean_px_stoch);

figure(2)
hold on
plot (T,px_stcoh(:,1:3),'linewidth',2);
hold on
plot (T,mean_px_stoch,'k-.','linewidth',2);
hold on
plot (T,mean_px_det,'b--','linewidth',2);
xlabel('Time')
ylabel('$\bar{p}_x$', 'interpreter', 'latex');
hold off

%% -----
% histograms
binCenters=linspace(0,pi);
theta_mod2p=pi-abs(pi-(mod(theta_s,2*pi)));
binCount= histc(theta_mod2p,binCenters);
probScale= sum(binCount)*pi/100;
hold on;
hold all
x = binCenters;
% Fisher distribution in case of no flow with gravitational bias
lambda=1/params.RD;
```

```

y=sin(x)*(lambda/(2.*sinh(lambda))).*exp(lambda.*cos(x));
%-----
binCenters_phi=linspace(0,2*pi);
phi_mod2p=2*pi-abs(2*pi-(mod(phi_s,2*pi)));
binCount_phi= histc(phi_mod2p,binCenters_phi);
probScale_phi= sum(binCount_phi)*2*pi/100;
hold on
%uniform distribution function
pd1 = makedist('Uniform','lower',0,'upper',2*pi);
x_phi = binCenters_phi;
pdf1 = pdf(pd1,x_phi);

figure(3)
subplot(1,2,1)%theta
histHandle = bar(binCenters,binCount/probScale,'hist');
hold on
plot(x,y,'r-','linewidth',2);%do not plot in case of shear flow
xlim([0 pi]);
xlabel('\theta');
subplot(1,2,2)%phi
histHandle = bar(binCenters_phi,binCount_phi/probScale_phi,'hist');
pd1 = makedist('Uniform','lower',0,'upper',2*pi);
hold on
stairs(x_phi,pdf1,'r','LineWidth',2);
xlim([0 2*pi]);
xlabel('\phi');

```

```

% -----
% Simulation to generate mat file for orientation of
% non-helical swimmers in still fluid and shear flow
% the same simulation can be done in still fluid or shear flow
% by modifying the parameters values in each case

```

```
% SDE solved using simByEuler
% ODE solved using ode45
% -----

%% ---Clear memory, close figure windows
clear all
close all
%% -----

%% Specify fixed parameters
params.t0 = 0; % start time of simulation
params.B=1; % gravitational term
params.v=0; % swimming speed
params.dt=0.01; % time increment
params.RD=0.01; % rotational diffusion
params.TD=0; % translational diffusion
params.Psi=0; % shear strength
nPeriods=1000; % number of simulated observations
params.tend = nPeriods*params.dt ; % end time
params.nsim=1000; % number of simulation
%% -----

% initial position
params.x0=0;
params.y0=0;
params.z0=0;

%% Preallocate stochastic matrix S and its column vectors theta and phi
S = zeros(nPeriods+1,5,params.nsim);
theta_stoch=zeros(nPeriods+1,1,params.nsim);
phi_stoch=zeros(nPeriods+1,1,params.nsim);
theta_s=zeros(1,params.nsim);
phi_s=zeros(1,params.nsim);

%% preallocate of expected mean matrix Y and its column vectors theta and phi
Y1=zeros(nPeriods+1,5,params.nsim);%preallocate Y,2
theta_Det_old=zeros(nPeriods+1,1,params.nsim);
phi_Det_old=zeros(nPeriods+1,1,params.nsim);
```

```

% theta_det_sd=zeros(nPeriods+1,1);
% phi_det_sd=zeros(nPeriods+1,1);
for k = 1:params.nsim
% initial orientation -----
params.theta0=pi*rand(1);
params.phi0=2*pi*rand(1);
% stochastic model -----
MDL=Nonhelical_traj(params);
[S(:, :, k), T]=simByEuler(MDL, nPeriods, 'DeltaTime', params.dt);
theta_stoch(:)=pi-abs(pi-(mod(S(:, 4, :), 2*pi)));
phi_stoch(:)=2*pi-abs(2*pi-mod(S(:, 5, :), 2*pi));
theta_s(:)=S(end, 4, :);
phi_s(:)=S(end, 5, :);
% ODE -----
[T, Y1(:, :, k)] =deterministic_ode_solver(params);
theta_Det_old=pi-abs(pi-(mod(Y1(:, 4, :), 2*pi)));
phi_Det_old=2*pi-abs(2*pi-mod(Y1(:, 5, :), 2*pi));
end
%% -----
phi_ss=squeeze(phi_stoch);
% ODE model
theta_dd_old=squeeze(theta_Det_old);
phi_dd_old=squeeze(phi_Det_old);
%% -----
mean_theta_stoch = mean(squeeze(theta_stoch), 2);
mean_phi_stoch = mean(squeeze(phi_stoch), 2);
mean_theta_D_old=mean(squeeze(theta_Det_old), 2);
mean_phi_D_old=mean(squeeze(phi_Det_old), 2);
%% -----
% save file
fname=['Nonhelical_still_fluid_Dr0,01.mat'];

```

```

% -----

```

```

%% Non-helical Swimmers Model
% SDE in 2D
% -----
function MDL=Nonhelical_traj(params)

%x=p(1)
%y=p(2)
%z=p(3)
%p(1)=theta;
%p(2)=phi;

F = @(t,p)[params.v.*sin(p(4)).*cos(p(5));...
params.v.*sin(p(4)).*sin(p(5));...
-params.Psi.*p(1)+params.v.*cos(p(4));...
-params.B.*sin(p(4))+params.Psi.*cos(p(5))+params.RD.*cot(p(4));...
-params.Psi.*cot(p(4)).*sin(p(5))];

G=@(t,p)[sqrt(2*params.TD) 0 0 0 0;...
0 sqrt(2*params.TD) 0 0 0;...
0 0 sqrt(2*params.TD) 0 0;...
0 0 0 sqrt(2*params.RD) 0 ;...
0 0 0 0 sqrt(2*params.RD)./sin(p(4)) ];

MDL=sde(F,G,'StartState',[params.x0;params.y0;params.z0;params.theta0;params.phi0],'StartTime',params.t0);

end

```

```

function [T,Y1] =deterministic_ode_solver(params)
% -----
%% Non-helical Swimmers ODE
% -----
%%Specify initial conditions
y0=zeros(1,3);
%swimming direction specified by theta, phi
y0(4)=params.theta0;
y0(5)=params.phi0;

%% ----- Run simulation ----- %

```

```
tspan = [params.t0:params.dt:params.tend];  
%solve differential equations specified by function p_n_model  
options = [];  
[T,Y1]=ode45(@deterministic_theta_phi_model,tspan,y0,options,params);
```

```
% -----  
%% Non-helical Swimmers  
%% Function containing ODEs  
% -----  
function dydt= deterministic_theta_phi_model(t,y,p)  
  
%function specifying differential equation  
%% random cell orientation  
xpos=y(1);  
ypos=y(2);  
zpos=y(3);  
theta = y(4);  
phi= y(5);  
  
%%  
v=p.v;  
Psi=p.Psi;  
ux=0;  
uz=-Psi*xpos;  
%  
dydt=[...  
ux+v*cos(phi)*sin(theta)%dx/dt  
v*sin(phi)*sin(theta) %dy/dt  
uz+v*cos(theta)%dz/dt  
theta_dot(theta,phi,p) % dtheta/dt  
phi_dot(theta,phi,p) %dphi/dt  
];
```

```
function soln=theta_dot(theta,phi,p)
```

```
Psi=p.Psi;
```

```
soln=-sin(theta)+Psi*cos(phi);
```

```
function soln=phi_dot(theta,phi,p)
```

```
Psi=p.Psi;
```

```
soln=-Psi*sin(phi)*cos(theta)./sin(theta);
```

Matlab codes to simulate and plot ensemble averages using SDE and mean of orientation angles using the deterministic model for helical swimmers.

```
% -----
```

```
% Plotting orientation distribution for helical swimmers
```

```
% -----
```

```
%% ---Clear memory, close figure windows
```

```
clear all
```

```
close all
```

```
%% -----
```

```
%% gamma=pi/4
```

```
%still fluid
```

```
fname=['Dist_Helical_Psi0_Theta1_gammpi4_Dr0,01_dt0,01_sim1000.mat'];
```

```
load(fname)
```

```
f1 = figure('PaperSize',[17.5 25],'PaperPosition',[1 1 16 16]);
```

```
%% -----
```

```
psi_ss=squeeze(psi_stoch);
```

```
for tp = 1:length(T)
```

```
theta_stoch=pi-abs(pi-(mod(S(tp,4,:),2*pi)));
```

```
phi_stoch=2*pi-abs(2*pi-mod(S(tp,5,:),2*pi));
```

```

psi_stoch=2*pi-abs(2*pi-mod(S(tp,6,:),2*pi));
calc_mean_theta(tp)=mean(theta_stoch);
calc_mean_phi(tp)=mean(phi_stoch);
calc_mean_psi(tp)=mean(psi_stoch);
end
%% -----
theta_DET=mean_theta_D_old; %from ODE
phi_DET=mean_phi_D_old; %from ODE
psi_DET=mean_psi_D_old; %from ODE
stoch_theta_av=mean(calc_mean_theta); % from SDE
stoch_phi_av=mean(calc_mean_phi); % from SDE
stoch_psi_av=mean(calc_mean_psi);% from SDE
cos_phi=squeeze(theta_Det_old);%from ODE
mean_cos=mean(cos_phi,2);%<cos(phi)>
%% -----
%plot theta phi psi
figure(1)
subplot(1,3,1)%plot theta
plot(T,theta_ss(:,1:3),'linewidth',1)
hold on
plot (T,calc_mean_theta,'k-.','linewidth',2);%<theta(t)>
hold on
plot (T,theta_DET,'b--','linewidth',2);
xlabel('Time')
ylabel('\theta')
%plot phi
subplot(1,3,2)
plot(T,phi_ss(:,1:3),'linewidth',1);
hold on
plot(T,calc_mean_phi,'k-.','linewidth',2);%<phi(t)>
hold on
plot(T,phi_DET,'b--','linewidth',2);
xlabel('Time')
ylabel('\phi')

```

```

%plot psi
subplot(1,3,3)
plot(T,psi_ss(:,1:3),'linewidth',1)
hold on
plot (T,calc_mean_psi,'k-.','linewidth',2);
hold on
plot(T,psi_DET,'b--','linewidth',2);
xlabel('Time')
ylabel('\psi')
%% -----
% px
theta_S=theta_ss;
phi_S=phi_ss;
theta_D=theta_dd_old;
phi_D=phi_dd_old;
px_stcoh=sin(theta_S).*cos(phi_S);
px_det=sin(theta_D).*cos(phi_D);
% compute mean over sim
%<px(t)>=<sin(theta)cos(phi)>
mean_px_stoch=mean(px_stcoh,2);
mean_px_det=mean(px_det,2);
px_av=mean(mean_px_stoch);
figure(2)
hold on
plot (T,px_stcoh(:,1:3),'linewidth',2);
hold on
plot (T,mean_px_stoch,'k-.','linewidth',2);
hold on
plot (T,mean_px_det,'b--','linewidth',2);
xlabel('Time')
ylabel('$p_x$', 'interpreter', 'latex');
hold off

%% -----

```

```

% Plot histogram
binCenters=linspace(0,pi);
theta_mod2p=pi-abs(pi-(mod(theta_s,2*pi)));
binCount= histc(theta_mod2p,binCenters);
probScale = sum(binCount)*pi/100;
x = binCenters;
%% -----
binCenters_phi=linspace(0,2*pi);
phi_mod2p=2*pi-abs(2*pi-(mod(phi_s,2*pi)));
binCount_phi= histc(phi_mod2p,binCenters_phi);
probScale_phi= sum(binCount_phi)*2*pi/100;
%% -----
binCenters_psi=linspace(0,2*pi);
psi_mod2p=2*pi-abs(2*pi-(mod(psi_s,2*pi)));
binCount_psi= histc(psi_mod2p,binCenters_psi);
probScale_psi= sum(binCount_psi)*2*pi/100;
%% -----
subplot(1,3,1)%theta
histHandle = bar(binCenters,binCount/probScale,'hist');
hold on
xlim([0 pi]);
xlabel('\theta');

subplot(1,3,2)%phi
histHandle = bar(binCenters_phi,binCount_phi/probScale_phi,'hist');
pd1 = makedist('Uniform','lower',0,'upper',2*pi);
x_phi = binCenters_phi;
pdf1 = pdf(pd1,x_phi);
hold on
stairs(x_phi,pdf1,'r','LineWidth',2);
xlim([0 2*pi]);
xlabel('\phi');

```

```
subplot(1,3,3)%psi
histHandle = bar(binCenters_psi,binCount_psi/probScale_psi,'hist');
% hold on
% pd2 = makedist('Uniform','lower',0,'upper',2*pi);
% x_psi = binCenters_psi;
% pdf_psi = pdf(pd2,x_psi);
% % Plot the pdfs
% stairs(x_psi,pdf_psi,'r','LineWidth',2);
xlim([0 2*pi]);
xlabel('\psi');
```

```
% -----
% Simulation to generate mat file and plot averages of
% orientation angles for helical swimmer
% SDE solved using simByEuler
% ODE is solved using ode45
% -----
%% ---Clear memory, close figure windows
clear all
close all
%% Specify fixed parameters
params.Theta=1; % propulsive torque strength
params.t0= 0; % start time of simulation
params.B=1; % gravitational time scale
params.v=0; % swimming speed
params.dt =0.01; % time increment
params.RD=0.01; % rotational diffusion
params.TD=0; % translational diffusion
params.Psi=0; % shear strength
params.gamma=pi/4; % angle between propulsive force and torque
nPeriods=2000; % number of simulated observations
params.tend = nPeriods*params.dt ; % end time
```

```

params.nsim=1000;                % number of simulation
%% -----
% initial position
params.x0=0;
params.y0=0;
params.z0=0;
%% Preallocate stochastic matrix S and its column vectors theta phi psi
S = zeros(nPeriods+1,6,params.nsim);
theta_stoch=zeros(nPeriods+1,1,params.nsim);
phi_stoch=zeros(nPeriods+1,1,params.nsim);
psi_stoch=zeros(nPeriods+1,1,params.nsim);
theta_s=zeros(1,params.nsim);
phi_s=zeros(1,params.nsim);
psi_s=zeros(1,params.nsim);
%% preallocate of expected mean matrix Y and its column vectors theta and phi
Y1=zeros(nPeriods+1,6,params.nsim);
theta_Det_old=zeros(nPeriods+1,1,params.nsim);
phi_Det_old=zeros(nPeriods+1,1,params.nsim);
psi_Det_old=zeros(nPeriods+1,1,params.nsim);
%% Simulation
for k = 1:params.nsim
% initial orientation -----
params.theta0=pi*rand(1);
params.phi0=2*pi*rand(1);
params.psi0=2*pi*rand(1);

MDL=helical_traj(params);
[S(:, :, k), T, Z]=simByEuler(MDL, nPeriods, 'DeltaTime', params.dt);
theta_stoch(:)=pi-abs(pi-(mod(S(:,4,:),2*pi)));
phi_stoch(:)=2*pi-abs(2*pi-mod(S(:,5,:),2*pi));
psi_stoch(:)=2*pi-abs(2*pi-mod(S(:,6,:),2*pi));
theta_s(:)=S(end,4,:);
phi_s(:)=S(end,5,:);
psi_s(:)=S(end,6,:);

```

```

% ODE -----
[T,Y1(:, :, k)] =deterministic_ode_solver(params);
theta_Det_old=pi-abs(pi-(mod(Y1(:,4,:),2*pi)));
phi_Det_old=2*pi-abs(2*pi-mod(Y1(:,5,:),2*pi));
psi_Det_old=2*pi-abs(2*pi-mod(Y1(:,6,:),2*pi));
end

%% -----
theta_ss=squeeze(theta_stoch);
phi_ss=squeeze(phi_stoch);
theta_dd=squeeze(theta_Det);
phi_dd=squeeze(phi_Det);
theta_dd_old=squeeze(theta_Det_old);
phi_dd_old=squeeze(phi_Det_old);
%% -----
mean_theta_stoch = mean(squeeze(theta_stoch),2);
mean_phi_stoch = mean(squeeze(phi_stoch),2);
mean_psi_stoch = mean(squeeze(psi_stoch),2);
mean_theta_D_old=mean(squeeze(theta_Det_old),2);
mean_phi_D_old=mean(squeeze(phi_Det_old),2);
mean_psi_D_old=mean(squeeze(psi_Det_old),2);
%% -----
% save file
fname=['Dist_Helical_Psi0_Theta1_gammpi4_Dr0,01_dt0,01_sim1000.mat'];
save(fname)

```

```

% -----
% Helical Swimmers Orientation
% -----
function MDL=helical_traj(params)

%x=p(1)
%y=p(2)
%z=p(3)
%p(4)=theta;
%p(5)=phi;

```

APPENDIX E. MATLAB CODES

```

%p(6)=psi;

F = @(t,p)[ params.v.*sin(p(4)).*cos(p(5));...
params.v.*sin(p(4)).*sin(p(5));...
-params.Psi.*p(1)+params.v.*cos(p(4));...
-params.B.*sin(p(4))+params.Theta.*sin(params.gamma).*sin(p(6))+params.Psi.*cos(p(5))+params.RD.*cot(p(4));...
-params.Theta.*(sin(params.gamma).*cos(p(6))./sin(p(4)))-params.Psi.*cot(p(4)).*sin(p(5));...
params.Theta.*(cot(p(4)).*cos(p(6)).*sin(params.gamma)+cos(params.gamma))+params.Psi.*(sin(p(5))./sin(p(4)))];

G=@(t,p)[sqrt(2*params.TD) 0 0 0 0 0;...
0 sqrt(2*params.TD) 0 0 0 0;...
0 0 sqrt(2*params.TD) 0 0 0;...
0 0 0 sqrt(2*params.RD) 0 0;...
0 0 0 0 (sqrt(2*params.RD+2*params.RD.*cos(p(4)))./2.*sin(p(4)))+(sqrt(2*params.RD-2*params.RD.*cos(p(4)))./2.*sin(p(4)));...
0 0 0 0 (sqrt(2*params.RD-2*params.RD.*cos(p(4)))./2.*sin(p(4)))-(sqrt(2*params.RD+2*params.RD.*cos(p(4)))./2.*sin(p(4)))];

MDL = sde(F,G,'StartState', [params.x0;params.y0;params.z0;params.theta0;params.phi0;params.psi0],'StartTime',para

end

```

```

function [T,Y1] =deterministic_ode_solver(params)
%calc_trajectory(params)
%simulate trajectory and calculate vertical transport

%%Specify initial conditions

y0=zeros(1,3);
%swimming direction specified by theta, phi, psi
y0(4)=params.theta0;
y0(5)=params.phi0;
y0(6)=params.psi0 ;

%% ----- Run simulation ----- %

```

```
tspan = [params.t0:params.dt:params.tend];

%solve differential equations specified by function p_n_model
options = [];
[T,Y1]=ode45(@deterministic_theta_phi_psi_model,tspan,y0,options,params);
```

```
%% Function containing ODEs %
```

```
function dydt= deterministic_theta_phi_psi_model(t,y,p)
```

```
%function specifying differential equation
```

```
%% random cell orientation
```

```
xpos=y(1);
```

```
ypos=y(2);
```

```
zpos=y(3);
```

```
theta = y(4);
```

```
phi= y(5);
```

```
psi= y(6);
```

```
%% uniform flow
```

```
v=p.v;
```

```
Psi=p.Psi;
```

```
ux=0;
```

```
uz=-Psi*xpos;
```

```
%
```

```
dydt=[...
```

```
ux+v*cos(phi)*sin(theta)%dx/dt
```

```
v*sin(phi)*sin(theta) %dy/dt
```

```
uz+v*cos(theta)%dz/dt
```

```
theta_dot(theta,phi,psi,p) % dtheta/dt
```

```
phi_dot(theta,phi,psi,p) %dphi/dt
```

```
psi_dot(theta,phi,psi,p) %dpsi/dt  
];
```

```
function soln=theta_dot(theta,phi,psi,p)  
%parameters  
Theta=p.Theta;  
Psi=p.Psi;  
gamma=p.gamma;
```

```
soln=-sin(theta)+Psi*cos(phi)...  
+Theta*sin(gamma)*sin(psi);
```

```
function soln=phi_dot(theta,phi,psi,p)  
%parameters  
Theta=p.Theta;  
Psi=p.Psi;  
gamma=p.gamma;
```

```
soln=(...  
-Psi*sin(phi)*cos(theta)-Theta*sin(gamma)*cos(psi)...  
)./sin(theta);
```

```
function soln=psi_dot(theta,phi,psi,p)  
%parameters  
  
Theta=p.Theta;  
Psi=p.Psi;  
gamma=p.gamma;
```

```
soln=(...  
Psi*sin(phi)+Theta*(cos(gamma)*sin(theta)+sin(gamma)*cos(psi)*cos(theta))...  
)./sin(theta);
```

E.3 Matlab Codes for Chapter 4

Simulations in this chapter are also similar. The difference between them is the values of considered parameters, duration of simulation or the time step. Presented codes are examples for each section.

```
% -----  
%% No bias diffusion motion in still fluid  
%% SDE model is solved using simByEuler  
% -----  
%% ---Clear memory, close figure windows  
clear all  
close all  
%% Specify fixed parameters  
params.t0= 0; % start time of simulation  
params.v=0.1; %swimming speed  
params.dt =0.01; %time increment  
params.RD=1; % rotational diffusion  
params.TD=0; % translational diffusion  
nPeriods=10000; % number of simulated observations  
params.tend = nPeriods*params.dt ; % end time  
params.nsim=5000; % number of simulations  
%% -----  
%%initial position  
params.x0=0;  
params.y0=0;  
params.z0=0;  
  
S = zeros(nPeriods+1,5,params.nsim);  
x_t=zeros(params.nsim,nPeriods+1);
```

```
average_x=zeros(2,nPeriods+1);

S1 = zeros(nPeriods+1,5,params.nsim);
for nsim=1:params.nsim
    params.theta0=pi*rand(1);
    params.phi0=2*pi*rand(1);
    MDL=Nonhelical_traj_compare_RD_TD(params);
    [S1(:,:,nsim),T]=simByEuler(MDL, nPeriods,'DeltaTime',params.dt);

    xs=S1(:,1,:);
    ys=S1(:,2,:);
    zs=S1(:,3,:);
    xmsd=xs.^2+ys.^2+zs.^2;

end

xmsd_mean=mean(squeeze(xmsd),2);
hold on
plot(T,xmsd_mean,'k','linewidth',2)
hold on
w=(params.v.^2./params.RD).*T;
plot(T,w,'g','linewidth',2)
xlim([0 params.tend])
xlabel('Time')
ylabel('mean square displacement <x^2(t)>')
%-----
%% displacement
x1_dis=squeeze(xs);
y1_dis=squeeze(ys);
z1_dis=squeeze(zs);
mean_x=mean(x1_dis,2);
mean_y=mean(y1_dis,2);
mean_z=mean(z1_dis,2);
dis=sqrt(mean_x.^2+mean_y.^2+mean_z.^2);
```

```

figure(2)
plot(T,dis,'linewidth',2)
hold on
% %-----
fname=['MSD_Dis_Dt0__T100_dt0_01_sim10000.mat'];
save(fname)

% -----
%% No bias diffusion in still fluid Model
% SDE in 2D
% -----
function MDL=Nonhelical_traj_compare_RD_TD(params)

%x=p(1)
%y=p(2)
%z=p(3)
%p(1)=theta;
%p(2)=phi;

F = @(t,p)[params.v.*sin(p(4)).*cos(p(5));...
params.v.*sin(p(4)).*sin(p(5));...
params.v.*cos(p(4));...
params.RD.*cot(p(4));...
0];

G=@(t,p)[sqrt(2*params.TD) 0 0 0 0;...
0 sqrt(2*params.TD) 0 0 0;...
0 0 sqrt(2*params.TD) 0 0;...
0 0 0 sqrt(2*params.RD) 0 ;...
0 0 0 0 sqrt(2*params.RD)./sin(p(4)) ];

MDL=sde(F,G,'StartState',[params.x0;params.y0;params.z0;params.theta0;params.phi0],'StartTime',params.t0);

end

```

```

clear all
close all

```

```
% generate all mat file first %
% plot MSD
%% -----
fname=['MSD_Dis_Dt0__T100_dt0_01.mat'];%T=100 dt=0.01 sim=500,Dt=0
load(fname)
MSD_x1=xmsd_mean;
T1=T;
dis1=dis;

fname=['MSD_Dis_Dt0__T100_dt0_05.mat'];%T=100 dt=0.05 sim=500,Dt=0
load(fname)
MSD_x2=xmsd_mean;
T2=T;
dis2=dis;

fname=['MSD_Dis_Dt0__T100_dt0_1.mat'];%T=100 dt=0.1 sim=500,Dt=0
load(fname)
MSD_x3=xmsd_mean;
T3=T;
dis3=dis;

figure(12)
plot(T1,MSD_x1,'k','linewidth',2)
hold on
plot(T,w,'g','linewidth',2)
xlim([0 params.tend])
hold on
plot(T2,MSD_x2,'b','linewidth',2)
hold on
plot(T3,MSD_x3,'r','linewidth',2)
xlabel('Time')
ylabel('mean square displacement <x^2(t)>')
%% -----
fname=['MSD_Dis_Dt0__T200_dt0_01.mat'];%T=200 dt=0.01 sim=500,Dt=0
```

```
load(fname)
MSD_x4=xmsd_mean;
T4=T;
dis4=dis;

fname=['MSD_Dis_Dt0__T200_dt0_05.mat'];%T=200 dt=0.05 sim=500,Dt=0
load(fname)
MSD_x5=xmsd_mean;
T5=T;
dis5=dis;

fname=['MSD_Dis_Dt0__T200_dt0_1.mat'];%T=200 dt=0.1 sim=500,Dt=0
load(fname)
MSD_x6=xmsd_mean;
T6=T;
dis6=dis;

figure(13)
plot(T4,MSD_x4,'k','linewidth',2)
hold on
plot(T,w,'g','linewidth',2)
xlim([0 params.tend])
hold on
plot(T5,MSD_x5,'b','linewidth',2)
hold on
plot(T6,MSD_x6,'r','linewidth',2)
xlabel('Time')
ylabel('mean square displacement <math>\langle x^2(t) \rangle</math>')
```

```
fname=['MSD_Dis_Dt0__T100_dt0_01.mat'];%T=100 dt=0.01 sim=500,Dt=0
load(fname)
MSD_x1=xmsd_mean;
T1=T;
```

```
dis1=dis;

fname=['MSD_Dis_Dt0__T100_dt0_05.mat'];%T=100 dt=0.05 sim=500,Dt=0
load(fname)
MSD_x2=xmsd_mean;
T2=T;
dis2=dis;

fname=['MSD_Dis_Dt0__T100_dt0_1.mat'];%T=100 dt=0.1 sim=500,Dt=0
load(fname)
MSD_x3=xmsd_mean;
T3=T;
dis3=dis;

% Plot displacement
figure(12)
hold on
plot(T1,dis1,'k','linewidth',2)
hold on
hold all
plot(T2,dis2,'b','linewidth',2)
hold on
plot(T3,dis3,'r','linewidth',2)
xlabel('Time')
ylabel('mean displacement')
hold off

%% -----
fname=['MSD_Dis_Dt0__T200_dt0_01.mat'];%T=200 dt=0.01 sim=500,Dt=0
load(fname)
MSD_x4=xmsd_mean;
T4=T;
dis4=dis;

fname=['MSD_Dis_Dt0__T200_dt0_05.mat'];%T=200 dt=0.05 sim=500,Dt=0
```

```
load(fname)
MSD_x5=xmsd_mean;
T5=T;
dis5=dis;

fname=['MSD_Dis_Dt0__T200_dt0_1.mat'];%T=200 dt=0.1 sim=500,Dt=0
load(fname)
MSD_x6=xmsd_mean;
T6=T;
dis6=dis;

% Plot displacement
figure(13)
hold on
plot(T4,dis4,'k','linewidth',2)
hold on
hold all
plot(T5,dis5,'b','linewidth',2)
hold on
plot(T6,dis6,'r','linewidth',2)
xlabel('Time')
ylabel('mean displacement')
```

```
fname=['MSD_Dis_Dt0__T100_dt0_01.mat'];%T=100 dt=0.01 sim=500,Dt=0
load(fname)
MSD_x1=xmsd_mean;
T1=T;
dis1=dis;
x_dis_end1=x1_dis(end,:);

fname=['MSD_Dis_Dt0__T100_dt0_05.mat'];%T=100 dt=0.05 sim=500,Dt=0
load(fname)
MSD_x2=xmsd_mean;
```

```
T2=T;
dis2=dis;
x_dis_end2=x1_dis(end,:);

fname=['MSD_Dis_Dt0__T100_dt0_1.mat'];%T=100 dt=0.1 sim=500,Dt=0
load(fname)
MSD_x3=xmsd_mean;
T3=T;
dis3=dis;
x_dis_end3=x1_dis(end,:);
%% histogram
figure(13)
h(1)=subplot(2,2,1)
x_dis_end1=x1_dis(end,:);
D=params.TD+params.v.^2/(6*params.RD);
binCenters1=linspace(-3,3);
binCount= histc(x_dis_end1,binCenters1);
bw=binCenters1(2)-binCenters1(1);
probScale =sum(binCount)*bw;
histHandle = bar(binCenters1,binCount/probScale,'hist');
hold on
hold all
x_bin1=binCenters1;
n=exp(-x_bin1.^2./(4*D*params.tend))./sqrt(4*pi*D*params.tend);
plot(x_bin1,n,'r-','linewidth',2);
h(2)=subplot(2,2,2)
x_dis_end2=x1_dis(end,:);
D=params.TD+params.v.^2/(6*params.RD);
binCenters2=linspace(-3,3);
binCount2= histc(x_dis_end2,binCenters2);
bw=binCenters2(2)-binCenters2(1);
probScale =sum(binCount2)*bw;
histHandle = bar(binCenters2,binCount2/probScale,'hist');
hold on
```

```
hold all
x_bin2=binCenters2;
n=exp(-x_bin2.^2./(4*D*params.tend))./sqrt(4*pi*D*params.tend);
plot(x_bin2,n,'r-','linewidth',2);
h(3)=subplot(2,2,[3 4])
x_dis_end3=x1_dis(end,:);
D=params.TD+params.v.^2/(6*params.RD);
binCenters3=linspace(-3,3);
binCount3= histc(x_dis_end3,binCenters3);
bw=binCenters3(2)-binCenters3(1);
probScale =sum(binCount3)*bw;
histHandle = bar(binCenters3,binCount3/probScale,'hist');
hold on
hold all
x_bin3=binCenters3;
n=exp(-x_bin3.^2./(4*D*params.tend))./sqrt(4*pi*D*params.tend);
plot(x_bin3,n,'r-','linewidth',2);
%% -----
fname=['MSD_Dis_Dt0__T200_dt0_01.mat'];%T=200 dt=0.01 sim=500,Dt=0
load(fname)
MSD_x4=xmsd_mean;
T4=T;
dis4=dis;
x_dis_end4=x1_dis(end,:);

fname=['MSD_Dis_Dt0__T200_dt0_05.mat'];%T=200 dt=0.05 sim=500,Dt=0
load(fname)
MSD_x5=xmsd_mean;
T5=T;
dis5=dis;
x_dis_end5=x1_dis(end,:);

fname=['MSD_Dis_Dt0__T200_dt0_1.mat'];%T=200 dt=0.1 sim=500,Dt=0
load(fname)
```

```
MSD_x6=xmsd_mean;
T6=T;
dis6=dis;
x_dis_end6=x1_dis(end,:);

figure(14)
h(1)=subplot(2,2,1)
D=params.TD+params.v.^2/(6*params.RD);
binCenters4=linspace(-3,3);
binCount= histc(x_dis_end4,binCenters4);
bw=binCenters4(2)-binCenters4(1);
probScale =sum(binCount)*bw;
histHandle = bar(binCenters4,binCount/probScale,'hist');
hold on;
hold all
x_bin4=binCenters4;
n=exp(-x_bin4.^2./(4*D*params.tend))./sqrt(4*pi*D*params.tend);
plot(x_bin4,n,'r-','linewidth',2);
h(2)=subplot(2,2,2)
D=params.TD+params.v.^2/(6*params.RD);
binCenters5=linspace(-3,3);
binCount5= histc(x_dis_end5,binCenters5);
bw=binCenters5(2)-binCenters5(1);
probScale =sum(binCount5)*bw;
histHandle = bar(binCenters5,binCount5/probScale,'hist');
hold on;
hold all
x_bin5=binCenters5;
n=exp(-x_bin5.^2./(4*D*params.tend))./sqrt(4*pi*D*params.tend);%size=100*1
plot(x_bin5,n,'r-','linewidth',2);
h(3)=subplot(2,2,[3 4])
D=params.TD+params.v.^2/(6*params.RD);
binCenters6=linspace(-3,3);
binCount6= histc(x_dis_end6,binCenters6);
```

```
bw=binCenters6(2)-binCenters6(1);
probScale =sum(binCount6)*bw;
histHandle = bar(binCenters6,binCount6/probScale,'hist');
hold on;
hold all
x_bin6=binCenters6;
n=exp(-x_bin6.^2./(4*D*params.tend))./sqrt(4*pi*D*params.tend);%size=100*1
plot(x_bin6,n,'r-','linewidth',2);
```

```
% -----
%% Non-helical trajectories in uniform flow
% -----

%% ---Clear memory, close figure windows
clear all
close all

%% Specify fixed parameters
params.B=1;      % gravitational time scale
params.t0 = 0;  % start time of simulation
params.v=0.1;   % swimming speed
params.dt =0.01;%time increment
params.TD=0;    % translational diffusion
nPeriods=10000;% number of simulated observations
params.tend = nPeriods*params.dt ; % end time
params.nn=3;%#of rows
params.n=3;%# of columns
%% -----
%%initial position
params.x0=0;
params.y0=0;
params.z0=0;

%% plot deterministic model
Psi_range=[0,0.5,1.5];
```

```
figure(4)
for j=1:3
    params.Psi=Psi_range(j);
    params.p=j;
    for i=1:5
        params.theta0=pi*rand(1);
        params.phi0=2*pi*rand(1);

        [T,Y] =deterministic_ode_solver(params);

        h(j)=subplot(params.nn,params.n,[params.p,params.p+6]);
        plot3(Y(:,1),Y(:,2),Y(:,3))
        xlabel('x')
        ylabel('y')
        if j==1
            zlabel('z')
        end
        grid on
        hold on
        hold all
        plot3(0,0,0,'k.','Markersize',20)
        view(-13,9)
        theta_DET=Y(:,4);
        phi_DET=Y(:,5);
        px_DET=sin(theta_DET).*cos(phi_DET);

    end

end

%% plot stochastic trajectories
Dr_range=[0.01,0.1,0.5];
for k=1:3
    params.RD=Dr_range(k);
```

```
figure(k)
for j=1:3
    params.Psi=Psi_range(j);
    params.p=j;
    for i=1:5
        params.theta0=pi*rand(1);
        params.phi0=2*pi*rand(1);

        MDL=Nonhelical_traj(params);
        [S,T]=simByEuler(MDL, nPeriods,'DeltaTime',params.dt);

        x_stoch=S(:,1);
        y_stoch=S(:,2);
        z_stoch=S(:,3);
        theta_stoch=S(:,4);
        phi_stoch=S(:,5);

        h(j)=subplot(params.nn,params.n,[params.p,params.p+6]);
        plot3(x_stoch,y_stoch,z_stoch)
        xlabel('x')
        ylabel('y')
        if j==1
            zlabel('z')

        end
        grid on
        hold on
        hold all
        plot3(0,0,0,'k.','Markersize',30)
        view(-13,9)

    end

end
```

end

```
function [T,Y1] =deterministic_ode_solver(params)
% -----
%% Non-helical Swimmers
% -----
%%Specify initial conditions
y0=zeros(1,3);

y0(4)=params.theta0;
y0(5)=params.phi0;
%% ----- Run simulation ----- %
tspan = [params.t0:params.dt:params.tend];
options = [];
[T,Y1]=ode45(@deterministic_theta_phi_model,tspan,y0,options,params);
```

```
%% Non-helical Swimmers
%% Function containing ODEs %
function dydt= deterministic_theta_phi_model(t,y,p)

%% random cell orientation
xpos=y(1);
ypos=y(2);
zpos=y(3);
theta = y(4);
phi= y(5);
%% uniform flow
v=p.v;
Psi=p.Psi;
ux=0;
```

```

uz=-Psi*xpos;
%
dydt=[...
ux+v*cos(phi)*sin(theta)%dx/dt
v*sin(phi)*sin(theta) %dy/dt
uz+v*cos(theta)%dz/dt
theta_dot(theta,phi,p) % dtheta/dt
phi_dot(theta,phi,p) %dphi/dt
];

function soln=theta_dot(theta,phi,p)
Psi=p.Psi;
soln=-sin(theta)+Psi*cos(phi);

function soln=phi_dot(theta,phi,p)
Psi=p.Psi;
soln=-Psi*sin(phi)*cos(theta)./sin(theta);

```

```

% -----
%% Non-helical Swimmers Model
% SDE in 2D
% -----
function MDL=Nonhelical_traj(params)

%x=p(1)
%y=p(2)
%z=p(3)
%p(1)=theta;
%p(2)=phi;

F = @(t,p)[params.v.*sin(p(4)).*cos(p(5));...
params.v.*sin(p(4)).*sin(p(5));...
-params.Psi.*p(1)+params.v.*cos(p(4));...
-params.B.*sin(p(4))+params.Psi.*cos(p(5))+params.RD.*cot(p(4));...
-params.Psi.*cot(p(4)).*sin(p(5))];

G=@(t,p)[sqrt(2*params.TD) 0 0 0 0;...

```

APPENDIX E. MATLAB CODES

```
0 sqrt(2*params.TD) 0 0 0;...
0 0 sqrt(2*params.TD) 0 0;...
0 0 0 sqrt(2*params.RD) 0 ;...
0 0 0 0 sqrt(2*params.RD)./sin(p(4)) ];

MDL=sde(F,G,'StartState',[params.x0;params.y0;params.z0;params.theta0;params.phi0],'StartTime',params.t0);

end
```

```
% -----
% Simulation to generate mat file to plot Mean vertical
% transport for non-helical swimmers
% -----
%% ---Clear memory, close figure windows
clear all
close all

%% Specify fixed parameters
params.B=1;      % gravitational time
params.t0 = 0;  % start time of simulation
params.v=0.1;    % swimming speed
params.dt =0.01; %time increment
params.TD=0;     %translational diffusion
params.sim =100; %number of simulations
nPeriods=10000; % number of simulated observations
params.tend =nPeriods*params.dt ; % end time
params.nn=3;%#of rows
params.n=3;%# of columns

%% Specify parameter ranges for variable parameters
Psi_range = [0:0.1:2];
Dr_range= [0.01,0.1,0.5];

%% Loop over variable parameters
%%initial position
```

```
params.x0=0;
params.y0=0;
params.z0=0;

Mean_vert_transport_D=zeros(1,length(Psi_range));
Mean_vert_transport_S=zeros(length(Dr_range),length(Psi_range));
vert_transport=zeros(1,params.sim);

for i=1:length(Dr_range)
    params.RD=Dr_range(i);
    for j=1:length(Psi_range)
        params.Psi=Psi_range(j);
        for nsim=1:params.sim

            params.theta0=pi*rand(1);
            params.phi0=2*pi*rand(1);

            [T,Y] =deterministic_ode_solver(params);
            vert_transport_D=(Y(end,3)-Y(1,3))/(T(end)-T(1));
            vert_transport_D_sim(nsim)=vert_transport_D;
            MDL=Nonhelical_traj(params);
            [S,T]=simByEuler(MDL,nPeriods,'DeltaTime',params.dt);
            vert_transport_S=(S(end,3)-S(1,3))/(T(end)-T(1));
            vert_transport_S_sim(nsim)=vert_transport_S;

        end
        Mean_vert_transport_D(i,j)=mean(vert_transport_D_sim);
        Mean_vert_transport_S(i,j)=mean(vert_transport_S_sim);

    end

end

figure(1)
```

```

plot(Psi_range,Mean_vert_transport_D(i,:),'-*')
hold on
for i=1:length(Dr_range)

plot(Psi_range,Mean_vert_transport_S(i,:),'-*')
xlabel('Psi')
ylabel('mean vertical transport')
hold on
hold all
end

legend(num2str(Dr_range(1)),num2str(Dr_range(2)),num2str(Dr_range(3)))
title('vertical transport for variable values of gamma')
fname=['Nonhelical_mean_vert_trans_Psi.mat'];
save(fname)

```

```

% -----
%% Plot mean vertical transport for non-helical swimmers
% -----
%% ---Clear memory, close figure windows
clear all
close all
%% Specify fixed parameters
fname=['Nonhelical_mean_vert_trans_Psi.mat'];
load(fname)
LineStyleOrder=[': ','-.';'- '];
Colororder=['b','g','r'];

figure (1)
plot(Psi_range,Mean_vert_transport_D(i,:),'k--')
hold on
for i=1:length(Dr_range)

plot(Psi_range,Mean_vert_transport_S(i,:),'Color',Colororder(i,:),'linewidth',2,'LineStyle',LineStyleOrder(i,:))

xlabel('\Psi')
ylabel('$\overline{Z}$','interpreter','latex')
hold on
hold all
end

```

```
hold on
hold all
plot([0,0],[-5,1], 'color','b','LineStyle','--')
plot([1,1],[-5,1], 'color','k','LineStyle','--')
```

```
% -----
% Simulation to generate mat file for
% mean vertical transport for helical swimmers as
% a function of propulsive torque strength
% -----
%% ---Clear memory, close figure windows
clear all
close all
%% Specify fixed parameters
params.B=1; % gravitational time scale
params.t0=0; % start time of simulation
params.v=0.1; % swimming speed
params.dt =0.01; %time increment
params.gamma=7*pi/16; % angle between propulsive force and torque
params.Psi=1; % shear strength
params.TD=0; % translational diffusion
params.sim =100;% number of simulations
nPeriods=10000; % number of simulated observations
params.tend =nPeriods*params.dt; % end time
params.nn=3;%#of rows
params.n=3;%# of columns
%% Specify parameter ranges for variable parameters
Dr_range= [0.01,0.1,0.5];
Theta_range=[0:0.1:3];
%% Loop over variable parameters
%%initial position
params.x0=0;
```

```
params.y0=0;
params.z0=0;
Mean_vert_transport_D=zeros(1,length(Theta_range));
Mean_vert_transport_S=zeros(length(Dr_range),length(Theta_range));
vert_transport=zeros(1,params.sim);

for i=1:length(Dr_range)
params.RD=Dr_range(i);
for j=1:length(Theta_range)

params.Theta=Theta_range(j);
for nsim=1:params.sim

params.theta0=pi*rand(1);
params.phi0=2*pi*rand(1);
params.psi0=2*pi*rand(1);

[T,Y]=deterministic_ode_solver(params);
vert_transport_D=(Y(end,3)-Y(1,3))/(T(end)-T(1));
vert_transport_D_sim(nsim)=vert_transport_D;
MDL=helical_traj(params);
[S,T]=simByEuler(MDL,nPeriods,'DeltaTime',params.dt);
vert_transport_S=(S(end,3)-S(1,3))/(T(end)-T(1));
vert_transport_S_sim(nsim)=vert_transport_S;

end

Mean_vert_transport_D(i,j)=mean(vert_transport_D_sim);
Mean_vert_transport_S(i,j)=mean(vert_transport_S_sim);
end

end

figure(1)
plot(Theta_range,Mean_vert_transport_D(i,:),'-*')
hold on
```

```
for i=1:length(Dr_range)

plot(Theta_range,Mean_vert_transport_S(i,:),'-*')
xlabel('\Theta')
ylabel('mean vertical transport')
hold on
hold all
end

legend(num2str(Dr_range(1)),num2str(Dr_range(2)),num2str(Dr_range(3)))
title('vertical transport for variable values of gamma')

fname=['Mean_vert_trans_gam7pi16_vary_Th.mat'];
save(fname)



---



function [T,Y1] =deterministic_ode_solver(params)
y0=zeros(1,3);
y0(4)=params.theta0;
y0(5)=params.phi0;
y0(6)=params.psi0;
%% ----- Run simulation ----- %
tspan = [params.t0:params.dt:params.tend];
%solve differential equations specified by function p_n_model
options = [];
[T,Y1]=ode45(@deterministic_theta_phi_psi_model,tspan,y0,options,params);



---



%% Function containing ODEs %
function dydt= deterministic_theta_phi_psi_model(t,y,p)

%% random cell orientation
```

```
xpos=y(1);
ypos=y(2);
zpos=y(3);
theta = y(4);
phi= y(5);
psi= y(6);
%% uniform flow
v=p.v;
Psi=p.Psi;
ux=0;
uz=-Psi*xpos;
%
dydt=[...
ux+v*cos(phi)*sin(theta)%dx/dt
v*sin(phi)*sin(theta) %dy/dt
uz+v*cos(theta)%dz/dt
theta_dot(theta,phi,psi,p) % dtheta/dt
phi_dot(theta,phi,psi,p) %dphi/dt
psi_dot(theta,phi,psi,p) %dpsi/dt
];

function soln=theta_dot(theta,phi,psi,p)
%parameters
Theta=p.Theta;
Psi=p.Psi;
gamma=p.gamma;
soln=-sin(theta)+Psi*cos(phi)...
+Theta*sin(gamma)*sin(psi);

function soln=phi_dot(theta,phi,psi,p)
%parameters
Theta=p.Theta;
Psi=p.Psi;
gamma=p.gamma;
```

```

soln=(...
-Psi*sin(phi)*cos(theta)-Theta*sin(gamma)*cos(psi)...
)./sin(theta);

function soln=psi_dot(theta,phi,psi,p)
%parameters
Theta=p.Theta;
Psi=p.Psi;
gamma=p.gamma;
soln=(...
Psi*sin(phi)+Theta*(cos(gamma)*sin(theta)+sin(gamma)*cos(psi)*cos(theta))...
)./sin(theta);

```

```

% SDE in
% Helical swimmers model

function MDL=helical_traj(params)

%x=p(1)
%y=p(2)
%z=p(3)
%p(4)=theta;
%p(5)=phi;
%p(6)=psi;

F = @(t,p) [ params.v.*sin(p(4)).*cos(p(5));...
params.v.*sin(p(4)).*sin(p(5));...
-params.Psi.*p(1)+params.v.*cos(p(4));...
-params.B.*sin(p(4))+params.Theta.*sin(params.gamma).*sin(p(6))+params.Psi.*cos(p(5))+params.RD.*cot(p(4));...
-params.Theta.*(sin(params.gamma).*cos(p(6))./sin(p(4)))-params.Psi.*cot(p(4)).*sin(p(5));...
params.Theta.*(cot(p(4)).*cos(p(6)).*sin(params.gamma)+cos(params.gamma))+params.Psi.*(sin(p(5))./sin(p(4)))];

G=@(t,p) [sqrt(2*params.TD) 0 0 0 0 0;...
0 sqrt(2*params.TD) 0 0 0 0;...
0 0 sqrt(2*params.TD) 0 0 0;...
0 0 0 sqrt(2*params.RD) 0 0;...
0 0 0 (sqrt(2*params.RD+2*params.RD.*cos(p(4)))./2.*sin(p(4)))+(sqrt(2*params.RD-2*params.RD.*cos(p(4)))./2.*sin(p(4))) (sqrt(2*params.RD-2*params.RD.*cos(p(4)))./2.*sin(p(4)));...
0 0 0 (sqrt(2*params.RD-2*params.RD.*cos(p(4)))./2.*sin(p(4)))-(sqrt(2*params.RD+2*params.RD.*cos(p(4)))./2.*sin(p(4))) (sqrt(2*params.RD+2*params.RD.*cos(p(4)))./2.*sin(p(4)))]

MDL=sde(F,G,'StartState',[params.x0;params.y0;params.z0;params.theta0;params.phi0;params.psi0],'StartTime',params.t0);

end

```

```

% -----
%% Non-helical trajectories in channel flow
%% SDE model is solved using simByEuler
% -----
%% ---Clear memory, close figure windows
clear all
close all
%% Specify fixed parameters
params.t0= 0;      % start time of simulation
params.v=0.1;     % swimming speed
params.dt =0.01;  %time increment
params.RD=0.1;    % rotational diffusion
params.TD=0;      % translational diffusion
params.Psi_max=2; % shear strngth
nPeriods=20000;  % number of simulated observations
params.tend = nPeriods*params.dt ; % end time
params.sim = 1000; % number of simulations
params.nn=3;%#of rows
params.n=3;%# of columns

%% plot stochastic trajectories
figure(1)
for nsim=1:params.sim
params.theta0=pi*rand(1);
params.phi0=2*pi*rand(1);
params.x0=2*rand(1)-1;
params.y0=0;
params.z0=0;
% solve SDE model
MDL=Channel_Nonhelical_traj_Stoch(params);
[S,T]=simByEuler(MDL, nPeriods,'DeltaTime',params.dt);

%*****
%%we impose the following boundary conditions on x and z such that cell that

```

```
%starts at wall stay at wall
index=find(S(:,1)>1);
if(isempty(index))~=1
S(index(1):end,1)=1;
S(index(1):end,3)=S(index(1),3);
end

index=find(S(:,1)<-1);
if(isempty(index))~=1
S(index(1):end,1)=-1;
S(index(1):end,3)=S(index(1),3);
end

plot(S(:,1),S(:,3))
xlabel('x')
ylabel('z')
grid on
hold on
hold all

[N,M]=size(S);
for i=1:N
for j=1:M
Matrix(nsim,i,j)=S(i,j);
end
end
end

mean_x=mean(Matrix(:,:,1),1);
var_x=var(Matrix(:,:,1),1,1);
figure(3)
plot(T,var_x,'r','linewidth',2)
hold on
plot(T,mean_x,'k','linewidth',2)
fname=['variance_nonhelical_1000sim_Dr,1.mat'];
save(fname)
```

APPENDIX E. MATLAB CODES

```
% -----
%% Non-helical Swimmers Model
% SDE in 2D
% -----
function MDL=Channel_Nonhelical_traj_Stoch(params)

%x=p(1)
%y=p(2)
%z=p(3)
%p(1)=theta;
%p(2)=phi;

F = @(t,p)[params.v.*sin(p(4)).*cos(p(5));...
params.v.*sin(p(4)).*sin(p(5));...
params.Psi_max*(p(1)^2-1)+params.v.*cos(p(4));...
-sin(p(4))-params.Psi_max*p(1).*cos(p(5))+params.RD.*cot(p(4));...
params.Psi_max*p(1).*cot(p(4)).*sin(p(5))];

G=@(t,p)[sqrt(2.*params.TD) 0 0 0 0;...
0 sqrt(2.*params.TD) 0 0 0;...
0 0 sqrt(2.*params.TD) 0 0;...
0 0 0 sqrt(2.*params.RD) 0 ;...
0 0 0 0 sqrt(2.*params.RD)./sin(p(4)) ];

MDL=sde(F,G,'StartState',[params.x0;params.y0;params.z0;params.theta0;params.phi0],'StartTime',params.t0);

end

% -----
% plot histogram
% generate all mat file first%
% -----

clear all
close all

%% -----

fname=['variance_nonhelical_1000sim_Dr,1.mat'];%Psi_max=2
```

```
load(fname)
[N,M]=size(S);
for k=1:N
for l=1:M
Matrix(nsim,k,l)=S(k,l);
end
end
horpos_stoch1=Matrix(:,end,1);
%% -----
hold on
hold all
fname=['variance_nonhelical_1000sim_Dr,3.mat'];%Psi_max=2
load(fname)
[N,M]=size(S);
for k=1:N
for l=1:M
Matrix(nsim,k,l)=S(k,l);
end
end
horpos_stoch2=Matrix(:,end,1);
hold on
hold all
%% -----
fname=['variance_nonhelical_1000sim_Dr,5.mat'];%Psi_max=2
load(fname)
[N,M]=size(S);
for k=1:N
for l=1:M
Matrix(nsim,k,l)=S(k,l);
end
end
horpos_stoch3=Matrix(:,end,1);
hold on
hold all
```

APPENDIX E. MATLAB CODES

```
%% -----  
fname=['variance_nonhelical_1000sim_Dr,7.mat'];%Psi_max=2  
load(fname)  
[N,M]=size(S);  
for k=1:N  
for l=1:M  
Matrix(nsim,k,l)=S(k,l);  
end  
end  
horpos_stoch4=Matrix(:,end,1);  
hold on  
hold all  
%% -----  
horpos_stoch=[horpos_stoch1,horpos_stoch2,horpos_stoch3,horpos_stoch4];  
bincentre=linspace(-1,1);  
for nplot=1:4  
sph(nplot)=subplot(2,2,nplot);  
hist(horpos_stoch(:,nplot),bincentre);  
hold on  
mymap2=[[0,0,0];[0.6,0.6,0.6]];  
colormap(mymap2)  
set(gca,'xlim',[-1, 1])  
end  
  
% plot variance as a function of time  
% generate all mat files first  
%% ---Clear memory, close figure windows  
clear all  
close all  
%% -----  
fname=['variance_nonhelical_1000sim_Dr,1.mat'];%Psi_max=2  
load(fname)
```

```
var_x=var(Matrix(:,:,1),1,1);
hold on
hold all
plot(T,var_x(:),'k','linewidth',2)
hold on
%% -----
fname=['variance_nonhelical_1000sim_Dr,3.mat'];%Psi_max=2
load(fname)
var_x=var(Matrix(:,:,1),1,1);
hold on
hold all
plot(T,var_x(:),'b','linewidth',2)
%% -----
fname=['variance_nonhelical_1000sim_Dr,5.mat'];%Psi_max=2
load(fname)
var_x=var(Matrix(:,:,1),1,1);
hold on
hold all
plot(T,var_x(:),'r','linewidth',2)
%% -----
fname=['variance_nonhelical_1000sim_Dr,7.mat'];%Psi_max=2
load(fname)
var_x=var(Matrix(:,:,1),1,1);
hold on
hold all
plot(T,var_x(:),'g','linewidth',2)
xlabel('time');
ylabel('variance');

% -----
% plot variance as a function of rotational diffusion
% generate all mat file first
```

```
% -----  
%% ---Clear memory, close figure windows  
clear all  
close all  
%% -----  
Dr_range=linspace(0.1,0.7,4);  
fname=['variance_nonhelical_1000sim_Dr,1.mat'];%Psimax=2;  
load(fname)  
var_x=var(Matrix(:,end,1),1,1);  
var_x1=var_x;  
hold on  
hold all  
hold on  
%% -----  
fname=['variance_nonhelical_1000sim_Dr,3.mat'];%Psimax=2;  
load(fname)  
var_x=var(Matrix(:,end,1),1,1);  
var_x2=var_x;  
hold on  
hold all  
%% -----  
fname=['variance_nonhelical_1000sim_Dr,5.mat'];%Psimax=2;  
load(fname)  
var_x=var(Matrix(:,end,1),1,1);  
var_x3=var_x;  
hold on  
hold all  
%% -----  
fname=['variance_nonhelical_1000sim_Dr,7.mat'];%Psimax=2;  
load(fname)  
var_x=var(Matrix(:,end,1),1,1);  
var_x4=var_x;  
hold on  
hold all
```

```
%% -----  
VarX=[var_x1,var_x2,var_x3,var_x4]  
plot(Dr_range,VarX,'k-', 'linewidth',2)  
xlabel('rotational diffusion D_r');  
ylabel('variance');
```

Bibliography

- [1] simByEuler Euler simulation of stochastic differential equations (SDEs). <https://uk.mathworks.com/help/finance/simbyeuler.html>. Accessed: 2018-07-18.
- [2] D. J. Acheson. *Elementary fluid dynamics*. Oxford University Press, 1990.
- [3] A. L. Alldredge, T. J. Cowles, S. MacIntyre, J. E. B. Rines, P. L. Donaghay, C. F. Greenlaw, D. V. Holliday, M. M. Deksheniaks, J. M. Sullivan, and J. R. V. Zaneveld. Occurrence and mechanisms of formation of a dramatic thin layer of marine snow in a shallow pacific fjord. *Marine Ecology Progress Series*, 233:1–12, 2002.
- [4] M. S. Alqarni and R. N. Bearon. Transport of helical gyrotactic swimmers in channels. *Physics of Fluids*, 28(7):071904, 2016.
- [5] G. B. Arfken and H. J. Weber. *Mathematical Methods for Physicists*. 2005.
- [6] R. N. Bearon. Helical swimming can provide robust upwards transport for gravitactic single-cell algae; a mechanistic model. *Journal of Mathematical Biology*, 66(7):1341–1359, 2013.
- [7] R. N. Bearon, M. A. Bees, and O. A. Croze. Biased swimming cells do not disperse in pipes as tracers: a population model based on microscale behaviour. *Physics of Fluids*, 24(12):121902, 2012.
- [8] R. N. Bearon, D. Grünbaum, and R. A. Cattolico. Relating cell-level swimming behaviors to vertical population distributions in *Heterosigma akashiwo* (raphidophyceae), a harmful alga. *Limnology and Oceanography*, 49(2):607–613, 2004.

- [9] R. N. Bearon and A. L. Hazel. The trapping in high-shear regions of slender bacteria undergoing chemotaxis in a channel. *Journal of Fluid Mechanics*, 771, 2015.
- [10] R. N. Bearon, A. L. Hazel, and G. J. Thorn. The spatial distribution of gyrotactic swimming micro-organisms in laminar flow fields. *Journal of Fluid Mechanics*, 680:602–635, 2011.
- [11] R. N. Bearon and T. J. Pedley. Modelling run-and-tumble chemotaxis in a shear flow. *Bulletin of Mathematical Biology*, 62(4):775, 2000.
- [12] M. A. Bees and O. A. Croze. Mathematics for streamlined biofuel production from unicellular algae. *Biofuels*, 5(1):53–65, 2014.
- [13] M. A. Bees, N. A. Hill, and T. J. Pedley. Analytical approximations for the orientation distribution of small dipolar particles in steady shear flows. *Journal of Mathematical Biology*, 36(3):269–298, 1998.
- [14] H. C. Berg. *Random walks in biology*. Princeton University Press, 1993.
- [15] H. C. Berg and D. A. Brown. Chemotaxis in *Escherichia coli* analysed by three-dimensional tracking. *Nature*, 239(5374):500–504, 1972.
- [16] P. K. Bjørnsen and T. G. Nielsen. Decimeter scale heterogeneity in the plankton during a pycnocline bloom of *Gyrodinium aureolum*. *Marine Ecology Progress Series*, pages 263–267, 1991.
- [17] D. E. Boakes, E. A. Codling, G. J. Thorn, and M. Steinke. Analysis and modelling of swimming behaviour in *Oxyrrhis marina*. *Journal of Plankton Research*, 33(4):641–649, 2010.
- [18] S. M. Bollens, G. Rollwagen-Bollens, J. A. Quenette, and A. B. Bochdansky. Cascading migrations and implications for vertical fluxes in pelagic ecosystems. *Journal of Plankton Research*, 33(3):349–355, 2011.
- [19] J. A. Bonachela, C. A. Klausmeier, K. F. Edwards, E. Litchman, and S. A. Levin. The role of phytoplankton diversity in the emergent oceanic stoichiometry. *Journal of Plankton Research*, 38(4):1021–1035, 2015.
- [20] B. Bradie. *A friendly introduction to numerical analysis*. Pearson Education India, 2006.

- [21] H. Brenner and M. H. Weissman. Rheology of a dilute suspension of dipolar spherical particles in an external field. II. effects of rotary brownian motion. *Journal of Colloid and Interface Science*, 41(3):499–531, 1972.
- [22] D. R. Brillinger. A particle migrating randomly on a sphere. *Journal of Theoretical Probability*, 10(2), 1997.
- [23] D. R. Brumley, K. Y. Wan, M. Polin, and R. E. Goldstein. Flagellar synchronization through direct hydrodynamic interactions. *Elife*, 3, 2014.
- [24] S. Childress. *Mechanics of swimming and flying*, volume 2. Cambridge University Press, 1981.
- [25] Y. Chisti. Biodiesel from microalgae beats bioethanol. *Trends in Biotechnology*, 26(3):126–131, 2008.
- [26] P. Collet, L. Lardon, A. Hélias, S. Bricout, I. Lombaert-Valot, B. Perrier, O. Lépine, J. P. Steyer, and O. Bernard. Biodiesel from microalgae—life cycle assessment and recommendations for potential improvements. *Renewable Energy*, 71:525–533, 2014.
- [27] F. Coquet, Y. Hu, J. Mémin, and S. Peng. Filtration-consistent nonlinear expectations and related g-expectations. *Probability Theory and Related Fields*, 123(1):1–27, 2002.
- [28] R. Cortez. The method of regularized stokeslets. *SIAM Journal on Scientific Computing*, 23(4):1204–1225, 2001.
- [29] H. C. Crenshaw. A new look at locomotion in microorganisms: rotating and translating. *American Zoologist*, 36(6):608–618, 1996.
- [30] H. C. Crenshaw, C. N. Ciampaglio, and M. McHenry. Analysis of the three-dimensional trajectories of organisms: estimates of velocity, curvature and torsion from positional information. *Journal of Experimental Biology*, 203(6):961–982, 2000.
- [31] O. A. Croze, R. N. Bearon, and M. A. Bees. Gyrotactic swimmer dispersion in pipe flow: experimental challenge of competing models. *Journal of Fluid Mechanics*, 2017.

- [32] O. A. Croze, G. Sardina, M. Ahmed, M. A. Bees, and L. Brandt. Dispersion of swimming algae in laminar and turbulent channel flows: consequences for photobioreactors. *Journal of The Royal Society Interface*, 10(81):20121041, 2013.
- [33] M. M. Deksheniaks, P. L. Donaghay, J. M. Sullivan, J. E. B. Rines, T. R. Osborn, and M. S. Twardowski. Temporal and spatial occurrence of thin phytoplankton layers in relation to physical processes. *Marine Ecology Progress Series*, 223:61–71, 2001.
- [34] N. Desai and A. M. Ardekani. Modeling of active swimmer suspensions and their interactions with the environment. *Soft Matter*, 13(36):6033–6050, 2017.
- [35] K. Drescher, R. E. Goldstein, N. Michel, M. Polin, and I. Tuval. Direct measurement of the flow field around swimming microorganisms. *Physical Review Letters*, 105(16):168101, 2010.
- [36] W. M. Durham, E. Climent, M. Barry, F. D. Lillo, G. Boffetta, M. Cencini, and R. Stocker. Turbulence drives microscale patches of motile phytoplankton. *Nature Communications*, 4, 2013.
- [37] W. M. Durham and R. Stocker. Thin phytoplankton layers: characteristics, mechanisms, and consequences. *Annual Review of Marine Science*, 4, 2012.
- [38] A. R. Edmonds. *Angular momentum in quantum mechanics*. Princeton University Press, 1960.
- [39] A. Engesmo, W. Eikrem, S. Seoane, K. Smith, B. Edvardsen, A. Hofgaard, and C. R. Tomas. New insights into the morphology and phylogeny of *Heterosigma akashiwo* (*Raphidophyceae*), with the description of *Heterosigma minor* sp. nov. *Phycologia*, 55(3):279–294, 2016.
- [40] B. Ezhilan and D. Saintillan. Transport of a dilute active suspension in pressure-driven channel flow. *Journal of Fluid Mechanics*, 777:482–522, 2015.
- [41] N. E. Farthing, R. C. Findlay, J. F. Jikeli, P. B. Walrad, M. A. Bees, and L. G. Wilson. Simultaneous two-color imaging in digital holographic microscopy. *Optics Express*, 25(23):28489–28500, 2017.
- [42] T. Fenchel. How dinoflagellates swim. *Protist*, 152(4):329–338, 2001.

- [43] I. Frankel and H. Brenner. Generalized Taylor dispersion phenomena in unbounded homogeneous shear flows. *Journal of Fluid Mechanics*, 230:147–181, 1991.
- [44] I. Frankel and H. Brenner. Taylor dispersion of orientable Brownian particles in unbounded homogeneous shear flows. *Journal of Fluid Mechanics*, 255:129–156, 1993.
- [45] C. Gardiner. *Stochastic methods*. Springer Berlin, 2009.
- [46] R. E. Goldstein. Green algae as model organisms for biological fluid dynamics. *Annual Review of Fluid Mechanics*, 47, 2015.
- [47] R. E. Goldstein, M. Polin, and I. Tuval. Noise and synchronization in pairs of beating eukaryotic flagella. *Physical Review Letters*, 103(16):168103, 2009.
- [48] E. G. Govorunova and O. A. Sineshchekov. Chemotaxis in the green flagellate alga *Chlamydomonas*. *Biochemistry*, 70(7):717–725, 2005.
- [49] G. Grimmett and D. Stirzaker. *Probability and random processes*. Oxford University Press, 2001.
- [50] J. S. Guasto, R. Rusconi, and R. Stocker. Fluid mechanics of planktonic microorganisms. *Annual Review of Fluid Mechanics*, 44:373–400, 2012.
- [51] E. Gurarie, D. Grünbaum, and M. T. Nishizaki. Estimating 3D movements from 2D observations using a continuous model of helical swimming. *Bulletin of Mathematical Biology*, 73(6):1358–1377, 2011.
- [52] W. F. Hall and S. N. Busenber. Viscosity of magnetic suspensions. *The Journal of Chemical Physics*, 51(1):137–144, 1969.
- [53] G. M. Hallegraeff. A review of harmful algal blooms and their apparent global increase. *Phycologia*, 32(2):79–99, 1993.
- [54] Y. Hara and M. Chihara. Morphology, ultrastructure and taxonomy of the raphidophycean alga *Heterosigma akashiwo*. *Journal of Plant Research*, 100(2):151–163, 1987.
- [55] D. J. Higham. An algorithmic introduction to numerical simulation of stochastic differential equations. *SIAM Review*, 43(3):525–546, 2001.

- [56] N. A. Hill and M. A. Bees. Taylor dispersion of gyrotactic swimming microorganisms in a linear flow. *Physics of Fluids*, 14(8):2598–2605, 2002.
- [57] N. A. Hill and D. P. Häder. A biased random walk model for the trajectories of swimming micro-organisms. *Journal of Theoretical Biology*, 186(4):503–526, 1997.
- [58] N. A. Hill and T. J. Pedley. Bioconvection. *Fluid Dynamics Research*, 37(1-2):1–20, 2005.
- [59] Y. Hwang and T. J. Pedley. Bioconvection under uniform shear: linear stability analysis. *Journal of Fluid Mechanics*, 738:522–562, 2014.
- [60] H. S. Jennings. On the significance of the spiral swimming of organisms. *The American Naturalist*, 35(413):369–378, 1901.
- [61] H. F. Jones. *Groups, representations and physics*. CRC Press, 1998.
- [62] V. Kantsler, J. Dunkel, M. Blayney, and R. E. Goldstein. Rheotaxis facilitates upstream navigation of mammalian sperm cells. *Elife*, 3, 2014.
- [63] T. Kaya and H. Koser. Direct upstream motility in *Escherichia coli*. *Biophysical Journal*, 102(7):1514–1523, 2012.
- [64] J. O. Kessler. Hydrodynamic focusing of motile algal cells. *Nature*, 313:218–220, 1985.
- [65] J. O. Kessler. The external dynamics of swimming micro-organisms. *Progress in Psychological Research*, 4:257–307, 1986.
- [66] S. Kim and S. J. Karrila. *Microhydrodynamics: Principles and Selected Applications*. Courier Corporation, 2005.
- [67] T. Kiørboe. *A mechanistic approach to plankton ecology*. Princeton University Press, 2008.
- [68] P. E. Kloeden and E. Platen. *Numerical solution of stochastic differential equations*. Applications of Mathematics: 23. Berlin ; Springer., 1999.
- [69] K. Koukaras and G. Nikolaidis. Dinophysis blooms in greek coastal waters (Thermaikos Gulf, NW Aegean Sea). *Journal of Plankton Research*, 26(4):445–457, 2004.

- [70] E. Lauga and T. R. Powers. The hydrodynamics of swimming microorganisms. *Reports on Progress in Physics*, 72(9):096601, 2009.
- [71] M. Lebert and D. P. Häder. How *Euglena* tells up from down. *Nature*, 379(6566):590–590, 1996.
- [72] T. Leiknes and H. Ødegaard. The development of a biofilm membrane bioreactor. *Desalination*, 202(1-3):135–143, 2006.
- [73] M. Lévy. The modulation of biological production by oceanic mesoscale turbulence. In *Transport and Mixing in Geophysical Flows*, pages 219–261. Springer, 2008.
- [74] G. Li and J. X. Tang. Accumulation of microswimmers near a surface mediated by collision and rotational Brownian motion. *Physical Review Letters*, 103(7):078101, 2009.
- [75] A. Manela and I. Frankel. Generalized Taylor dispersion in suspensions of gyrotactic swimming microorganisms. *Journal of Fluid Mechanics*, 490:99–127, 2003.
- [76] R. M. Mazo. *Brownian motion: fluctuations, dynamics, and applications*, volume 112. Oxford, 2008.
- [77] T. D. Montenegro-Johnson, A. A. Smith, D. J. Smith, D. Loghin, and J. R. Blake. Modelling the fluid mechanics of cilia and flagella in reproduction and development. *The European Physical Journal*, 35(10):111, 2012.
- [78] T. D. Montenegro-Johnson, D. J. Smith, and D. Loghin. Physics of rheologically enhanced propulsion: different strokes in generalized stokes. *Physics of Fluids*, 25(8):081903, 2013.
- [79] B. Øksendal. *Stochastic differential equations*. Springer, 2003.
- [80] S. O’Malley and M. A. Bees. The orientation of swimming biflagellates in shear flows. *Bulletin of mathematical biology*, 74(1):232–255, 2012.
- [81] O. S. Pak and E. Lauga. Generalized squirming motion of a sphere. *Journal of Engineering Mathematics*, 88(1):1–28, 2014.
- [82] T. J. Pedley and J. O. Kessler. A new continuum model for suspensions of gyrotactic microorganisms. *Journal of Fluid Mechanics*, 212:155–182, 1990.

- [83] T. J. Pedley and J. O. Kessler. Hydrodynamic phenomena in suspensions of swimming microorganisms. *Annu. Rev. Fluid Mech.*, 24(1):313–358, 1992.
- [84] S. Peng. Backward stochastic differential equation, nonlinear expectation and their applications. In *Proceedings of the International Congress of Mathematicians 2010 (ICM 2010) (In 4 Volumes) Vol. I: Plenary Lectures and Ceremonies Vols. II–IV: Invited Lectures*, pages 393–432. World Scientific, 2010.
- [85] S. L. Phillips, H. Ozbek, A. Igbene, and G. Litton. Viscosity of NaCl and other solutions up to 350°C and 50MPa pressures. 1980.
- [86] J. R. Platt. Bioconvection patterns in Cultures of Free-Swimming Organisms. *Science*, 133(3466):1766–1767, 1961.
- [87] M. Polin, I. Tuval, K. Drescher, J. P. Gollub, and R. E. Goldstein. *Chlamydomonas* swims with two “gears” in a eukaryotic version of run-and-tumble locomotion. *Science*, 325(5939):487–490, 2009.
- [88] E. M. Purcell. Life at low Reynolds number. *American Journal of Physics*, 45(1):3–11, 1977.
- [89] J. A. Raven and P. G. Falkowski. Oceanic sinks for atmospheric CO₂. *Plant, Cell and Environment*, 22(6) : 741 – 755, 1999.
- [90] J. E. J. Rensel, N. Haigh, and T. J. Tynan. Fraser river sockeye salmon marine survival decline and harmful blooms of heterosigma akashiwo. *Harmful Algae*, 10(1):98–115, 2010.
- [91] G. A. Riley. The relationship of vertical turbulence and spring diatom flowerings. *Journal of Marine Research*, 5(1):67–87, 1942.
- [92] K. F. Riley, M. P. Hobson, and S. J. Bence. *Mathematical methods for Physics and Engineering: a comprehensive guide*. Cambridge University Press, 2006.
- [93] H. Risken. *The Fokker-Planck Equation*. Springer, second edition, 1996.
- [94] J. P. Ryan, M. A. McManus, and J. M. Sullivan. Interacting physical, chemical and biological forcing of phytoplankton thin-layer variability in Monterey Bay, California. *Continental Shelf Research*, 30(1):7–16, 2010.
- [95] L. F. Shampine and M. W. Reichelt. The matlab ode suite. *SIAM journal on scientific computing*, 18(1):1–22, 1997.

- [96] T. J. Smayda. Harmful algal blooms: their ecophysiology and general relevance to phytoplankton blooms in the sea. *Limnology and Oceanography*, 42(5part2):1137–1153, 1997.
- [97] K. Sobczyk. *Stochastic differential equations: with applications to Physics and Engineering*, volume 40. Springer Science and Business Media, 2013.
- [98] A. Sournia. Red tide and toxic marine phytoplankton of the world ocean: an inquiry into biodiversity. *Harmful Marine Algal Blooms*, pages 103–112, 1995.
- [99] M. T. Stacey, M. A. McManus, and J. V. Steinbeck. Convergences and divergences and thin layer formation and maintenance. *Limnology and Oceanography*, 52(4):1523–1532, 2007.
- [100] J. V. Steinbeck, A. Genin, S. G. Monismith, J. R. Koseff, R. Holzman, and R. G. Labiosa. Turbulent mixing in fine-scale phytoplankton layers: Observations and inferences of layer dynamics. *Continental Shelf Research*, 30(5):442–455, 2010.
- [101] S. C. Takatori and J. F. Brady. Swim stress, motion, and deformation of active matter: effect of an external field. *Soft Matter*, 10(47):9433–9445, 2014.
- [102] S. Y. Tan and Y. Tatsumura. Alexander Fleming (1881–1955): discoverer of penicillin. *Singapore Medical Journal*, 56(7):366, 2015.
- [103] F. J. R. Taylor and R. Haigh. The ecology of fish-killing blooms of the chloromonad flagellate *Heterosigma* in the strait of Georgia and adjacent waters. *Toxic Phytoplankton Blooms in the Sea*, pages 705–710, 1993.
- [104] G. J. Thorn and R. N. Bearon. Transport of spherical gyrotactic organisms in general three-dimensional flow fields. *Physics of Fluids*, 22(4):041902, 2010.
- [105] M. Vesik and Ø Moestrup. The flagellar root system in *Heterosigma akashiwo* (*Raphidophyceae*). *Protoplasma*, 137(1):15–28, 1987.
- [106] R. R. Vuppula, M. S. Tirumkudulu, and K. V. Venkatesh. Chemotaxis of *Escherichia coli* to L-serine. *Physical Biology*, 7(2):026007, 2010.
- [107] K. Y. Wan and R. E. Goldstein. Coordinated beating of algal flagella is mediated by basal coupling. *Proceedings of the National Academy of Sciences*, 113(20):E2784–E2793, 2016.

BIBLIOGRAPHY

- [108] G. Werner, H. Hagenmaier, H. Drautz, A. Baumgartner, and H. Zähler. Metabolic products of microorganisms. *The Journal of Antibiotics*, 37(2):110–117, 1984.
- [109] C. W. Wolgemuth. Biomechanics of cell motility. In *Comprehensive Biophysics*. Elsevier Inc., 2012.
- [110] J. M. Yeomans, D. O. Pushkin, and H. Shum. An introduction to the hydrodynamics of swimming microorganisms. *European Physical Journal Special Topics*, 223(9):1771–1785, 2014.
- [111] Y. Zhu. Immobilized cell fermentation for production of chemicals and fuels. In *Bioprocessing for Value-Added Products from Renewable Resources*, pages 373–396. Elsevier, 2007.